RICE UNIVERSITY

# Modeling Fluid Flow Effects on Shallow Pore Water Chemistry and Methane Hydrate Distribution in Heterogeneous Marine Sediment

by

**Sayantan Chatterjee**

A THESIS SUBMITTED
IN PARTIAL FULFILLMENT OF THE
REQUIREMENTS FOR THE DEGREE

**Doctor of Philosophy**

APPROVED, THESIS COMMITTEE:

George J. Hirasaki, Chair
A. J. Hartsook Professor in Chemical
and Biomolecular Engineering

Walter G. Chapman, co-Chair
William W. Akers Professor in Chemical
and Biomolecular Engineering

Kyriacos Zygourakis
A.J. Hartsook Professor in Chemical and
Biomolecular Engineering

Gerald R. Dickens
Professor in Earth Science

Brandon Dugan
Assistant Professor in Earth Science

Houston, Texas
April, 2012

ABSTRACT

Modeling Fluid Flow Effects on Shallow Pore Water Chemistry and Methane Hydrate Distribution in Heterogeneous Marine Sediment

by

Sayantan Chatterjee

The depth of the sulfate-methane transition (SMT) above gas hydrate systems is a direct proxy to interpret upward methane flux and hydrate saturation. However, two competing reaction pathways can potentially form the SMT. Moreover, the pore water profiles across the SMT in shallow sediment show broad variability leading to different interpretations for how carbon, including $CH_4$, cycles within gas-charged sediment sequences over time. The amount and distribution of marine gas hydrate impacts the chemistry of several other dissolved pore water species such as the dissolved inorganic carbon (DIC). A one-dimensional (1-D) numerical model is developed to account for downhole changes in pore water constituents, and transient and steady-state profiles are generated for three distinct hydrate settings. The model explains how an upward flux of $CH_4$ consumes most $SO_4^{2-}$ at a shallow SMT implying that anaerobic oxidation of methane (AOM) is the dominant $SO_4^{2-}$ reduction pathway, and how a large flux of $^{13}\mathrm{C}$-enriched DIC enters the SMT from depth impacting chemical changes across the SMT. Crucially, neither the

concentration nor the $\delta^{13}\mathrm{C}$ of DIC can be used to interpret the chemical reaction causing the SMT.

The overall thesis objective is to develop generalized models building on this 1-D framework to understand the primary controls on gas hydrate occurrence. Existing 1-D models can provide first-order insights on hydrate occurrence, but do not capture the complexity and heterogeneity observed in natural gas hydrate systems. In this study, a two-dimensional (2-D) model is developed to simulate multiphase flow through porous media to account for heterogeneous lithologic structures (e.g., fractures, sand layers) and to show how focused fluid flow within these structures governs local hydrate accumulation. These simulations emphasize the importance of local, vertical, fluid flux on local hydrate accumulation and distribution. Through analysis of the fluid fluxes in 2-D systems, it is shown that a local Peclet number characterizes the local hydrate and free gas saturations, just as the Peclet number characterizes hydrate saturations in 1-D, homogeneous systems. Effects of salinity on phase equilibrium and co-existence of hydrate and gas phases can also be investigated using these models.

Finally, infinite slope stability analysis assesses the model to identify for potential subsea slope failure and associated risks due to hydrate formation and free gas accumulation. These generalized models can be adapted to specific field examples to evaluate the amount and distribution of hydrate and free gas and to identify conditions favorable for economic gas production.

# Acknowledgments

This dissertation would not have been possible without the help and support of several individuals who in one way or another have contributed to the preparation and successful completion of this work. First and foremost, I offer my sincerest gratitude to my advisor, Dr George Hirasaki, for being a great mentor. His plethora of knowledge, diligent work ethic, patience and enthusiasm towards research motivated me to conduct this multidisciplinary research project. I express my deepest appreciation to him for his invaluable advice, support and guidance.

I convey my profound gratitude and indebtedness to Dr Walter Chapman for co-advising me on this study. His continued encouragement and engaging discussions made my graduate school a truly memorable experience. I thank Dr Kyriacos Zygourakis, Dr Jerry Dickens and Dr Brandon Dugan for serving on my thesis committee.

A special note of appreciation goes to Dr Jerry Dickens for his insightful suggestions and several stimulating discussions which not only broadened my thinking and exposed me to the field of geochemistry but also helped me tackle some of the challenging problems from an earth science perspective. I attribute my improved quality of scientific writing to him. I gratefully thank Dr Brandon Dugan

for strengthening my foundation in hydrogeology, geomechanics and providing constructive comments and critical assessment of my research work.

A notable acknowledgement to the gas hydrate group at Rice including Dr Gaurav Bhatnagar, Dr Glen Snyder, Dr Hugh Daigle and Guangsheng Gu for their invaluable time, helpful discussions, and critical commentary through numerous meetings, papers and presentations. Special thanks to Dr Jan Hewitt and Dr Tracy Volz for greatly honing my technical writing and presentation skills.

I am truly grateful to all the faculty and staff of the Chemical and Biomolecular Engineering department for their kind cooperation and support. I am blessed to be surrounded by extremely helpful colleagues, especially in the Transport and Thermodynamic Properties lab, a compassionate and cheerful group of friends, and a considerate housemate throughout my graduate career which made my stay at Rice not only fruitful, but also a delightful experience to remember.

I acknowledge financial support from the Department of Energy under Award No. DE-FC26-06NT42960, the Shell Center for Sustainability and the Consortium of Processes in Porous Media at Rice University. I thank the captains, crews and fellow shipboard scientists of Ocean Drilling Program (ODP) Legs 112, 201, 204 and Gulf of Mexico Joint Industry Program (JIP) for successful drilling and the collection and analyses of samples. My thesis work was supported in part by the Shared University Grid at Rice funded by NSF under Grant EIA-0216467, and a partnership between Rice University, Sun Microsystems, and Sigma Solutions, Inc.

Lastly, I owe a heartfelt thank you to my beloved parents, sister, fiancee, and my family in India for their endless love and continued support. My fulfilling upbringing, education, and this advanced degree would not have been possible without their selfless sacrifices and encouragement. I convey my deepest appreciation and most sincere regards to them.

Sayantan Chatterjee

# Contents

# Illustrations

# Tables

# Glossary

1-D: One-dimensional
2-D: Two-dimensional
AGHS: Average Gas Hydrate Saturation
AOM: Anaerobic Oxidation of Methane
BHSZ: Base of Hydrate Stability Zone
BSR: Bottom Simulating Reflector
DIC: Dissolved Inorganic Carbon
DOE: Department of Energy
FS: Factor of Safety
GHOZ: Gas Hydrate Occurrence Zone
GHSZ: Gas Hydrate Stability Zone
GOM: Gulf of Mexico
HS: Head Space
IODP: Integrated Ocean Drilling Program
JIP: Joint Industry Program
KC: Keathley Canyon
LWD: Logging While Drilling
MBSL: Meters Below Sealevel
MBSF: Meters Below Seafloor
NGHP: National Gas Hydrate Program
ODP: Ocean Drilling Program
OSR: Organoclastic Sulfate Reduction
PCS: Pressure Core Sampler
PDB: Pee Dee Belemnite
POC: Particulate Organic Carbon
SMI: Sulfate Methane Interface
SMT: Sulfate Methane Transition
SRZ: Sulfate Reduction Zone
TOC: Total Organic Carbon
VE: Vertical Exaggeration

# Notations

$c_i^j$: Mass fraction of component $i$ in phase $j$

$\tilde{c}_i^j$: Normalized mass fraction of component $i$ in phase $j$

$c_{m,eqb}$: Equilibrium $CH_4$ mass fraction in pore water at the base of the GHSZ

$c_{s,o}$: Mass fraction of $SO_4^{2-}$ in seawater

$c_{b,o}$: Mass fraction of dissolved inorganic carbon (DIC) in seawater

$c_{Ca,o}$: Mass fraction of $Ca^{2+}$ in seawater

$D_m$: $CH_4$ diffusivity in seawater

$D_s$: $SO_4^{2-}$ diffusivity in seawater

$D_b$: DIC diffusivity of in seawater

$D_{Ca}$: $Ca^{2+}$ diffusivity in seawater

$D_{Cl}$: $Cl^-$ diffusivity in seawater

$Da$: Damkohler number for methanogenesis

$Da_{AOM}$: Damkohler number for anaerobic oxidation of methane (AOM)

$Da_{POC}$: Damkohler number for organoclastic sulfate reduction (OSR)

$dT/dz$: Geothermal gradient

$g$: Acceleration due to gravity

$\mathbf{k}$: Absolute sediment permeability tensor

$\mathbf{k}_o$: Absolute sediment permeability at the seafloor

$k_{rj}$: Relative permeability of phase $j$

$k_{r,j}^o$: End-point value of $k_{rj}$

$L_o$: Seafloor depth

$L_t$: Depth to the base of the GHSZ

$L_z$: Depth to the base of the simulation domain

$L_x$: Width of the simulation domain

$L_s$: SMT depth

$L_\phi$: Characteristic depth of compaction

$M_{CH_4}$: Molecular weight of $CH_4$

$M_{SO_4}$: Molecular weight of $SO_4^{2-}$

$M_{HCO_3}$: Molecular weight of DIC

$M_{Ca}$: Molecular weight of $Ca^{2+}$

$M_{POC}$: Molecular weight of particulate organic carbon (POC)

$M_{org}$: Molecular weight of organic matter

$N_{sc}$: Sedimentation and compaction group

$N_{t\phi}$: Porosity and compaction group

$n$: Pore size distribution index

$P_o$: Hydrostatic pressure at the seafloor

$p_j$: Pressure of phase $j$

$P_c$: Capillary pressure

$P_{c,o}$: Capillary pressure at reference value

$P_{ce,o}$: Capillary entry pressure at reference value

$Pe_1$: Peclet number for compaction driven flow

$Pe_2$: Peclet number for external fluid flow

$r$: Reaction rate

$\dot{S}$: Sedimentation rate at the seafloor

$S_j$: Saturation of phase $j$

$S_{jr}$: Residual saturation of phase $j$

$t$: Dimensional time

$\tilde{t}$: Dimensionless time

$T_o$: Seafloor temperature

$U_f$: Net fluid flux

$U_{sed}$: Sediment flux

$\tilde{U}_f$: Dimensionless net fluid flux

$\tilde{U}_{sed}$: Dimensionless sediment flux

$U_{f,sed}$: Fluid flux due to sedimentation and compaction

$U_{f,ext}$: Fluid flux due to external fluid flow

$v_j$: Velocity of phase $j$

$z$: Vertical depth below seafloor

$\tilde{z}$: Normalized vertical depth below seafloor

$\alpha$: Organic carbon content in sediment

$\tilde{\alpha}$: Normalized organic carbon content in sediment

$\alpha_o$: Labile organic carbon content at seafloor

$\beta$: Normalized labile organic carbon content at seafloor

$\delta^{13}\mathrm{C}_{POC}$: $\delta^{13}\mathrm{C}$ of POC

$\delta^{13}\mathrm{C}_{CH_4}$: $\delta^{13}\mathrm{C}$ of $CH_4$

$\delta^{13}\mathrm{C}_{HCO_3}$: $\delta^{13}\mathrm{C}$ of DIC

$\delta^{13}\mathrm{C}_{CH_4,meth}$: $\delta^{13}\mathrm{C}$ of $CH_4$ generated by methanogenesis

$\delta^{13}\mathrm{C}_{HCO_3,meth}$: $\delta^{13}\mathrm{C}$ of DIC generated by methanogenesis

$\delta^{13}\mathrm{C}_{HCO_3,POC}$: $\delta^{13}\mathrm{C}$ of DIC generated by OSR

$\epsilon_m$: Fractionation factor for methanogenesis

$\phi$: Sediment porosity

$\tilde{\phi}$: Reduced sediment porosity

$\phi_o$: Sediment porosity at the seafloor

$\phi_\infty$: Minimum porosity at greatest depth

$\gamma$, $\eta$: Reduced porosity parameters

$\lambda$: Reaction rate constant for methanogenesis

$\lambda_{AOM}$: Reaction rate constant for AOM

$\lambda_{POC}$: Reaction rate constant for OSR

$\mu_j$: Viscosity of phase $j$

$\rho_j$: Density of phase $j$

$\tilde{\rho}_j$: Normalized density of phase $j$

$\sigma_v$: Total vertical stress

$\sigma_{gw}$: Interfacial tension at gas-water contact

$\sigma_\phi$: Characteristic stress of compaction

$\theta$: Gas-water contact angle

**Subscripts and superscripts**

Components:

$w$: Water

$s$: Sulfate or $SO_4^{2-}$

$m$: Methane or $CH_4$

$b$: DIC or $HCO_3^-$

$Ca$: Calcium or $Ca^{2+}$

$Cl$: Chloride or $Cl^-$

$CaCO_3$: Calcium carbonate or Calcite

Phases:

$l$: Liquid or dissolved

$h$: Hydrate

$g$: Free gas

$sed$: Sediment

Reactions:

$AOM$: Anaerobic oxidation of methane

$POC$: POC-driven sulfate consumption or OSR

$meth$: Methanogenesis reaction

$ppt$: Calcite precipitation reaction

# Chapter 1

# Introduction

Solid gas hydrates form when water molecules encapsulate low molecular weight gas molecules at relatively high pressure, low temperature, high water activity, and high gas concentration (*Sloan*, 2003; *Sloan and Koh*, 2007). These favorable conditions exist along many continental margins and in permafrost environments where hydrocarbon gases, usually $CH_4$, accumulate in sediment pore space within a shallow depth interval commonly called the gas hydrate stability zone (GHSZ). This thesis focuses on natural gas hydrates found in marine sediments. Primarily, hydrates can form one of the three crystalline structures, namely: structure I, structure II and structure H, depending on the guest gas composition. Methane hydrates are most commonly found in nature, mostly as structure I hydrates. Compositional studies have shown that trace amounts of higher hydrocarbons such as ethane and propane or other gases such as carbon dioxide and hydrogen sulfide also form hydrates (*Kastner et al*., 1998; *Milkov and Sassen*, 2000; *Milkov et al*., 2005). Combinations of methane along with higher hydrocarbons result in formation of structure II and H hydrates (*Subramanian et al*., 2000). While their global abundance and distribution remain uncertain (e.g., *Kvenvolden*, 1988, 1993;

*Dickens*, 2001a; *Milkov*, 2004; *Buffett and Archer*, 2004; *Klauda and Sandler*, 2005; *Archer*, 2007), marine gas hydrates may constitute a future energy resource (e.g., *Collett*, 2002; *Walsh et al*., 2009), a deep water geohazard (e.g., *Borowski and Paull*, 1997; *Briaud and Chaouch*, 1997; *Kwon et al*., 2010), and an important constituent of the global carbon cycle (e.g., *Dickens*, 2003, 2011; *Archer et al*., 2009).

Behind much of the current interest lie two related questions: where and how much gas hydrate is distributed with respect to sedimentary depth at a given location? The amount and distribution of marine gas hydrates have been investigated for more than four decades through several sediment core analyses, logging and geophysical data and numerous numerical modeling efforts. However, there are still some open questions, and it is of paramount importance to understand the factors that govern the accumulation and distribution of these hydrates in subsea sediments. Therefore, to elucidate the role of natural gas hydrates as a potential energy resource, an agent for climate change or a submarine geohazard, this thesis focuses on generalized numerical modeling techniques for multiphase flow through porous media to discuss some of the primary controls on hydrate accumulation in space and time. As a part of this dissertation study, a basin-scale numerical model is developed to simulate spatial and temporal distribution of hydrate and free gas over geologic timescales. The overall thesis objective is to model these dynamic marine systems with

heterogeneous lithologic structures and investigate local and regional distribution of elevated saturations of hydrates as a result of focused fluid flow. In addition to developing these generalized numerical models, detailed pore water geochemistry is discussed to interpret the carbon cycling processes in shallow sediment below the seafloor. In essence, these models can be used to identify ”sweet-spots” to detect and locate concentrated gas hydrate deposits that may be favorable for economic gas production or to assess geohazards associated with slope failures in submarine sediment.

These generalized models can be adapted to study field examples and explain some of the classic hydrate settings that have been investigated in the last forty years of ocean drilling expeditions. This thesis impacts existing gas hydrate literature and answers some of the open-ended questions pertaining to gas hydrate amount and distribution in heterogeneous marine sediments.

## 1.1 Organization

This thesis is divided into eight chapters. Chapter two briefly discusses the background literature on natural gas hydrates and the motivation to model the amount and distribution of these hydrates in marine sediments. Existing state-of-the-art hydrate accumulation models and their respective drawbacks are reviewed.

The first-order distribution of gas hydrate in marine sediment sequences has

been simulated previously at multiple drill sites using numerical models and site-specific parameters. Recently, these modeling efforts have been modified to show that the production of methane and the accumulation of gas hydrate impacts the pore water profiles of several dissolved species, as observed. However, this leads to two basic issues: both the concentration and the carbon isotope composition of dissolved inorganic carbon (DIC) vary considerably across the sulfate-methane transition (SMT) in shallow marine sediment at locations with gas hydrate. This variability has led to different interpretations for how carbon, including $CH_4$, cycles within gas-charged sediment sequences over time.

Chapter three discusses development of a one-dimensional (1-D) model for the formation of gas hydrate to account for downhole changes in dissolved $CH_4$, $SO_4^{2-}$, DIC, and $Ca^{2+}$, and the $\delta^{13}\mathrm{C}$ of DIC. The model includes advection, diffusion, and two reactions that consume $SO_4^{2-}$: organoclastic sulfate reduction (OSR) and anaerobic oxidation of methane (AOM). Using this model and site-specific parameters, steady-state pore water profiles are simulated for two sites containing gas hydrate but different carbon chemistry across the SMT: Site 1244 (Hydrate Ridge; DIC = 38 mM, $\delta^{13}\mathrm{C}$ of DIC = -22.5 $^{0}/_{00}$ PDB) and Site Keathley Canyon (KC) 151-3 (Gulf of Mexico; DIC = 16 mM, $\delta^{13}\mathrm{C}$ of DIC = -49.6 $^{0}/_{00}$ PDB).

In chapter four, the 1-D model is used to illustrate another unique Site 685/1230 in the Peru Margin with extreme carbon chemistry at the SMT (DIC = 55 mM, $\delta^{13}\mathrm{C}$ of DIC = -13 $^{0}/_{00}$ PDB). The pore water constituents at this site, measure extreme

values compared to those that have been reported in the forty years history of deep-sea research. Steady-state profiles are simulated which resemble those as measured at this site, and carbon cycling is interpreted along with other chemical changes across the SMT in shallow sediment. However, these steady-state results are unable to explain the 4.3 Myr hiatus at this site. Transient results are generated to interpret the chemical changes across the SMT. The transient profiles resemble the field data favorably.

A series of 1-D dynamic flow hydrate models that have been published including the one described here provide a first-order approximation of pore water profiles, hydrate and free gas saturation at different geologic sites. However, they are inadequate to show how focused fluid flow dictates gas hydrate accumulation and distribution, which needs to be modeled in two or more spatial dimensions. Therefore, chapter five develops a two-dimensional (2-D) sedimentation-compaction fluid flow model to simulate gas hydrate and free gas accumulation in heterogeneous marine sediment over geologic timescales. The model includes several physical processes such as sedimentation and compaction, biogenic methane generation, diffusion, multiphase fluid flow, and migration of dissolved methane, water, and free gas. The system of equations is normalized using a novel scaling scheme developed in *Bhatnagar et al*. (2007). This leads to a few key dimensionless groups that are used to characterize distinct geologic settings, as compared to a series of site-specific studies published in the literature.

Models of clay-dominated systems show that over thousands to millions of years, gas hydrate can occlude the pore system, which results in pressure build-up and hydraulic fracturing. These fractures then fill with hydrate. In chapter six, focused fluid flow through a fracture network and/or high permeability sand layers affecting local hydrate saturation is illustrated using the two-dimensional model. Numerous observations of heterogeneous hydrate accumulation can be explained and finally, the effects of salinity on phase equilibria and methane solubility are briefly discussed.

Chapter seven evaluates seafloor stability, potential slope failure and discusses associated risks due to hydrate formation in subsea sediments. Chapter eight summarizes the conclusions of this thesis and proposes some significant research directions for the future arising from this study.

# Chapter 2

# Background

## 2.1 Overview

Gas hydrates are solids comprised of low molecular weight gas and water that form at relatively high pressure, low temperature, low salinity and high gas concentrations (*Sloan*, 2003; *Sloan and Koh*, 2007). Such conditions prevail along many continental margins (Figure 2.1) where hydrocarbon gases, principally $CH_4$, have accumulated in pore space of a depth horizon known as the gas hydrate stability zone (GHSZ; Figure 2.2). Marine gas hydrates have attracted attention because they may constitute a potential energy resource (e.g., *Collett*, 2002; *Walsh et al*., 2009), a subsea geohazard (e.g., *Borowski and Paull*, 1997; *Briaud and Chaouch*, 1997; *Kwon et al*., 2010), and a large component of the global carbon cycle (e.g., *Dickens*, 2003, 2011; *Archer et al*., 2009).

## 2.2 Marine Gas Hydrate Systems

Considerable current interest is focused on how and why gas hydrate occurs at a given concentration with sedimentary depth at a given location. For many

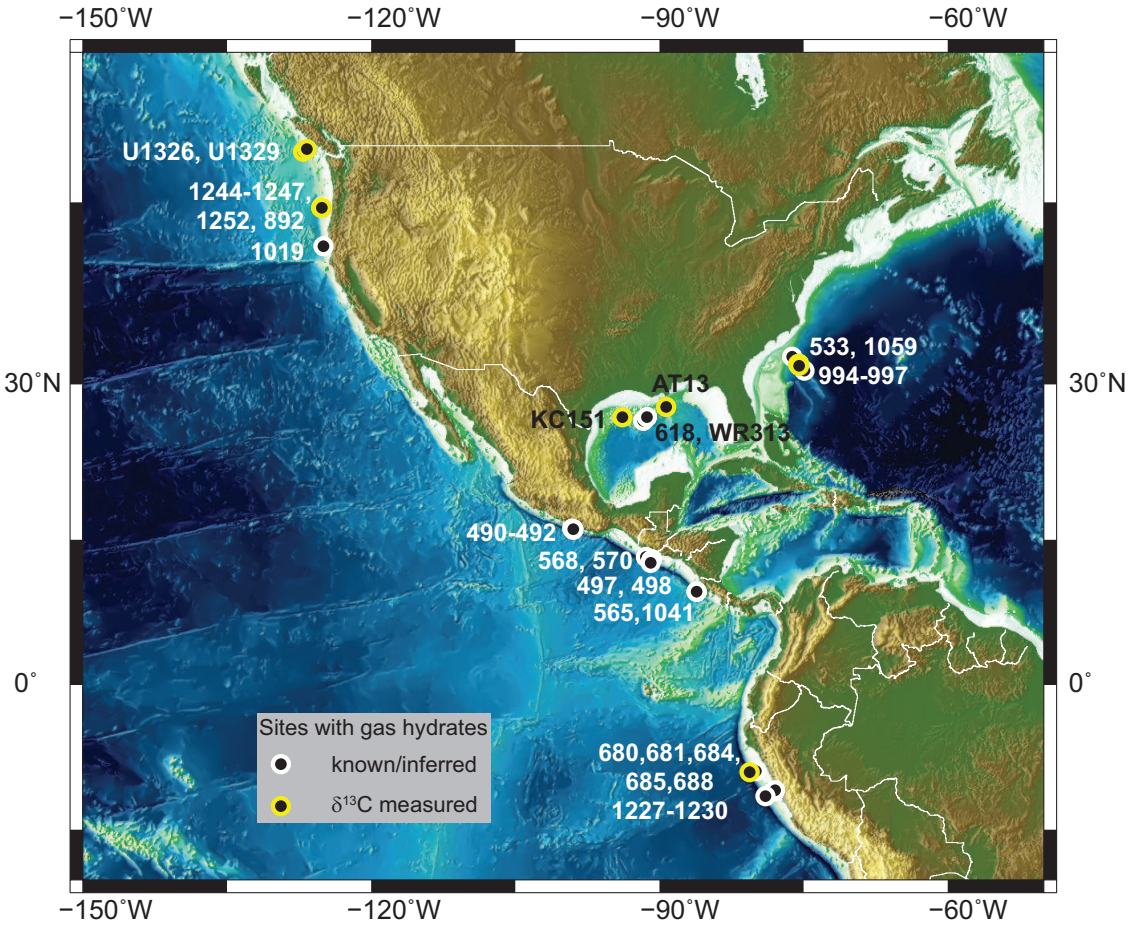


Figure 2.1 : Map showing locations with gas hydrate bearing sites drilled in the continental margins of north and south America. At some of these sites, cores have been sampled and pore water chemistry has been measured along with carbon isotope composition of DIC. Three sites with differing carbon chemistry have been chosen among those where extensive datasets exist and are modeled as a part of this study.

sites, a basic template has emerged (*Dickens*, 2001a; 2003; *Davie and Buffett*, 2001, 2003a; *Bhatnagar et al*., 2007; *Burdige*, 2011; Figure 2.2). With increasing overburden stress due to overlying sediments and geothermal heat, both pressure and temperature increase with depth below the seafloor. A GHSZ extends from the seafloor to a depth where temperatures along the local geothermal gradient exceed those on a three-phase gas hydrate-free gas-dissolved gas equilibrium curve appropriate for local pore water chemistry. The depth at which the geothermal gradient intersects the three-phase equilibrium curve is called the base of the hydrate stability zone (BHSZ).

Particles, including organic carbon, settle on the seafloor to become sediment with seawater in the pore space. As this sediment moves into and through the GHSZ during burial, pressure and temperature increase, porosity decreases, and various solid organic carbon and pore water constituents succumb to a series of microbially mediated reactions. At locations with high total organic carbon (TOC) input and within the upper few hundred meters of sediment, ”biogenic” $CH_4$ extremely depleted in $^{13}C$ is a major product. This $CH_4$ can occur in the dissolved phase, as free gas bubbles, or as gas hydrate, the latter precipitating when $CH_4$ concentrations in pore water surpass solubility conditions within the GHSZ. Methane can also cycle within the sediment column (including below the GHSZ) because of burial, diffusion and fluid flow. Furthermore, $CH_4$ can escape the system through venting into the water column (e.g., *Westbrook et al*., 1994; *Trehu*

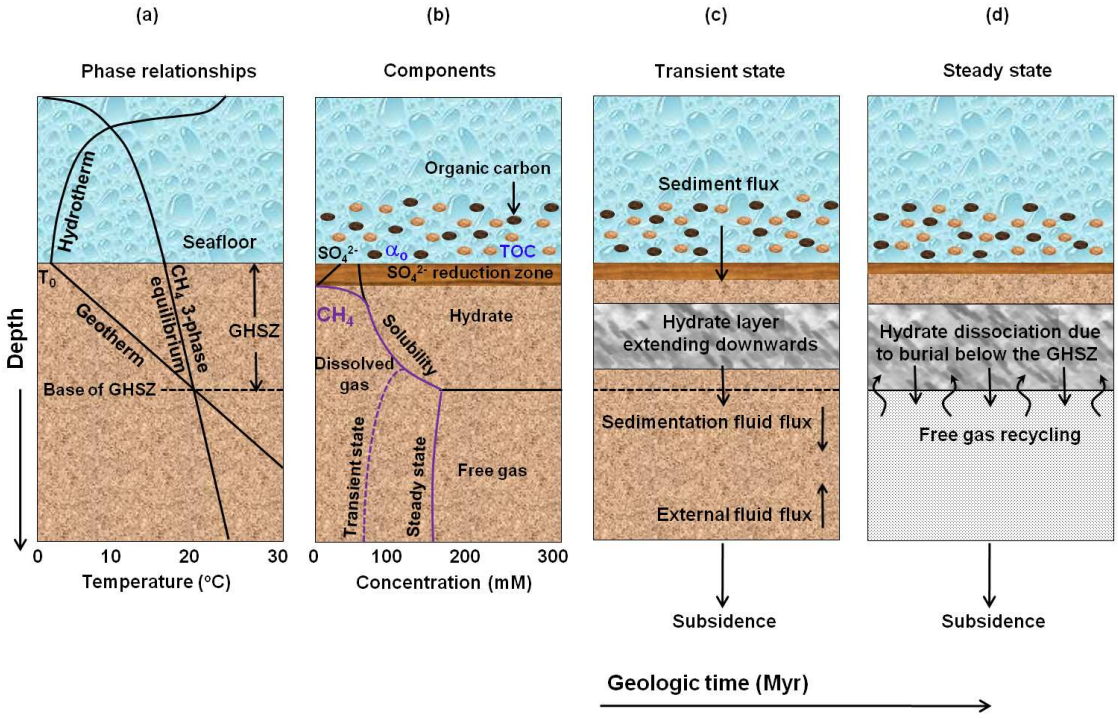


Figure 2.2 : Basic schematic of static and dynamic gas hydrate systems. (a) Relationships that exist between three phases of methane, geotherm, hydrotherm and the finite zone of gas hydrate stability (GHSZ). (b) A static description of gas hydrate in marine sediment showing the GHSZ, $SO_4^{2-}$ reduction zone, the three-phase boundary, and generic transient and steady-state dissolved gas concentration profiles. (c) A dynamic perspective showing relevant sediment and fluid fluxes, and the hydrate layer in the GHSZ that can move down with the sediment. (d) The steady-state snapshot view of these hydrate systems showing the hydrate layer overlying a free gas zone that are in equilibrium over geologic timescales.

*et al*., 2004), or through anaerobic oxidation of methane (AOM) in shallow sediment (e.g., *Borowski et al*., 1996; *Snyder et al*., 2007). At all ocean locations with gas hydrate, there exists a thin sulfate-methane transition (SMT) somewhere between the seafloor and about 30 m below the seafloor (mbsf). This is a biogeochemical horizon, where upward migrating $CH_4$ reacts with downward diffusing $SO_4^{2-}$ via AOM (*Reeburgh*, 1976; *Borowski et al*., 1996; *Valentine and Reeburgh*, 2000; *Dickens*, 2001b; *D'Hondt et al*., 2002).

The amount and distribution of gas hydrate in a marine sediment sequence hinge on a dynamic and somewhat complex framework (Figure 2.2). This is because they depend on an array of parameters and processes that define the GHSZ, describe the burial and degradation of organic carbon, and characterize dissolved, solid and gaseous $CH_4$ fluxes, all operating over geological timescales. Within this context, a series of one-dimensional (1-D) models have been developed to simulate gas hydrate occurrence (*Rempel and Buffett*, 1997; *Egeberg and Dickens*, 1999; *Xu and Ruppel*, 1999; *Davie and Buffett*, 2001, 2003a, 2003b; *Gering*, 2003; *Luff and Wallman*, 2003; *Haeckel et al*., 2004; *Torres et al*., 2004; *Wallman et al*., 2006; *Liu and Flemings*, 2006, 2007; *Bhatnagar et al*., 2007; *Marquardt et al*., 2010). The models have a similar generic framework: a series of mathematical expressions for mass, momentum and energy transfer account for three main factors: the dimensions of the GHSZ, the burial and degradation of organic carbon, and the movement of dissolved, solid and gaseous $CH_4$ fluxes.

The expressions are then solved simultaneously using site-specific parameters, numerical methods and incremental steps in time to obtain $CH_4$ profiles with respect to depth. However, several problems remain with these 1-D models. In general, they do not consider localized flow along sub-vertical permeable layers, changes in salinity with gas hydrate formation and dissociation, and small-scale heterogeneities in sediment composition and physical properties. Nonetheless, when the simulations are run over millions of years, they give fairly accurate amounts and distributions of gas hydrate at multiple locations, such as Blake Ridge and Cascadia Margin. Some of these existing models used to quantify the amount and distribution of marine hydrate abundance are reviewed.

## 2.3 Existing Methods to Quantify the Amount and Distribution of Marine Gas Hydrate

### 2.3.1 Observations

Over the last two decades, a series of scientific expeditions have drilled boreholes dedicated to understanding the amount and distribution of gas hydrate on continental slopes (e.g., *Paull et al.,* 1996, 2000c; *Trehu et al.,* 2003, 2004). Results of the Ocean Drilling Program (ODP), particularly Legs 146, 164, 201, 204, the Integrated Ocean Drilling Program (IODP) Leg 311 and the Joint Industry Project (JIP) drilling expeditions in the Gulf of Mexico have investigated gas hydrate

distribution along active and passive margins (e.g., *Westbrook et al.,* 1994; *Paull et al.,* 1996; *Trehu et al.,* 2003; *Riedel et al.,* 2006; *Jones et al*., 2008; Figure 2.1). Unarguably, at many locations, lithology dictates gas hydrate distribution at the local scale (*Kraemer et al*., 2000; *Weinberger et al*., 2005). Importantly, local-scale variations in hydrate distribution across different geologic settings are observed due to effects of focused fluid flow and lateral migration. At a given site, gas hydrate has been quantified using several geochemical or geophysical techniques (see above references). These include analyses of seismic data, well logs, pore fluid geochemistry, pressurized sediment cores, and sediment properties (e.g., *Paull et al.,* 2000c; *Trehu et al.,* 2004).

Natural gas hydrates are often identified by seismic data surveys in the form of a reverse polarity in reflection that parallels the seafloor, known as the bottom simulating reflector (BSR). This reflection is caused due to the differences in acoustic impedance between the overlying sediment with gas hydrate and sediment with associated free gas below the GHSZ (*MacKay et al*., 1994). Prior to drilling a borehole, a logging well is drilled to carry out logging-while-drilling (LWD) operations and to estimate the downhole characteristics. These well logs (e.g., resistivity) are used to calculate the gas hydrate saturations using deviations in resistivity (*Archie*, 1942). Scientific drilling expeditions have recently focused on collection and sampling of sediment cores to examine the physical properties of hydrate bearing sediment and to measure the interstitial pore water chemistry

(*Westbrook et al*., 1994; *Paull et al., 1996*; *Trehu et al*., 2003; *D'Hondt et al*., 2003; *Riedel et al*., 2006; *Jones et al*., 2008). Geochemical techniques and analysis of pore water constituents released into the pore fluids (e.g., $Cl^{-}$, $Sr^{2+}$, $Li^{2+}$) are used to interpret anomalies caused as a result of hydrate formation. During core recovery, gas hydrate dissociates and pore fluid freshens thus resulting in local deviations in concentration of pore water species. These pore water anomalies are related to local hydrate occurrence in the recovered cores to estimate downhole distribution of gas hydrate. Pressurized sediment coring is a more recent technique that retains the in situ pressure during core recovery to mitigate gas hydrate dissociation. These cores are sampled to examine the pore fluid chemistry and to investigate in situ hydrate occurrence and distribution. Although, at many sites these methods give similar values and show first-order versus second-order distributions, they can only quantify the presence of gas hydrates as a snapshot in time. However, none of these methods can explain the formation of hydrates and the physical processes governing their accumulation and distribution.

### 2.3.2 One-dimensional Modeling

This limitation has led to the development of a series of numerical models with site-specific parameters that describe the physical processes to account for inputs and outputs of carbon, principally $CH_4$ over geologic timescales. The basic framework of these models remains somewhat similar with some notable

differences (e.g., *Rempel and Buffett*, 1997; *Egeberg and Dickens*, 1999; *Xu and Ruppel*, 1999; *Davie and Buffett*, 2001, 2003a, 2003b; *Gering*, 2003; *Luff and Wallman*, 2003; *Haeckel et al*., 2004; *Torres et al*., 2004; *Wallman et al*., 2006; *Liu and Flemings*, 2006, 2007; *Garg et al*., 2008). These dynamic hydrate models couple fluid, mass and energy transport with thermodynamics and kinetics for methane formation. In particular, *Davie and Buffett* (2001) proposed a 1-D numerical model for hydrate accumulation where methane was supplied from biogenic sources. These 1-D models can be used to explain first-order observations at many sites and provide insights into gas hydrate systems behavior. However, its dependence on site-specific transport and geologic parameters restricts its applicability to specific geologic locations.

The fundamental drawback of these models is that they do not incorporate both the sources of $CH_4$ (i.e., in situ biogenic generated $CH_4$ and thermogenic $CH_4$ rising from depth) in a generalized model and therefore validates the model only for specific hydrate settings, e.g., Blake Ridge (*Egeberg and Dickens*, 1999; *Davie and Buffett*, 2001, 2003a; *Gering*, 2003; *Marquardt et al*., 2010) or Cascadia Margin (*Luff and Wallman*, 2003; *Haeckel et al*., 2004; *Torres et al*., 2004; *Liu and Flemings*, 2006). Moreover, most of these models use first-order rate kinetics to model the formation of hydrate in porous media. In *Davie and Buffett's* model (2001), the difference between pore water methane concentration and the local solubility has been used as the key driving force for hydrate formation.

By inappropriately choosing a large value for the rate constant, thermodynamic equilibrium may not be well constrained in these models. Porosity reduction and compaction-driven fluid flow have been modeled using empirical relationships as opposed to using intrinsic physical and diagenetic processes common to most sedimentary basin models. These models are consistent and accurate with data measured during LWD and other geochemical analyses, but they often require sensitivity analysis to understand the alterations in gas hydrate distribution due to changes in site-specific parameters. Thus, different sites in spite of having similar processes remain disconnected and are evaluated as isolated examples.

Recent modeling efforts have been made to develop a generalized, 1-D, dynamic flow model in thermodynamic equilibrium to quantify the hydrate distribution over geologically relevant timescales (*Bhatnagar et al.,* 2007, 2011). Their model neglects hydrate formation kinetics. In addition, this model relates various hydrate occurrences at different isolated geologic sites in a unified model. Furthermore, they develop a novel scaling scheme to normalize the primary variables to characterize hydrate occurrence on the basis of a few dimensionless groups. Thus, the model is made applicable to any generalized geologic setting (*Bhatnagar et al.,* 2007). Moreover, appropriate scaling of dimensionless groups enabled collapsing numerous simulations for hydrate accumulation and saturation over a wide range of parameters into two simple contour plots (Figures 2.3 and 2.4). One of these plots simulated gas hydrate accumulation due to biogenic

methane generated within the GHSZ (Figure 2.3), while the other illustrated cases where methane was migrated with pore fluids rising from depth (Figure 2.4). In essence, they established a correlation between the net fluid flux and the average hydrate saturation through component balances, thermodynamic equilibrium, and a few key dimensionless groups (*Bhatnagar et al*., 2007). Similar correlations are developed in this work albeit in more complex gas hydrate systems dominated by lithology, stratigraphy and fluid flow.

### 2.3.3 Two-dimensional Modeling

Most models developed over the last decade to simulate gas hydrate accumulation have focused on first-order gas hydrate distribution. A handful of these existing models are capable of incorporating lithologic heterogeneity and lateral fluid flow to explain the local and regional distribution of hydrate occurrence (e.g., *Bhatnagar*, 2008; *Malinverno*, 2010; *Schnurle et al*., 2011). *Bhatnagar* (2008) acknowledged that gas hydrate distribution in heterogeneous sediments necessitates modeling in two or more spatial dimensions to account for lateral fluid flow and heterogeneity, and so later extended the generalized 1-D model to two-dimensions to simulate more complex and heterogeneous gas hydrate settings.

*Malinverno* (2010) studied the natural hydrate systems similar to Bhatnagar's 2-D work and incorporated 1-D heterogeneity in the form of thin sand layers. This study involves modeling gas hydrate formation in marine sediments by accounting

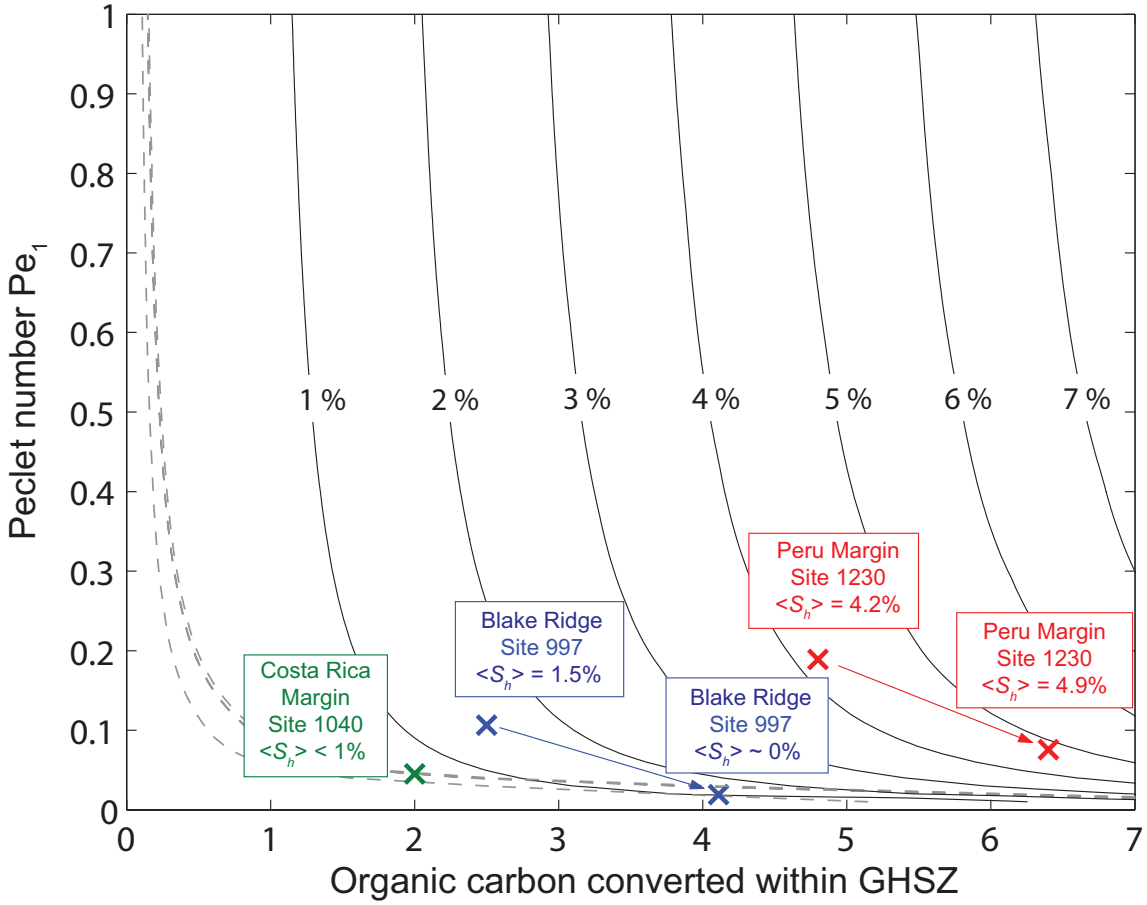


Figure 2.3 : Average gas hydrate saturation contours within the GHSZ for systems where all methane is supplied from in situ biogenic sources. Low values of Peclet number ($Pe_1$), imply dominant diffusive losses and that greater methane has to be generated within the GHSZ to form any gas hydrate. Average gas hydrate saturation at different geologic settings can be obtained from a single contour map (Taken from *Bhatnagar et al*., 2007).

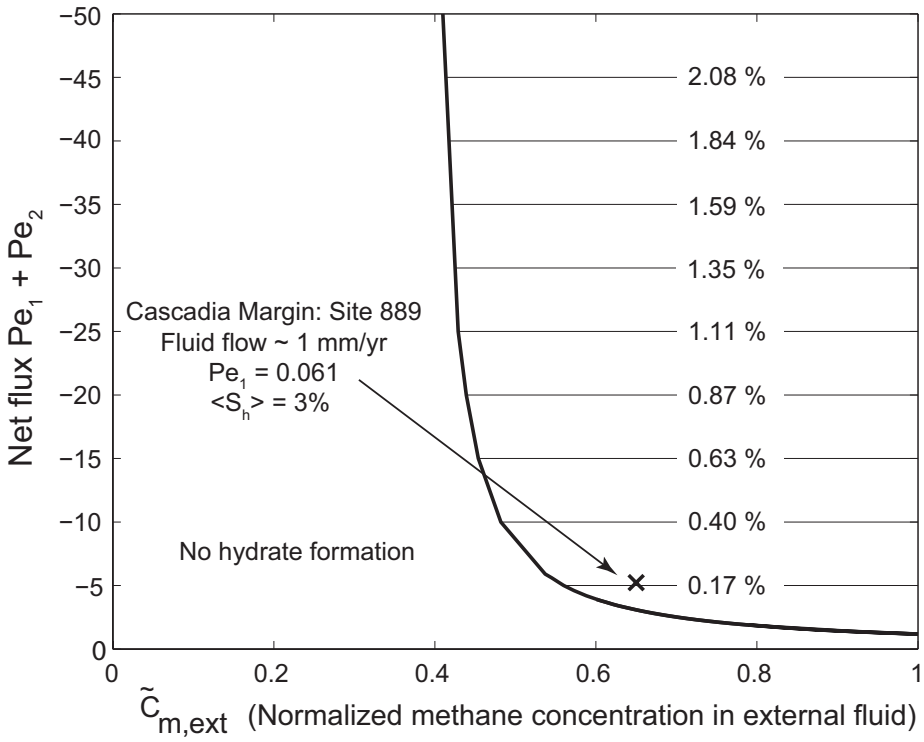


Figure 2.4 : Gas hydrate flux $Pe_1\langle S_h\rangle$ contours plotted along with the curves distinguishing two regions of hydrate occurrence, for the case of non-zero, finite, sedimentation and $Pe_1 < |Pe_2|$. Average hydrate saturation $\langle S_h\rangle$ can be calculated by dividing the contour values by $Pe_1$ (Taken from *Bhatnagar et al*., 2007).

for in-situ methane generation and diffusion. As a typical example, gas hydrate accumulation (30-60%) is shown in the pore spaces of thin sand layers ($\sim$5 cm thick), with no evidence of hydrates in the neighboring marine mud layers of thickness $\sim$2.5 m at IODP Site U1325 along the Cascadia Margin. As a consequence, the inhibition of hydrate formation in marine mud is evaluated and the diffusive transport of methane into thin sands is determined to result in concentrated deposits of hydrate ($\sim$50%) in thin sand layers. However, natural gas hydrates are often distributed in heterogeneous sediments in the form of nodules and lenses over larger length scales. These observations cannot be explained using a diffusion dominant transport model.

Recently, *Schnurle et al.,* (2011) developed a 2-D numerical model to show gas hydrate emplacement in marine sediment. This model is simplistic in the sense that it excludes sedimentation, porosity reduction due to compaction and lateral variation in temperature, salinity and solubility; however, lateral fluid migration and mobile free gas are modeled using a finite-element model that solves for mass, momentum and energy conservation equations in space and geologic time.

All the above models assume methane as the principal hydrate former, neglecting the presence of higher hydrocarbons such as ethane and propane. *Gu et al.* (2008) presented their work on compositional effects of gas hydrate and free gas transition and related it to the presence of BSRs. However, $CH_4$ has been assumed as the only hydrate former throughout this study, and compositional

effects are neglected.

In this study, pore water chemistry across shallow sediment above gas hydrate systems discusses the chemical changes across the SMT using the existing generalized 1-D models. In the subsequent chapters, Bhatnagar's 1-D model (2007, 2011) extends into lateral dimensions to develop a 2-D, heterogeneous sedimentation-fluid flow model to simulate spatial and temporal evolution of gas hydrate accumulation over geologic timescales. Thereafter, the 2-D model illustrates the effects of heterogeneity and lateral fluid flow on gas hydrate distribution. To give a completeness to this research, these models are tested and validated against field examples where sediment cores have been sampled, pore fluid geochemistry has been analyzed, extensive datasets exist, and elevated hydrate and free gas are observed. Finally, subsea sediment instability and associated risks in slope failure are assessed.

# Chapter 3

# Pore Water Sulfate, Alkalinity, and Carbon Isotope Profiles in Shallow Sediment Above Marine Gas Hydrate Systems

## 3.1 Introduction

* The amount and distribution of gas hydrate within the GHSZ at a given location depend on in situ concentrations of light hydrocarbons (e.g., *Dickens et al*., 1997; *Xu and Ruppel*, 1999; *Davie and Buffett*, 2001; *Milkov et al*., 2003; *Bhatnagar et al*., 2007). In most marine settings with gas hydrate, $CH_4$ concentration dominates total hydrocarbon concentration, and gas hydrate arises when $CH_4$ concentrations exceed those on a dissolved gas-gas hydrate saturation curve. Usually, however, such excess solubility does not occur in the upper part of the GHSZ (Figure 3.1). Instead, two biogeochemical zones, separated by a thin (generally $<$2 m) sulfate-methane transition (SMT), distinguish shallow sediment. From near the seafloor to the SMT, dissolved $SO_4^{2-}$ decreases from seawater concentration ($\sim$28 mM) at the seafloor to near-zero concentration at the SMT; from the SMT to

*Chatterjee, S., G.R. Dickens, G. Bhatnagar, W.G. Chapman, B. Dugan, G.T. Snyder, and G.J. Hirasaki (2011), Pore water sulfate, alkalinity, and carbon isotope profiles in shallow sediment above marine gas hydrate systems: A numerical modeling perspective, *J. Geophys. Res*., 116, B09103, doi:10.1029/2011JB008290.

deeper zones, dissolved $CH_4$ increases from near zero concentration at the SMT to a concentration on the saturation curve (Figure 3.1). This means that the top occurrence of gas hydrate at most locations lies below the seafloor and within the GHSZ (e.g., *Dickens et al*., 1997; *Xu and Ruppel*, 1999; *Davie and Buffett*, 2001; *Dickens, 2001a*; *Milkov et al.*, 2003; *Bhatnagar et al*., 2007; *Malinverno et al*., 2008). Although a bottom simulating reflector (BSR) on seismic profiles often marks the deepest presence of gas hydrate (*Kvenvolden*, 1993; *Paull and Matsumoto*, 2000; *Trehu et al*., 2004), remote sensing methods face difficulties detecting the shallowest gas hydrate, presumably because physical properties of sediment do not change significantly when small amounts of gas hydrate are present. In addition, this boundary can be hard to locate accurately in well logs and sediment cores from drill holes (*Paull and Matsumoto*, 2000; *Trehu et al*., 2004).

Pore water $SO_4^{2-}$ gradients in shallow sediment may offer a geochemical means to determine underlying $CH_4$ gradients and the uppermost occurrence of gas hydrate. Many papers have attributed SMTs in shallow marine sediment to anaerobic oxidation of methane (AOM) (e.g., *Borowski et al*., 1996, 1999; *Valentine and Reeburgh*, 2000; *Dickens*, 2001b; *D'Hondt et al*., 2002; *Snyder et al*., 2007). Specifically, the SMT represents an interface where microbes utilize $SO_4^{2-}$ diffusing down from the seafloor and $CH_4$ rising up from depth according to (*Reeburgh*, 1976)

$$\mathrm{CH_4(aq) + SO_4^{2-} \quad \longrightarrow \quad HCO_3^- + HS^- + H_2O.} \tag{3.1}$$

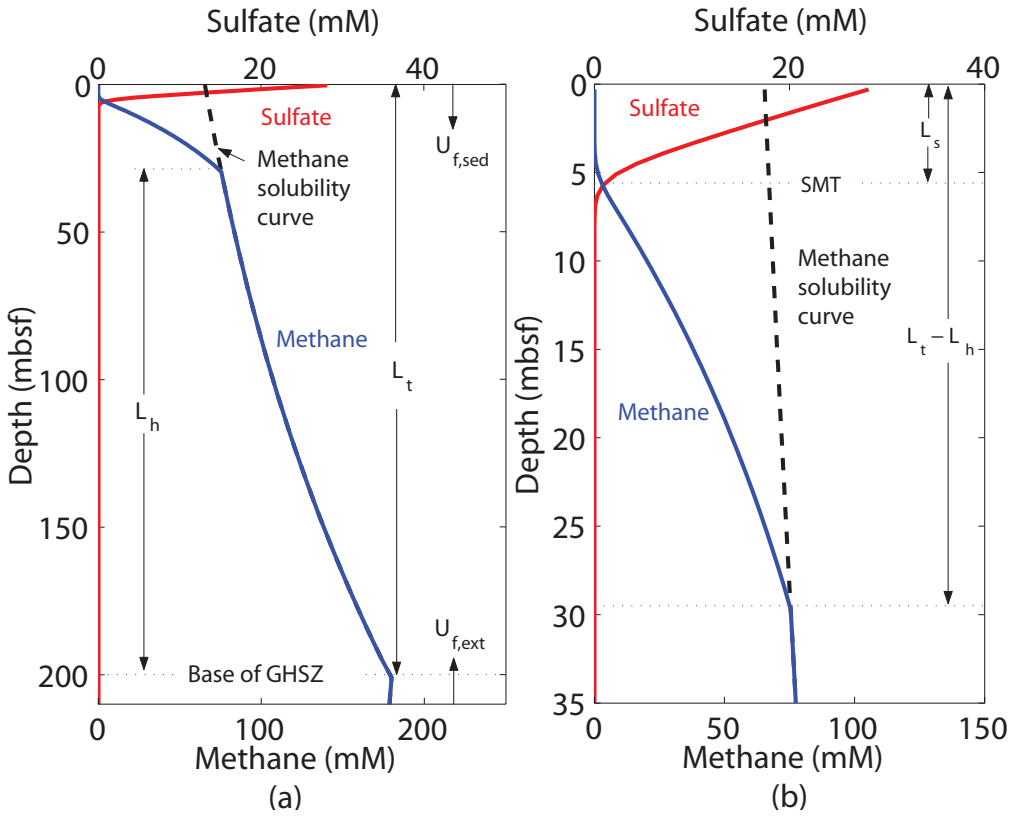


Figure 3.1 : (a) Schematic representation of a gas hydrate system showing pore water sulfate (red) and methane (blue) concentrations, which go to near zero within the sulfate-methane transition (SMT) at shallow depths due to AOM. The dashed line represents the methane solubility curve. Fluid fluxes due to compaction-driven flow and external flow are denoted as $U_{f,sed}$ and $U_{f,ext}$ respectively; $L_t$ is the depth to the base of the gas hydrate stability zone. (b) Zoomed sulfate-methane transition (SMT) zone showing an overlap of sulfate and methane profiles and its depth below the seafloor ($L_s$) (*Bhatnagar et al*., 2008a). It should be noted, though, that accurate, high-resolution in situ $CH_4$ concentration gradients have not been measured below the SMT (e.g., *Dickens et al*., 1997; *Milkov et al*., 2004).

This interpretation implies a 1:1 ratio of $SO_4^{2-}$ and $CH_4$ fluxes into the SMT, and is important to gas hydrate studies. If AOM principally causes the SMT in shallow sediment above gas hydrate, and the overall system is near steady state conditions, the $SO_4^{2-}$ gradient and the SMT depth should relate to the underlying $CH_4$ gradient and the shallowest occurrence of gas hydrate (Figure 3.1).

Field observations, mass balance calculations, and numerical modeling results support the assumptions and expected relationships between $SO_4^{2-}$ and $CH_4$ fluxes (*Borowski et al*., 1996, 1999; *Dickens*, 2001b; *Davie and Buffett*, 2003b; *Paull et al*., 2005; *Snyder et al*., 2007; *Bhatnagar et al*., 2008a, 2011). Nonetheless, the use of pore water $SO_4^{2-}$ profiles to constrain gas hydrate distribution remains controversial because of unresolved issues. A source of current debate concerns the concentration and carbon isotope composition ($\delta^{13}$C, expressed relative to Pee Dee Belemnite) of dissolved inorganic carbon (DIC) at the SMT (cf. *Kastner et al*., 2008a; *Dickens and Snyder*, 2009). The $CH_4$ in many regions with gas hydrate has a $\delta^{13}$C of -50 $^0/_{00}$ or lower (*Milkov*, 2005). Moreover, given the ubiquitous 7.0-8.3 pH of pore water in these systems (e.g., *Shipboard Scientific Party*, 1996, 2003a, 2003b), almost all DIC consists of $HCO_3^-$. If AOM (equation 3.1) primarily drives the SMT, and the systems were closed, one might predict DIC at this interface to be $<$28 mM with a $\delta^{13}\mathrm{C} <$ -50 $^0/_{00}$ (*Kastner et al*., 2008a) (the DIC being less than the loss of $SO_4^{2-}$ because of authigenic carbonate precipitation). Although this has been observed at some locations with underlying gas hydrate, often DIC

at the SMT is >30 mM and has a $\delta^{13}\mathrm{C} >$ -30 $^{0}/_{00}$ (Figure 3.2) (*Paull et al*., 2000b; *Borowski et al*., 2000; *Claypool et al*., 2006; *Torres and Rugh*, 2006; *Pohlman et al*. , 2008; *Kastner et al*. , 2008b; *Torres and Kastner*, 2009; *Kim et al*., 2011).

There are two basic explanations for relatively high DIC and $\delta^{13}\mathrm{C}$ across the SMT in regions with gas hydrate (cf. *Kastner et al*., 2008a; *Dickens and Snyder*, 2009). First, rather than AOM, sulfate reduction of particulate organic carbon (POC) consumes much of the pore water $SO_4^{2-}$ in shallow sediment. This bacterially mediated reaction (*Berner*, 1980; *Boudreau and Westrich*, 1984), here and elsewhere alternatively referred to as degradation of POC or organoclastic sulfate reduction (OSR), can be expressed as

$$2\mathrm{CH_2O(s)} + \mathrm{SO_4^{2-}} \quad \longrightarrow \quad 2\mathrm{HCO_3^-} + \mathrm{HS^-} + \mathrm{H^+}. \tag{3.2}$$

Notably, the reaction generates two moles of $HCO_3^-$ for each mole of $SO_4^{2-}$, in contrast to AOM where the stoichiometry is 1:1 (equation 3.1). The $\delta^{13}\mathrm{C}$ of POC in marine sediments typically lies between -26 $^{0}/_{00}$ and -16 $^{0}/_{00}$ (e.g., *Conrad*, 2005; *Kim et al*., 2007), and there is minimal fractionation of carbon isotopes during such sulfate reduction. Sulfate consumption via POC, therefore, should lead to higher DIC concentrations with greater $\delta^{13}\mathrm{C}$ than expected from AOM (*Claypool et al*., 2006; *Kastner et al*., 2008a; *Torres and Kastner*, 2009). However, this explanation fails to explain the high DIC (>40 mM) and modest $^{13}\mathrm{C}$ depletion in DIC ($<$ -15 $^{0}/_{00}$) at some sites (Figure 3.2). Alternatively, along with $CH_4$, $HCO_3^-$

enriched in $^{13}\mathrm{C}$ can enter the SMT from below. Such $^{13}\mathrm{C}$-rich $HCO_3^-$ forms during methanogenesis (e.g., *Conrad*, 2005), and a contribution from this source would also lead to elevated DIC concentrations with relatively high $\delta^{13}\mathrm{C}$ across the SMT (*Dickens and Snyder*, 2009; *Kim et al*., 2011).

Alternate explanations are assessed for DIC concentration and carbon isotopic composition within the context of a numerical model for gas hydrate distribution. First, two sites are reviewed with gas hydrate but very different carbon chemistry across the SMT. The 1-D model for gas hydrate accumulation in marine sediment is extended (*Bhatnagar et al*., 2007, 2008a, 2011) such that it more fully incorporates carbon chemistry. Specifically, equations for both sulfate consumption reactions are included (equations 3.1 and 3.2), to couple mass balance equations for $CH_4$, $SO_4^{2-}$, DIC and $Ca^{2+}$, and couple mass balance equations for the $^{12}\mathrm{C}$ and $^{13}\mathrm{C}$ of $CH_4$ and DIC. It is shown how mixtures of DIC derived from AOM and from depth can explain the wide difference in concentrations and $\delta^{13}\mathrm{C}$ of DIC across the SMT at both sites, and the implications of this result are discussed.

## 3.2 Pore Water Profiles Across the Sulfate-Methane Transition

### 3.2.1 Overview

Sediment cores have been recovered from many continental margins where underlying strata hosts gas hydrate (e. g., *Kvenvolden*, 1993; *Paull et al*., 1996; *Shipboard Scientific Party*, 1996, 2003a, 2003b; *Snyder et al*., 2007; *Hiruta et*

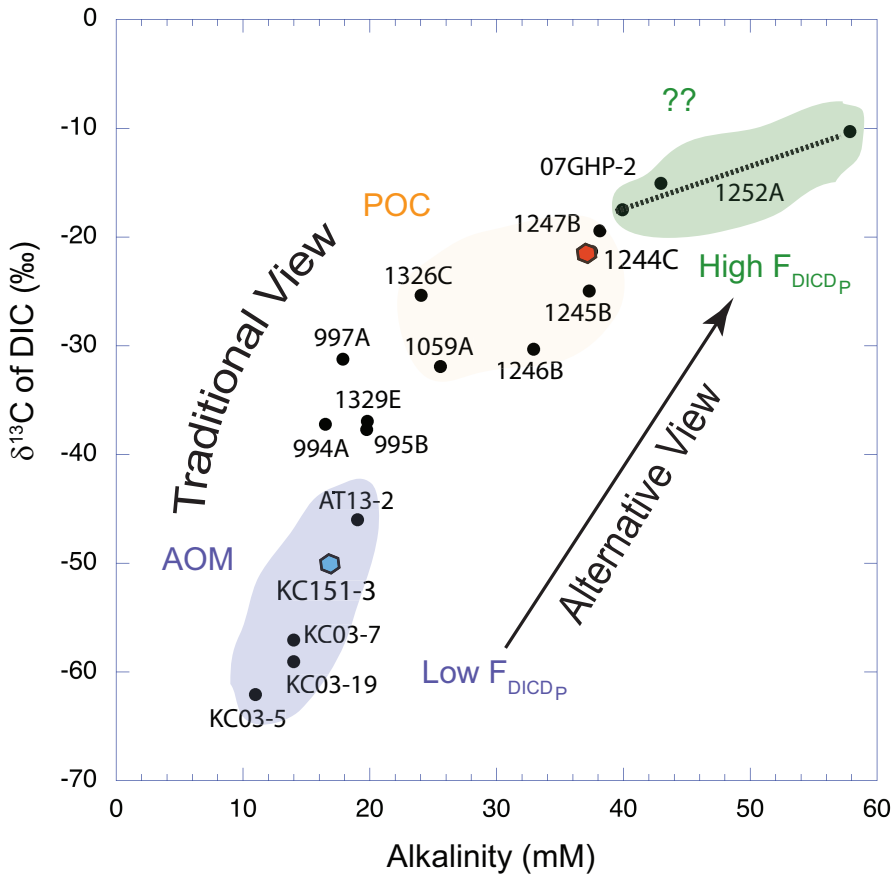


Figure 3.2 : Alkalinity versus $\delta^{13}\mathrm{C}$ of DIC at the SMT for multiple locations known to have gas hydrate at depth. Note the general trend from sites with low alkalinity and low $\delta^{13}\mathrm{C}$ of DIC to those with high alkalinity and relatively high $\delta^{13}\mathrm{C}$ of DIC. Traditionally, alkalinity and $\delta^{13}\mathrm{C}$ of DIC at the SMT were being used to discriminate between AOM and POC-driven sulfate reduction to explain this trend. The dominant cause for this trend is suggested to arise from the relative flux of upward $^{13}\mathrm{C}$-enriched DIC ($F_{DIC_{Dp}}$). Data from ODP 994-997, *Paull et al*. (2000b); ODP Site 1059, *Borowski et al*. (2000); ODP Sites 1244-1252, *Claypool et al*. (2006), *Torres and Rugh* (2006); 1326, 1329, *Torres and Kastner* (2009); KC03-5-19, *Pohlman et al*. (2008); KC151-3, AT13-2 , *Kastner et al*. (2008b); O7GHP-1, *Kim et al*. (2011). The hachured line for Hole 1252A represents a range of values spanning the SMT. Hexagons represent the two sites (1244C and KC151-3) modeled within this chapter.

*al*., 2009; *Kim et al*., 2011). From these cores, pore water profiles have been generated, showing how concentrations of dissolved constituents change beneath the seafloor. Not all cores (or sets of cores in the case of drilling) penetrate the SMT, and very few cores have been examined for a wide array of dissolved constituents at high depth resolution. Nonetheless, two ”end-member” cases appear to exist with regards to the concentration and $\delta^{13}\mathrm{C}$ of DIC across the SMT (Figure 3.2). These can be highlighted with data from two locations, which frame current discussions regarding carbon cycling across the SMT (e.g., *Claypool et al*., 2006; *Kastner et al*., 2008a; *Dickens and Snyder*, 2009), as well as in the modeling.

### 3.2.2 Site 1244: Hydrate Ridge

Ocean Drilling Program (ODP) Leg 204 drilled Site 1244 at 890 m below sea level (mbsl) on the eastern flank of Hydrate Ridge offshore the central coast of Oregon (*Trehu et al*., 2003). The pressure and temperature at the seafloor are 8.72 MPa and 3.8$^{o}$C. Given a measured geothermal gradient of 0.061$^{o}$C/m and the predominance of $CH_4$ ($>$99 %) in gas samples (*Kvenvolden*, 1995), the base of the GHSZ should be $\sim$133 m below seafloor (mbsf). Seismic data indicate a BSR at $\sim$124 mbsf (*Trehu et al*., 2003). As true with many locations, however, the amount and distribution of gas hydrates between the seafloor and the base of the GHSZ remain uncertain. Various approaches for detecting and quantifying gas hydrate suggest average gas hydrate saturation between 2 and 10% of pore space

below a depth at around 50 mbsf, which is apparently the top of the gas hydrate zone (*Trehu et al*., 2003; *Lee and Collett*, 2006).

Headspace $CH_4$ concentrations rise from 0.2 to 6.5 mM between 7 and 16 mbsf (*Shipboard Scientific Party*, 2003b). Beyond this depth, in situ methane concentrations exceed those for gas solubility after core recovery ($\sim$STP), so they have little meaning (*Paull et al*., 2000a; *Shipboard Scientific Party*, 2003b). Methane $\delta^{13}\mathrm{C}$ values range between -65 $^0/_{00}$ and -77 $^0/_{00}$ (*Milkov et al*., 2005; *Claypool et al*., 2006). The amount and average isotopic composition of organic carbon through the sequence are 1.27 wt% (*Shipboard Scientific Party*, 2003b) and -24 $^0/_{00}$ (*Yu et al*., 2006), respectively.

The $SO_4^{2-}$ profile at Site 1244 (Figure 3.3a) (*Trehu et al*., 2003) is somewhat complicated. Values decrease from 29.7 mM near the seafloor to 21.3 mM at $\sim$4 mbsf; below, they drop nearly linearly to $<$1 mM by 9.2 mbsf. This is where $CH_4$ rises above 1.8 mM, and dissolved $Ba^{2+}$ increases markedly (*Trehu et al*., 2003). The latter is noteworthy because $Ba^{2+}$ profiles (when measured) often show a steep rise just below the SMT (e.g., *Snyder et al*., 2007).

Alkalinity increases from 2.8 mM near the seafloor to 37 mM at 8.5 mbsf; below, it rises to $\sim$64 mM at 37 mbsf (Figure 3.3b) (*Trehu et al*., 2003). The pH throughout the interval is between 7.1 and 8.1 (*Shipboard Scientific Party*, 2003b), strongly suggesting that alkalinity, DIC and $HCO_3^-$ concentrations are nearly the same. Thus, there is a distinct change in $HCO_3^-$ gradients across SMT, but values

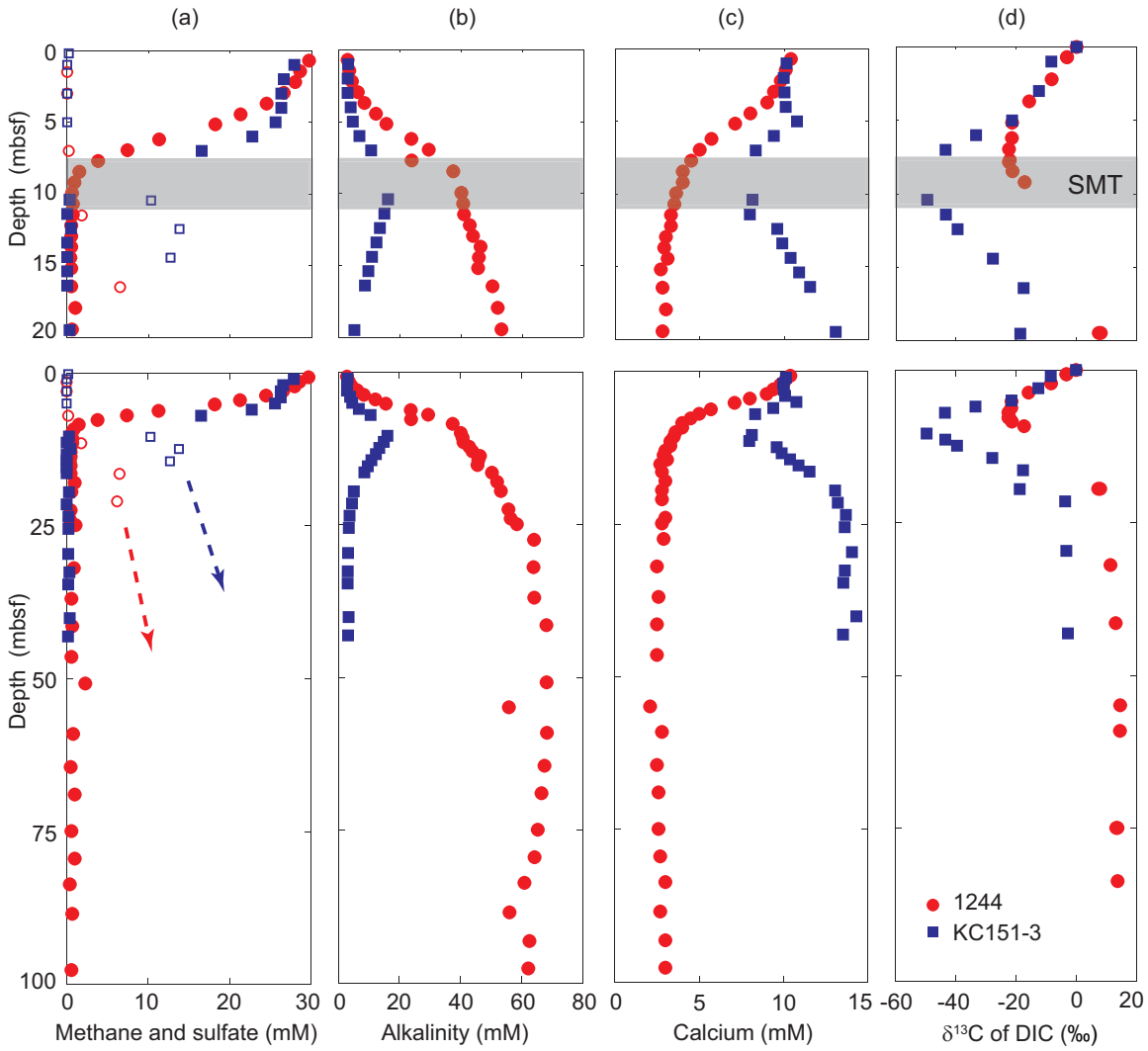


Figure 3.3 : Pore water (a) $SO_4^{2-}$ (closed circles and squares), $CH_4$ (open circles and squares), (b) alkalinity (DIC), (c) $Ca^{2+}$ concentration and (d) $\delta^{13}$C of DIC profiles in shallow sediment at Site 1244 in Hydrate Ridge and KC151-3 in Gulf of Mexico. Top panel shows the zoomed pore water profiles for the upper 20 m of sediment and the shaded region represents the SMT zone. The arrows indicate increasing trend in $CH_4$ concentration. Data from 1244, *Trehu et al*. (2003) and *Torres and Rugh* (2006); KC151-3, *Kastner et al*. (2008b).

continue to rise with depth.

Dissolved $Ca^{2+}$ is ~10 mM near the seafloor and decreases to ~4 mM at the SMT; below, it slowly decreases (Figure 3.3c) (*Trehu et al*., 2003). An obvious inflection in $Ca^{2+}$ concentrations, opposite to that of alkalinity, spans the SMT.

Profiles of DIC $\delta^{13}\mathrm{C}$ also display inflections across the SMT. The $\delta^{13}\mathrm{C}$ of DIC is 0 $^{0}/_{00}$ near the sediment-water interface and decreases to a minimum of -22.5 $^{0}/_{00}$ at ~7.8 mbsf. Values then increase to +15 $^{0}/_{00}$ by ~55 mbsf (Figure 3.3d) (*Torres and Rugh*, 2006). Importantly, the $\delta^{13}\mathrm{C}$ profile displays concave-down curvature below the SMT.

### 3.2.3 Site KC151-3: Keathley Canyon

A Department of Energy-sponsored Joint Industry Program drilled Site KC151-3 at 1322 mbsl in Keathley Canyon in the northern Gulf of Mexico (*Ruppel* et al., 2008). The pressure and temperature at the seafloor are 12.95 MPa and 4$^{o}$C. Given the geothermal gradient of 0.038$^{o}$C/m and the predominance of $CH_4$ in gas samples, the base of the GHSZ should be at ~314 mbsf. A BSR is present between ~380 mbsf (*Kastner et al*., 2008b) and 390 mbsf (*Ruppel et al*., 2008). Several studies showed uneven distribution of gas hydrates in fractured silty-clayey sediments between 220 and 300 mbsf occupying 1-12% of pore volume (e.g., *Cook et al*., 2008; *Lee and Collett*, 2008; *Kastner et al*., 2008b). *Cook et al*. (2008) reported a few occurrences of fracture-filled hydrates in the shallow sandy clays between 110

and 115 mbsf, which might be interpreted as being near the top of the gas hydrate zone.

Headspace $CH_4$ concentrations rise from 0 to 13.8 mM between 5 and 12 mbsf (*Lorenson et al*., 2008). Again, deeper values probably represent residual $CH_4$ after significant degassing (*Paull et al*., 2000a; *Lorenson et al*., 2008). Methane $\delta^{13}\mathrm{C}$ values increase from -78.2 $^0/_{00}$ to -73.8 $^0/_{00}$ between 16 and 44 mbsf, and remain $\sim$ -72 $^0/_{00}$ in deeper strata (*Lorenson et al*., 2008). The amount of organic matter in the sediment sequence ranges from 0.44% to 0.95% (*Winters et al*., 2008). The $\delta^{13}\mathrm{C}$ of bulk sediment organic matter ranges from -19.7 $^0/_{00}$ to -21.7 $^0/_{00}$ in this region, at least near the sediment-water interface (*Goni et al*., 1998).

The $SO_4^{2-}$ concentration profile at Site KC151-3 (Figure 3.3a) (*Kastner et al*., 2008b) has a profile somewhat similar to that at Site 1244. Values decrease from $\sim$28 mM near the seafloor to 16.5 mM at $\sim$7 mbsf; below, they drop to $<$1 mM at $\sim$10.4 mbsf.

By contrast, the alkalinity profile (Figure 3.3b) (*Kastner et al*., 2008b) is much different than that at Site 1244. Alkalinity gradually increases from $<$3 to 6.7 mM across the upper 6 m of sediment, and reaches a maximum of 16.1 mM at 10.4 mbsf. Alkalinity then drops, such that it is $<$4 mM at 24 mbsf. Assuming that alkalinity comprises mostly $HCO_3^-$, there is an obvious bicarbonate peak at the SMT.

Dissolved $Ca^{2+}$ is $\sim$10 mM near the seafloor and decreases to $\sim$8 mM at

the SMT; below, it slowly increases to $\sim$14 mM at greater depths of $\sim$40 mbsf (Figure 3.3c) (*Kastner et al*., 2008b). Thus, as at Site 1244, there is a minimum in $Ca^{2+}$ at the SMT. However, the $Ca^{2+}$ profile is complicated at Site KC151-3 because a brine exists at depth (*Kastner et al*., 2008b). Extremely saline water with high concentrations of $Ca^{2+}$ (and other species) fills pore space of deep sediment across much of the northern Gulf of Mexico (e.g., *Kharaka et al*., 1987; *Macpherson*, 1989; *Castellini et al*., 2006).

As at Site 1244, the $\delta^{13}\mathrm{C}$ of DIC has a minimum at the depth of maximum alkalinity (Figure 3.3d) (*Kastner et al*., 2008b). However, it drops from 0 $^{0}/_{00}$ near the seafloor to -49.6 $^{0}/_{00}$ at this horizon, and increases to only +6 $^{0}/_{00}$ by 100 mbsf. Thus, the $\delta^{13}\mathrm{C}$ of DIC exhibits a clear inflection across the SMT, but is generally lower beneath the SMT compared to Site 1244.

## 3.3 Numerical Model

### 3.3.1 General Framework

Several one-dimensional (1-D) numerical models for gas hydrate accumulation in marine sediment have been developed (e. g., *Rempel and Buffett*, 1997; *Egeberg and Dickens*, 1999; *Xu and Ruppel*, 1999; *Davie and Buffett*, 2001, 2003a, 2003b; *Liu and Flemings*, 2007; *Bhatnagar et al*., 2007). Although they have notable differences, the models have similar conceptual frameworks. A series of coupled mathematical expressions (i.e., mass, momentum and energy transport equations)

express the following basic processes. Particles, including organic carbon, settle on the seafloor and become part of sediment, which has seawater within pore space. During burial, pressure and temperature increase, porosity decreases, and a fraction of POC converts to $CH_4$ below the SMT. Methane can also be contributed from depth. Dissolved $CH_4$ can move between sediment depths during burial because of diffusion, advection, or both. At appropriate pressure, temperature and water activity, dissolved $CH_4$ concentrations can surpass those for gas hydrate or free gas saturation. Eventually, steady state conditions are reached. At this point, as well as at transient states before, there is a distribution of $CH_4$ with respect to depth. The $CH_4$ can occur dissolved in water, as gas hydrate, or within free gas.

There are problems with current 1-D models. In particular, they do not account for changes in water activity ($\sim$salinity) caused by gas hydrate formation and dissociation (e.g., *Egeberg and Dickens*, 1999; *Milkov et al*., 2004), for heterogeneities in sediment properties over depth (e.g., *Trehu et al*., 2003; *Malinverno et al*., 2008), or for lateral variations in various parameters. As such, resulting simulations give broad profiles for the amount of $CH_4$ occurring dissolved in water, in gas hydrate, and in free gas with respect to depth. The various models also include several assumptions. For example, reaction rates and diffusion coefficients do not change with depth and temperature in the model by *Bhatnagar et al*. (2007). Nonetheless, when appropriate parameters are incorporated, the $CH_4$ profiles generated from numerical modeling provide good

first-order descriptions of $CH_4$ profiles at sites that have been examined by direct measurements (e.g., *Davie and Buffett*, 2001, 2003a; *Liu and Flemings*, 2007; *Bhatnagar et al*., 2007, 2011).

### 3.3.2 Basic Model

One recent and encompassing 1-D numerical model for gas hydrate accumulation in marine sediments has been developed and described by *Bhatnagar et al*. (2007). This model differs from others in two important aspects. First, it computes mass balances for a system in thermodynamic equilibrium over geologic timescales, so avoids the necessity of kinetics regarding hydrate formation. Second, it frames results in terms of dimensionless groups. This enables identification of key factors controlling gas hydrate distribution and accumulation, and allows results to be compiled (and compared) for a wide range of model parameters.

Three sets of mathematical expressions underpin this model (*Bhatnagar et al*., 2007). There are those that: (1) calculate appropriate $CH_4$ phase equilibrium and solubility curves; (2) describe sediment burial and porosity reduction; and (3) account for mass conservation of $CH_4$, water, and organic carbon. The latter includes expressions for $CH_4$ diffusion driven by concentration gradients, fluid advection resulting from sediment burial and compaction, and external fluid flow caused by overpressure in deeper sediments. Parameters and equations for this

model are presented, defined and explained by *Bhatnagar et al*. (2007). Some of these are reintroduced here for clarification and expansion.

In the original model, $CH_4$ escaped the GHSZ over time through burial (as dissolved gas or free gas) or through the seafloor. Clearly, the latter does not happen at most locations, because of an SMT at or near the seafloor (Figure 3.1). The model was thus extended with mathematical expressions that coupled $CH_4$ and $SO_4^{2-}$ consumption in shallow sediment (*Bhatnagar et al*., 2008a, 2011). It was assumed that $CH_4$ drove all net $SO_4^{2-}$ consumption, following arguments made by numerous authors (e.g., *Reeburgh*, 1976; *Borowski et al*., 1996, 1999; *Snyder et al*., 2007). Both the original and revised models give good first-order estimates for the amount and distribution of gas hydrate at different sites (e.g., ODP Sites 889 and 997; IODP Sites U1325 and U1326) with appropriate input parameters (*Bhatnagar et al*., 2007, 2008a, 2011). However, the models were not evaluated with coupled mass balances for carbon. Other models for gas hydrate accumulation likewise do not track DIC, its carbon isotope composition, and authigenic carbonate precipitation. Without revision, they cannot be used to assess the divergent explanations for the concentration and $\delta^{13}\mathrm{C}$ of pore water DIC across the SMT.

### 3.3.3 Updated Model: Reactions

Carbon cycling within and above marine gas hydrate systems involves multiple chemical reactions. At the most basic level, four must be considered (excluding those relating to $CH_4$ phase changes). These are, with their corresponding rates:

Methanogenesis (fermentation in sediment below the SMT)

$$2\mathrm{CH_2O} + \mathrm{H_2O} \quad \longrightarrow \quad \mathrm{CH_4} + \mathrm{HCO_3^-} + \mathrm{H^+} \qquad r_{meth} = -\lambda\alpha \tag{3.3}$$

Anaerobic oxidation of methane (at the SMT)

$$\mathrm{CH_4(aq)} + \mathrm{SO_4^{2-}} \quad \longrightarrow \quad \mathrm{HCO_3^-} + \mathrm{HS^-} + \mathrm{H_2O} \qquad r_{AOM} = -\lambda_{AOM} c_m^l c_s^l \tag{3.4}$$

Organoclastic sulfate consumption (between the seafloor and the SMT)

$$2\mathrm{CH_2O(s)} + \mathrm{SO_4^{2-}} \quad \longrightarrow \quad 2\mathrm{HCO_3^-} + \mathrm{HS^-} + \mathrm{H^+} \qquad r_{POC} = -\lambda_{POC}\alpha c_s^l \tag{3.5}$$

Authigenic carbonate (calcite) precipitation (below the seafloor)

$$\mathrm{HCO_3^-} + \mathrm{Ca^{2+}} \rightleftharpoons \mathrm{H^+} + \mathrm{CaCO_3}\downarrow \qquad r_{ppt} = \frac{\Delta c_{CaCO_3}}{\Delta t} \tag{3.6}$$

where $r$ is rate of reaction, $\lambda$ is first-order methanogenesis reaction rate constant, $\lambda_{AOM}$ and $\lambda_{POC}$ refer to second-order reaction rate constants for AOM

and POC-driven sulfate consumption respectively; $\alpha$ is organic carbon content in sediment, $c_i^j$ is mass fraction of component $i$ in phase $j$, and $t$ is time; and, the subscripts $m$, $s$, $CaCO_3$ refer to $CH_4$, $SO_4^{2-}$, and $CaCO_3$ components respectively, and the superscript $l$ refers to the liquid phase (see notation section). Note that the first three reactions (equations 3.3 - 3.5) are modeled as irreversible and expressed with a kinetic rate, while the fourth reaction (equation 3.6) is modeled as a reversible equilibrium reaction. Whenever pore water concentrations exceed equilibrium, stoichiometric amounts of DIC and $Ca^{2+}$ are assumed to precipitate as calcium carbonate. The rate of this reaction in the model is the amount of calcium carbonate formed over a unit time step. Thus, this model ignores hydrate formation kinetics but includes $CH_4$ formation kinetics (equation 3.3).

It is acknowledged that methanogenesis (equation 3.3) involves intermediate reactions (Appendix A). Excess $H^+$ produced by the above reactions is assumed to form dissolved organic acids and ammonium ion, because pore waters in gas hydrate systems can have a deep yellow color and very high $NH_4^+$ concentrations (e.g., *Shipboard Scientific Party*, 1996, 2003a, 2003b). These species can then advect or diffuse, although these are not modeled here. Last, carbonate precipitation is equated to calcite precipitation throughout this work for simplicity. Authigenic calcite certainly forms near the SMT above many gas hydrate systems (e.g., *Rodriguez et al*., 2000; *Snyder et al*., 2007), although other carbonate minerals (aragonite and dolomite) can also precipitate (*Bohrmann et al*., 1998;

*Greinert et al*., 2001).

### 3.3.4 Updated Model: Mass balances

Starting with the existing model framework (*Bhatnagar et al*., 2007, 2008a), key mass balance equations are revised to include organoclastic sulfate consumption (equation 3.5) and calcite precipitation (equation 3.6). Additionally, the $^{12}\mathrm{C}$ and $^{13}\mathrm{C}$ isotope compositions of $CH_4$ and DIC, the two carbon species in the model are tracked. The $^{12}\mathrm{C}$ and $^{13}\mathrm{C}$ compositions of $CH_4$ and DIC are determined by multiplying the concentration and $^{13}\mathrm{C}/^{12}\mathrm{C}$ ratio of the species. Isotope compositions are then normalized to those of the Pee Dee Belemnite (PDB) standard, such that they are computed and expressed in conventional delta notation ($\delta^{13}\mathrm{C}$) over time and depth.

#### Organic Carbon

During sediment burial, microbes use a portion of POC in chemical reactions. This labile (utilizable) organic carbon is defined as $\alpha_o$. For this work, the reactions are methanogenesis (equation 3.3) and organoclastic sulfate consumption (equation 3.5). The overall mass balance equation for labile organic carbon is:

$$\frac{\partial}{\partial t}\left[(1-\phi)\rho_{sed}\alpha\right]+\frac{\partial}{\partial z}\left[(1-\phi)\rho_{sed}v_s\alpha\right] = -\rho_{sed}(1-\phi)\lambda\alpha-\frac{\phi(1-\phi)}{M_{SO_4}}\lambda_{POC}(\rho_{sed}\alpha)(\rho_w c_s^l), \tag{3.7}$$

where $\rho_{sed}$ is sediment density, $\rho_w$ is water density, $z$ is depth, $v_s$ is sediment velocity, $c_s^l$ is dissolved $SO_4^{2-}$ concentration, $\lambda$ is first-order rate constant of methanogenesis (equation 3.3), $\phi$ is porosity, $M_{SO_4}$ is molecular weight of $SO_4^{2-}$, and $\lambda_{POC}$ is second-order rate constant of organoclastic sulfate reduction (equation 3.5).

The two terms on the left of equation 3.7 represent the accumulation of labile organic carbon with time, and divergence of the transport of this component with depth. The two terms on the right correspond to the reactions that consume labile POC (equations 3.3 and 3.5, respectively). Note three simplifications: the amount of degradable POC at the seafloor is constant with time; organic carbon is buried (down) with $v_s$ equivalent to the sedimentation rate ($\dot{S}$); and the sedimentation rate is constant over time.

**Methane**

Once $CH_4$ forms in sediment, it can accumulate as dissolved gas, gas hydrate, or free gas. In a dynamic system, $CH_4$ also moves with respect to the seafloor over time. It can advect down with sediment (burial) as gas hydrate, advect up or down with fluid as dissolved or free gas, or diffuse due to concentration gradients in the dissolved phase. It can also rise as free gas; however, free gas migration is not modeled in this study (*n.b.*, compelling evidence for free gas migration through the GHSZ does not exist at the sites examined (e.g., *Cook et al.*, 2008; *Lee and*

*Collett*, 2006)). Furthermore, dissolved $CH_4$ transported toward the seafloor can react with $SO_4^{2-}$ (equation 3.4). The overall mass balance equation for dissolved $CH_4$ is:

$$\frac{\partial}{\partial t}\left[\phi\rho_w c_m^l\right] + \frac{\partial}{\partial z}\left[U_f\rho_w c_m^l\right] = \frac{\partial}{\partial z}\left[\phi\rho_w D_m \frac{\partial c_m^l}{\partial z}\right]$$

$$+\frac{M_{CH_4}}{2M_{POC}}\rho_{sed}(1-\phi)\lambda\alpha - \frac{\phi\lambda_{AOM}(\rho_w c_m^l)(\rho_w c_s^l)}{M_{SO_4}}, \tag{3.8}$$

where $U_f$ is net fluid flux, $c_m^l$ is dissolved $CH_4$ concentration, $\lambda_{AOM}$ is AOM reaction rate constant (equation 3.4), $D_m$ is $CH_4$ diffusivity, $M_{CH_4}$ and $M_{POC}$ are molecular weights of $CH_4$ and POC, respectively (and other parameters are defined above). The net fluid flux $U_f$ is the sum of the fluid flux due to sedimentation (i.e., that carried down in pore space through burial and compaction) and the external fluid flux (i.e., that moved relative to the sediment from deeper sources).

The two terms on the left of equation 3.8 represent the accumulation and divergence of $CH_4$ advection; the three terms on the right correspond to $CH_4$ diffusion, methanogenesis (equation 3.3), and AOM (equation 3.4). Methane production and concentration are assumed zero at and above the SMT. Hence, methanogenesis in the model only occurs in the absence of pore water $SO_4^{2-}$.

The mass balance equations in *Bhatnagar et al*. (2007, 2008a) include three phases for $CH_4$ (e.g., dissolved, hydrate, and free gas). In this study, the hydrate and free gas phases are neglected in the calculations, and only solve for the dissolved $CH_4$ concentration (basically, $CH_4$ concentrations exceeding solubility

do not form gas hydrate or free gas). This simplifies the model, and allows us to focus on shallow pore water chemistry profiles, the primary concern of this work. This simplification also does not affect the remaining pore water chemistry profiles (e.g., $SO_4^{2-}$, DIC, $Ca^{2+}$) as they are all dissolved species and only relate to the dissolved phase concentration of $CH_4$.

**Sulfate**

Deep ocean $SO_4^{2-}$ concentrations have been a constant value, ~28 mM, for millions of years (*Lowenstein et al*., 2001), with the exception of anoxic zones. With sediment burial, however, pore water $SO_4^{2-}$ concentrations can vary significantly (Figure 3.3a) because of fluid advection, diffusion, and two consumption reactions (equations 3.4 and 3.5). The overall $SO_4^{2-}$ mass balance equation that incorporates these factors is:

$$\frac{\partial}{\partial t}\left[\phi\rho_w c_s^l\right] + \frac{\partial}{\partial z}\left[U_f\rho_w c_s^l\right] = \frac{\partial}{\partial z}\left[\phi\rho_w D_s\frac{\partial c_s^l}{\partial z}\right]$$

$$-\frac{\phi\lambda_{AOM}(\rho_w c_m^l)(\rho_w c_s^l)}{M_{CH_4}} - \frac{\phi(1-\phi)}{2M_{POC}}\lambda_{POC}(\rho_{sed}\alpha)(\rho_w c_s^l), \qquad (3.9)$$

where $D_s$ is sulfate diffusivity (and other parameters are defined above).

The two terms on the left of equation 3.9 represent the accumulation and divergence of $SO_4^{2-}$ advection; the three terms on the right correspond to $SO_4^{2-}$ diffusion, AOM, and organoclastic sulfate reduction, respectively.

**Dissolved Inorganic Carbon**

The DIC of deep ocean water has also been fairly constant on long timescales (*Lowenstein et al*., 2001). However, like $SO_4^{2-}$, several processes can change its concentration in pore water (Figure 3.3b). Transport by advection and diffusion occurs, as well as production by methanogenesis (equation 3.3), AOM (equation 3.4), organoclastic sulfate reduction (equation 3.5), and removal by carbonate precipitation (equation 3.6). The overall DIC mass balance equation is:

$$\frac{\partial}{\partial t}\left[\phi\rho_w c_b^l\right] + \frac{\partial}{\partial z}\left[U_f\rho_w c_b^l\right] = \frac{\partial}{\partial z}\left[\phi\rho_w D_b\frac{\partial c_b^l}{\partial z}\right] + \frac{M_{HCO_3}}{2M_{POC}}\rho_{sed}(1-\phi)\lambda\alpha$$

$$+\frac{M_{HCO_3}\phi}{M_{CH_4}M_{SO_4}}\lambda_{AOM}(\rho_w c_m^l)(\rho_w c_s^l)+\frac{M_{HCO_3}\phi(1-\phi)}{M_{POC}M_{SO_4}}\lambda_{POC}(\rho_{sed}\alpha)(\rho_w c_s^l)-\phi\rho_w\frac{\Delta c_{CaCO_3}}{\Delta t}, \tag{3.10}$$

where $c_b^l$ is dissolved DIC concentration, $D_b$ is DIC diffusivity, and $M_{HCO_3}$ is molecular weight of DIC, $c_{CaCO_3}$ is concentration of $CaCO_3$ precipitated (and other parameters are defined above).

The two terms on the left of equation 3.10 represent the accumulation and divergence of DIC advection; the five terms on the right correspond to diffusion, followed by the three reactions that generate DIC (equations 3.3 - 3.5), and the one reaction that consumes DIC (equation 3.6). The DIC mass balance equation does not imply that all DIC will be consumed in sediment. In fact, as will be shown, significant loss of DIC to the ocean can occur through the sediment-water interface.

**Calcium**

Dissolved $Ca^{2+}$ concentrations of deep ocean water have also been relatively constant on long timescales (*Lowenstein et al*., 2001), but often change in sediment (Figure 3.3c) because of advection, diffusion, and carbonate precipitation. The $Ca^{2+}$ mass balance equation is:

$$\frac{\partial}{\partial t}\left[\phi\rho_w c^l_{Ca}\right] + \frac{\partial}{\partial z}\left[U_f\rho_w c^l_{Ca}\right] = \frac{\partial}{\partial z}\left[\phi\rho_w D_{Ca}\frac{\partial c^l_{Ca}}{\partial z}\right] - \phi\rho_w\frac{\Delta c_{CaCO_3}}{\Delta t}, \qquad (3.11)$$

where $c^l_{Ca}$ is dissolved $Ca^{2+}$ concentration, and $D_{Ca}$ is $Ca^{2+}$ diffusivity (and other parameters are defined above).

The two terms on the left of equation 3.11 represent the accumulation and divergence of $Ca^{2+}$ advection; the two terms on the right correspond to $Ca^{2+}$ diffusion and carbonate precipitation (equation 3.6). As mentioned earlier, carbonate precipitation has been modeled as an equilibrium reaction with calcite as the mineral precipitate.

**Carbon Isotope Composition**

The carbon isotope composition ($\delta^{13}\mathrm{C}$) of $CH_4$ and DIC clearly change in sediment (Figure 3.3d). Consequently, the $^{12}\mathrm{C}$ and $^{13}\mathrm{C}$ contents of these carbon-bearing phases should be tracked, for which there are two main considerations. POC buried with sediment has a $\delta^{13}\mathrm{C}$ between -26$^0/_{00}$ and -16 $^0/_{00}$ (*Conrad*, 2005; *Kim*

*et al*., 2007). During methanogenesis, however, fractionation of carbon isotope values occurs, such that the $CH_4$ becomes depleted in $^{13}\mathrm{C}$ while the DIC becomes enriched in $^{13}\mathrm{C}$ (e.g., *Conrad*, 2005).

For $CH_4$, carbon isotopes are incorporated into equation 3.8 as follows:

$$\frac{\partial}{\partial t}\left[\phi\rho_w c_m^l \delta^{13}\mathrm{C}_{CH_4}\right] + \frac{\partial}{\partial z}\left[U_f \rho_w c_m^l \delta^{13}\mathrm{C}_{CH_4}\right] = \frac{\partial}{\partial z}\left[\phi\rho_w D_m \frac{\partial(c_m^l \delta^{13}\mathrm{C}_{CH_4})}{\partial z}\right]$$

$$+\frac{M_{CH_4}}{2M_{POC}}\rho_{sed}(1-\phi)\lambda\alpha\delta^{13}\mathrm{C}_{CH_4,meth} - \frac{\phi\lambda_{AOM}(\rho_w c_m^l)(\rho_w c_s^l)}{M_{SO_4}}\delta^{13}\mathrm{C}_{CH_4}, \qquad (3.12)$$

where $\delta^{13}\mathrm{C}_{CH_4}$ is $\delta^{13}\mathrm{C}$ of dissolved $CH_4$, and $\delta^{13}\mathrm{C}_{CH_4,meth}$ is $\delta^{13}\mathrm{C}$ of $CH_4$ produced during methanogenesis (fixed site-specific parameter).

Likewise for DIC, we incorporate carbon isotope values into equation 3.10 as follows:

$$\frac{\partial}{\partial t}\left[\phi\rho_w c_b^l \delta^{13}\mathrm{C}_{HCO_3}\right] + \frac{\partial}{\partial z}\left[U_f \rho_w c_b^l \delta^{13}\mathrm{C}_{HCO_3}\right] = \frac{\partial}{\partial z}\left[\phi\rho_w D_b \frac{\partial(c_b^l \delta^{13}\mathrm{C}_{HCO_3})}{\partial z}\right]$$

$$+\frac{M_{HCO_3}}{2M_{POC}}\rho_{sed}(1-\phi)\lambda\alpha\delta^{13}\mathrm{C}_{HCO_3,meth} + \frac{M_{HCO_3}\phi\lambda_{AOM}(\rho_w c_m^l)(\rho_w c_s^l)}{M_{CH_4}M_{SO_4}}\delta^{13}\mathrm{C}_{CH_4}$$

$$+\frac{M_{HCO_3}\phi(1-\phi)}{M_{POC}M_{SO_4}}\lambda_{POC}(\rho_{sed}\alpha)(\rho_w c_s^l)\delta^{13}\mathrm{C}_{HCO_3,POC} - \phi\rho_w\frac{\Delta\left(c_{CaCO_3}\delta^{13}\mathrm{C}_{HCO_3}\right)}{\Delta t}, \qquad (3.13)$$

where $\delta^{13}\mathrm{C}_{HCO_3}$ is $\delta^{13}\mathrm{C}$ of dissolved DIC, $\delta^{13}\mathrm{C}_{HCO_3,meth}$ is $\delta^{13}\mathrm{C}$ of DIC generated by methanogenesis (a fixed, site-specific parameter), and $\delta^{13}\mathrm{C}_{HCO_3,POC}$ is $\delta^{13}\mathrm{C}$ of DIC generated by sulfate reduction of POC (a fixed, site-specific parameter).

The two terms on the left of equation 3.13 represent the accumulation and divergence of advection of $^{12}\mathrm{C}$ and $^{13}\mathrm{C}$ in DIC; the five terms on the right correspond to the diffusion of $^{12}\mathrm{C}$ and $^{13}\mathrm{C}$ in DIC, followed by the three reactions that generate DIC (equations 3.3 - 3.5), and the one that consumes DIC (equation 3.6).

**Normalized Variables and Key Dimensionless Groups**

The mass balance equations (equations 3.7 - 3.13) can be rewritten in dimensionless form (*Bhatnagar et al*., 2007, 2008a, 2011). This reduces the number of parameters describing a particular system, and allows for straightforward comparisons of different systems from a mechanistic perspective. To accomplish this, key variables need to be normalized. The scaling schemes developed by *Bhatnagar et al*. (2007) are followed. All dimensionless variables are represented with a tilde $(\tilde{})$ to distinguish them from their corresponding dimensional forms.

Vertical depth is scaled to the base of the GHSZ ($L_t$):

$$\tilde{z} = \frac{z}{L_t}. \tag{3.14}$$

This means that, for all gas hydrate systems examined, various calculations are made and results presented with the seafloor and the base of the GHSZ having values of 0 and 1, respectively (e.g., Figures 3.4 and 3.5).

Time is normalized through a combination of $L_t$ and diffusivity of methane ($D_m$):

$$\tilde{t} = \frac{t}{L_t^2/D_m}. \tag{3.15}$$

Initial time is denoted by $\tilde{t}$ = 0 when sediments start to land on the seafloor. Normalized time $\tilde{t}$ = 1 implies the diffusion time required to travel the distance between the base of the GHSZ and the seafloor.

Contents of degradable POC in the sediment column ($\alpha$) are normalized to the initial quantity deposited at the seafloor ($\alpha_0$). The initial POC content deposited at the seafloor is normalized with the equilibrium $CH_4$ concentration at the base of GHSZ ($c_{m,eqb}$). These are expressed as:

$$\tilde{\alpha} = \frac{\alpha}{\alpha_o}, \quad \tilde{\beta} = \frac{\alpha_o}{c_{m,eqb}}. \tag{3.16}$$

Likewise, dissolved $CH_4$ concentrations through the sediment column ($c_m^l$) are normalized to the equilibrium $CH_4$ concentration at the base of GHSZ. This is because, for the upper few hundreds of meters of marine sediment, the maximum possible $c_m^l$ will typically occur at this depth (*Zatsepina and Buffett*, 1998; *Bhatnagar et al.*, 2007; Figure 3.1a). The normalization is expressed as:

$$\tilde{c}_m^l = \frac{c_m^l}{c_{m,eqb}}. \tag{3.17}$$

By contrast, pore water $SO_4^{2-}$, DIC, and $Ca^{2+}$ concentrations are normalized to their respective values in seawater, $c_{s,o}$, $c_{b,o}$, and $c_{Ca,o}$:

$$\tilde{c}_s^l = \frac{c_s^l}{c_{s,o}}, \quad \tilde{c}_b^l = \frac{c_b^l}{c_{b,o}}, \quad \tilde{c}_{Ca}^l = \frac{c_{Ca}^l}{c_{Ca,o}}. \tag{3.18}$$

In general, normalized $SO_4^{2-}$ and $Ca^{2+}$ concentrations will diminish from 1 with depth, while normalized DIC concentrations will exceed 1 with depth (Figures 3.4 and 3.5).

Porosity at a given depth is normalized to the minimum value at great depth ($\phi_\infty$):

$$\tilde{\phi} = \frac{\phi - \phi_\infty}{1 - \phi_\infty}. \tag{3.19}$$

However, to obtain appropriate porosity profile with depth and to simplify equations, two additional parameters are introduced:

$$\eta = \frac{\phi_o - \phi_\infty}{1 - \phi_\infty}, \quad \gamma = \frac{1 - \phi_\infty}{\phi_\infty}, \tag{3.20}$$

where $\phi_o$ is porosity at the seafloor and $\eta$ is the normalized porosity at the seafloor. In general, porosity decreases with depth because of compaction, so that $\phi_o > \phi > \phi_\infty$ and $\eta > \tilde{\phi}$. At great depth, porosity approaches a minimum value and the fluid and sediment velocities approach a common asymptotic value (*Berner*, 1980; *Davie and Buffett*, 2001; *Bhatnagar et al*., 2007). Fluid gets buried (downward) with the sediment and its velocity increases with depth. However, the fluid flux

(product of its velocity and porosity) at any depth remains constant at steady state conditions.

The downward component of the net fluid flux ($U_f$), defined as $U_{f,sed}$, can be expressed as a combination of sedimentation rate ($\dot{S}$) and porosity parameters (*Bhatnagar et al*., 2007):

$$U_{f,sed} = \frac{1-\phi_o}{1-\phi_\infty}\dot{S}\phi_\infty. \tag{3.21}$$

The sediment flux ($U_{sed}$) can be defined as:

$$U_{sed} = (1-\phi_o)\dot{S}. \tag{3.22}$$

It represents the downward transport of sediment grains, and is assumed to be constant. For convenience, it can be scaled with respect to $U_{f,sed}$, which can be related to $\gamma$ (*Bhatnagar et al*., 2007):

$$\tilde{U}_{sed} = \frac{U_{sed}}{U_{f,sed}} = \frac{(1-\phi_o)\dot{S}}{U_{f,sed}} = \frac{\left(\frac{1-\phi_\infty}{\phi_\infty}\right)U_{f,sed}}{U_{f,sed}} = \frac{1-\phi_\infty}{\phi_\infty} = \gamma. \tag{3.23}$$

Other than through fluid burial, dissolved species can move through external fluid flow and diffusion. The relative significance of these processes are perhaps best understood by defining two dimensionless groups known as Peclet numbers. The first Peclet number ($Pe_1$) we define characterizes the ratio of

sedimentation-compaction-driven fluid flux to methane diffusion:

$$Pe_1 = \frac{U_{f,sed} L_t}{D_m}. \tag{3.24}$$

By contrast, the second Peclet number ($Pe_2$) characterizes the ratio of external fluid flux (generally upward from deeper sediment) to $CH_4$ diffusion:

$$Pe_2 = \frac{U_{f,ext} L_t}{D_m}. \tag{3.25}$$

These dimensionless numbers are scaled by $CH_4$ difussion to enable quick comparison of relative amounts of advection and diffusion of methane. Crucially, $Pe_1$ and $Pe_2$ typically act in downward and upward directions respectively, and have opposite signs.

Another set of dimensionless groups, the Damkohler numbers, are also convenient because they characterize the ratio of reaction to diffusion. Three Damkohler numbers are defined here:

Methanogenesis:

$$Da = \frac{\lambda L_t^2}{D_m}, \tag{3.26}$$

AOM:

$$Da_{AOM} = \frac{\rho_w c_{m,eqb}}{M_{CH_4}} \frac{\lambda_{AOM} L_t^2}{D_m}, \tag{3.27}$$

Organoclastic sulfate reduction:

$$Da_{POC} = \frac{\rho_w c_{m,eqb}}{M_{POC}} \frac{\lambda_{POC} L_t^2}{D_s}. \tag{3.28}$$

All parameters and dimensionless groups are defined collectively, along with specific values in the notation section and Table 3.1.

**Dimensionless Mass Balance Equations**

The dimensional mass balance equations (equations 3.7-3.13) can be rewritten in dimensionless form using the normalized variables and dimensionless groups defined above. The evolution of POC through depth and time can be expressed as:

$$\frac{\partial}{\partial \tilde{t}} \left[ (1-\tilde{\phi})\tilde{\alpha} \right] + Pe_1 \frac{\partial}{\partial \tilde{z}} \left[ \left( \frac{1+\gamma}{\gamma} \right) \tilde{U}_{sed} \tilde{\alpha} \right] = -Da(1-\tilde{\phi})\tilde{\alpha}$$

$$- \frac{(1-\tilde{\phi})(1+\gamma\tilde{\phi})}{1+\gamma} \frac{D_s M_{POC} c_{s,o}}{D_m M_{SO_4} c_{m,eqb}} Da_{POC} \tilde{\alpha} \tilde{c}_s^l. \tag{3.29}$$

For $CH_4$, the dimensionless mass balance equation is:

$$\frac{\partial}{\partial \tilde{t}} \left[ \left( \frac{1+\gamma\tilde{\phi}}{\gamma} \right) \tilde{c}_m^l \right] + \left( \frac{1+\gamma}{\gamma} \right) (Pe_1 + Pe_2) \frac{\partial \tilde{c}_m^l}{\partial \tilde{z}} = \frac{\partial}{\partial \tilde{z}} \left[ \left( \frac{1+\gamma\tilde{\phi}}{\gamma} \right) \frac{\partial \tilde{c}_m^l}{\partial \tilde{z}} \right]$$

$$+ \frac{M_{CH_4}}{2M_{POC}} \tilde{\rho}_{sed} Da(1-\tilde{\phi})\tilde{\alpha}\beta - \left( \frac{1+\gamma\tilde{\phi}}{\gamma} \right) \frac{M_{CH_4} c_{s,o}}{M_{SO_4} c_{m,eqb}} Da_{AOM} \tilde{c}_m^l \tilde{c}_s^l. \tag{3.30}$$

For $SO_4^{2-}$:

$$\frac{\partial}{\partial\tilde{t}}\left[\left(\frac{1+\gamma\tilde{\phi}}{\gamma}\right)\tilde{c}_s^l\right]+\left(\frac{1+\gamma}{\gamma}\right)(Pe_1+Pe_2)\frac{\partial\tilde{c}_s^l}{\partial\tilde{z}}=\frac{\partial}{\partial\tilde{z}}\left[\left(\frac{1+\gamma\tilde{\phi}}{\gamma}\right)\frac{D_s}{D_m}\frac{\partial\tilde{c}_s^l}{\partial\tilde{z}}\right]$$

$$-\left(\frac{(1+\gamma\tilde{\phi})}{\gamma}\right)Da_{AOM}\tilde{c}_m^l\tilde{c}_s^l-\frac{(1+\gamma\tilde{\phi})(1-\tilde{\phi})}{1+\gamma}\frac{D_s}{2D_m}\tilde{\rho}_{sed}Da_{POC}\tilde{\alpha}\beta\tilde{c}_s^l. \tag{3.31}$$

For DIC:

$$\frac{\partial}{\partial\tilde{t}}\left[\left(\frac{1+\gamma\tilde{\phi}}{\gamma}\right)\tilde{c}_b^l\right]+\left(\frac{1+\gamma}{\gamma}\right)(Pe_1+Pe_2)\frac{\partial\tilde{c}_b^l}{\partial\tilde{z}}=\frac{\partial}{\partial\tilde{z}}\left[\left(\frac{1+\gamma\tilde{\phi}}{\gamma}\right)\frac{D_b}{D_m}\frac{\partial\tilde{c}_b^l}{\partial\tilde{z}}\right]$$

$$+\frac{M_{HCO_3}c_{m,eqb}}{2M_{POC}c_{b,o}}\tilde{\rho}_{sed}Da(1-\tilde{\phi})\tilde{\alpha}\beta+\left(\frac{1+\gamma\tilde{\phi}}{\gamma}\right)\frac{M_{HCO_3}c_{s,o}}{M_{SO_4}c_{b,o}}Da_{AOM}\tilde{c}_m^l\tilde{c}_s^l$$

$$\frac{M_{HCO_3}c_{s,o}}{M_{SO_4}c_{b,o}}\frac{(1+\gamma\tilde{\phi})(1-\tilde{\phi})}{1+\gamma}\frac{D_s}{D_m}\tilde{\rho}_{sed}Da_{POC}\tilde{\alpha}\beta\tilde{c}_s^l-\left(\frac{1+\gamma\tilde{\phi}}{\gamma}\right)\frac{C_{Ca,o}}{C_{b,o}}\frac{\Delta\tilde{c}_{CaCO_3}}{\Delta\tilde{t}}. \tag{3.32}$$

For $Ca^{2+}$:

$$\frac{\partial}{\partial\tilde{t}}\left[\left(\frac{1+\gamma\tilde{\phi}}{\gamma}\right)\tilde{c}_{Ca}^l\right]+\left(\frac{1+\gamma}{\gamma}\right)(Pe_1+Pe_2)\frac{\partial\tilde{c}_{Ca}^l}{\partial\tilde{z}}$$

$$=\frac{\partial}{\partial\tilde{z}}\left[\left(\frac{1+\gamma\tilde{\phi}}{\gamma}\right)\frac{D_{Ca}}{D_m}\frac{\partial\tilde{c}_{Ca}^l}{\partial\tilde{z}}\right]-\left(\frac{1+\gamma\tilde{\phi}}{\gamma}\right)\frac{\Delta\tilde{c}_{CaCO_3}}{\Delta\tilde{t}}. \tag{3.33}$$

For $^{12}\mathrm{C}$ and $^{13}\mathrm{C}$ of $CH_4$:

$$\frac{\partial}{\partial\tilde{t}}\left[\left(\frac{1+\gamma\tilde{\phi}}{\gamma}\right)\tilde{c}_m^l\delta^{13}\mathrm{C}_{CH_4}\right]+\left(\frac{1+\gamma}{\gamma}\right)(Pe_1+Pe_2)\frac{\partial\left(\tilde{c}_m^l\delta^{13}\mathrm{C}_{CH_4}\right)}{\partial\tilde{z}}$$

$$= \frac{\partial}{\partial \tilde{z}} \left[ \left( \frac{1+\gamma\tilde{\phi}}{\gamma} \right) \frac{\partial \left( \tilde{c}_m^l \delta^{13}\mathrm{C}_{CH_4} \right)}{\partial \tilde{z}} \right] + \frac{M_{CH_4}}{2M_{POC}} \tilde{\rho}_{sed} Da (1-\tilde{\phi}) \tilde{\alpha} \beta \delta^{13}\mathrm{C}_{CH_4,\ meth}$$

$$- \left( \frac{1+\gamma\tilde{\phi}}{\gamma} \right) \frac{M_{CH_4} c_{s,o}}{M_{SO_4} c_{m,eqb}} Da_{AOM} \tilde{c}_m^l \tilde{c}_s^l \delta^{13}\mathrm{C}_{CH_4}. \tag{3.34}$$

For $^{12}\mathrm{C}$ and $^{13}\mathrm{C}$ of DIC:

$$\frac{\partial}{\partial \tilde{t}} \left[ \left( \frac{1+\gamma\tilde{\phi}}{\gamma} \right) \tilde{c}_b^l \delta^{13}\mathrm{C}_{HCO_3} \right] + \left( \frac{1+\gamma}{\gamma} \right) (Pe_1 + Pe_2) \frac{\partial \left( \tilde{c}_b^l \delta^{13}\mathrm{C}_{HCO_3} \right)}{\partial \tilde{z}}$$

$$= \frac{\partial}{\partial \tilde{z}} \left[ \left( \frac{1+\gamma\tilde{\phi}}{\gamma} \right) \frac{D_b}{D_m} \frac{\partial \left( \tilde{c}_b^l \delta^{13}\mathrm{C}_{HCO_3} \right)}{\partial \tilde{z}} \right] + \frac{M_{HCO_3} c_{m,eqb}}{2M_{POC} c_{b,o}} \tilde{\rho}_{sed} Da (1-\tilde{\phi}) \tilde{\alpha} \beta \delta^{13}\mathrm{C}_{HCO_3,\ meth}$$

$$+ \left( \frac{1+\gamma\tilde{\phi}}{\gamma} \right) \frac{M_{HCO_3} c_{s,o}}{M_{SO_4} c_{b,o}} Da_{AOM} \tilde{c}_m^l \tilde{c}_s^l \delta^{13}\mathrm{C}_{CH_4}$$

$$+ \frac{M_{HCO_3} c_{s,o}}{M_{SO_4} c_{b,o}} \frac{(1+\gamma\tilde{\phi})(1-\tilde{\phi})}{1+\gamma} \frac{D_s}{D_m} \tilde{\rho}_{sed} Da_{POC} \tilde{\alpha} \beta \tilde{c}_s^l \delta^{13}\mathrm{C}_{HCO_3,\ POC}$$

$$- \left( \frac{1+\gamma\tilde{\phi}}{\gamma} \right) \frac{C_{Ca,o}}{C_{b,o}} \frac{\Delta \left( \tilde{c}_{CaCO_3} \delta^{13}\mathrm{C}_{HCO_3} \right)}{\Delta \tilde{t}}. \tag{3.35}$$

The above differential mass balance equations can be solved for finite solutions, with initial conditions and boundary conditions.

**Initial Conditions ($\tilde{t} = 0$)**

Seafloor temperature ($T_0$) and the geothermal gradient ($dT/dz$) are specified and remain invariant through time. Consequently, there is a fixed, increasing temperature profile with depth.

Pressure is set to hydrostatic conditions throughout the sediment column. This appears valid for $z < L_t$ because, in several drill holes, the base of the GHSZ lies close to a depth predicted from gas hydrate stability conditions, measured temperatures, salinities and hydrostatic pressure (e.g., *Paull et al*.,1996; *Trehu et al*., 2003). With this assumption, the normalized porosity profile can be computed as an analytical expression (*Bhatnagar et al*., 2007):

$$\tilde{\phi} = \frac{\eta}{\eta + (1-\eta)e^{N_{t\phi}\tilde{z}}}, \tag{3.36}$$

where $N_{t\phi}$ is the depth to the base of the GHSZ relative to the compaction depth ($L_\phi$). These parameters are defined as:

$$N_{t\phi} = \frac{L_t}{L_\phi}, \quad L_\phi = \frac{\sigma_\phi}{(1-\phi_\infty)(\rho_{sed} - \rho_w)g}, \tag{3.37}$$

where $\sigma_\phi$ is characteristic constant with units of stress, and $g$ is acceleration due to gravity. In all the following simulations, $N_{t\phi}$ = 1, implying compaction depth ($L_\phi$) is equal to the thickness of the GHSZ ($L_t$). Unit compaction depth further implies porosity at this depth is reduced by $1/e$ (or 36.8%) from its initial porosity at the seafloor.

The labile organic carbon content ($\alpha$) is assumed to be 0% throughout all sediment at initial time $\tilde{t}$ = 0. No $CH_4$ is present at this time in the sediment column, so the $CH_4$ concentration ($c_m^l$) is zero. Therefore, the normalized labile

organic content ($\tilde{\alpha}$), and the $CH_4$ concentration ($\tilde{c}_m^l$) are zero (equation 3.38).

$$\tilde{\alpha}(\tilde{z},0)=0, \quad \tilde{c}_m^l(\tilde{z},0)=0. \tag{3.38}$$

The pore water $SO_4^{2-}$ ($c_s^l$), DIC ($c_b^l$), $Ca^{2+}$ ($c_{Ca}^l$) concentrations, and the carbon isotope compositions ($\delta^{13}\mathrm{C}$) are assumed to be seawater values at initial time for any depth $\tilde{z}$. The normalized pore water concentrations of $SO_4^{2-}$ ($\tilde{c}_s^l$), DIC ($\tilde{c}_b^l$), $Ca^{2+}$ ($\tilde{c}_{Ca}^l$) are unity at $\tilde{t}=0$ (equation 3.39). At the same time, carbon isotope compositions in $CH_4$ and DIC are zero because the carbon isotope compositions are normalized relative to a marine carbonate standard.

$$\tilde{c}_s^l(\tilde{z},0)=1, \quad \tilde{c}_b^l(\tilde{z},0)=1, \quad \tilde{c}_{Ca}^l(\tilde{z},0)=1,$$

$$\delta^{13}\mathrm{C}_{CH_4}(\tilde{z},0)=0, \quad \delta^{13}\mathrm{C}_{HCO_3}(\tilde{z},0)=0. \tag{3.39}$$

In essence, at $\tilde{t}=0$, there is a sediment column with prescribed physical conditions (i.e., temperature, pressure, and porosity). This column has no POC, and pore space is filled with seawater. For all $\tilde{t}>0$, POC is continuously deposited on the seafloor. A fraction of this is labile and, upon burial, drives a sequence of chemical reactions. These lead to changes in pore water $CH_4$, $SO_4^{2-}$, DIC, and $Ca^{2+}$ concentrations, as well as the $\delta^{13}\mathrm{C}$ of DIC. The amounts of $CH_4$, DIC and $Ca^{2+}$ are restricted because of solubility.

**Boundary Conditions**

As time progresses, pore water concentrations throughout the sediment column change from their initial values. Boundary values are specified to all variables at the seafloor, and at the bottom of the simulation domain. Normalized labile POC content is unity at the seafloor. By contrast, due to very low $CH_4$ concentrations in seawater, normalized $CH_4$ concentration is zero at the seafloor. These boundary values are:

$$\tilde{\alpha}(0,\tilde{t}) = 1, \quad \tilde{c}_m^l(0,\tilde{t}) = 0. \tag{3.40}$$

As discussed earlier, $CH_4$ concentration is also zero below the seafloor until the SMT. Importantly, however, this is not prescribed as a boundary value. Instead, this condition arises in the model because minimal methanogenesis occurs in the presence of $SO_4^{2-}$, and because $CH_4$ reacts with $SO_4^{2-}$ via AOM.

At the seafloor, normalized pore water $SO_4^{2-}$, DIC and $Ca^{2+}$ concentrations are unity, while normalized carbon isotope compositions in $CH_4$ and DIC are zero. These are:

$$\tilde{c}_s^l(0,\tilde{t}) = 1, \quad \tilde{c}_b^l(0,\tilde{t}) = 1, \quad \tilde{c}_{Ca}^l(0,\tilde{t}) = 1,$$

$$\delta^{13}\mathrm{C}_{CH_4}(0,\tilde{t}) = 0, \quad \delta^{13}\mathrm{C}_{HCO_3}(0,\tilde{t}) = 0. \tag{3.41}$$

Upward fluid flux is modeled so as to transport dissolved $CH_4$, DIC, $Ca^{2+}$, and other pore water species from deeper sediments. Consequently, pore water concentrations need to be specified at the base of the simulation domain ($L_z =$

$2L_t$). Pore water $CH_4$ concentration at this depth ($c_{m,ext}$) equals the equilibrium $CH_4$ concentration $c_{m,eqb}$ at this depth (equation 3.42):

$$\tilde{c}_m^l(\tilde{L}_z, \tilde{t}) = \tilde{c}_{m,ext} = c_{m,eqb}(\tilde{L}_z). \tag{3.42}$$

where $\tilde{c}_{m,ext}$ is normalized specified $CH_4$ concentration at depth $\tilde{L}_z$ (=$L_z/L_t$). The system, therefore, is charged with $CH_4$ saturated water at the lowermost boundary.

Similarly, normalized concentrations are specified at $\tilde{L}_z$ for $SO_4^{2-}$ ($\tilde{c}_{s,ext}$), DIC ($\tilde{c}_{b,ext}$) and $Ca^{2+}$ ($\tilde{c}_{Ca,ext}$). Pore water $SO_4^{2-}$ is consumed above or at the SMT; hence, ($\tilde{c}_{s,ext}$) is zero. Dissolved DIC and $Ca^{2+}$ concentrations are set so they are in equilibrium with solubility concentrations of $CaCO_3$ at depth. Collectively,

$$\tilde{c}_s^l(\tilde{L}_z, \tilde{t}) = \tilde{c}_{s,ext} = 0, \quad \tilde{c}_b^l(\tilde{L}_z, \tilde{t}) = \tilde{c}_{b,ext}, \quad \tilde{c}_{Ca}^l(\tilde{L}_z, \tilde{t}) = \tilde{c}_{Ca,ext}. \tag{3.43}$$

During methanogenesis, a range of solid organic molecules with a range of carbon isotope compositions produces $CH_4$ relatively depleted in $^{13}\mathrm{C}$, and DIC relatively enriched in $^{13}\mathrm{C}$. The pathways involved are somewhat complex, especially regarding isotope fractionation (Appendix A; *Conrad*, 2005). To simplify the modeling, we assume a fixed $\delta^{13}\mathrm{C}$ for POC and labile POC ($\delta^{13}\mathrm{C}_{POC}$), and a fixed $\delta^{13}\mathrm{C}$ for $CH_4$ generated during methanogenesis ($\delta^{13}\mathrm{C}_{CH_4,meth}$). Both values will be site specific. The $\delta^{13}\mathrm{C}_{CH_4,meth}$ values are determined by computing the average values of $\delta^{13}\mathrm{C}$ of $CH_4$ (*Milkov et al*., 2005; *Lorenson et al*., 2008)

measured at the two sites. This implies that the fractionation factor ($\epsilon_m$) and the $\delta^{13}\mathrm{C}$ of DIC produced during methanogenesis ($\delta^{13}\mathrm{C}_{HCO_3,meth}$) will also be fixed at a given site. For the two sites of immediate interest, the values are:

$$\delta^{13}\mathrm{C}_{POC} = -24\,‰, \quad \delta^{13}\mathrm{C}_{CH_4,meth} = -70\,‰, \quad (\text{Site } 1244), \tag{3.44}$$

$$\delta^{13}\mathrm{C}_{POC} = -22\,‰, \quad \delta^{13}\mathrm{C}_{CH_4,meth} = -75\,‰, \quad (\text{Site KC151} - 3). \tag{3.45}$$

Fractionation factor ($\epsilon_m$) is defined as the ratio of $\delta^{13}\mathrm{C}$ of labile POC and $CH_4$:

$$\epsilon_m = \frac{\delta^{13}\mathrm{C}_{POC} + 1000}{\delta^{13}\mathrm{C}_{CH_4,meth} + 1000}. \tag{3.46}$$

The $\delta^{13}\mathrm{C}_{HCO_3,meth}$ values and the fractionation factors at these sites are calculated using the carbon isotope compositions $\delta^{13}\mathrm{C}_{POC}$, and $\delta^{13}\mathrm{C}_{CH_4,meth}$:

$$\delta^{13}\mathrm{C}_{HCO_3,meth} = +22\,‰, \quad \epsilon_m = 1.049 \quad (\text{Site } 1244), \tag{3.47}$$

$$\delta^{13}\mathrm{C}_{HCO_3,meth} = +31\,‰, \quad \epsilon_m = 1.057 \quad (\text{Site KC151} - 3). \tag{3.48}$$

The carbon isotope composition of DIC ($\delta^{13}\mathrm{C}_{HCO_3}$) produced by organoclastic sulfate reduction is equated to that of POC ($\delta^{13}\mathrm{C}_{POC}$). For sediment at respective sites:

$$\delta^{13}\mathrm{C}_{HCO_3,POC} = \delta^{13}\mathrm{C}_{POC} = -24\,‰ \ (\text{Site } 1244), \tag{3.49}$$

$$\delta^{13}\mathrm{C}_{HCO_3,POC} = \delta^{13}\mathrm{C}_{POC} = -22\,‰\ \ (\mathrm{Site\ KC151-3}). \tag{3.50}$$

The $\delta^{13}\mathrm{C}$ of $CH_4$ ($\delta^{13}\mathrm{C}_{CH_4}$) and DIC ($\delta^{13}\mathrm{C}_{HCO_3}$) at the basal boundary ($\tilde{L}_z$) are specified as observed in field data (*Milkov et al*., 2005; *Torres and Rugh*, 2006; *Lorenson et al*., 2008; *Kastner et al*., 2008a):

For Site 1244:

$$\delta^{13}\mathrm{C}_{CH_4}(\tilde{L}_z,\tilde{t}) = \delta^{13}\mathrm{C}_{CH_4,ext} = -65\,‰,$$

$$\delta^{13}\mathrm{C}_{HCO_3}(\tilde{L}_z,\tilde{t}) = \delta^{13}\mathrm{C}_{HCO_3,ext} = +20\,‰. \tag{3.51}$$

For Site KC151-3:

$$\delta^{13}\mathrm{C}_{CH_4}(\tilde{L}_z,\tilde{t}) = \delta^{13}\mathrm{C}_{CH_4,ext} = -70\,‰,$$

$$\delta^{13}\mathrm{C}_{HCO_3}(\tilde{L}_z,\tilde{t}) = \delta^{13}\mathrm{C}_{HCO_3,ext} = +10\,‰. \tag{3.52}$$

### 3.3.5 Numerical Solution

The dimensionless mass balance equations (equations 3.29 - 3.35) were solved in conservative form for specified initial and boundary conditions (equations 3.38 - 3.52) to obtain steady state solutions. The hyperbolic dimensionless partial differential equation for POC (equation 3.29) was solved numerically using an implicit, block-centered, finite difference scheme. To solve the other six equations (equations 3.30 - 3.35), explicit numerical schemes were formulated. These six

partial differential equations were recast in a finite difference form and solved with simultaneous update of the POC profile in time. Solution to the above equations ensured no material loss (all simulations had material balance errors $< 10^{-8}$). A single-point, upstream weighting was used to formulate the sediment and fluid advection terms. To calculate fluxes across numerical grid faces, upstream grid point values (for species concentration) were used, as opposed to using average values at two adjacent grid points.

## 3.4 Results and Discussion

### 3.4.1 Steady State Concentration Profiles

#### Case 1: Site 1244

Site 1244 is characterized by significant $CH_4$ generation at relatively shallow depth ($z < L_t$), and relatively low fluid advection (*Pohlman et al*., 2009). Steady state concentration profiles were simulated (Figure 3.4) for parameters (Table 3.1) given or inferred from reports for this location (*Trehu et al*., 2003). The sedimentation rate was used to calculate a $Pe_1$ of 0.044. Because this relates to sediment burial and porosity reduction (equation 3.24), this parameter was fixed for all simulations at this location.

The thickness of the SMT (as opposed to depth) should depend on $Da_{AOM}$ (*Bhatnagar et al*., 2008a). The dimensionless number, $Da_{AOM}$ characterizes the

Table 3.1 : Model Parameters for Sites 1244 and KC151

| Symbol | Definition (units) | Hydrate Ridge 1244[a] | Keathley Canyon 151[b] |
|---|---|---|---|
| $L_o$ | Seafloor depth (m) | 890 | 1322 |
| $P_0$ | Seafloor pressure (MPa) | 8.72 | 12.95 |
| $T_0$ | Seafloor temperature ($^o$C) | 3.8 | 4 |
| $dT/dz$ | Geothermal gradient ($^o$C/m) | 0.061 | 0.038 |
| $L_t$ | Depth to GHSZ (mbsf) | 133.4 | 314.1 |
| $L_s$ | Depth to SMT (mbsf) | 9.2 | 10.4 |
| $\dot{S}$ | Sedimentation rate (m/Myr) | 270 | 250 |
| $U_{f,sed}$ | Fluid flux due to sedimentation (m/s) | 2.85 $\times 10^{-13}$ | 2.64 $\times 10^{-13}$ |
| $Pe_1$ | First Peclet number - sedimentation and compaction driven fluid flow | 0.044 | 0.095 |
| $Pe_2$ | Second Peclet number - external fluid flow | -1, -2, -3 | -2, -3, -5 |
| $TOC$ | Total organic carbon (%) | 1.27 | 0.44 |
| - | Labile fraction[c] (%) | 32 | 20 |
| $\alpha_o$ | Labile organic carbon at seafloor (%) | 0.4 | 0.08 |
| $\beta$ | Normalized organic carbon at seafloor | 2.4 | 0.38 |
| $c_{m,eqb}$ | $CH_4$ solubility at base of the GHSZ | 1.701 $\times 10^{-3}$ | 2.101 $\times 10^{-3}$ |
| $c_{s,o}$ | Seawater $SO_4^{2-}$ concentration (mM) | 28 | 28 |
| $c_{b,o}$ | Seawater DIC concentration (mM) | 2.4 | 2.4 |
| $c_{Ca,o}$ | Seawater $Ca^{2+}$ concentration (mM) | 10 | 10 |
| $D_m$ | $CH_4$ diffusivity[d] (m$^2$/s) | 0.87 $\times 10^{-9}$ | 0.87 $\times 10^{-9}$ |
| $D_s$ | $SO_4^{2-}$ diffusivity[d] (m$^2$/s) | 0.56 $\times 10^{-9}$ | 0.56 $\times 10^{-9}$ |

[a] *Trehu et al*. (2003)

[b] *Ruppel et al*. (2008)

[c] Labile fraction has been reported as a wide range in the literature. *Davie and Buffett* (2001, 2003a) and *Bhatnagar et al*. (2007) assumed 75% of the organic carbon to be labile and available for methanogenesis. A lower estimate was chosen for this fraction based on unconverted organic carbon data at sites 1244 and KC151-3.

[d] *Iversen and Jorgensen* (1993)

Table 3.1 contd. Model Parameters for Sites 1244 and KC151

| Symbol | Definition (units) | Hydrate Ridge 1244 | Keathley Canyon 151 |
|---|---|---|---|
| $D_b$ | DIC diffusivity[a] ($m^2/s$) | 0.6 $\times 10^{-9}$ | 0.6 $\times 10^{-9}$ |
| $D_{Ca}$ | $Ca^{2+}$ diffusivity[e] ($m^2/s$) | 0.4 $\times 10^{-9}$ | 0.4 $\times 10^{-9}$ |
| $Da$ | Damkohler number (methanogenesis) | 0.22 | 0.22 |
| $Da_{POC}$ | Damkohler number (OSR) | 2.5 | 2.5 |
| $Da_{AOM}$ | Damkohler number[b] (AOM) | $10^8$ | $10^8$ |
| $\lambda$ | Rate constant for methanogenesis ($s^{-1}$) | [c]1.07 $\times 10^{-14}$ | 1.94 $\times 10^{-15}$ |
| $\lambda_{POC}$ | Rate constant for OSR ($m^3/(mol.s)$) | 5.55 $\times 10^{-16}$ | 8.1 $\times 10^{-17}$ |
| $\lambda_{AOM}$ | Rate constant for AOM ($m^3/(mol.s)$) | 4.60 $\times 10^{-8}$ | 6.71 $\times 10^{-9}$ |
| $N_{t\phi}$ | Ratio of $L_t$ to $L_\phi$ | 1 | 1 |
| $\rho_{sed}$ | Sediment density $(kg/m^3)$ | 2650 | 2650 |
| $\rho_w$ | Water density $(kg/m^3)$ | 1000 | 1000 |
| $M_{CH_4}$ | $CH_4$ molecular weight (g/mol) | 16 | 16 |
| $M_{SO_4}$ | $SO_4^{2-}$ molecular weight (g/mol) | 96 | 96 |
| $M_{HCO_3}$ | DIC molecular weight (g/mol) | 61 | 61 |
| $M_{Ca}$ | $Ca^{2+}$molecular weight (g/mol) | 40 | 40 |
| $M_{POC}$ | POC molecular weight[d] (g/mol) | 12 | 12 |

[a] *Li and Gregory* (1974)

[b] *Bhatnagar et al*. (2008a)

[c] *Davie and Buffett* (2001), *Bhatnagar et al*. (2007)

[d] $M_{org}$ used in *Davie and Buffett* (2001, 2003a) and *Bhatnagar et al*. (2007) was interpreted as generic organic matter (MW = 30 g/mol). After *Malinverno* (2010), these parameters were rededined based on organic carbon ($M_{POC}$) and mass of carbon (MW =12 g/mol) is used for these calculations in this work.

rate of AOM reaction to diffusion. The chosen value for $Da_{AOM}$ = $10^8$ for all simulations unless otherwise specified, because this results in a thin overlap of $CH_4$ and $SO_4^{2-}$ profiles at the SMT, as observed in many locations (although difficult to prove at Site 1244 with the low sample resolution, Figure 3.3a).

The normalized dissolved $CH_4$ concentration profile (Figure 3.4a) shows near-zero values at the SMT ($\tilde{z}$ = 0.08 or 10.6 mbsf) underlain by a rapid rise with increasing depth (*n.b.*, concentration profiles are plotted to the base of the GHSZ, $\tilde{z}$ = 1, although simulated to $\tilde{z}$ = 2). Upon exceeding local solubility conditions, excess $CH_4$ would form gas hydrate. This depth occurs at $\tilde{z}$ = 0.65 (or 86 mbsf), with the chosen parameters (Table 3.1) and $Pe_2 = -1,$ which relates to an upward fluid velocity 0.3 mm/yr at the seafloor. There should exist relationships between pore water $SO_4^{2-}$ concentrations, pore water $CH_4$ concentrations, $CH_4$ solubility, and the shallowest occurrence of gas hydrate (Figure 3.1). These are emphasized elsewhere (*Bhatnagar et al.*, 2008a, 2011). Here, the primary points are that $CH_4$ rises from depth due to a combination of advection and diffusion, and it decreases to near zero concentration at the SMT. The overall profile emerges because of dissolved $CH_4$ production below the SMT, because of internal cycling of methane phases within the GHSZ (although not specifically modeled in this chapter), and because of AOM at the SMT. Moreover, as discussed below, an increase in upward fluid flux moves the methane profile and the SMT to shallower depths.

Normalized $SO_4^{2-}$ concentrations drop nearly linearly from unity at the seafloor

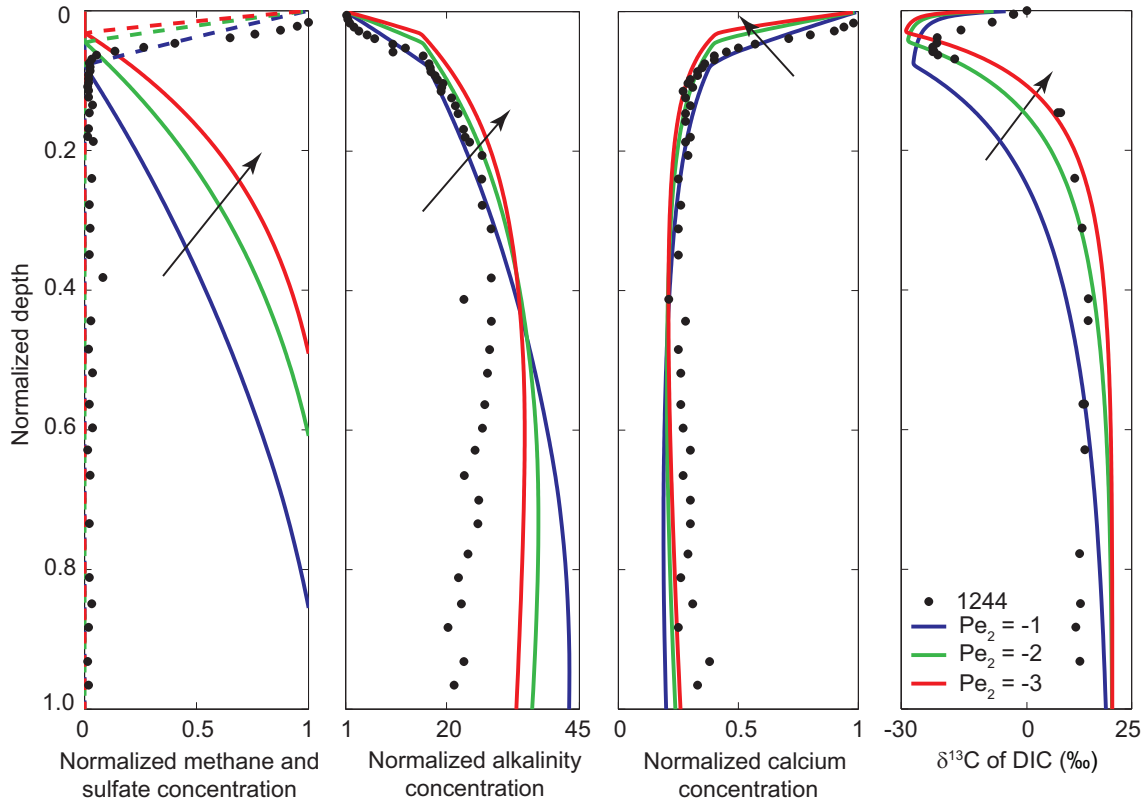


Figure 3.4 : Steady state normalized pore water concentration profiles at Site 1244. (a) $CH_4$ (solid), and $SO_4^{2-}$ (dashed), (b) DIC, (c) $Ca^{2+}$, and (d) $\delta^{13}$C of DIC. The blue, green and red curves correspond to increasing magnitude of $Pe_2$ (fluid flux from depth) shown by direction of arrow. Site 1244 data (black circles) (*Trehu et al*., 2003; *Torres and Rugh*, 2006). Parameters: $Pe_1$ = 0.044, $Da$ = 0.22, $Da_{POC}$ = 2.5, $Da_{AOM}$ = $10^8$, $\beta$ = 2.4, $\tilde{c}_{b,ext}$= 27 and $\delta^{13}C_{HCO_{3,ext}}$= 20.

to effectively zero at the SMT (Figure 3.4a). This depth lies at $\tilde{z}$ = 0.08 (10.6 mbsf) with the aforementioned initial estimates, and relatively high and low values for dimensionless groups related to rates for AOM ($Da_{AOM} = 10^8$) and organoclastic sulfate reduction ($Da_{POC} = 2.5$). The combination of AOM (at the SMT) and organoclastic sulfate reduction (between the seafloor and the SMT) removes all $SO_4^{2-}$. However, with these group values, AOM dominates net $SO_4^{2-}$ consumption.

The depth of the SMT should change with upward methane flux (e.g., *Borowski et al*., 1996; *Davie and Buffett*, 2003b; *Bhatnagar et al*., 2008a). This can be simulated under conditions of finite $Pe_1$ but varying $Pe_2$ (Figure 3.4). For example, with conditions stated so far, as the magnitude of $Pe_2$ rises from 1 to 3, the SMT shoals from $\tilde{z}$ = 0.08 to $\tilde{z}$ = 0.03 (4 mbsf). The $SO_4^{2-}$ profile at Site 1244 exhibits a slight concave-up curvature above the SMT, which could reflect a drop in sediment porosity with increasing depth over the upper few meters (*Dickens*, 2001b). Physical property records at Site 1244 appear consistent with this interpretation (*Shipboard Scientific Party*, 2003b), although such heterogeneity has not been incorporated into these simulations.

The case where $Pe_2$ is -1 is particularly interesting. This gives pore water $CH_4$ and $SO_4^{2-}$ profiles similar to those at Site 1244, including an SMT at 10.6 mbsf ($\tilde{z}$ = 0.08) (Figure 3.4a). Moreover, with $Pe_2$ = -1, the $CH_4$ profile intersects the solubility curve at $\sim$z = 0.65 (86 mbsf), (not shown here). This would mark the shallowest occurrence of gas hydrate, which is about the depth (50 mbsf) reported

in field observations (*Trehu et al*., 2003; *Lee and Collett*, 2006).

With the initial estimate ($Pe_2$ = -1), the model simultaneously simulates normalized pore water profiles of DIC and $Ca^{2+}$ concentrations, and the $\delta^{13}\mathrm{C}$ of DIC. For DIC, values increase from unity at the seafloor ($c_{b,o}$ = 2.4 mM) to 16.6 (= 39.8 mM) at the SMT ($\tilde{z}$ = 0.08); below, values increase more gradually with depth, giving rise to a curvature similar to observations (Figure 3.4b). The overall shape arises for three primary reasons: first, methanogenesis generates considerable DIC at depth; second, this DIC enters the SMT through advection and diffusion to mix with DIC generated by AOM; third, DIC decreases from the SMT to the seafloor as it leaves the sediment through advection and diffusion. Calcite precipitation also removes a small amount of DIC within 0.5 m around the SMT.

The previously noted simulations with different $Pe_2$ demonstrate the effect of increasing upward fluid flux upon the shape of the DIC profile (Figure 3.4b). As external advection (and $CH_4$ input from depth) increases, the SMT shallows and the production of DIC at this horizon (by AOM) accelerates. In addition, greater amounts of DIC generated by methanogenesis ascend with pore fluids. The total effect is to amplify the ”kink” in the DIC profile, such that greater amounts of DIC leave the system through the seafloor.

Normalized $Ca^{2+}$ concentrations (Figure 3.4c) decrease from unity at the sediment-water interface ($c_{Ca,o}$ = 10 mM) to 0.37 (= 3.7 mM) at the SMT. Below this, values continue to drop, although at a more gradual rate. The generic shape

of the $Ca^{2+}$ profile arises for three reasons: first, seawater $Ca^{2+}$ enters the SMT from above, through diffusion; second, advection carries the fluid upward ($Pe_1$ + $Pe_2 < 0$); and third, $Ca^{2+}$ reacts with DIC to precipitate as carbonate. These factors also make the $Ca^{2+}$ concentration profile a ”mirror image” of the DIC profile (albeit somewhat distorted). As such, an increase in upward fluid flux changes the shape of the $Ca^{2+}$ profile predictably: above the SMT, the gradient steepens; below the SMT, the gradient lessens slightly (Figure 3.4c). This is because fluids depleted in $Ca^{2+}$ rise from depth and increased fluid flux causes greater $CaCO_3$ precipitation. Additionally, increased delivery of DIC from below promotes $CaCO_3$ precipitation and likewise the demand for $Ca^{2+}$ from seawater, resulting in the steepened $Ca^{2+}$ gradients above the SMT.

The steady state profile for the $\delta^{13}\mathrm{C}$ of DIC (Figure 3.4d) is especially interesting. For the initial estimates, the $\delta^{13}\mathrm{C}$ of DIC drops from zero at the seafloor to -26 $^0/_{00}$ at the SMT, but with ”concave-down” curvature; below the SMT, it increases with depth to more positive values (+20 $^0/_{00}$), again with ”concave-down” curvature. Importantly, the value at the SMT and the shape around the SMT are not prescribed in the model. Instead, these occur for two reasons. First, DIC produced during methanogenesis and having an initial $\delta^{13}\mathrm{C}$ of +20 $^0/_{00}$ rises from depth to mix with DIC generated at the SMT and having a $\delta^{13}\mathrm{C}$ of -65 $^0/_{00}$. Second, this ”mixed source” DIC moves toward the seafloor, where DIC is fixed at 0 $^0/_{00}$. With an increase in external fluid flux, the $\delta^{13}\mathrm{C}$ of DIC at the SMT attains a negative peak

($\sim$-25 $^{0}/_{00}$ when $Pe_2$ = -3) at a relatively shallower depth. In summary, this pore water $\delta^{13}C$ profile arises in a system where AOM dominates net consumption of $SO_4^{2-}$ in shallow sediment.

**Case 2: Site KC151-3**

Site KC151-3 differs from Site 1244 in two fundamental ways: fluids rich in $CH_4$ and poor in $SO_4^{2-}$ rise from depth but at a relatively high rate (*Dugan*, 2008; *Daigle and Dugan*, 2010a); and concentrations of pore water DIC and $Ca^{2+}$ are low ($<$10 mM) and high ($>$20 mM), respectively, at the base of the simulated domain. Pore water concentration profiles are modeled at Site KC151-3 (Figure 3.5) in an identical manner to those at Site 1244, but with a different set of parameters based on observations for Site KC151-3 (Table 3.1).

From the sedimentation rate, a $Pe_1$ of 0.095 is calculated. An initial estimate for $Pe_2$ was -2, which relates to an upward fluid velocity 0.25 mm/yr at the seafloor (comparable to $Pe_2$ = -1 at Site 1244). The dimensionless groups related to AOM rate ($Da_{AOM} = 10^8$) and organoclastic sulfate reduction ($Da_{POC} = 2.5$) used to model location KC151-3 were the same as used for Site 1244. The combined effects of AOM (at the SMT) and organoclastic sulfate reduction (between the seafloor and the SMT) are responsible for net $SO_4^{2-}$ consumption, although owing to the relatively low value of $Da_{POC}$, AOM is dominant also at KC151-3.

The normalized dissolved $CH_4$ profile (Figure 3.5a) is zero between the seafloor

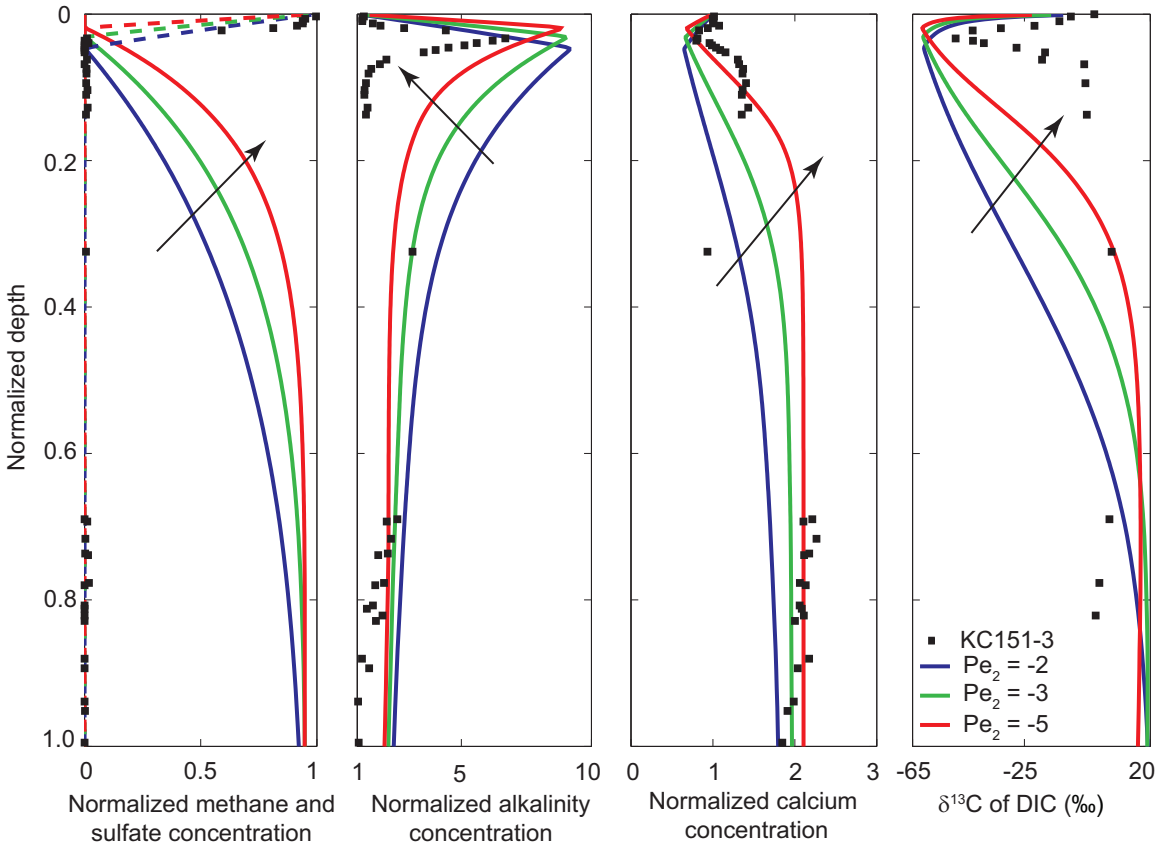


Figure 3.5 : Steady state normalized pore water concentration profiles at Site KC151-3. (a) $CH_4$ (solid), and $SO_4^{2-}$ (dashed), (b) DIC, (c) $Ca^{2+}$, and (d) $\delta^{13}C$ of DIC. The blue, green and red curves correspond to increasing magnitude of $Pe_2$ (fluid flux from depth) shown by direction of arrow. Site KC151-3 data (black circles) (*Kastner et al*., 2008b). Parameters: $Pe_1$ = 0.095, $Da$ = 0.22, $Da_{POC}$ = 2.5, $Da_{AOM}$ = $10^8$, $\beta$ = 0.38, $\tilde{c}_{b,ext}$ = 1.5 and $\delta^{13}C_{HCO_{3,ext}}$ = 10.

and the SMT ($\tilde{z}$ = 0.05 or 15.7 mbsf). Below 15.7 mbsf, it shows a rapid increase with depth. Methane concentrations intersect those on the solubility curve at $\tilde{z}$ = 0.45 (or 141 mbsf). This should mark the shallowest possible occurrence of gas hydrate, but log interpretations suggest gas hydrate occurs between 110 and 115 mbsf (*Cook et al*., 2008).

Normalized, steady state $SO_4^{2-}$ concentrations (Figure 3.5a) decrease nearly linearly from unity at the sediment-water interface to near-zero at the SMT ($\tilde{z}$ = 0.05). As at Site 1244, the $SO_4^{2-}$ data exhibit a slight concave-up curvature above the SMT at Site KC151-3. The simulated $SO_4^{2-}$ profile does not show such curvature, and this may again relate to a drop in porosity over the first few meters.

Upon increasing the external fluid flux (and the magnitude of $Pe_2$), the SMT shoals (Figure 3.5a). For one particular parameter choice ($Pe_2$ = -3), the $SO_4^{2-}$ profile drops to near-zero concentration at $\tilde{z}$ = 0.031. This implies that the SMT and the top of gas hydrate occur at $\sim$9.8 mbsf and $\sim$82 mbsf ($\tilde{z}$ = 0.26), respectively. These values agree favorably with field data.

Normalized DIC profiles (Figure 3.5b) contrast markedly with those at Site 1244, irrespective of fluid flux. For the initial estimate, concentrations increase with depth until the SMT, below which they decrease to very low values ($\sim$4 mM). The prominent DIC peak at the SMT arises for four primary reasons: first, and most importantly, AOM generates DIC at the SMT; second, this DIC, through advection and diffusion, leaves the SMT; third, methanogenesis produces DIC at

depth; fourth, pore fluids enriched in $Ca^{2+}$ react with DIC below the SMT. Calcite precipitation also removes relatively more DIC below the SMT at this location.

An increase in upward fluid flux changes the shape of the DIC profile above and below the SMT (Figure 3.5b). However, the reason is somewhat different than that for Site 1244. A higher fluid flux results in greater $CH_4$ input to the SMT, greater DIC generation by AOM, greater DIC input to the SMT from depth, and greater DIC removal from the SMT toward the seafloor. It also raises the $Ca^{2+}$ input from depth, which leads to greater calcite precipitation, below the SMT. Similar to $SO_4^{2-}$, DIC profiles also approach the field data for a value of $Pe_2$ = -3.

Normalized pore water $Ca^{2+}$ concentrations (Figure 3.5c) drop from unity at the seafloor to a low value at the SMT and then increase to a constant value at depth. The shape of $Ca^{2+}$ profiles arises for multiple reasons: first, $Ca^{2+}$ from the ocean water enters the SMT from above due to diffusion; second, a high flux of $Ca^{2+}$ enters the SMT from deeper strata, through advection and diffusion; a third, significant amount of calcite precipitates. The combination gives rise to the unusual $Ca^{2+}$ profile with a ”dip” below the SMT. A higher upward fluid flux compresses this dip because of greater $Ca^{2+}$ input from depth, and because of greater calcite precipitation (Figure 3.5c). These model simulations render results approaching those of field data when $Pe_2$ = -3.

The modeled profiles of DIC $\delta^{13}\mathrm{C}$ differ significantly from those at Site 1244 in terms of magnitude (Figure 3.5d). For the initial estimate ($Pe_2$ = -2), normalized

$\delta^{13}\mathrm{C}$ of DIC is zero at the seafloor, drops to an extreme of -62 $^{0}/_{00}$ at the SMT, and then increases gradually with depth, but only to 10 $^{0}/_{00}$. On increasing fluid flux from depth, the $\delta^{13}\mathrm{C}$ values similarly drops from 0 $^{0}/_{00}$ to a negative peak at a relatively shallower SMT, then increases more rapidly to more positive values at greater depth.

Crucially, the values and the curvature of the DIC $\delta^{13}\mathrm{C}$ profile result from modeling the $CH_4$ and $SO_4^{2-}$ mass balances using basic parameters for the site; they are not specified. Moreover, and importantly, the values and the curvature arise for same general reasons as at Site 1244. The difference between the sites mainly occurs because the flux and carbon isotopic composition of DIC entering the SMT from below are less at KC151-3, and because the DIC produced at SMT (by AOM) has a more $^{13}\mathrm{C}$-depleted value ($\delta^{13}\mathrm{C}$ = -70 $^{0}/_{00}$). In other words, the proportion of DIC entering the SMT from depth versus that produced by AOM is much lower at Site KC151-3 compared to Site 1244. This gives a lower DIC concentration at the SMT and a more negative peak in DIC $\delta^{13}\mathrm{C}$ at the SMT.

### 3.4.2 Variations in AOM and Organoclastic Sulfate Reduction

Anaerobic oxidation of methane at the SMT with minimal organoclastic sulfate reduction at or above this horizon explains pore water profiles across the SMT at Sites 1244 and KC151-3. The very different carbon chemistry at these sites is predicted by the numerical simulations because of major differences in the supply

and isotope composition of DIC from depth. So far, an unresolved issue is how changes in the relative proportion of AOM and organoclastic sulfate reduction would affect the profiles. This can be assessed by changing $Da_{AOM}$ and $Da_{POC}$ in model simulations for Site 1244.

A decrease in $Da_{AOM}$ from its initial value of $10^8$ to $10^5$ illustrates the effect of this dimensionless number on pore water profiles (Figure 3.6a) with same parameters used to simulate the field data at Site 1244 (see notation section). As reported by *Bhatnagar et al*. (2008a), a decrease in $Da_{AOM}$ slows the AOM reaction, and leads to a thicker SMT. Because the SMT horizon is usually thin ($<$2 m), this small value of $Da_{AOM}$ is probably unrealistic. Moreover, a smaller $Da_{AOM}$ lowers the DIC generation at the SMT by AOM, and the $Ca^{2+}$ removal by calcite formation. This would render higher $Ca^{2+}$ concentrations at and above the SMT, and a more negative $\delta^{13}\mathrm{C}$ values for DIC. These simulated profiles ($Da_{AOM} = 10^5$) would not match data at the site, suggesting typical values of $Da_{AOM}$ are slightly on the high side.

An increase in $Da_{POC}$ should result in higher consumption of POC and $SO_4^{2-}$ between the seafloor and the SMT. This results in higher DIC generation above the SMT and a non-linear $SO_4^{2-}$ profile with a ”concave-down” curvature. Moreover, POC gets removed faster in shallow sediment, which means there is less POC to form $CH_4$ in deeper sediment. As a result, the flux and $\delta^{13}\mathrm{C}$ value of DIC entering the SMT from below are lower (Figure 3.6b). A greatly increased $Da_{POC}$ ($= 2.5 \times$

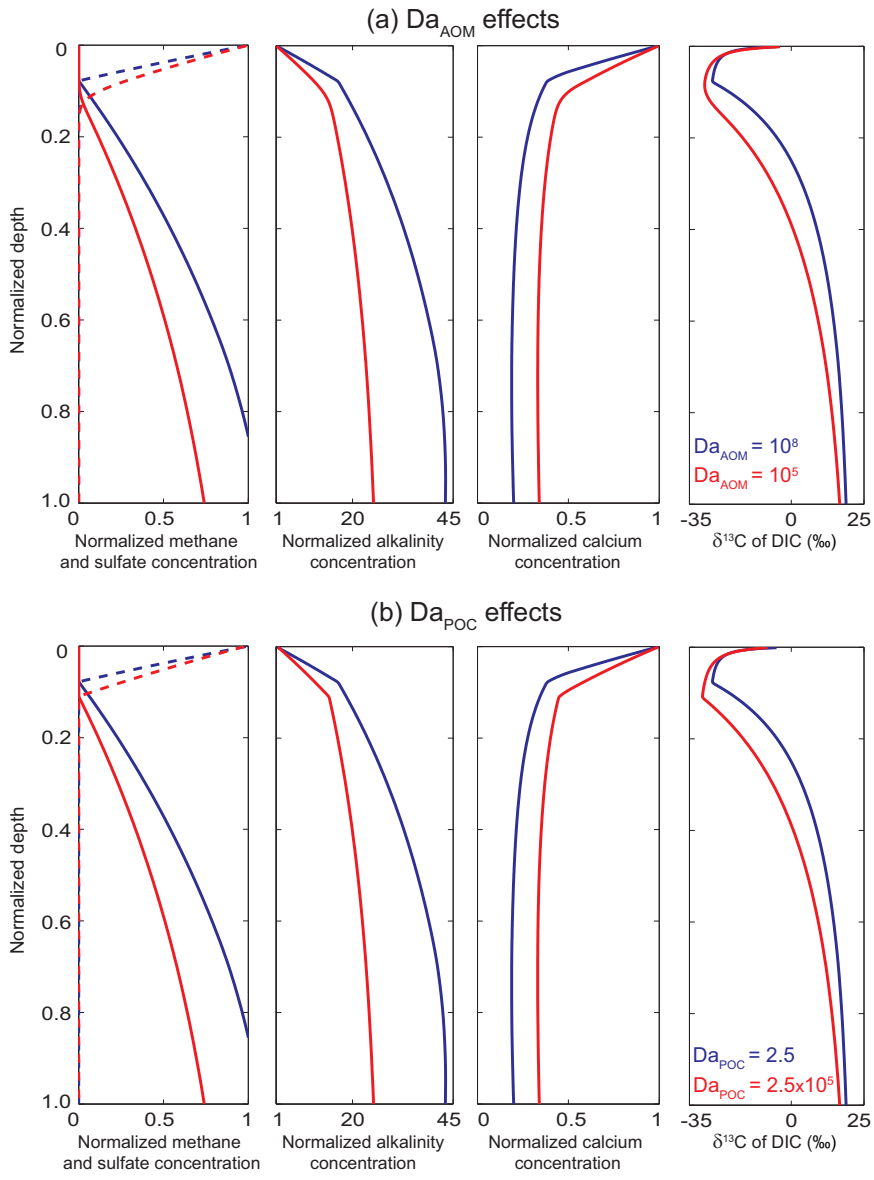


Figure 3.6 : (a) Steady state pore water profiles to study the effect of $Da_{AOM}$ at Site 1244. Decrease in $Da_{AOM}$ results in a thicker SMT horizon. Parameters: $Pe_1$ = 0.044, $Pe_2$ = -1, $Da$ = 0.22, $Da_{POC}$ = 2.5, $\beta$ = 2.4, $\tilde{c}_{b,ext}$ = 27 and $\delta^{13}\mathrm{C}_{HCO_{3,ext}}$ = 20. (b) Effect of $Da_{POC}$ on pore water chemistry at Site 1244. Parameters: $Pe_1$ = 0.044, $Pe_2$ = -1, $Da$ = 0.22, $Da_{AOM}$ = $10^8$, $\beta$ = 2.4, $\tilde{c}_{b,ext}$ = 27 and $\delta^{13}\mathrm{C}_{HCO_{3,ext}}$ = 20. In both cases, decreasing $Da_{AOM}$ and increasing $Da_{POC}$ result in higher POC depletion, lesser $CH_4$ and DIC production, greater $Ca^{2+}$ concentration in pore fluids above and below the SMT and a more negative $\delta^{13}\mathrm{C}$ of DIC at the SMT.

$10^5$) is not realistic because it does not give results that resemble field data.

### 3.4.3 Concentration Crossplots of Alkalinity and Sulfate

Excess alkalinity ($\Delta Alk^*$) represents the amount of DIC that would occur in pore water if authigenic carbonate had not precipitated; it can be calculated by summing the deviations in pore water alkalinity, $Ca^{2+}$, and $Mg^{2+}$ relative to their respective concentrations in seawater. Plots can be constructed showing changes in excess alkalinity ($\Delta Alk^*$) versus changes in $SO_4^{2-}$ ($\Delta SO_4^{2-}$) (Figure 3.7). Such crossplots have been used to interpret the relative influence of organoclastic sulfate reduction and AOM upon $SO_4^{2-}$ consumption in sediment above the SMT (e.g., *Claypool et al*., 2006; *Kastner et al*., 2008a; *Torres and Kastner*, 2009). Because of the different molar quantities in the reactions (equations 3.1 and 3.2), the idea has been that a 1:1 slope would support $SO_4^{2-}$ removal by AOM, a 2:1 slope would support $SO_4^{2-}$ removal by POC, and a slope in between would support consumption by both processes. Data from Site KC151-3 above the SMT lie on a 1:1 slope (Figure 3.7). By contrast, at Site 1244, a nearly 2:1 slope in $\Delta Alk^* : \Delta SO_4^{2-}$ characterizes pore waters above the SMT (Figure 3.7). This observation has been argued to indicate POC driven $SO_4^{2-}$ consumption at Site 1244 (*Kastner et al*., 2008a). However, presentation and discussion of the data in such a manner assumes a closed system with little or no mass transfer of dissolved constituents, and fails to account for changes in DIC below the SMT (*Dickens and Snyder*, 2009).

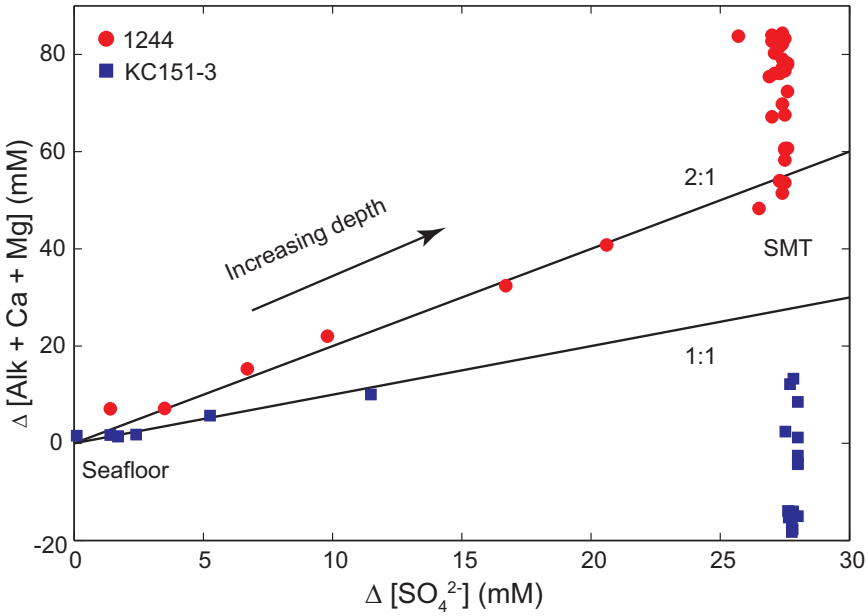


Figure 3.7 : Concentration crossplot of "excess alkalinity" ($\Delta Alk^*$) corrected for carbonate precipitation versus $\Delta SO_4^{2-}$ (mM) relative to the seafloor for shallow sediment at Site 1244 on Hydrate Ridge (*Trehu et al*., 2003) and Site KC151-3 (*Kastner et al*., 2008b). As emphasized by *Kastner et al*. (2008b), there is a 2:1 relationship for pore water concentrations above the SMT for Site 1244 (red circles) and 1:1 for Site KC151-3 (blue squares). Note, however, that excess alkalinity continues to rise below the SMT at Site 1244. This clearly implies an upward flux of alkalinity from depth; whereas, at Site KC151-3, excess alkalinity decrease below the SMT. This decrease is because DIC is consumed by $Ca^{2+}$ resulting in calcite precipitation.

The departure of alkalinity (DIC) and $SO_4^{2-}$ concentrations relative to their respective seawater values can be obtained from the simulated steady state pore water profiles. Because $Mg^{2+}$ was not included in this modeling, $\Delta Alk^*$ is only computed using DIC and $Ca^{2+}$ concentrations. A series of simulations is considered.

For the first three simulations, parameters pertain to Site 1244. However, the fluid flux and the relative proportion of $SO_4^{2-}$ consumption by AOM and organoclastic sulfate reduction are adjusted by changing $Pe_2$, $Da_{AOM}$ and $Da_{POC}$ (Figure 3.8). All three simulations give a 2:1 relation in $\Delta Alk^* : \Delta SO_4^{2-}$ (Figure 3.8).

In the first case, there is zero external fluid flux, no methanogenesis, no AOM and only organoclastic sulfate reduction. Although a 2:1 slope in $\Delta Alk^* : \Delta SO_4^{2-}$ occurs, pore water profiles (not shown here) do not conform to observations. Pore water $SO_4^{2-}$ decreases gradually with a concave-down curvature. Pore water DIC increases with depth until the SMT, below which it attains a constant value as DIC is carried down by advection (burial) and diffusion. The $\delta^{13}\mathrm{C}$ of DIC is zero at the seafloor, and attains a constant negative value at and below the SMT. Without methanogenesis, there is no change in the DIC and $\delta^{13}\mathrm{C}$ of DIC below the SMT.

In the second and the third cases, there is a low fluid flux ($Pe_2$ = -0.1), methanogenesis (and thus a deep source of DIC), and AOM. The third case includes organoclastic sulfate reduction. In these cases, a 2:1 slope in $\Delta Alk^*$:

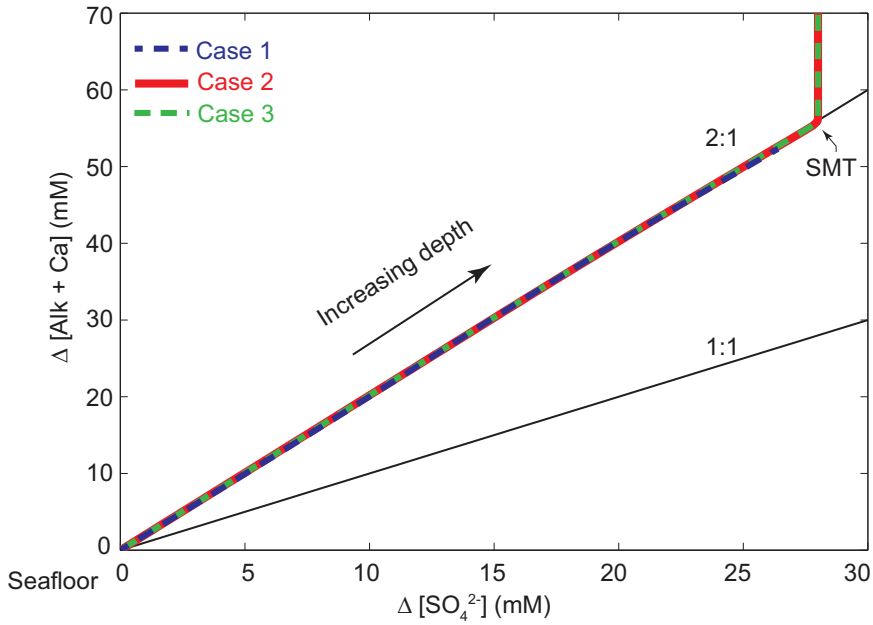


Figure 3.8 : Concentration crossplots for $\Delta Alk^*$ and $\Delta SO_4^{2-}$ relative to seawater. Three cases are illustrated here corresponding to a 2:1 slope. Blue dashed line represents a case with organoclastic sulfate reduction, no upward fluid flux, no AOM and no deep DIC source (methanogenesis). Parameters: $Pe_1$ = 0.044, $Pe_2$ = 0, $Da$ = 0, $Da_{POC}$ = 2.5, $Da_{AOM}$ = 0, $\beta$ = 2.4 and $\tilde{c}_{b,ext}$ = 0. Red solid line represents another case with low and finite upward fluid flux, AOM, methanogenesis, and a deep DIC source, but no organoclastic sulfate reduction. Parameters: $Pe_1$ = 0.044, $Pe_2$ = -0.1, $Da$ = 1, $Da_{POC}$ = 0, $Da_{AOM}$ = $10^8$, $\beta$ = 2.4 and $\tilde{c}_{b,ext}$ = 79. The green dashed line represents a third case (combination of the first two cases). It is characterized by AOM, organoclastic sulfate reduction, methanogenesis, deep DIC source and low upward fluid flux. Parameters: $Pe_1$ = 0.044, $Pe_2$ = -0.1, $Da$ = 1, $Da_{POC}$ = 2.5, $Da_{AOM}$ = $10^8$, $\beta$ = 2.4 and $\tilde{c}_{b,ext}$ = 79. A 2:1 slope not only results from organoclastic sulfate reduction alone, but also by a combination of AOM, methanogenesis and a deep DIC source. The depth from the seafloor to the SMT is shown by the arrow; below the SMT, $\Delta Alk^*$ increases with no change in $\Delta SO_4^{2-}$, implying a high DIC flux entering the SMT from below.

$\Delta SO_4^{2-}$ occurs and the profiles generally match the data.

Clearly, a crossplot showing 2:1 slope for in $\Delta Alk^*$:$\Delta SO_4^{2-}$ above the SMT concentration does not imply organoclastic consumption of $SO_4^{2-}$. It can result from multiple combinations of fluid flux with AOM and a deep source of DIC (from methanogenesis). More interestingly, changes in the fluid flux or the rate of methanogenesis and deep source DIC concentration can affect the slope (Figure 3.9). An increase in upward fluid flux (greater magnitude of $Pe_2$) will generally decrease the slope on a $\Delta Alk^*$:$\Delta SO_4^{2-}$ crossplot. This is because the SMT shoals (Figure 3.4) and because a high flux of DIC enters the SMT from depth. By contrast, an increase in methanogenesis (higher Da) and a higher concentration of DIC at depth will generally increase the slope (Figure 3.9). This is because greater methanogenesis results in more DIC at depth, which can then enter the SMT through advection and diffusion.

Simulated profiles for Site KC151-3 consistently render points that lie beneath a 2:1 slope; in fact, the slope in $\Delta Alk^*$:$\Delta SO_4^{2-}$ is less than 1:1 (Figure 3.10). This reflects the dual facts that a portion of DIC leaves the SMT to accumulate as carbonate beneath this horizon, and that excess $Ca^{2+}$ enters shallow sediment from below. An increase in upward fluid flux would decrease the slope of the crossplot similar to our above result shown at Site 1244 (Figure 3.9). In any case, the slope of the line does not indicate the reaction.

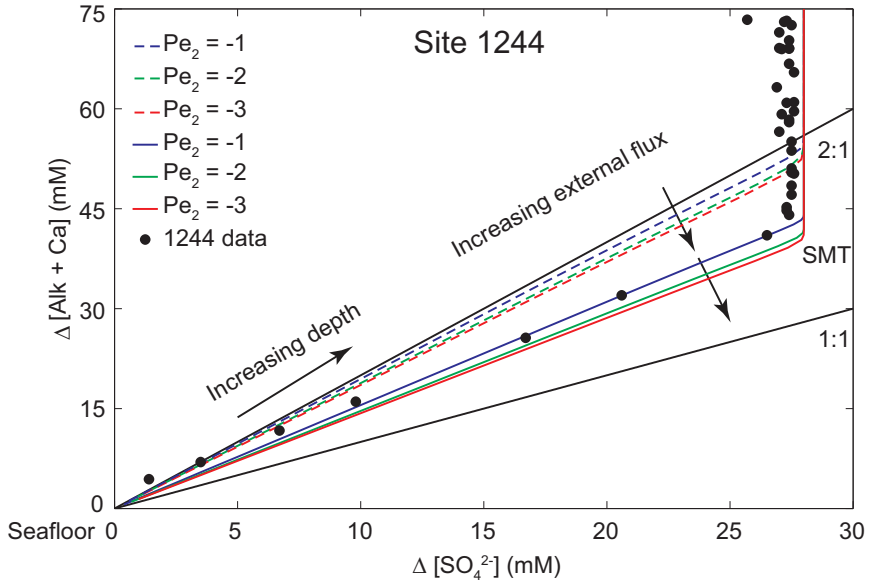


Figure 3.9 : Concentration crossplots for $\Delta Alk^*$ and $\Delta SO_4^{2-}$ relative to the seafloor with AOM, organoclastic sulfate reduction, methanogenesis, deep DIC source and upward fluid flux at Site 1244. The solid lines correspond to parameters same as in Figure 3.4. Dashed lines correspond to a case with higher rate of methanogenesis rate and greater DIC flux from depth ($Da$ = 1 and $\tilde{c}_{b,ext}$ = 50). The blue, green, and red colors indicate increasing fluid flux (corresponding to $Pe_2$ = -1, -2 and -3). Crossplot constructed from Site 1244 data (black circles) (*Trehu et al.*, 2003) matches well with the simulated crossplots. The slope decreases with increase in fluid flux from depth. Higher DIC input (due to higher methanogenesis and/or high DIC source at depth) results in a greater slope. Notably, negligence of $Mg^{2+}$ in $\Delta Alk^*$ calculations above, results in a slope less than 2:1 as compared to Figure 3.7.

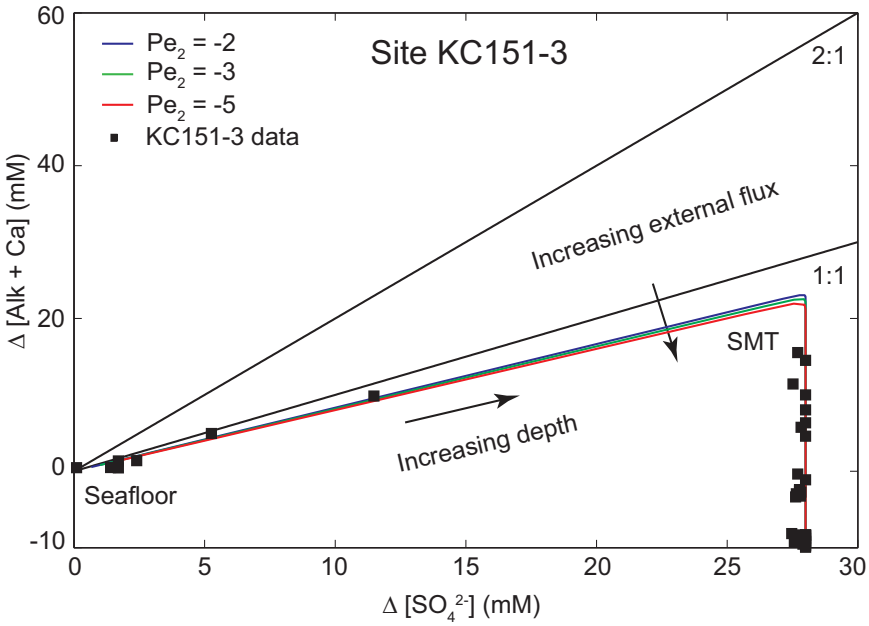


Figure 3.10 : Concentration crossplots for $\Delta Alk^*$ and $\Delta SO_4^{2-}$ relative to the seafloor with AOM, organoclastic sulfate reduction, methanogenesis, relatively depleted DIC source at depth and upward fluid flux at Site KC151-3. Parameters used are same as in 3.5. Increasing upward fluid flux (corresponding to $Pe_2$ = -2, -3 and -5) are represented by blue, green and red curves. Data from Site KC151-3 data (*Kastner et al*., 2008b) is used to construct crossplots shown by black circles. The slope of the crossplot decreases as fluid flux increases (same as in Figure 3.9). Contrary to Figure 3.9, $\Delta Alk^*$ decreases with no change in $\Delta SO_4^{2-}$ beyond the SMT, implying DIC flux leaving the SMT both above and below.

### 3.4.4 Flux Crossplots

In contrast to using $\Delta Alk^*$: $\Delta\ SO_4^{2-}$ crossplots, concentration gradients of alkalinity (DIC), $SO_4^{2-}$ and $Ca^{2+}$ in and out of the SMT might be used to evaluate the role of AOM (*Luff and Wallman*, 2003; *Snyder et al*., 2007; *Dickens and Snyder*, 2009; *Kim et al*., 2011). The basic idea is that the gradients are proportional to fluxes, so that the sum of changes across the SMT should balance.

Starting from the above simulated results, concentration gradients are computed by linearly fitting the profiles above and below the SMT. Using these gradients, and multiplying by sediment diffusion coefficients, diffusive fluxes of $CH_4$, $SO_4^{2-}$ and DIC are computed across the SMT horizon. Advective flux of any dissolved species is a function of fluid flux and the solute concentration. In the vicinity of the SMT, both the $CH_4$ and $SO_4^{2-}$ concentrations approach zero. Thus, in the vicinity of the SMT both the transport of $CH_4$ and $SO_4^{2-}$ are diffusion dominated. Furthermore, the net advective DIC flux across the SMT is calculated as a difference in deeper flux from/to deeper sediment and shallow flux to/from the seafloor. Across the SMT, this net advective DIC flux is zero as the individual deep and shallow advective DIC fluxes are equal and opposite in sign. Hence, the total flux (sum of advective and diffusive flux) is equal to the diffusive flux across the SMT.

The diffusive fluxes of $CH_4$ and DIC are now plotted relative to the $SO_4^{2-}$ flux (Figure 3.11). Crucially, this cross-plot (Figure 3.11) not only represents a diffusive

flux cross-plot, but it is also equivalent to a net flux crossplot for a given pair of species. Both $CH_4$ and DIC fluxes show a unique 1:1 correspondence relative to the $SO_4^{2-}$ flux. This 1:1 correspondence implies dominance of the AOM at the SMT, due to its stoichiometric balance (equation 3.1). Increasing the reaction rate of organoclastic sulfate reduction ($Da_{POC}$) by few orders of magnitude ($\sim 2.5 \times 10^2$) does not alter the slope of the flux crossplot (Figure 3.11). Interestingly, increasing the rate of methanogenesis ($Da$) and consequently, a high DIC source at depth also correspond to a 1:1 relation between respective fluxes. In essence, the difference between DIC flux leaving the SMT toward the seafloor and the flux entering the SMT from below is equal to the flux added at the SMT by AOM. This DIC flux added due to AOM at the SMT corresponds to the $SO_4^{2-}$ flux entering the SMT from above by a simple 1:1 correlation, again because of the stoichiometric relationship between $CH_4$, DIC, and $SO_4^{2-}$ (equation 3.1). In all these cases, the rate of downward $SO_4^{2-}$ flux via diffusion is able to keep pace with $CH_4$ delivery from below, allowing DIC fluxes to also balance across the SMT.

### 3.4.5 Relationship Between AOM and $\delta^{13}\mathrm{C}$ Values

Field data show a wide range in $\delta^{13}\mathrm{C}$ values of DIC at the SMT in shallow sediment of gas hydrate systems (Figure 3.2). A series of papers have used this to discriminate between potential causes for pore water $SO_4^{2-}$ consumption (*Claypool et al*., 2006; *Kastner et al*., 2008a; *Torres and Kastner*, 2009). The basic idea

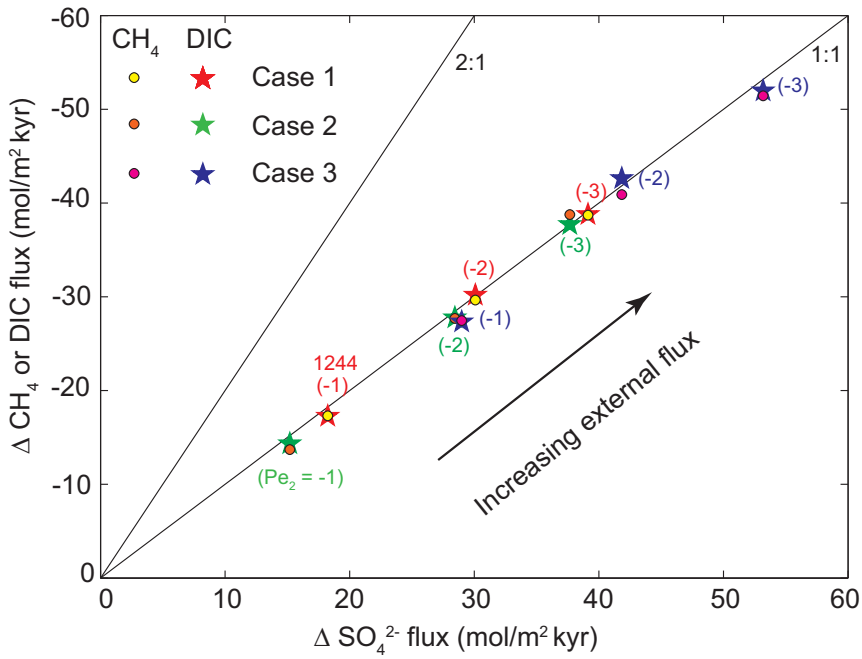


Figure 3.11 : Flux crossplots of $CH_4$ (circles) and DIC (stars) versus $SO_4^{2-}$ across the SMT corresponds to a 1:1 slope. Case 1 corresponds to simulations shown in Figure 3.4. The simulation results that best matches Site 1244 data ($Pe_2$ = -1; Figure 3.4) show 17 mol/m$^2$kyr of $SO_4^{2-}$ entering the SMT from above, 17 mol/m$^2$kyr is the difference between amounts of DIC entering from below and leaving toward the seafloor (including carbonate precipitation). This gives a net change of 17 mol/m$^2$kyr of DIC across the SMT, which balances the downward flux of $SO_4^{2-}$ and supports a 1:1 stoichiometry and dominance of AOM at the SMT. Case 2 increases the rate of organoclastic sulfate reduction by two orders of magnitude ($Da_{POC} = 2.5 \times 10^2$; all other parameters are same as Case 1) and the relative flux correspondence across the SMT is unaltered. Case 3 corresponds to high DIC flux entering the SMT from below and high methanogenesis rate also results in the same 1:1 correlation between $CH_4$ and DIC fluxes relative to $SO_4^{2-}$ flux (parameters same as dashed curves in Figure 3.9). The $Pe_2$ values (equivalent to upward fluid flux) are noted in parenthesis and the arrow indicates increase in upward fluid flux.

has been that the $\delta^{13}\mathrm{C}$ of DIC at the SMT relates to the relative proportion of DIC generated through AOM and organoclastic sulfate reduction (equations 3.1 and 3.2); the first reaction would produce DIC exceptionally depleted in $^{13}\mathrm{C}$ ($\delta^{13}\mathrm{C} <$ -40 $^{0}/_{00}$, depending on the $CH_4$ source) whereas the second reaction would produce DIC moderately depleted in $^{13}\mathrm{C}$ ($\delta^{13}\mathrm{C} \sim$ -23 $^{0}/_{00}$), roughly corresponding the $\delta^{13}\mathrm{C}$ values of POC.

This approach, however, is fundamentally flawed because it neglects other inputs (and outputs) of DIC to the SMT, especially DIC rising from depth. At most locations including Sites 1244 and KC151-3, the $CH_4$ is derived from methanogenesis (equation 3.3 and Appendix A). As such, both $^{13}\mathrm{C}$-depleted $CH_4$ and $^{13}\mathrm{C}$-enriched DIC are generated (e.g., *Conrad*, 2005), and the latter can enter and leave the SMT through advection and diffusion. The $\delta^{13}\mathrm{C}$ of DIC at the SMT, therefore, depends on the mixing of DIC with different carbon isotope compositions. The simulations highlighted in this thesis clearly show that a range of DIC $\delta^{13}\mathrm{C}$ can (and should) occur across the SMT, even when AOM consumes all $SO_4^{2-}$ in shallow sediment.

### 3.4.6 Influence of Carbonate Precipitation

Methane-charged sediment deposited on modern continental margins (including Cascadia Margin and the Gulf of Mexico) often contains authigenic carbonate (e.g., *Botz et al*, 1988; *Greinert et al*., 2001; *Formolo et al*., 2004). Certainly,

some of this carbonate precipitates at or near an SMT (e.g., *Rodriguez et al*., 2000; *Snyder et al*., 2007), consistent with this model (Figures 3.4 and 3.5). Authigenic carbonate has also been found in sedimentary rocks deposited along ancient continental margins that presumably contained high $CH_4$ concentrations (e.g., *Campbell*, 2006). Various lines of evidence (e.g., biomarkers) suggest that some of this carbonate formed in association with AOM (*Peckmann and Thiel*, 2004; *Allison et al*., 2008).

Authigenic carbonates, both modern and ancient, exhibit a wide range in $\delta^{13}\mathrm{C}$ (e.g., *Greinert et al*., 2001; *Campbell*, 2006). Various workers have generally attributed this spread to the relative inputs of $HCO_3^-$ from AOM, the oxidation of higher hydrocarbons, and organoclastic sulfate reduction (*Botz et al*., 1988; *Greinert et al*., 2001; *Formolo et al*., 2004; *Peckmann and Thiel*, 2004; *Campbell*, 2006; *Allison et al*., 2008). The model results discussed above highlight a basic problem with this approach. As discussed for pore water, carbonate precipitating at or near the SMT should have a wide range in $\delta^{13}\mathrm{C}$, even when AOM is the proximal cause for carbonate precipitation. Vertical inputs and outputs of DIC to and from the SMT must be considered.

## 3.5 Conclusions

A 1-D numerical model has been updated for the formation of gas hydrate in marine sediment (*Bhatnagar et al*., 2007, 2008a, 2011) so that it has coupled

mass balance equations for $CH_4$, $SO_4^{2-}$, DIC, $Ca^{2+}$ and the $\delta^{13}\mathrm{C}$ of $CH_4$ and DIC in pore water. This is an important progression because concentrations and carbon isotope composition of these species must be impacted collectively if $CH_4$ cycling in marine gas hydrate systems includes sediment burial, $CH_4$ production from organic carbon, an upward flux of methane, and significant loss of $CH_4$ by AOM. Moreover differences in key parameters, including solute transport from deeper sediment though advection and diffusion, should cause significant variations in the pore water chemistry of shallow sediment.

Model simulations were conducted at two locations: Site 1244 (Hydrate Ridge) and Site KC151-3 (Gulf of Mexico). These locations were chosen because they have very different DIC concentrations and $\delta^{13}\mathrm{C}$ of DIC across the SMT. At both sites, the simulations give good first-order descriptions for the profiles of $CH_4$, $SO_4^{2-}$, DIC, $Ca^{2+}$ and the $\delta^{13}\mathrm{C}$ of $CH_4$ and DIC in shallow sediment (Figures 3.4 and 3.5). Importantly, model results are constrained by field measurements of physical and chemical parameters, and the concentrations and shapes of model profiles. Crucially, the concentrations and shapes of various profiles stem from coupled mass balance equations and site-specific parameters; in other words, the inputs and outputs of $CH_4$ drive the profiles. Although problems with this model remain (e.g., changing water activity, sediment heterogeneities, lateral flow), the fact that $CH_4$ distributions and multiple pore water profiles can be simulated simultaneously and fairly accurately at different locations supports the approach.

Our numerical modeling gives a mathematically robust, process-based explanation for SMT depth as well as the difference in carbon chemistry across the SMT at Sites 1244 and KC151-3. At both sites, an upward flux of dissolved $CH_4$ reacts with dissolved $SO_4^{2-}$ at the SMT via AOM. Moreover, at both sites, AOM dominates the net consumption of $SO_4^{2-}$ in shallow sediment. At Site 1244, however, a high flux of $^{13}\mathrm{C}$-enriched DIC, produced by methanogenesis at depth, enters the SMT from below. This is not the case at Site KC151-3, where a flux of $^{13}\mathrm{C}$-enriched DIC leaves the SMT in both directions. As such, the SMT has relatively high concentrations of moderately $^{13}\mathrm{C}$-depleted DIC at Site 1244 and relatively low concentrations of very $^{13}\mathrm{C}$-depleted DIC at Site KC151-3. Other factors, notably fluid flow and carbonate precipitation, secondarily affect the carbon chemistry across the SMT at these sites. In any case, the differences in DIC concentration and $\delta^{13}\mathrm{C}$ of DIC do not indicate the relative importance of AOM and organoclastic sulfate reduction.

Crossplots showing changes in alkalinity and $SO_4^{2-}$ concentrations have been used to assess the relative influence of AOM in marine sediment. The $\delta^{13}\mathrm{C}$ of DIC and the $\delta^{13}\mathrm{C}$ of carbonate also have been used for this purpose. These approaches are not appropriate for open systems without additional information, especially those where large fluxes of $^{13}\mathrm{C}$-enriched DIC enter shallow sediment from depth. Wide deviations in $\Delta Alk^*$:$\Delta SO_4^{2-}$ slopes and DIC $\delta^{13}\mathrm{C}$ are expected, even when AOM consumes all net $SO_4^{2-}$ (Figure 3.2).

The DIC concentration and $\delta^{13}\mathrm{C}$ of DIC across the SMT exhibit broad ranges for locations with underlying gas hydrate (Figure 3.2). On the basic of preliminary flux arguments (*Dickens and Snyder*, 2009) and results presented here, it is suspected that this range mostly signifies differences in fluid flux regime, and the relative proportions of $^{13}\mathrm{C}$-depleted $CH_4$ and $^{13}\mathrm{C}$-enriched DIC entering the SMT.

# Chapter 4

# Modeling Pore Water Profiles of Marine Gas Hydrate Systems: The Extreme Case of ODP Site 685/1230, Peru Trench

## 4.1 Introduction

*Pore water profiles of $SO_4^{2-}$, $Ca^{2+}$ and alkalinity (≈DIC) have been generated at numerous marine locations with gas hydrate. Some of these sites, as exemplified by Site 1244 (Cascadia Margin) and KC151-3 (Gulf of Mexico), also have profiles for the $\delta^{13}\mathrm{C}$ of DIC (Figure 4.1). Although various pore water profiles at different locations exhibit certain similarities with respect to generalized depth, notably including inflections across the SMT, they clearly exhibit wide ranges in terms of concentration. Indeed, the alkalinity and $\delta^{13}\mathrm{C}$ of DIC at the SMT provides an interesting approach to distinguish sites. Available data show an obvious trend from locations with relatively low alkalinity and $\delta^{13}\mathrm{C}$ of DIC at the SMT to locations with relatively high alkalinity and $\delta^{13}\mathrm{C}$ of DIC at the SMT (Figure 4.2). Possible origins for this trend were examined using a simplified 1-D model for gas hydrate

*Chatterjee, S., G.R. Dickens, G. Bhatnagar. W.G. Chapman, B. Dugan, G.T. Snyder, and G.J. Hirasaki (2012), Modeling pore water profiles of marine gas hydrate systems: The extreme case of ODP site 685/1230, Peru Trench, *to be submitted*.

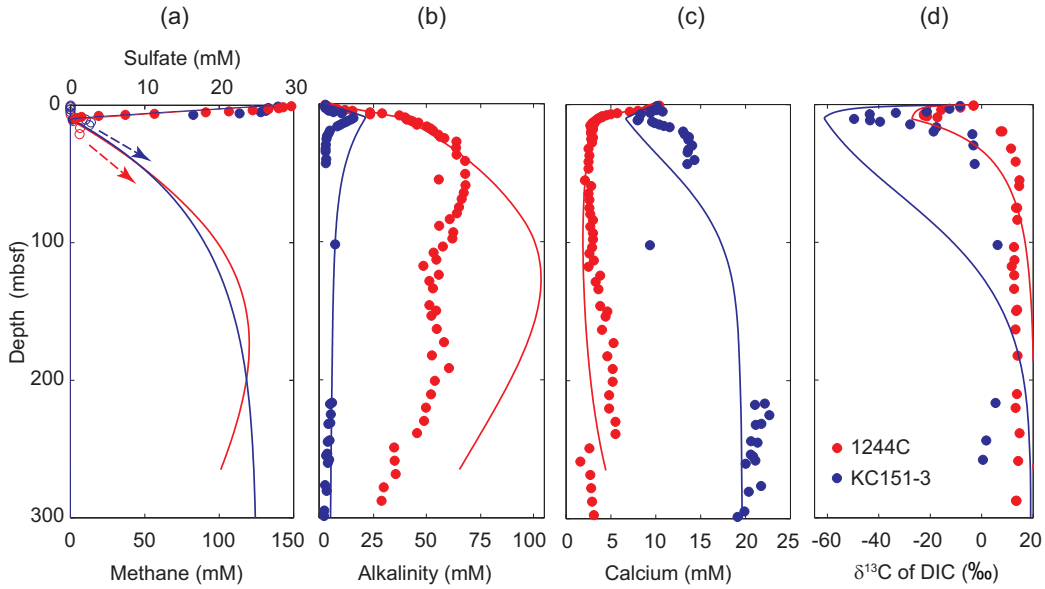


Figure 4.1 : Panels showing data and modeling results from KC151-3 (blue) and 1244C (red) in a general format. The four panels show pore water concentrations of (a) methane and sulfate, (b) alkalinity, (c) calcium and (d) $\delta^{13}\mathrm{C}$ of DIC measured and modeled at two sites. The simulated profiles (lines) match the measured data (dots) favorably at two sites modeled in Chapter 3 and *Chatterjee et al*. (2011a).

occurrence in marine sediment, one that included additional coupled mathematical expressions for the temporal evolution of pore water alkalinity, $SO_4^{2-}$ and $Ca^{2+}$, as well as the $\delta^{13}\mathrm{C}$ of DIC (*Chatterjee et al*., 2011a). After simulating multiple pore water profiles at two sites (sites 1244 and KC151-3; Figure 4.1), *Chatterjee et al*. (2011a) suggested the trend represents differential mixing of $HCO_3^-$ produced by AOM at the SMT and $HCO_3^-$ produced by methanogenesis fluxing upward into the SMT. Crucially, the simulated profiles for alkalinity, $SO_4^{2-}$, $Ca^{2+}$ and $\delta^{13}\mathrm{C}$ of DIC were driven by a dynamic view of gas hydrate systems (i.e., through expressions for the production, cycling, and consumption of $CH_4$).

The work by *Chatterjee et al*. (2011a) raises two open issues. First, the

formation and dissociation of gas hydrate were not explicitly modeled. Rather, the distribution was fixed by steady state conditions for dissolved methane. Thus, amounts of gas hydrate cannot be linked to pore water chemistry. Second, the chosen sites represented the low and medium portions of the "alkalinity vs $\delta^{13}C$ of DIC" trend (Figure 4.2). The modeling did not provide simulations for a location with high alkalinity and high $\delta^{13}C$ of DIC at the SMT. In this work, we expand on current ideas and modeling (*Chatterjee et al*., 2011a), by attempting to simulate pore water profiles at a location on the Peru Margin.

## 4.2 Site 685/1230, Peru Margin

### 4.2.1 Basic Parameters and Methane

Ocean Drilling Program (ODP) Leg 112 drilled and cored Site 685 on the lower continental slope of the Peru Trench at 09$^{o}$07' S, 80$^{o}$35' W, and 5071 m below sea level (mbsl) (Figure 4.3; *Suess et al*., 1988). The recovered sedimentary record extends from 0 to 469 m below seafloor (mbsf). Three new holes were drilled at this location during ODP Leg 201, although to shallower depths beneath the seafloor (*D'Hondt et al*., 2003): 1230A (278 mbsf), 1230B (102 mbsf), and 1230C (14 mbsf). The stratigraphic sequence has been divided into two lithologic units (*Shipboard Scientific Party*, 1988): Unit 1 (0-203.6 mbsf), and Unit II (203.6-468.6 mbsf). Both units consist of diatomaceous mud. However, the upper one accumulated during the Quaternary (0-1.8 Ma) at an average rate of 100 m/Myr, while the lower one

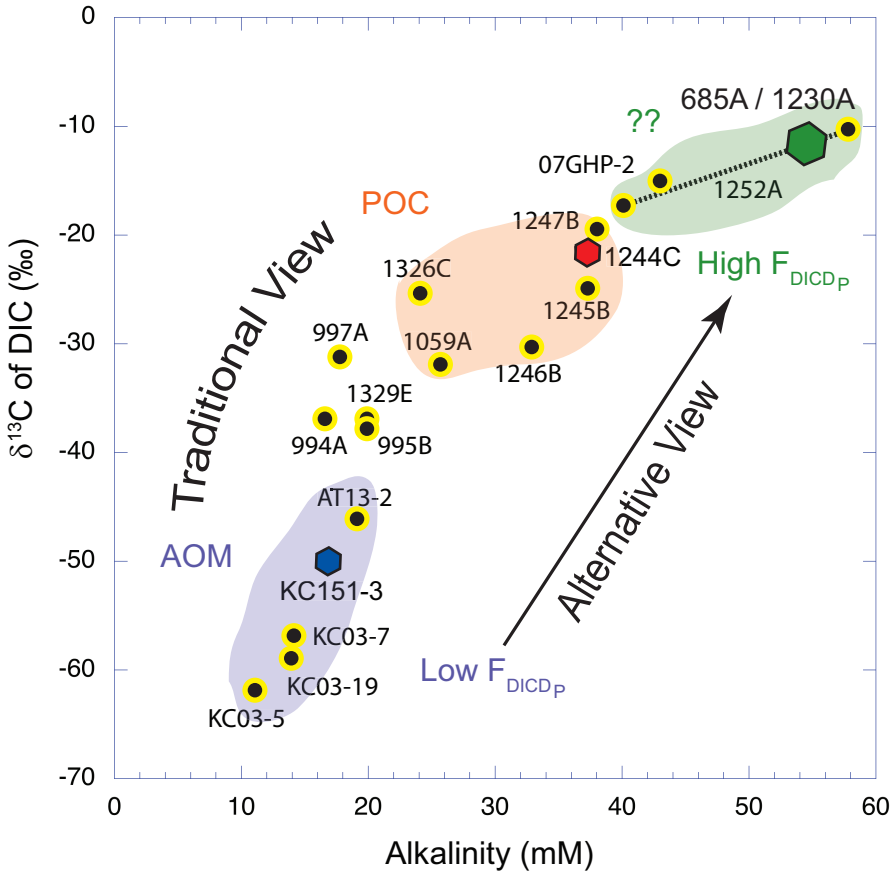


Figure 4.2 : Alkalinity versus $\delta^{13}\mathrm{C}$ of DIC at the SMT for multiple locations known to have gas hydrate at depth. Note the general trend from sites with low alkalinity and low $\delta^{13}\mathrm{C}$ of DIC to those with high alkalinity and relatively high $\delta^{13}\mathrm{C}$ of DIC. Traditionally, alkalinity and $\delta^{13}\mathrm{C}$ of DIC at the SMT were being used to discriminate between AOM and organoclastic sulfate reduction to explain this trend. We suggest the dominant cause for this trend arises from the relative flux of upward $^{13}\mathrm{C}$-enriched DIC ($F_{DIC_{Dp}}$). Data from: ODP Sites 994-997, *Paull et al*. (2000b); ODP Site 1059, *Borowski et al*. (2000); ODP Sites 1244-1252, *Claypool et al*. (2006), *Torres and Rugh* (2006); Sites 1326 and 1329, *Torres and Kastner* (2009); KC03-5-19, *Pohlman et al*. (2008); KC151-3, AT13-2, *Kastner et al*. (2008b); O7GHP-1, *Kim et al*. (2011); Site 1230, *Donohue et al*., (2006), *Meister et al*., (2007). The hachured line for Hole 1252A represents a range of values spanning the SMT. Hexagons represent Sites 1244C, KC151-3, 1230 (and 685) modeled within *Chatterjee et al*. (2011a) and here, respectively. The relationship between $\delta^{13}\mathrm{C}$ of DIC and alkalinity is probably more tightly coupled than shown.

accumulated during the late Miocene (6.1-8.5 Ma) at an average rate of 250 m/Myr. Thus, a stratigraphic hiatus of about 4.3 Myr exists at $\sim$204 mbsf (Figure 4.4; *Suess et al*., 1988; *Shipboard Scientific Party*, 1988, 2003a; *D'Hondt et al*., 2003). This hiatus represents an unconformity formed due to sediment uplift and erosion (as a result of Nazca plate subduction) where the Pleistocene slope deposits overlie the upper Miocene accreted sediments (*Shipboard Scientific Party*, 1988, 2003a).

Total organic carbon (TOC) concentrations are relatively high for marine sediment (Figure 4.4). For Unit I, they range between 1.9% and 5.2%, and average about 3%; values are generally less for Unit II, varying between 0.2% and 4.4%, and averaging about 2% (*Shipboard Scientific Party*, 1988, 2003a; *Meister et al*., 2005). The high organic carbon input at Site 685/1230 leads to production of abundant $CH_4$ (*Suess et al*., 1988; *Shipboard Scientific Party*, 1988, 2003a). The $CH_4$ is evidenced through gas expansion features in recovered cores (e.g., cracks and voids), as well as gas analyses of samples collected by multiple techniques (*Dickens et al*., 2003; *Spivack et al*., 2006). The first order distribution of $CH_4$ can be determined through measurements of physical properties and gas concentration profiles.

The hydrostatic pressure and temperature at the sediment-water interface are 50.9 MPa and 1.7$^{o}$C, respectively (Figure 4.4). With a measured geothermal gradient of 0.0343$^{o}$C/m and the predominance of $CH_4$ ($>$99%) in gas samples (e.g., *Kvenvolden and Kastner*, 1990; *Shipboard Scientific Party*, 2003a), the

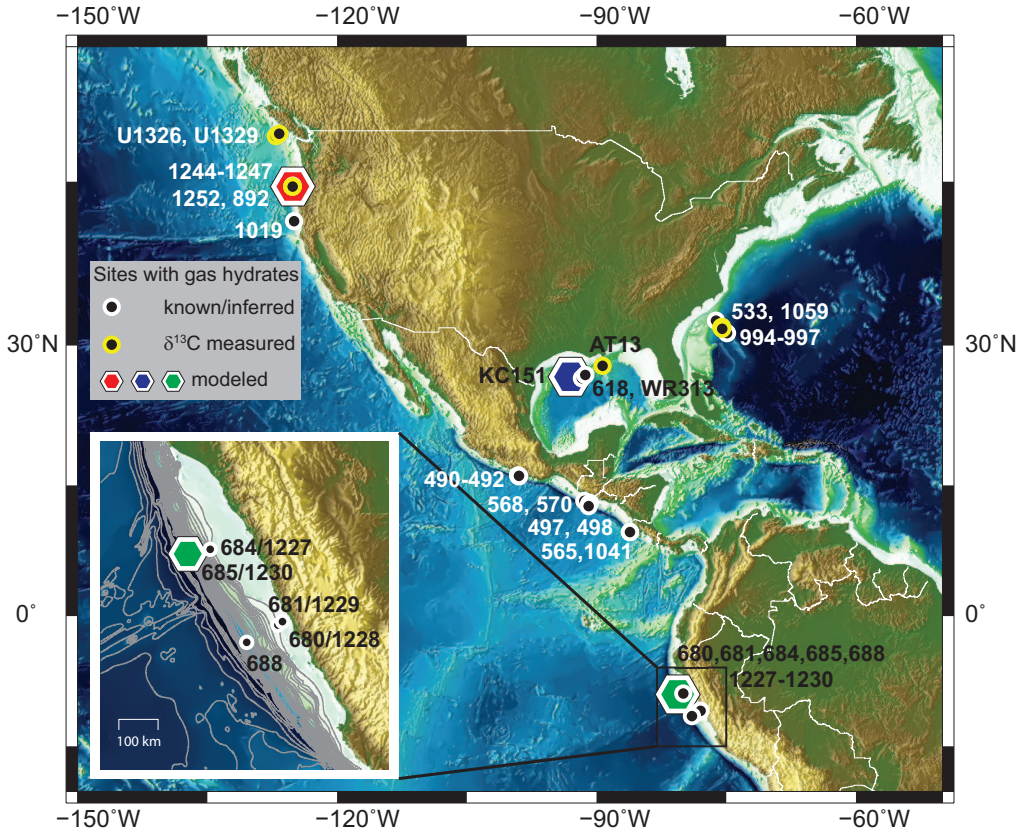


Figure 4.3 : Map showing locations with gas hydrate bearing sites drilled in the continental margins of north and south America. At some of these sites cores have been sampled and pore water chemistry has been measured along with carbon isotope composition of DIC. Three sites with differing carbon chemistry have been chosen among those where extensive datasets exist. The two sites (Hydrate Ridge 1244 in the Cascadia Margin and the Keathley Canyon KC151 in the Gulf of Mexico) are modeled elsewhere (*Chatterjee et al*., 2011a) and Site 685/1230 in the Peru Margin is modeled in this chapter. Inset shows blown up drilled location in the Peru Margin showing Sites from ODP Legs 112 and 201.

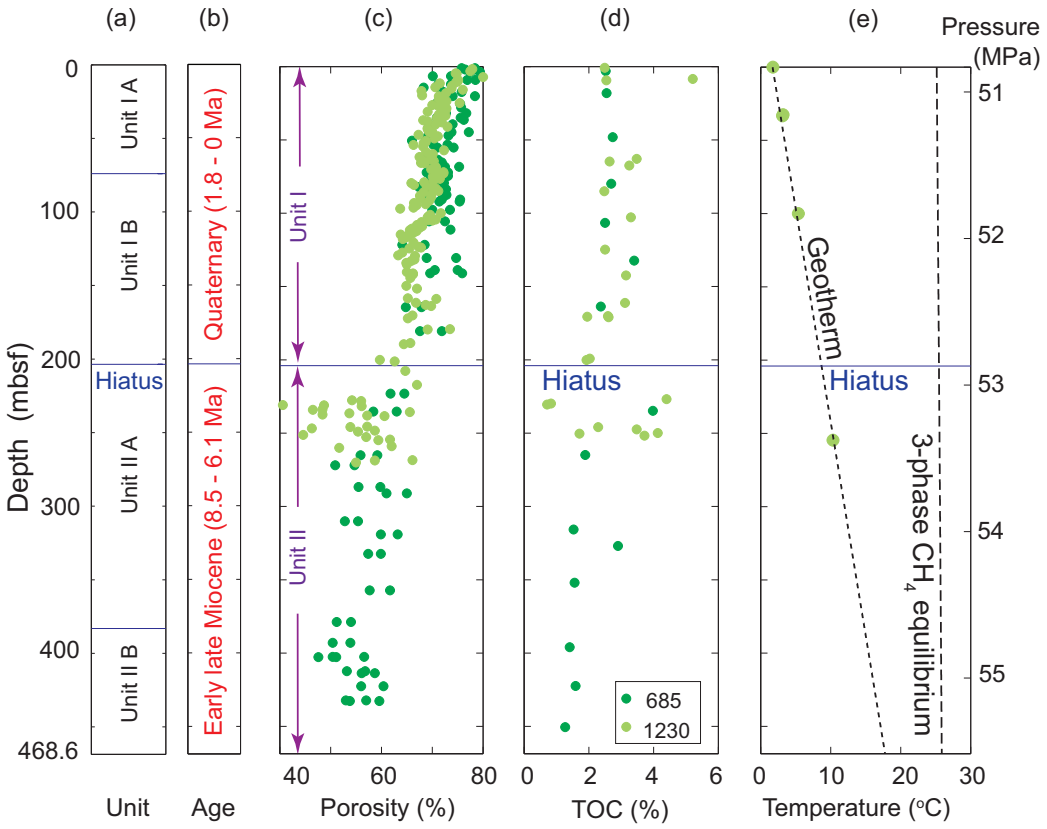


Figure 4.4 : Panels showing age, lithology and physical properties at Site 685/1230. (a) Lithologic units, (b) age, (c) porosity for both Sites 685 and 1230, (d) Total Organic Carbon (wt %) and (e) temperature and equilibrium curve.

base of the GHSZ should be ~715 mbsf. This thickness can be determined by simultaneously equating pressures and temperatures along the three-phase equilibrium curve for methane and seawater with those along the geothermal gradient (e.g., *Bhatnagar et al*., 2007). Note that this depth is shallower at Site 685, with an assumed seafloor temperature 1.5°C and geothermal gradient 0.045°C/m, as the temperature profile was not measured at this site (*Kvenvolden and Kastner*, 1990). *Marquardt et al*. (2010) interpret this thickness as 620 mbsf consistent with assumed values reported in *Kvenvolden and Kastner* (1990). Requisite high porosity also marks the sediment sequence (Figure 4.4). In Unit I, it drops from 78% to 70% in the upper 20 mbsf; below, it decreases slightly to 68%. In Unit II, porosity averages 55%, but ranges between 40% and 65%.

Based on organic carbon supply and physical properties, one might think that Site 685/1230 has a thick sedimentary zone with high amounts of gas hydrate (*Marquardt et al*., 2010). In fact, however, specimens of gas hydrate were only recovered at 99 and 164 mbsf at Site 685, and at 82 and 148 mbsf at Site 1230 (*Kvenvolden and Kastner*, 1990; *Shipboard Scientific Party*, 1988, 2003a). Three pieces of information support a distribution where relatively small amounts of gas hydrate span a portion of the 715 m-thick GHSZ. First, seismic records do not show a bottom-simulating reflector (BSR) at this site (e.g., *Kvenvolden and Kastner*, 1990; *von Huene and Pecher*, 1999; *Pecher et al*., 2001). Such a reflector is commonly regarded as representing the case when gas hydrate directly overlies

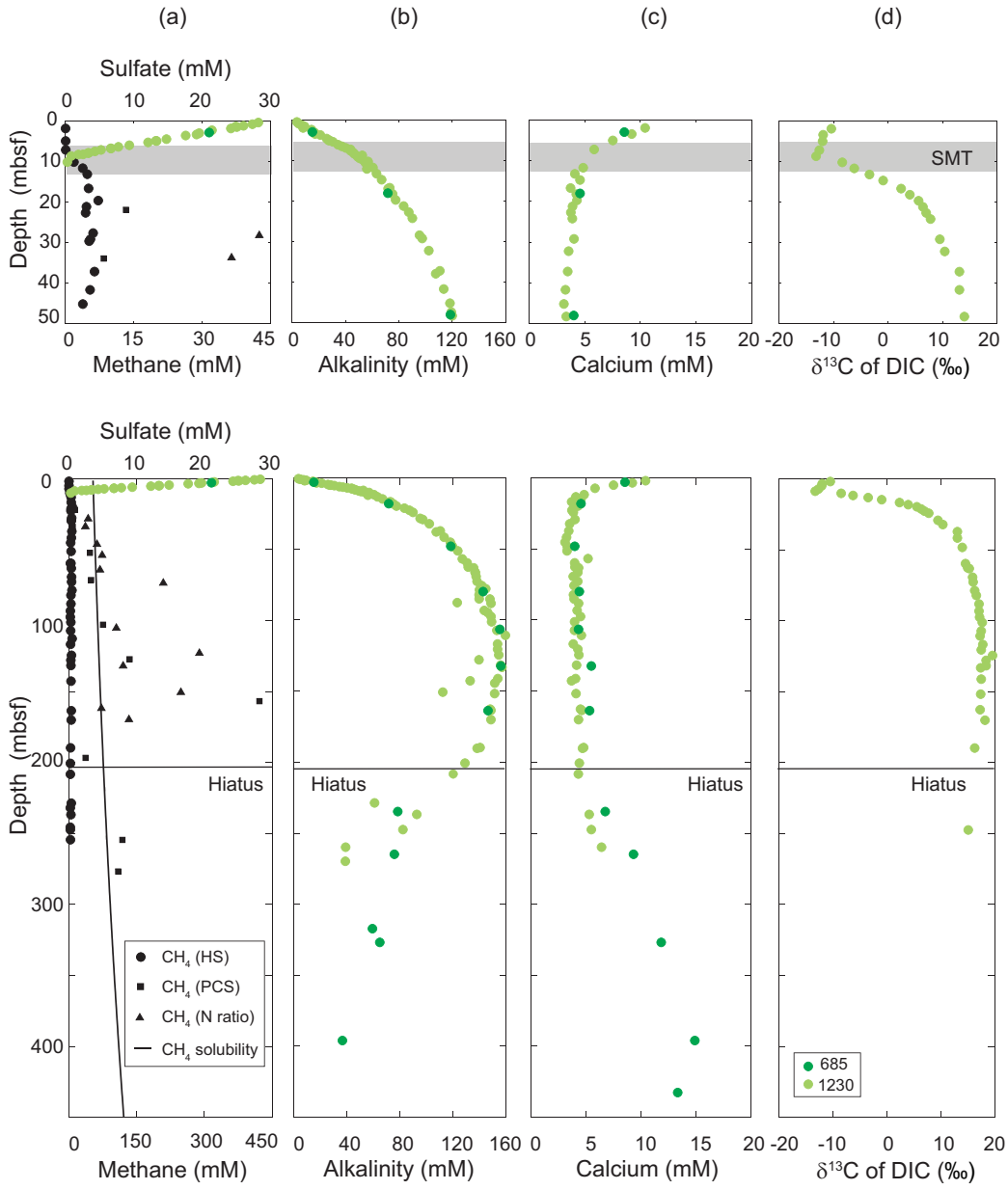


Figure 4.5 : Pore water (a) $SO_4^{2-}$ (green circles) noted on upper axis, $CH_4$ (black squares, triangles and circles) marked on lower axis, (b) alkalinity (DIC), (c) $Ca^{2+}$ concentration and (d) $\delta^{13}$C of DIC profiles in shallow sediment at Sites 685 and 1230 in Peru Margin (*Suess et al*., 1988; *Shipboard Scientific Party*, 1988, 2003a; *D'Hondt et al*., 2003; *Donohue et al*., 2006; *Meister et al*., 2007). Top panel shows the zoomed pore water profiles for the upper 50 m of sediment and the shaded region represents the SMT zone.

free gas (e.g., *Mackay et al*., 1994). Second, pore water profiles of $Cl^-$ and other conservative species (e.g., Sr and Li) do not show numerous deviations to lower concentrations (*Shipboard Scientific Party*, 2003a). These often result from gas hydrate dissociation during core recovery (e.g., *Hesse and Harrison*, 1981). Third, various approaches for quantifying $CH_4$ concentrations suggest low values (*D'Hondt et al*., 2003; *Shipboard Scientific Party*, 2003a).

Methane concentrations at Site 1230 were determined by several techniques. These included measurements of samples obtained through headspace (HS), gas void, and pressurized cores (*Dickens et al*., 2003; *Shipboard Scientific Party*, 2003a). Headspace (HS) $CH_4$ concentrations are $<$0.1 mM in the upper 7 m of sediment, where pore water $SO_4^{2-}$ is $>$5 mM. Below, where $SO_4^{2-}$ drops $<$0.8 mM, $CH_4$ concentrations rise sharply from $<$1.8 mM at $<$10.2 mbsf to 7 mM at 19.7 mbsf (Figure 4.5a). The scattered and generally low HS $CH_4$ concentrations below this depth undoubtedly reflect significant degassing during core recovery (*Paull et al*., 2000a), because the solubility of $CH_4$ at shipboard conditions ($\sim$0.1 MPa; $\sim$20$^{o}$C) is 1.8 mM. By contrast, $CH_4$ concentrations measured using nitrogen ratios range between 42 mM at 28 mbsf and $>$200mM below 70 mbsf (*Spivack et al*., 2006). These measurements are reaffirmed as the pressure core sampler (PCS) show $CH_4$ concentration values between 46 mM at 52 mbsf and 422 mM at 156 mbsf (*Dickens et al*., 2003; Figure 4.5a).

Methane $\delta^{13}$C values range between -72 $^{0}/_{00}$ and -65 $^{0}/_{00}$ (e.g., *Biddle et al*.,

2006). Hydrate saturation $<$5% of pore space exists below a depth at around 82 mbsf, which is assumed to be shallowest occurrence of the gas hydrate. However, these high values including the zones of hydrate occurrence are above the hiatus; below, $CH_4$ concentrations show scattered data below saturation.

### 4.2.2 Key Pore Water Profiles

Pore waters at Sites 685 and 1230 were collected using standard ODP sediment "squeezing" procedures (*Geiskes et al*., 1991). However, the sheer number of samples (112) and aliquots thereof from the three holes at Site 1230 warrant two notes. First, the detailed pore water sampling suggests core gaps and overlaps between holes (*D'Hondt et al*., 2003), a fact long recognized by paleoceanograpic community (e.g., *Lisiecki and Herbert*, 2007). We have adjusted initial depths for pore waters to a meter composite depth (mcd) scale accordingly, which has particular importance over the upper 20 mbsf. Second, while many species (e.g, $SO_4^{2-}$, alkalinity, DIC, and $Sr^{2+}$, $Ba^{2+}$) were measured on board the ship, major cations were not, in contrast to almost all other ODP Legs. Given the very high alkalinity concentrations (discussed below) and the potential for carbonate precipitation during storage of pore waters, we only discuss $Ca^{2+}$ profiles generated from aliquots acidified (with ultrapure $HNO_3$) immediately after retrieval (*Donohue et al*., 2006).

The $SO_4^{2-}$ profile at Site 1230 (Figure 4.5a) exhibits characteristics similar to

those measured at other locations with gas hydrate. Concentrations decrease nearly linearly from ∼28 mM near the seafloor to <1 mM by ∼8.7 mbsf. This depth, approximately the SMT, is where dissolved $CH_4$ and $Ba^{2+}$ concentrations begin to increase sharply. The steep rise in $Ba^{2+}$ (*D'Hondt et al*., 2003; *Shipboard Scientific Party*, 2003a) is important because it marks the SMT at numerous locations (*Dickens*, 2001b; *Snyder et al*., 2007).

Alkalinity increases rapidly from 2.7 mM near the seafloor to 100 mM at ∼30 mbsf; below, it rises gradually to a broad maximum of 160 mM between 100 and 150 mbsf (Figure 4.5b; *D'Hondt et al*., 2003; *Shipboard Scientific Party*, 2003a). Deeper in the sediment column, alkalinity drops to ∼40 mM at 250 mbsf. The alkalinities at the SMT (∼53 mM) and between 100-150 mbsf are extreme (Figure 4.5b). Indeed, these alkalinities are the highest recorded in over 40 years of deep-sea drilling. The pH throughout the interval is between 6.9 and 8.3 (*Shipboard Scientific Party*, 2003a), suggesting that alkalinity and DIC are nearly equal. In fact, this was confirmed at Site 1230 by measuring alkalinity and DIC separately (*Shipboard Scientific Party*, 2003a).

Profiles of DIC $\delta^{13}\mathrm{C}$ show a wide variance in values, including a distinct peak spanning the SMT (Figure 4.5d; *Meister et al*., 2007). The $\delta^{13}\mathrm{C}$ of DIC is 0 $‰$ near the seafloor and decreases to a minimum of -13 $‰$ at ∼8.7 mbsf. Values then increase rapidly to +10 $‰$ at ∼2 mbsf. Below, it steadily increases to +17 $‰$ by ∼88 mbsf and remains essentially constant to greater depths. Notably, the

$\delta^{13}C$ of DIC at the SMT is much greater than predicted through sulfate reduction of particulate organic carbon (POC) (*Claypool et al*., 2006; *Kastner et al*., 2008a; *Torres and Kastner*, 2009), unless solid organic carbon landing on the seafloor has an unusual carbon isotopic composition.

Dissolved $Ca^{2+}$ is 10 mM near the seafloor but decreases to 5 mM at $\sim$12 mbsf; it then increases steadily to 7 mM at the bottom of the drilled section at 260 mbsf (Figure 4.5c; *Donohue et al*., 2006). The significant drop in $Ca^{2+}$ concentrations across the SMT has been attributed to authigenic carbonate precipitation (*Suess et al*., 1988; *D'Hondt et al*., 2003; *Meister et al*., 2007).

Pore waters collected at Site 685/1230 have three other attributes relevant to understanding carbon cycling in gas hydrate systems. First, upon collection, many samples from Unit I had a rich golden color. Pore water collected close to the seafloor is nearly clear but rapidly becomes more "yellow" with depth, approaching a golden color ($>$0.50 JWBL units) by 40 mbsf. Below, at 250 mbsf, the water becomes clear again, dropping to below 0.15 JWBL. Second, dissolved $NH_4^+$ increases from 1mM at the seafloor to a broad maximum of 35-40 mM between 100 and 200 mbsf; below, they drop to lower values ($\sim$10 mM) at 400 mbsf. Third, phosphate concentrations at Site 685 increase from near zero values at the seafloor to 0.37 mM at 18 mbsf. Concentrations reach an extreme high of 0.83 mM at 107 mbsf (*Suess et al*., 1988). Below the hiatus, values decrease but remain relatively high ($\sim$0.1 mM). The distinct yellow color is unusual across pore

water studies of scientific boreholes, but is found at other sites with gas hydrate (e.g., Site 1244; *Trehu et al*., 2003). It probably results from the presence of dissolved organic matter (e.g., *Smith*, 2005). The exceptionally high ammonium and phosphate concentrations almost assuredly reflect major decomposition of organic carbon at depth.

### 4.2.3 Additional Data

We analyzed 34 samples of bulk sediment from the upper 24 m for their carbon isotope composition of organic carbon (Appendix B). The average value is -22 $^{0}/_{00}$.

## 4.3 Numerical Model

### 4.3.1 Model Framework

Over the last 15 years, several 1-D numerical models have been developed to understand the accumulation of gas hydrate in marine sediment (*Rempel and Buffett*, 1997; *Egeberg and Dickens*, 1999; *Xu and Ruppel*, 1999; *Davie and Buffett*, 2001, 2003a, 2003b; *Luff and Wallman*, 2003; *Haeckel et al*., 2004; *Torres et al*., 2004; *Wallman et al*., 2006; *Liu and Flemings*, 2006, 2007; *Bhatnagar et al*., 2007; *Marquardt et al*., 2010). Most of these models have a similar framework, and serve to simulate methane transport for transient and steady state conditions. These models solve coupled mass, momentum and energy transport equations for methane, organic carbon and pore fluids over space and time. Transient and

steady state solutions are generated with site-specific parameters when these models are run over geologic time scales. The simulated profiles give a broad distribution of $CH_4$ and pore water constituents with respect the sediment depth.

Existing 1-D models have several known problems (see above references). In particular, they typically provide broad profiles for the amount of $CH_4$ occurring dissolved in water, in gas hydrate, and in free gas with respect to depth. This is because small-scale heterogeneities in sediment composition and horizontal fluid flow are not considered. Nonetheless, when appropriate parameters are used, the models generate first-order $CH_4$ profiles that approximate those constructed using direct and indirect methods at multiple locations (e.g., *Davie and Buffett*, 2001, 2003a; *Liu and Flemings*, 2007; *Bhatnagar et al*., 2007, 2011; *Chatterjee et al*., 2011a). Along with this work, a generalized, 1-D numerical model for gas hydrate accumulation in marine sediments over geologic timescales has been developed (*Bhatnagar et al*., 2007). Their model operates in thermodynamic equilibrium thereby neglecting the hydrate formation kinetics. In addition, their model summarizes the key results into two simple contour plots illustrating the amount of gas hydrate and its distribution for a wide range of parameters applicable to any generalized geologic location.

In their original model (*Bhatnagar et al*., 2007), $CH_4$ escaped a sedimentary column through two processes: below the GHSZ through burial, or above the seafloor through oxidation. The latter is not correct, because $CH_4$ is consumed

at the SMT via AOM, which typically lies below the seafloor (e.g., *Paull et al*., 1996; *Trehu et al*., 2003). The model was therefore amended so that $CH_4$ and $SO_4^{2-}$ consumption co-occurred across a sediment interval (*Bhatnagar et al*., 2008a, 2011). This is because $CH_4$ drives net $SO_4^{2-}$ consumption (e.g., *Reeburgh*, 1976; *Borowski et al*., 1996, 1999; *Snyder et al*., 2007). Methane production and consumption should impact other pore water constituents. Therefore, coupling all these pore water constituents and its carbon isotopes in a unified model would help explain carbon cycling processes in shallow sediment. For example, production of methane is depleted in $^{13}\mathrm{C}$ and is associated with generation of $^{13}\mathrm{C}$-enriched DIC. Thus, previous models were partly updated so that they included pertinent mass balance equations and reactions for DIC, dissolved $Ca^{2+}$, and the carbon isotope composition ($\delta^{13}\mathrm{C}$) of DIC (*Chatterjee et al*., 2011a).

The latest modeling exercise rendered reasonably good profiles for multiple pore water species at two sites with very different carbon chemistry (*Chatterjee et al*., 2011a). However, dissolved methane was the only methane phase tracked in calculations (i.e., amounts of gas hydrate and free gas were not accounted for). Furthermore, diffusion coefficients and reaction rates were assumed to be independent of depth and temperature, and transient states were not considered.

### 4.3.2 Modifications to Previous Modeling

Two modifications to previous modeling exercises are made in this chapter. First, we incorporate gas hydrate and free gas phases in our computations. When $CH_4$ concentrations exceed solubility, excess methane precipitates as gas hydrate or forms free gas, depending on the thermodynamic conditions. Mathematical formulae for this modification are presented in Appendix C. Second, we make the reaction rate constant for methanogenesis temperature dependent.

Both theory and observations suggest that, at low temperatures ($<40^{o}$C), rates of microbial methanogenesis increase significantly with temperature (e.g., *Price and Sowers*, 2004). Although a series of models published in the last decade assumed that methanogenesis reaction rate was independent of temperature (e.g., *Bhatnagar et al*., 2007, 2008a; *Chatterjee et al*., 2011a). Recent studies showed the dependence of temperature on the reaction rate constant (e.g., *Gu et al*., 2011; *Burdige*, 2011). Following their work, we have also shown effect of temperature on the reaction rate constant ($\lambda$).

### 4.3.3 Initial Parameters

The seafloor and geologic parameters measured at Site 685/1230 and recorded in ODP reports are used as input parameters in our model. These site-specific parameters include the seafloor depth (5086 mbsl), seafloor temperature (1.7$^{o}$C), geothermal gradient (0.0343$^{o}$C/m), sedimentation rate (100 m/Myr), and an

average TOC (3 wt %) at the seafloor (Table 4.1).

The model has several dimensionless parameters (Equation C.3). These are: Peclet numbers ($Pe_1$, and $Pe_2$), and Damkohler numbers ($Da$, $Da_{AOM}$ and $Da_{POC}$). Peclet numbers characterizes the ratio of fluid advection to methane diffusion. Two Peclet numbers represent the two fluid fluxes due to sedimentation-compaction and external fluid flow. Damkohler numbers relate the reaction rates to the rate of diffusion. The three Damkohler numbers correspond to the reactions that form methane (methanogenesis), and consume sulfate at or above the SMT (AOM and organoclastic sulfate reduction (OSR)).

Steady state pore water concentration profiles were simulated (Figure 6) using the modeling approach discussed in *Chatterjee et al*. (2011a) for parameters (Table 4.1) obtained or inferred from reports for this location (*Suess et al*., 1988; *D'Hondt et al*., 2003). The sedimentation rate (100 m/Myr) during the Pleistocene was used to calculate a $Pe_1$ of 0.085. This parameter was fixed for all simulations at this location (unless otherwise specified) as this relates to sediment burial and porosity reduction. Based on the upward fluid velocity values reported at this location ($>$200 m/Myr), our initial estimate for $Pe_2$ is -6 at this site.

The thickness of the SMT (as opposed to the depth of the SMT) depends on $Da_{AOM}$ (*Bhatnagar et al*., 2008a). A large value for $Da_{AOM}$ represents a fast rate of AOM relative to the rate of $CH_4$ diffusion, which results in a thin overlap of $CH_4$ and $SO_4^{2-}$ profiles at the SMT. This occurs at many locations, including at Site

1230 (Figure 4.5a). Consequently, we initialize simulations with a relatively high value ($Da_{AOM} = 10^8$), the same as in previous work (*Chatterjee et al*., 2011a). The dimensionless numbers $Da$ (=3), and $Da_{POC}$ (=25) were calculated based on reaction rate values used in existing models (e.g., *Davie and Buffett*, 2001; *Bhatnagar et al*., 2007; *Chatterjee et al*., 2011a).

### 4.3.4 General Approach for Solving

The dimensionless mass balance equations were solved conservatively with specific initial and boundary conditions to obtain solutions (Appendix C). An implicit, block-centered, finite-difference scheme was formulated to numerically solve the hyperbolic, dimensionless, partial differential equation for organic carbon. The remaining partial differential equations were expressed in a finite difference form and solved using an explicit numerical scheme (*Chatterjee et al*., 2011a). The spatial simulation domain was assumed to be $2L_t$ (=1430 mbsf) and the equations were solved from initial time ($t = 0$) to steady state in small increments of time. A strict material balance check ensured no loss (all simulations had errors $< 10^{-8}$) and mass conservation. The sediment and fluid advection terms were computed using single-point, upstream weighting. Upstream grid point values (as opposed to mean values between two neighboring grid points) were used for concentration to calculate fluxes across each grid interface.

As emphasized in previous publications (*Bhatnagar et al*., 2007, 2008a;

*Chatterjee et al*., 2011a), the generation of mathematical solutions in dimensionless units is appealing because it enables countless numerical simulations of different gas hydrate systems to be compared systematically. However, such presentation does not lead to obvious comparisons with field data. Thus, we convert normalized depths and concentrations to actual depths and concentrations at Site 1230. This can be accomplished by multiplying the normalized depth by the depth to the base of the GHSZ ($L_t$ = 715 mbsf), multiplying normalized $CH_4$ concentrations by the three-phase equilibrium value at the base of the GHSZ ($c_{m,eqb}$ = 206 mM), and multiplying normalized $SO_4^{2-}$, $HCO_3^-$ and $Ca^{2+}$ concentrations by their respective values in seawater values ($c_{s,o}$ = 28 mM; $c_{b,o}$ = 2.4 mM; $c_{Ca,o}$ = 10 mM). Note that concentration profiles are therefore simulated to 1430 mbsf, even though we generally plot them across shallower intervals (e.g., 400 mbsf, Figure 4.6).

### 4.3.5 Steady State Solutions

Steady state solutions are obtained by solving the mass balance equations from the initial time of sediment deposition through long time scales ($\sim$20 Myr) until pore water concentration profiles of all relevant geochemical species ($CH_4$, $SO_4^{2-}$, DIC, $Ca^{2+}$ and $\delta^{13}$C of $CH_4$ and DIC) cease to change. Site 1230 presents a challenge to models for gas hydrate accumulation because the depth (204 mbsf), termination age ($\sim$1.8 Ma), and duration ($\sim$4.3 Myr) of the hiatus strongly suggest

that the system has not reached steady state conditions. Consequently, to explain complicated processes at this location, transient simulations must be considered. Of particular importance, Site 1230 should be viewed as a system where a young package of sediment, rich in organic carbon, lies on top of an older package of sediment. The $CH_4$ and DIC (as well as other products of microbial activity) in the upper $\sim$200 m of sediment have mostly been generated in the last $\sim$2 Myr.

### 4.3.6 Transient Solutions

Transient solutions are obtained using time evolved simulations from a known set of initial conditions. At the start of time ($t = 0$), steady state profiles are generated over $\sim$10 Myr for a thick sediment column ($z$ = 1575 mbsf). These profiles are obtained by depositing the sediment at the rate 250 m/Myr at the seafloor. The hiatus is modeled in our simulations as an erosion event. The upper 1075 m of sediment is removed to model the hiatus (equivalent to duration of 4.3 Myr). Consequently, the older sediment (1075-1575 mbsf) is retained along with its pore water constituents at steady state. These pore water profiles act as initial conditions for time after hiatus. At the start of this new time, organic carbon rich sediment deposits on the seafloor and moves down with a lower sedimentation rate (100 m/Myr). The hiatus which was at the top of the sediment column $\sim$2 Myr ago is tracked through time. The present day hiatus has moved 204 mbsf into the sediment since this new time. During this time (post-hiatus) pore water

profiles evolve in the upper ∼200 m of sediment. However, the profiles below the hiatus remain unaltered from pre-hiatus conditions. These time evolved pore water profiles in the last ∼2 Myr are generated as transient solutions at this location.

## 4.4 Results

### 4.4.1 Steady State Solutions

#### Base Case

Our initial simulations have a set of site-specific parameters (Table 4.1), and chosen values for key dimensionless groups. As explained above, these are: $Pe_1$ = 0.085, $Pe_2$ = -6, $Da$ = 3, $Da_{AOM}$ = $10^8$ and $Da_{POC}$ = 25.

With these starting parameters, a set of pore water profiles arises from our numerical model at steady state conditions (Figure 4.6). Simulated $CH_4$ and $SO_4^{2-}$ profiles provide a first-order check on model accuracy. Dissolved $CH_4$ concentrations are nearly zero above the SMT, which occurs at 12 mbsf, and then rapidly increase in concentration with depth. Excess dissolved $CH_4$ forms gas hydrate as local solubility values are surpassed. With the above set of parameters, $CH_4$ first exceeds solubility conditions at 122 mbsf. Gas hydrate saturations increase with depth with a peak saturation of 30% at the base of the GHSZ. Free gas saturations increase from 10% at the base of the GHSZ to 21% at the base of the simulation domain (Figure 4.6e). Dissolved $SO_4^{2-}$ exhibits a near-linear profile

Table 4.1 : Model Parameters for Sites 685/1230

| Symbol | Definition (units) | Value[a] |
|---|---|---|
| $L_o$ | Seafloor depth (m) | 5086 |
| $P_0$ | Seafloor pressure (MPa) | 50.86 |
| $T_0$ | Seafloor temperature ($^o$C) | 1.7 |
| $dT/dz$ | Geothermal gradient ($^o$C/m) | 0.0343 |
| $L_t$ | Depth to GHSZ (mbsf) | 715 |
| $L_s$ | Depth to SMT (mbsf) | 8.7 |
| $\dot{S}$ | Sedimentation rate (m/Myr) | 100, 250 |
| $U_{f,sed}$ | Fluid flux due to sedimentation (m/s) | 1.05 $\times 10^{-13}$ |
| $Pe_1$ | First Peclet number - sedimentation-compaction driven fluid flow | 0.085, 0.21 |
| $Pe_2$ | Second Peclet number - external fluid flow | -9 |
| $TOC$ | Total organic carbon (%) | 3-6 |
| - | Labile fraction (%) | 50 |
| $\alpha_o$ | Labile organic carbon at seafloor (%) | 1.5-3 |
| $\beta$ | Normalized organic carbon at seafloor | 4.5-9 |
| $c_{m,eqb}$ | $CH_4$ solubility at base of the GHSZ (mM) | 206 |
| $c_{s,o}$ | Seawater $SO_4^{2-}$ concentration (mM) | 28 |
| $c_{b,o}$ | Seawater DIC concentration (mM) | 2.4 |
| $c_{Ca,o}$ | Seawater $Ca^{2+}$ concentration (mM) | 10 |
| $D_m$ | $CH_4$ diffusivity[b] (m$^2$/s) | 0.87 $\times 10^{-9}$ |
| $D_s$ | $SO_4^{2-}$ diffusivity[b] (m$^2$/s) | 0.56 $\times 10^{-9}$ |
| $D_b$ | DIC diffusivity[c] (m$^2$/s) | 0.6 $\times 10^{-9}$ |
| $D_{Ca}$ | $Ca^{2+}$ diffusivity[c] (m$^2$/s) | 0.4 $\times 10^{-9}$ |
| $Da$ | Damkohler number (methanogenesis) | 6 |
| $Da_{POC}$ | Damkohler number (OSR) | 25 |
| $Da_{AOM}$ | Damkohler number[d] (AOM) | $10^8$ |
| $\lambda$ | Rate constant for methanogenesis (s$^{-1}$) | 1 $\times 10^{-14}$ |
| $\lambda_{POC}$ | Rate constant for OSR (m$^3$/(mol.s)) | 1 $\times 10^{-16}$ |
| $\lambda_{AOM}$ | Rate constant for AOM (m$^3$/(mol.s)) | 8.4 $\times 10^{-8}$ |

[a] *Shipboard Scientific Party*. (2003a)
[b] *Iversen and Jorgensen* (1993)
[c] *Li and Gregory* (1974)
[d] *Bhatnagar et al*. (2008a)

between the seafloor and the SMT.

Pore water profiles of DIC, $Ca^{2+}$ and the $\delta^{13}\mathrm{C}$ of DIC are simultaneously simulated in the model (Figure 4.6), and provide an important cross check. DIC concentrations increase from 2.4 mM at the sediment-water interface to 65 mM at the SMT; below, values rise steadily with depth. Simulated $Ca^{2+}$ concentrations drop from 10 mM at the seafloor to 7 mM at the SMT; below, values continue to decrease to 4.5 mM, although less rapidly with respect to depth. The steady state profile for $\delta^{13}\mathrm{C}$ of DIC is intriguing. For the initial set of parameters, it decreases with a concave-down curvature from zero at the seafloor to a minimum (-9 $^{0}/_{00}$) at the SMT; below, it increases with a concave-down curvature to more positive values (+17 $^{0}/_{00}$).

The simulated geochemical profiles for Site 1230, assuming steady state conditions, render the generic shape of measured profiles at this location. However, there are obvious discrepancies (Figure 4.6). For example, the simulated $Ca^{2+}$ values at depth are lower than measured at this site. Comparisons between model results and field data can be improved by changing various free parameters.

**Modified Dimensionless Groups**

A crucial variable in our modeling is the external fluid flux, which is incorporated in the parameter $Pe_2$. This is because upward advection of fluids moves pore water constituents from depth. A series of simulations with different $Pe_2$ (from -3 to

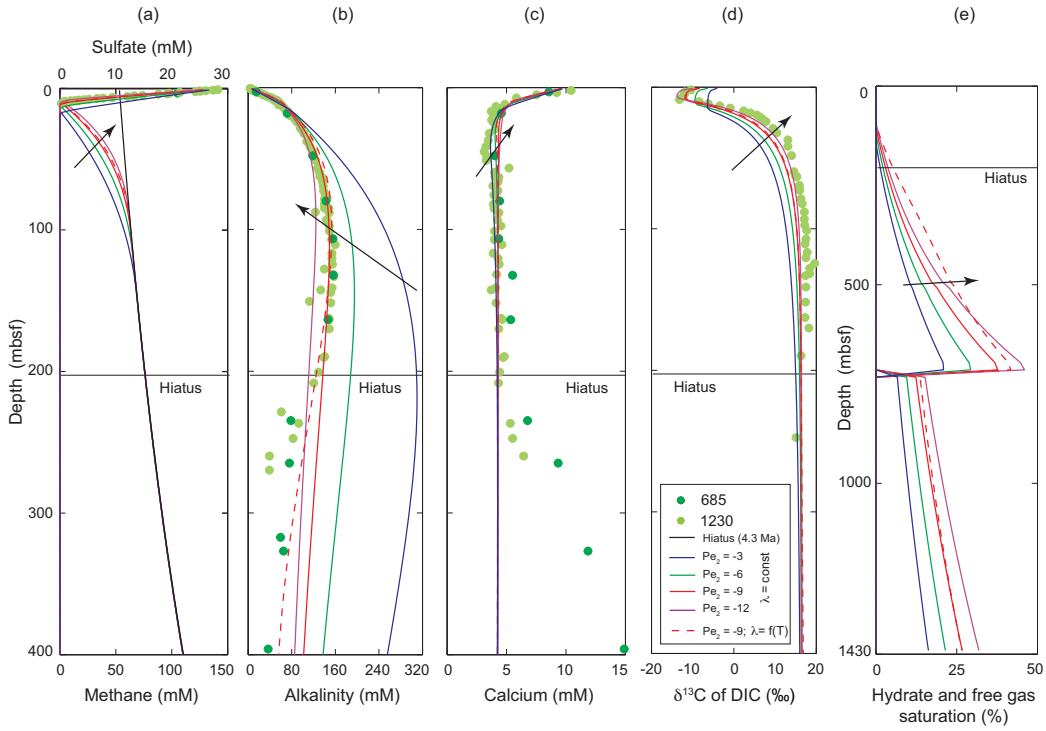


Figure 4.6 : Steady state pore water concentration profiles at Site 685/1230 in the Peru Margin with present day parameters. (a) $CH_4$, and $SO_4^{2-}$, (b) DIC, (c) $Ca^{2+}$, (d) $\delta^{13}$C of DIC, (e) gas hydrate and free gas saturations. Note that these simulations are completed for a 1430 m sediment below the seafloor, however, figures (a)-(d) are shown for the upper 400 mbsf to focus on the profiles at shallow depth. The solid curves correspond to increasing magnitude of $Pe_2$ (fluid flux from depth) shown by direction of arrow. The dashed curves correspond to simulations with a temperature-dependent methanogenesis rate constant. Field data from Sites 685 and 1230 are shown (green circles; *D'Hondt et al*., 2003; *Donohue et al*., 2006; *Meister et al*., 2007). Parameters: $Pe_1 = 0.085$, $Da = 3$, $Da_{POC} = 25$, $Da_{AOM} = 10^8$, $\beta = 4.5$, $c_{b,ext} = 48$ mM, $c_{ca,ext} = 4.3$ mM and $\delta^{13}$C = 17.

-12) and all other parameters constant illustrates the effect of fluid flux (Figure 4.6). Changes in upward fluid advection generate different pore water chemistry profiles, but with the same basic shape. One obvious change is the depth of the SMT, consistent with theory and previous modeling (e.g., *Borowski et al*., 1996; *Davie and Buffett*, 2003b; *Bhatnagar et al*., 2008a; *Chatterjee et al*., 2011a). Specifically, for the initial model conditions at Site 1230, the SMT shoals from 14 to 7 mbsf as the magnitude of $Pe_2$ doubles from -3 to -12. A simulation with $Pe_2$ = -9 produces dissolved $CH_4$, and $SO_4^{2-}$ profiles that better resemble inferred profiles at Site 1230. This includes an SMT at 9 mbsf and a shallowest occurrence of gas hydrate (where the $CH_4$ profile surpasses solubility conditions) at 105 mbsf.

The profiles of DIC and the $\delta^{13}\mathrm{C}$ of DIC also change with increasing fluid flux. In particular, the ”kink” in the DIC profile at the SMT becomes more prominent, and the $\delta^{13}\mathrm{C}$ of this DIC at the SMT becomes less with increasing flux from depth. This is because greater advection escalates the flow of $^{13}\mathrm{C}$-enriched DIC to shallower sediment. Again, for $Pe_2$ = -9, the simulated profiles of $\delta^{13}\mathrm{C}$ better match observed data, at least at the SMT. The profile of dissolved $Ca^{2+}$ also changes slightly at shallow depths with differences in fluid flux.

Changing $Pe_1$ in our simulations does not impact the pore water profiles significantly (not shown here). The pore water profiles are affected by the net fluid flux ($Pe_1 + Pe_2$), and $Pe_1$ has a very small contribution in these upward fluid flux dominated systems ($|Pe_2| > Pe_1$). Moreover, the $Pe_1$ value is prescribed in the

model based on sedimentation rate at this site, so it should remain constant for a particular geologic setting assuming constant sedimentation rate.

Simulations were performed with changes in other dimensionless groups ($Da$, $Da_{AOM}$ and $Da_{POC}$). These are not presented and discussed here because it has been shown that they do not significantly affect the basic shape of key pore water profiles (*Bhatnagar et al*., 2008a; *Chatterjee et al*., 2011a). On the basis of these sensitivity analyses, all dimensionless groups were kept the same as the "initial guess", except $Pe_2$, which was set to -9 for all remaining simulations. Clearly, however, some problems remain. Notably, the modeling significantly underestimates $Ca^{2+}$ concentrations at depth, and generally fails to explain pore water profiles across the hiatus (Figure 4.6).

**Activity Correction**

Three potential problems might explain the low $Ca^{2+}$ concentrations in our initial simulations (Figure 4.6). First, there are complications regarding the pH of pore waters at this location. Second, the basic model does not include ion pairing and corrections for ion activity. Third, multiple phases of carbonate could precipitate.

The simulated $Ca^{2+}$ profiles are primarily governed by two factors in our model: the simulated DIC profile and the solubility product of $CaCO_3$ (as calcite), which determines the extent of $Ca^{2+}$ that precipitates as calcite (Equation 6 in *Chatterjee et al*., 2011a). The solubility product of calcite is determined from the activity

product of $Ca^{2+}$ and $CO_3^{2-}$ ions, as well as pressure, temperature and salinity (*Mucci*, 1983). The pH profile is used to associate the $CO_3^{2-}$ and $HCO_3^-$ ion activities (*Roy et al*., 1993). Assuming constant salinity with depth (which we note is incorrect because of extreme alkalinity, *D'Hondt et al*., 2003), temperature and pH should dictate the ion activity product of $Ca^{2+}$ and $HCO_3^-$ in pore fluids. However, a problem arises in available data: although they should be the same, the measured pore water pH profiles differ significantly between Sites 685 and 1230 (Figure 4.7a). This leads to different ion activity products and different $Ca^{2+}$ profiles (Figure 4.7b and 4.7c).

More crucially, preliminary examinations of pore water at this location using PHREEQC software package (*Snyder, G*., pers. comm.), suggests that $\sim$40% of the DIC in pore water forms complex species, particularly $Na(HCO_3)^o$ and $Mg(HCO_3)_2^o$. This results in limited availability of $CO_3^{2-}$ for reaction with $Ca^{2+}$. These corrections were made by using 60% of the DIC to form calcite allowing the rest to form complexes. Simulations including this correction precipitated less $Ca^{2+}$ to form calcite. Therefore, steady state simulations were matched against observations by choosing an intermediate pH profile between measured data at two sites and assuming correct activity coefficients for different species to model calcite precipitation (Figure 4.6c).

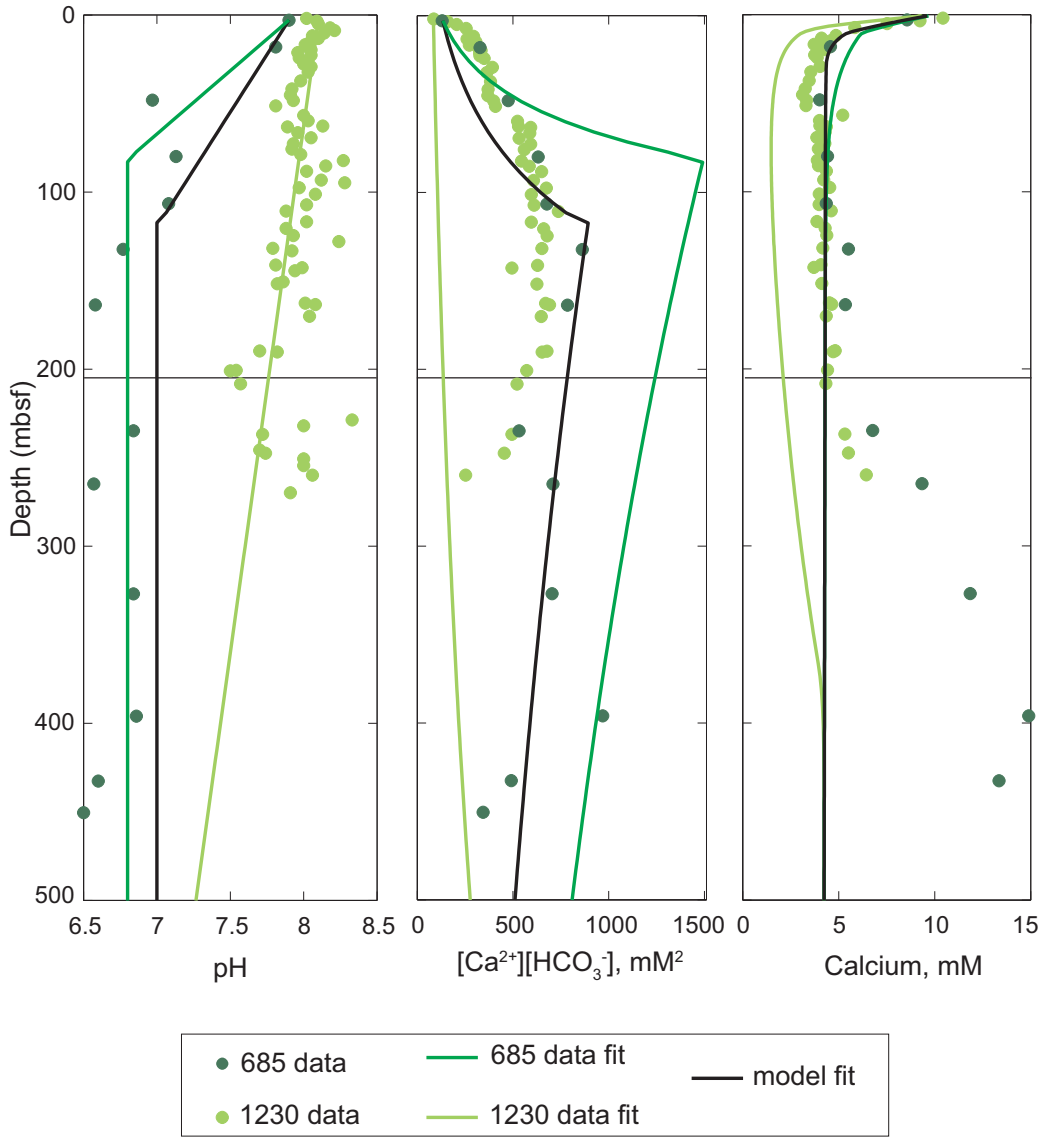


Figure 4.7 : Panels show (a) pH data at Sites 685, 1230 and the best fit profile used in the model, (b) ion concentration product of $Ca^{2+}$ and $HCO_3^-$ for different pH profiles and (c) simulated $Ca^{2+}$ based on these different pH profiles. Measured pH differs at the same site, although simulations using a pH profile bracketed by the measured profiles at two sites can describe the measured $Ca^{2+}$ profiles.

**Geotherm Effect**

Many papers regarding microbial organic carbon degradation in marine sediment assume that reaction rates decrease with depth below the seafloor (e.g., *Middleburg*, 1989). However, numerous studies have shown that the reaction rate of microbial methanogenesis increases significantly with temperature below 40$^{o}$C (e.g., *Zeikus and Winfrey*, 1976; *Price and Sowers*, 2004). Presumably, this means that in rapidly accumulating sediment on the continental slope, such as at Site 685/1230, methanogenesis may increase with depth because of the geotherm (Figure 4.9a; *Wellsbury et al*., 1997; *Burdige*, 2011; *Gu et al*., 2011). The idea is controversial, but we have included for completeness.

A ”geotherm correction” to microbial methanogenesis improves comparisons between simulated and measured profiles. An increasing rate in microbial methanogenesis with greater temperature and depth affects pore water profiles considerably. Due to high methanogenic activity, the organic matter depletes faster and completely exhausts the organic carbon in the sediment (Figure 4.9b). Reduced organic carbon restricts generation of $CH_4$ and associated $^{13}$C-enriched DIC at depth. The methane generated due to this effect lessens thus reducing the hydrate saturation at greater depths (Figure 4.6e). The resultant DIC profiles is closer to the measured data at this site (Figure 4.6b) including this effect. Overall, good first-order representative profiles are generated on including these geotherm effects. However, the $Ca^{2+}$ and $\delta^{13}$C of DIC profiles vary little with increasing

temperature along depth (Figure 4.6c and 4.6d).

A basic model for gas hydrate accumulation under steady state conditions explains the generalities of pore water profiles at Site 685/1230, at least for dissolved species of interest (Figure 4.6). Considerations of fluid flux, ion activity and temperature improve these simulations when compared to field data (Figure 4.6). Nonetheless, a major problem remains: we cannot model pore water profiles at depth, specifically across the hiatus. This is a fundamental problem facing interpretations of gas hydrate systems. As indicated by *Marquardt et al*. (2010), a steady state perspective necessitates that gas hydrate extends to the base of the GHSZ (Figure 4.6e). Such a view is not supported by field data, which show no evidence for deep gas hydrate or a BSR at this location.

### 4.4.2 Transient Solutions

With the general model framework, we examine possible transient systems at Site 685/1230. The modeling starts with similar initial conditions ($t = 0$), and runs to steady state. However, key parameters were changed: there is now a higher sedimentation rate (250 m/Myr), and a lower carbon input ($\beta$ = 6; equivalent to $TOC$ = 4%) in sediment relative to present day (Table 4.1; Figure 4.8a-f). These parameters were modified so as to simulate the observable Miocene sedimentary record (6.7 Myr and older). The pre-hiatus Miocene sedimentation rate was used to specify $Pe_1$ = 0.21. Steady state profiles generated now serve as an initial

condition for simulations after the hiatus.

The exact cause of the hiatus remains uncertain. We assume, for simplicity, that 1075 m of sediment (equivalent to duration of 4.3 Myr at a pre-hiatus rate of 250m/Myr) was removed from the seafloor by erosion. The depth horizon at the hiatus (1075 mbsf) thus becomes a new seafloor with new initial conditions (set $t = 0$; 2.4 Myr ago). Post hiatus time is then modeled keeping all parameters the same except with increased amount of organic carbon ($\beta$ = 9; TOC = 6%) and higher methanogenic activity ($Da$ = 6). Effectively, a new time zero started 2.4 Myr ago, but with inherited conditions, and pore water profiles evolve to present day (Figure 4.8g-l). Given our modeling framework, these are non-steady state (transient) profiles.

The temporal organic carbon profile acts a good indicator to track post-hiatus sedimentation (Figure 4.8g). Organic carbon rich sediment rains on the seafloor with a greater reaction activity. The depth traveled by this new sediment is tracked over time and its present day depth below the seafloor would represent the observed hiatus ($\sim$200 mbsf). Furthermore, the low organic carbon values below this horizon would represent sediment depleted in organic carbon deposited before the hiatus formation. Overall the broad, present day profile matches the TOC data at this location.

Considering the hiatus, the pore water $SO_4^{2-}$ profile remains similar to previous steady state results (Figure 4.8h). The SMT still lies at $\sim$9 mbsf. This is because

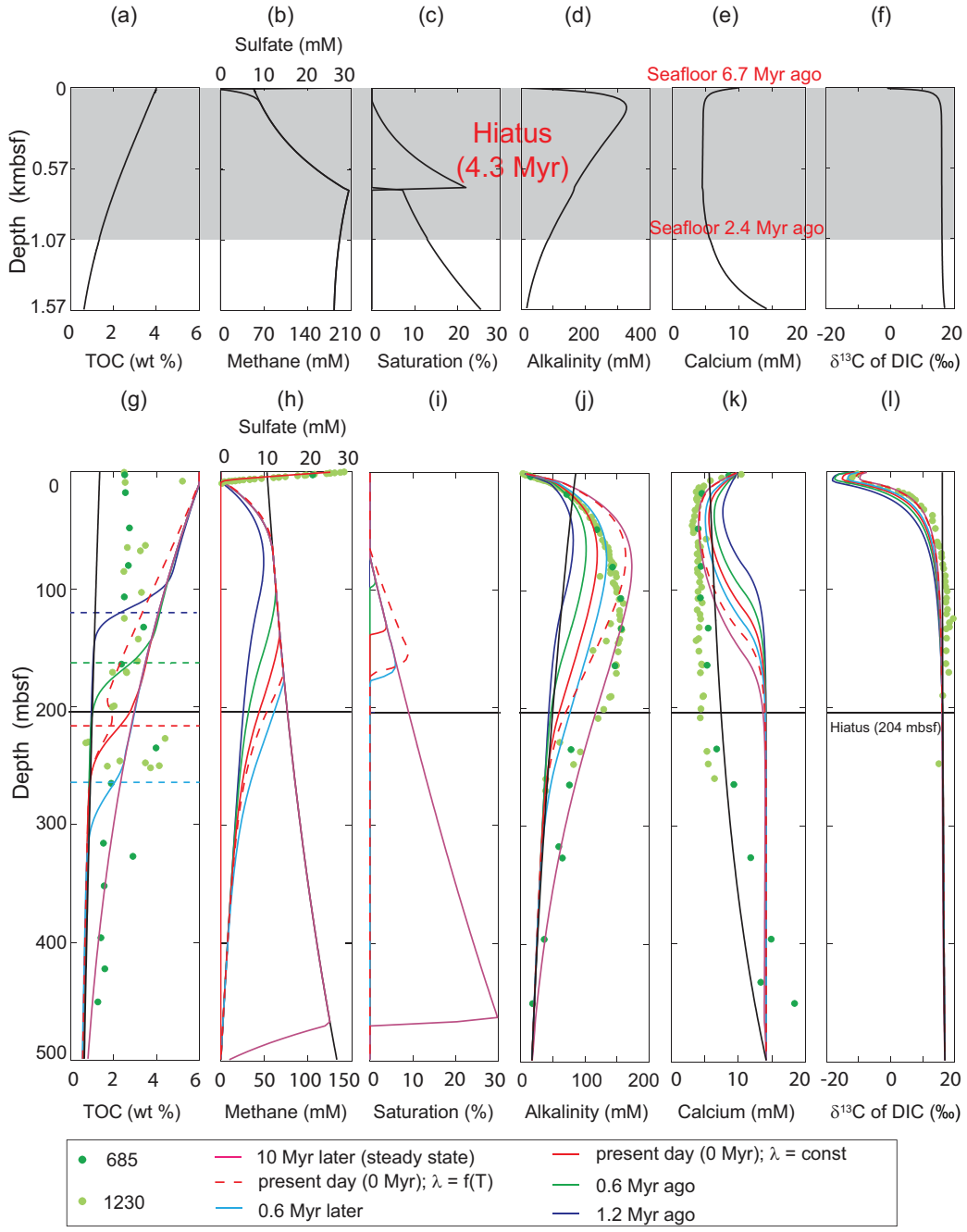


Figure 4.8 : Transient state profiles at Site 685/1230 before (a-f) and after (g-l) hiatus formation. Pre-hiatus steady state simulations (a-f) show shaded region that represents the lost sediment column forming the hiatus corresponding to duration of 4.3 Myr. Post-hiatus time evolved profiles: (g) organic carbon content with time evolved hiatus, (h) dissolved $CH_4$, and $SO_4^{2-}$, (i) gas hydrate saturation, (j) DIC, (k) $Ca^{2+}$, and (l) $\delta^{13}C$ of DIC. The solid curves correspond to temporal profiles with constant $\lambda$ (methanogenesis rate constant) and dashed line shows present day profile with temperature dependent $\lambda$. Field data at Sites 685 and 1230 are shown (green circles; *D'Hondt et al.*, 2003; *Donohue et al.*, 2006; *Meister et al.*, 2007). Common parameters: $Pe_2 = -9$, $Da_{POC} = 25$, $Da_{AOM} = 10^8$, $c_{b,ext} = 18$ mM, $c_{ca,ext} = 15$ mM and $\delta^{13}C$ = 17. Pre-hiatus parameters: $Pe_1 = 0.21$, $Da = 3$, $\beta = 6$ and post-hiatus parameters: $Pe_1 = 0.085$, $Da = 6$, $\beta = 9$.

it is primarily driven by upward methane flux and AOM at the SMT. The overall $CH_4$ profile emerges because of dissolved $CH_4$ generation below the SMT, internal cycling of hydrate and free gas phases within the GHSZ, and combined advection and diffusion effects that migrates $CH_4$ from depth which ultimately gets consumed by AOM to near zero values at the SMT (Figure 4.8h).

The ensuing gas hydrate and free gas profiles change showing 6% peak saturation between 72 and 175 mbsf at present day. These are consistent with field data. As the $CH_4$ concentration grows in pore fluids and exceeds the phase solubility values, it forms hydrates. These hydrates can move downward with the sediment with burial. The hydrate saturation increases with time and the peak values appear at greater depths as sediment is buried with time (Figure 4.8i). The transient saturation profiles show hydrates forming within the GHSZ but does not extend till the base of the GHSZ as shown in the steady state results above. The free gas phases are absent in these transient simulations as the hydrate front has not exit the GHSZ which matches with observation.

The DIC concentrations increase with depth to a broad maximum due to increased methanogenic activity above the hiatus. Below, concentrations drop to lower values below the hiatus as observed in field data (Figure 4.8j). The generic shape of the DIC profiles arise due to the same reasons as discussed in the steady state modeling. First, methanogenesis generates significant amounts of DIC at depth; second, this DIC enters the SMT to mix with DIC generated by AOM; third,

DIC leaves the sediment through the seafloor. Calcium also precipitates small amounts of DIC to precipitate as calcite around the SMT.

The overall shape of the $Ca^{2+}$ profile matches the field data in shallow depth. However, at greater depths, the $Ca^{2+}$ is greater than the observed profile at this location. This aberration can be explained due to poor constraints of pH and consequently ion activity product in the model. Nonetheless, these profiles are driven due to three factors: first, seawater $Ca^{2+}$ enters the SMT from above, second, advection and diffusion carries the $Ca^{2+}$ in the pore fluids upward; and third, DIC reacts with $Ca^{2+}$ to precipitate as carbonate (Figure 4.8k).

The $\delta^{13}\mathrm{C}$ of DIC profiles are simultaneously simulated with the other pore water constituents in the model. With increasing time, DIC concentration grows and more $^{13}\mathrm{C}$-enriched DIC enters the SMT from depth. These $^{13}\mathrm{C}$-enriched DIC fluxing from depth mixes with the $^{13}\mathrm{C}$-depleted DIC formed at the SMT. This ”mixing” leads to less negative $\delta^{13}\mathrm{C}$ of DIC at the SMT as more $^{13}\mathrm{C}$-enriched DIC ascends over time. Crucially, the shape of these profiles spanning the SMT remains the same as the steady state modeling. Basically, these less negative $\delta^{13}\mathrm{C}$ values ($\sim$-13 $\%_{00}$) appear at the SMT even though AOM consumes most *net* $SO_4^{2-}$ in shallow sediment (Figure 4.8l).

The geotherm effects discussed above show that reaction rate can vary exponentially over depth with increasing temperature (Figure 4.9a). As a consequence, the organic carbon profile and $CH_4$ generation rate are affected

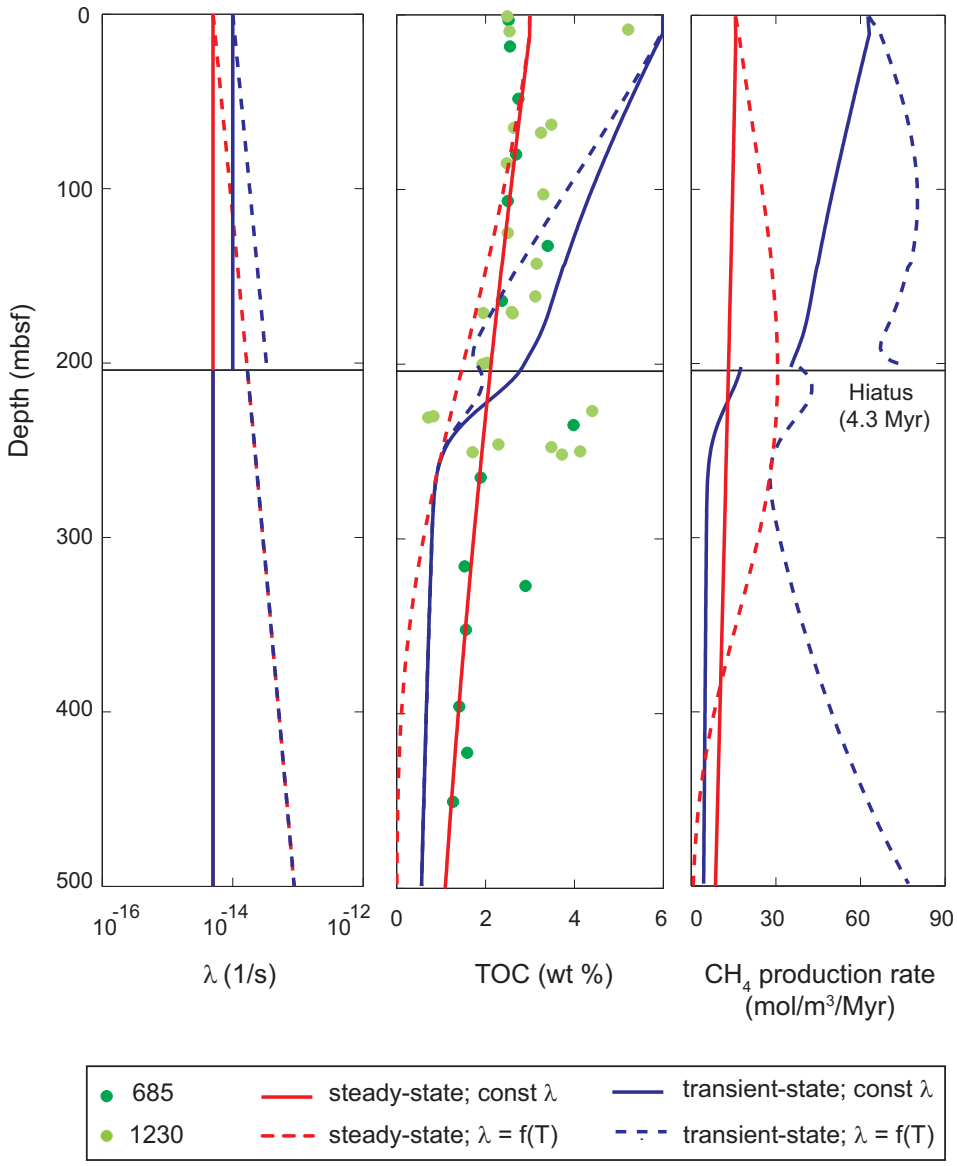


Figure 4.9 : Panels showing rate constant, organic carbon profiles in sediment and $CH_4$ production rates with and without geotherm effects. (a) Methanogenesis rate constant, $\lambda$, (b) organic carbon profiles and (c) rates of $CH_4$ production for transient and steady state simulations (Figures 4.6 and 4.8).

due to these effects (Figures 4.9b and 4.9c). For the transient state simulations, the pre-hiatus simulations (Figure 4.8a-f) are assumed to have constant methanogenesis reaction rate ($\lambda$), independent of temperature. The fresh sediment packet that rains on the seafloor post hiatus includes temperature (or geotherm) effects driving the reaction rates. Thus, including these geotherm effects match the observed pore water and the gas hydrate saturation profiles at present day (Figure 4.8g-l).

### 4.4.3 Concentration and Flux Crossplots of Alkalinity and Sulfate

A theoretical value known as excess alkalinity ($Alk^*$) can be calculated for a given interstitial water sample given its chemical composition. Assuming closed system behavior, it represents the amount of DIC that should exist in pore water before precipitation of authigenic carbonate. It can be computed by adding the pore water alkalinity, $Ca^{2+}$ (and $Mg^{2+}$). Plots showing deviations in excess alkalinity ($\Delta Alk^*$) with respect to seawater versus to those of pore water $SO_4^{2-}$ ($\Delta SO_4^{2-}$) above the SMT have been used to interpret the relative proportions of OSR and AOM consuming $SO_4^{2-}$ above the SMT (e.g., *Claypool et al*., 2006; *Kastner et al*., 2008a; *Torres and Kastner*, 2009; Figure 4.10). The basic idea has been that the slope on such crossplots relates to the relative proportion of the two potential reactions via stoichiometry (*Claypool et al*., 2006; *Kastner et al*., 2008a; *Torres and Kastner*, 2009). Basically, a 1:1 slope would imply $SO_4^{2-}$ removal by AOM,

and a 2:1 slope would imply $SO_4^{2-}$ consumption by OSR, and a slope in between would imply combination of both processes (Equations 1 and 2 in *Chatterjee et al*., 2011a).

Field data from Site 1230 is complex. First, the $Mg^{2+}$ concentration rises with depth. Therefore, deviations in excess alkalinity with respect to its seawater values would drop due to this elevated pore water $Mg^{2+}$ values. However, the nominal 2:1 slope in $\Delta Alk^*$: $\Delta\ SO_4^{2-}$ could indicate dominant organoclastic sulfate consumption at this site (Figure 4.10).

Concentration gradients are computed by linear fitting steady state concentration profiles (Figure 4.6). Fluxes entering and leaving the SMT are evaluated by multiplying these gradients with diffusivities and these fluxes are calculated above and below the SMT. Diffusive fluxes of $CH_4$, $SO_4^{2-}$ and DIC are cross-plotted across the SMT horizon (Figure 4.11). These fluxes also represent the total flux across the SMT as the advective component is zero near the SMT.

## 4.5 Discussion

Site 685/1230 presents a real challenge in multiple regards. Pore water concentrations measure extreme values at this location and the presence of a 4.3 Myr hiatus indicates that this sediment sequence is in transition. The key points of discussion are extreme pore water chemistry measured at Site 685/1230 and that the SMT at this site is primarily caused due to AOM. Although, the 2:1 slope in

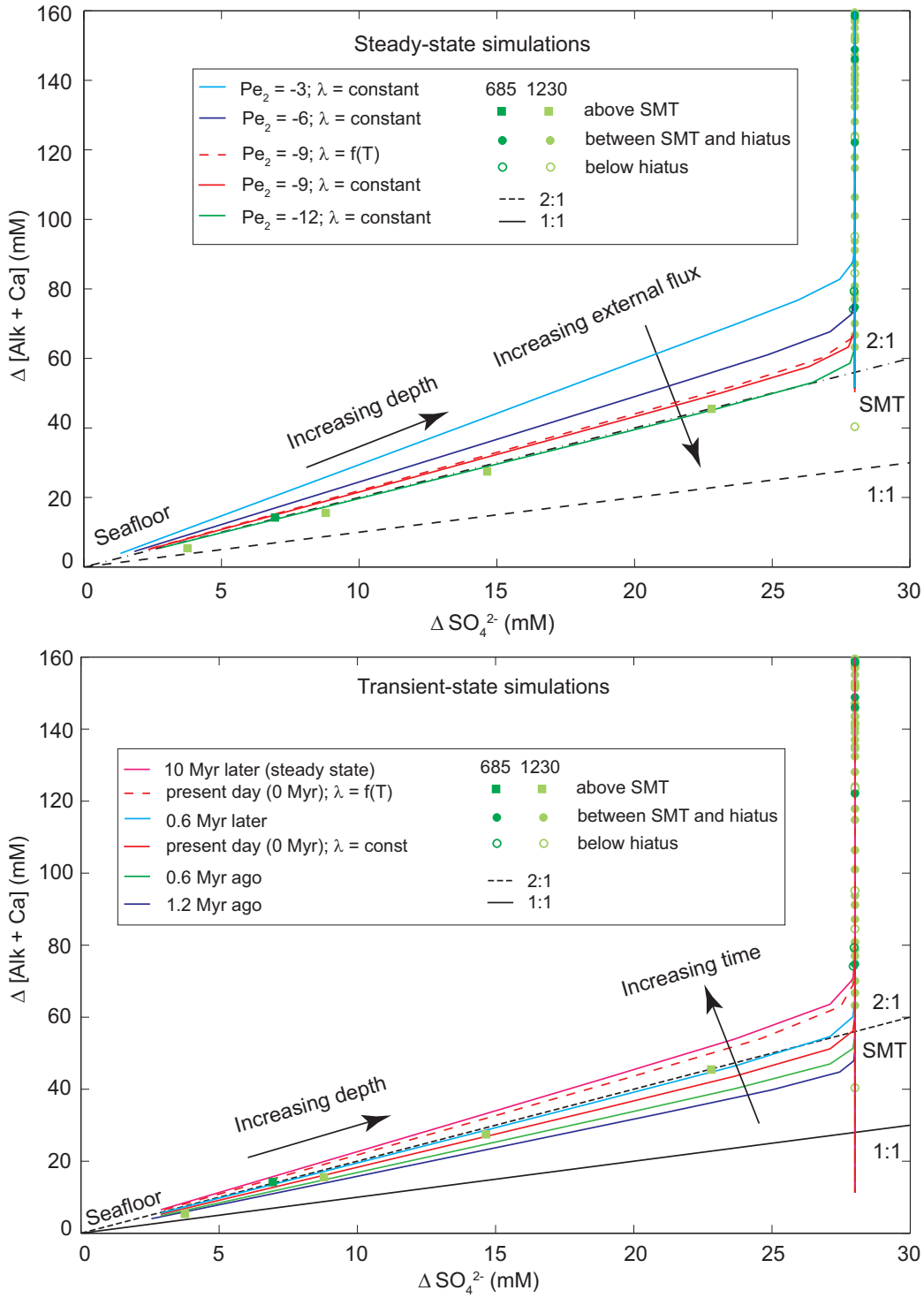


Figure 4.10 : Concentration cross-plot of "excess alkalinity" ($\Delta Alk^*$) corrected for carbonate precipitation versus $\Delta SO_4^{2-}$ (mM) relative to the seafloor for (a) steady state (Figure 4.6), and (b) transient state simulations (Figure 4.8). Crossplots constructed using field data Site 685 and 1230 (green markers; *Suess et al*., 1988; *D'Hondt et al*., 2003) and simulations match measured data. Notably, $\Delta Alk^*$ continues to rise below the SMT at this site. This clearly implies high flux of DIC from depth.

$\Delta Alk^*$: $\Delta\ SO_4^{2-}$ and $\delta^{13}\mathrm{C}$ of DIC at the SMT greater than that of $CH_4$ (e.g., -13 $\%_{00}$) might indicate organoclastic sulfate reduction, our simulations show that the AOM consumes most $SO_4^{2-}$. Within this context, we will discuss some of the implications of our simulations and how an upward flux of $\delta^{13}\mathrm{C}$-enriched DIC mixes with the $^{13}\mathrm{C}$-depleted DIC formed due to AOM at the SMT to govern the net $\delta^{13}\mathrm{C}$ of DIC at the SMT in these dynamic marine gas hydrate systems.

Previous modeling has shown a similar approach to explain some of the sites in marine environments where a low to moderate trend in "alkalinity versus $\delta^{13}\mathrm{C}$ of DIC" exists (Figure 4.2; *Chatterjee et al*., 2011a). This approach was used to model two sites (Hydrate Ridge 1244 and Keathley Canyon 151-3; Figure 4.1) containing gas hydrate but with differing carbon chemistry and showed that AOM is the dominant sulfate reduction pathway at the SMT. They proposed that vertically upward flux of $^{13}\mathrm{C}$-enriched DIC from depth produced by methanogenesis mixes with the $^{13}\mathrm{C}$-depleted DIC formed by AOM at the SMT and results in less negative $\delta^{13}\mathrm{C}$ of DIC observed at the SMT. In this chapter, we choose a site that lies on the highest end of the "alkalinity and $\delta^{13}\mathrm{C}$ of DIC" trend, expand the modeling by *Chatterjee et al*., (2011a), couple the hydrate and free gas phases to the their pore water chemistry model and explain an extreme Site 685/1230 in the Peru Trench.

There are sites where organoclastic sulfate reduction could be the dominant sulfate reduction pathway. However, based on our current understanding, these sites would show a curvilinear pore water sulfate profile with a deep SMT.

Moreover, these sites would show low or negligible methane fluxes from depth and would not bear any gas hydrates at depth. Although data exists from these deep drilled sites, there are very few of these sites with reasonably good pore water chemistry and $\delta^{13}\mathrm{C}$ of DIC. Furthermore, these are of no interest in regard to gas hydrate research. However, the key parameters that would characterize these sites are low or no upward fluid flux and a low methane concentration due to a slow methanogenic activity at depth. We have identified these characteristics as a part of our modeling exercise to delineate conditions necessary for the two sulfate reduction pathways. The key idea here is that the drilled sites known or inferred to have gas hydrates invariably have AOM causing the SMT with a near-linear sulfate profile. In addition, the upward flux of $^{13}\mathrm{C}$-enriched DIC impacts the net $\delta^{13}\mathrm{C}$ of DIC at the SMT.

The broad pore water profiles at Site 685/1230 can be simulated using a steady state model. The steady state profiles provide good match with observations and basic interpretations similar to other locations. However several problems remain. Most of these problems can be understood by considering activity, the geotherm and the hiatus. We revise our modeling to include some of the subtleties that were not considered in previous modeling. However, we note that these modifications to our existing model do not change the generic shape of our simulated profiles. The simulated $SO_4^{2-}$ profile is near-linear between the seafloor and the SMT, suggesting AOM dominates *net* $SO_4^{2-}$ consumption. The broad profiles for $CH_4$ and other

pore water chemistry constituents still provide a first-order explanation to chemical changes across the SMT in shallow sediment.

However, these steady state modeling exercises cannot explain the observed data across hiatuses. A transient state modeling approach should be adapted to explain the pore water chemistry spanning the SMT and the underlying hiatus at this site. The transient models generate profiles similar to previous steady state models, albeit more consistent with field data. These models explain the change in physical properties and associated pore water chemistry across the hiatus and help understand these dynamic systems in transition. This approach might be extended to explain some of the evolving sites bearing gas hydrates around the world.

Concentration crossplots cannot be used to infer processes governing the SMT. However, deviations of alkalinity ($Alk^*$) and $SO_4^{2-}$ relative to their seawater values are obtained from the steady state (Figure 4.6) and transient profiles (Figure 4.8) and $\Delta Alk^*$: $\Delta\ SO_4^{2-}$ crossplots are constructed. The simulated steady state profiles ($Pe_2$ = -9) favorably match the data and increasing flux shows reduction in the slope of these crossplots as shown (Figure 4.10a; *Chatterjee et al*., 2011a). Transient state profiles show that elevated DIC generation with increasing time changes the slope of these crossplots. Constructed temporal crossplots show that the present-day profiles match the measured data (Figure 4.10b). The key message from these simulations is that the slopes of these crossplots do not

indicate stoichiometry of the sulfate reduction pathway at the SMT as emphasized elsewhere (*Dickens and Snyder*, 2009; *Chatterjee et al*., 2011a).

Crossplots constructed using the concentration gradient of alkalinity (DIC) and $SO_4^{2-}$ entering and leaving the SMT (equivalent to fluxes) as opposed to the concentration deviation ($\Delta Alk^*$: $\Delta\ SO_4^{2-}$) crossplots are better candidates to indicate the reactions causing the SMT (*Luff and Wallman*, 2003; *Snyder et al*., 2007; *Dickens and Snyder*, 2009; *Kim et al*., 2011; *Chatterjee et al*., 2011a). Both $CH_4$ and DIC fluxes balance the $SO_4^{2-}$ flux along a 1:1 slope. This 1:1 correspondence implies dominant AOM at the SMT if steady state conditions prevail. Basically, the DIC flux entering the SMT from below adds to the DIC flux due to the AOM and the net DIC flux leaves the sediment towards the seafloor. This additional DIC flux that is added at the SMT balance the $SO_4^{2-}$ flux clearly implying AOM at the SMT as a 1:1 stoichiometric correspondence exists between $CH_4$, DIC, and $SO_4^{2-}$.

## 4.6 Conclusions

One of the key points is that alkalinity and $\delta^{13}\mathrm{C}$ of DIC cannot be used to discriminate between two sulfate reduction pathways. We show that the mixing of deep flux of $^{13}\mathrm{C}$-enriched DIC with the $^{13}\mathrm{C}$-depleted DIC from AOM impacts the pore water chemistry across the SMT at shallow depth. Here, we choose sites with high alkalinity and high $\delta^{13}\mathrm{C}$ of DIC which cannot be explained by the traditional

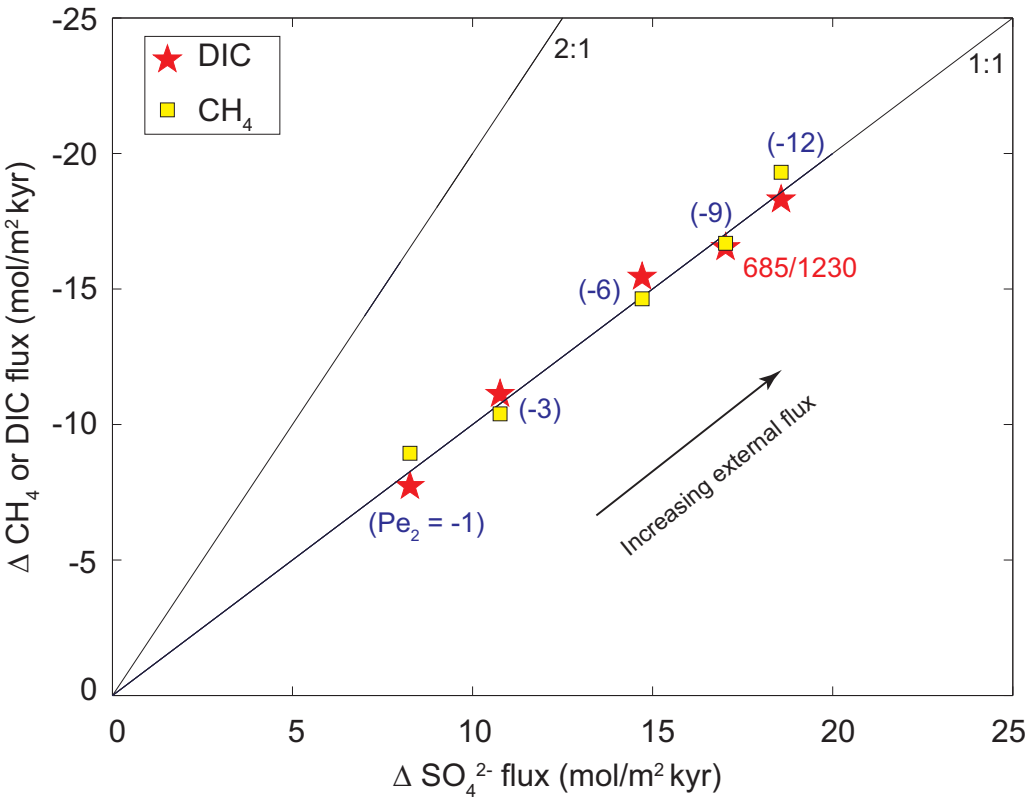


Figure 4.11 : Flux crossplots of $CH_4$ (squares) and DIC (stars) versus $SO_4^{2-}$ across the SMT corresponds to a 1:1 slope implying dominant AOM reaction at the SMT. The $Pe_2$ values (equivalent to upward fluid flux) shown in parenthesis is indirectly proportional to the SMT depth.

view. This will delineate the idea that the alkalinity and the $\delta^{13}\mathrm{C}$ of DIC cannot be used to distinguish between the chemical reactions at the SMT; instead, the deep flux of $^{13}\mathrm{C}$-enriched DIC governs the overall carbon chemistry at shallow depth. A steady state model expands a recent pore water chemistry model and links it to existing hydrate accumulation models to describe the broad pore water profiles and hydrate distribution at a unique site 685/1230 in the Peru Trench. These models also include crucial effects that are characterized by changes in ion activities due to ion pairing and reaction rates due to geothermal gradients. A transient state model is developed to simulate the hiatus and to explain some of these evolving sites containing gas hydrate such as the Site 1230 on the lower Peru slope.

# Chapter 5

# Two-dimensional Model for Quantification of Hydrate and Free Gas Accumulations

## 5.1 Introduction

*†A series of one-dimensional (1-D) numerical models have been built to explain gas hydrate accumulation in the marine environment over geological time (e.g., *Rempel and Buffett*, 1997; *Egeberg and Dickens*, 1999; *Xu and Ruppel*, 1999; *Davie and Buffett*, 2001, 2003a, 2003b; *Gering*, 2003; *Luff and Wallman*, 2003; *Haeckel et al*., 2004; *Torres et al*., 2004; *Wallman et al*., 2006; *Liu and Flemings*, 2006, 2007; *Bhatnagar et al*., 2007, 2011; *Garg et al*., 2008). Although the models differ in details and applicability, for the most part they have similar conceptual frameworks, where coupled equations for mass, momentum and energy transport generate, distribute and remove methane from the fluid-sediment system. These 1-D models provide first-order distribution of gas hydrate in subsea sediment

*Chatterjee S., G. Gu, G. Bhatnagar, W.G. Chapman, B. Dugan, G.R. Dickens, G.J. Hirasaki (2011), Effects of heterogeneous lithology and focused fluid flow on gas hydrate distribution in marine sediments, *Proceedings of the 7th International Conference on Gas Hydrates* (ICGH), Edinburgh, Scotland, United Kingdom, July 17-21, 2011

†Chatterjee S., G. Bhatnagar, B. Dugan, G.R. Dickens, W.G. Chapman and G.J. Hirasaki (2012), Lithologic heterogeneity and focused fluid flow governing gas hydrate distribution in marine sediments, *to be submitted*

sequences at numerous locations worldwide using site-specific parameters.

Recent modeling efforts have been made to couple the pore water chemistry to the existing hydrate accumulation models and to interpret the carbon cycling processes in shallow sediment (*Chatterjee et al*., 2011a). These revised models can explain multiple first-order observations in pore water chemistry (e.g., Site 1244), but fail to explain some of the second-order subtleties. In essence, these 1-D models provide first-order insights on gas hydrate occurrence, but do not capture the complexity and heterogeneity observed in natural gas hydrate systems. Numerous studies have shown that natural gas hydrate and free gas accumulation in marine sediments is highly heterogeneous at the m-scale (e.g., *Weinberger and Brown*, 2006; *Cook et al*., 2008; *Malinverno et al*., 2008), which complicates views on their formation.

To address this issue, we modify existing 1-D models and extend them to two spatial dimensions. A 2-D, heterogeneous sedimentation-fluid flow model is developed that tracks spatial and temporal gas hydrate accumulation over geologic time scales. This 2-D model accounts for heterogeneous lithologic features and lateral fluid migration to broaden our knowledge of primary controls on local and regional hydrate concentration and distribution. Fracture network systems and dipping permeable layers are common heterogeneities in natural gas hydrate settings; these localize flow, resulting in accumulation of localized, concentrated hydrate deposits (*Weinberger and Brown*, 2006). The 2-D model is

formulated through component mass balances and some key results are presented to show how lithologic heterogeneity causes regions of focused fluid flux. Higher saturations of hydrate and free gas are observed in these higher permeability regions as a result of the increased, localized, focused fluid flux. Conditions for generalized parameters are simulated but the generalized model can be applicable to many heterogeneous sites.

## 5.2 Mathematical Model

### 5.2.1 General Framework

The 2-D model is a spatial extension of the 1-D model developed by *Bhatnagar et al*. (2007). The mass balance equations for organic carbon, sediment, water and methane are solved simultaneously over geologic time scales. Labile organic carbon lands on the seafloor and moves down with sedimentation. Sedimentation is associated with compaction and thus porosity is reduced with respect to depth. Pore fluids are expelled from the pore space as a result of compaction and can move down relative to the seafloor. Fluids can also migrate up due to overpressure at depth. The organic carbon forms methane via a microbially mediated reaction. Methane and other pore water species can diffuse in the pore space as well as advect with the pore fluids. Thus, the 2-D model incorporates deposition and compaction of heterogeneous sediment, in situ $CH_4$ generation, diffusion and migration of dissolved gas with water. Two sediment heterogeneities are

considered in the model: fracture networks, and high permeability layers.

### 5.2.2 Component mass balances

Similar to 1-D models, the current 2-D effort begins with a series of coupled mass balance equations for various constituents. Our initial model contains water, sediment, organic carbon, and methane. We include an additional mass balance for chloride which will be coupled with the remaining mass balance equations and discussed in the subsequent chapter. The appropriate mass balance equations are (*Bhatnagar*, 2008; *Chatterjee et al*., 2011b).

For water,

$$\frac{\partial}{\partial t}[\phi S_w c_w^l \rho_w + \phi S_h c_w^h \rho_h] + \nabla \cdot [\phi S_w c_w^l \rho_w \mathbf{v}_w + \phi S_h c_w^h \rho_h \mathbf{v}_s] = 0 \ . \tag{5.1}$$

For sediment,

$$\frac{\partial}{\partial t}[(1-\phi)\rho_{sed}] + \nabla \cdot [(1-\phi)\rho_{sed}\mathbf{v}_s] = 0 \ . \tag{5.2}$$

For organic carbon,

$$\frac{\partial}{\partial t}[(1-\phi)\rho_{sed}\alpha] + \nabla \cdot [(1-\phi)\rho_{sed}\mathbf{v}_s\alpha] = -\rho_{sed}\lambda(1-\phi)\alpha \ . \tag{5.3}$$

For methane,

$$\frac{\partial}{\partial t}[\phi S_w c_m^l \rho_w + \phi S_h c_m^h \rho_h + \phi S_g c_m^g \rho_g] + \nabla \cdot [\phi S_w c_m^l \rho_w \mathbf{v}_w + \phi S_h c_m^h \rho_h \mathbf{v}_s + \phi S_g c_m^g \rho_g \mathbf{v}_g]$$

$$= \nabla \cdot [\phi S_w \rho_w D_m \nabla \cdot c_m^l] + \frac{M_{CH_4}}{M_{org}} \rho_{sed} \lambda (1-\phi) \alpha \ . \tag{5.4}$$

For chloride,

$$\frac{\partial}{\partial t}[\phi S_w c_{cl}^l \rho_w] + \nabla \cdot [\phi S_w c_{cl}^l \rho_w \mathbf{v}_w] = \nabla \cdot [\phi S_w \rho_w D_{cl} \nabla \cdot c_{cl}^l] \ . \tag{5.5}$$

The mass balance equations are the same as described in previous 1-D model, although expressed and solved in two dimensions (*Bhatnagar et al*., 2007). The parameters are: $c_i^j$ for mass fraction of component $i$ in phase $j$, $S_j$ for saturation of phase $j$, $\mathbf{v_j}$ for velocity vector of phase $j$, and $\rho_j$ for density of phase $j$. The kinetic rate constant for the methanogenesis reaction is represented by $\lambda$, porosity is denoted by $\phi$, $D_m$ and $D_{cl}$ are the diffusivities of methane and chloride in seawater, $\alpha$ is the organic carbon content in the sediment. Subscript $s$ corresponds to sediment, $w$ to water, $m$ to methane, $cl$ to chloride, $h$ to hydrate, and $g$ to free gas components. Superscript $l$ corresponds to water, $h$ to hydrate and $g$ to free gas phases.

Currently 1-D models have included additional components, notably $SO_4^{2-}$, dissolved inorganic carbon (DIC), $Ca^{2+}$, and carbon isotope compositions of $CH_4$ and DIC (*Chatterjee et al*., 2011a). These are not considered in this formulation.

## 5.3 Constitutive relationships

### Water and free gas flux

The existing 1-D model developed by *Bhatnagar et al*. (2007) assumes hydrostatic pressure. By contrast, our 2-D model simulates non-hydrostatic conditions and tracks pore pressures as a function of space and time. Consequently, water and gas fluxes in a compacting medium are given by Darcy's law (*Bear*, 1988):

$$\phi S_w(\mathbf{v}_w - \mathbf{v}_s) = -\frac{\mathbf{k}k_{rw}}{\mu_w}(\nabla p_w - \rho_w g \nabla z), \tag{5.6}$$

$$\phi S_g(\mathbf{v}_g - \mathbf{v}_s) = -\frac{\mathbf{k}k_{rg}}{\mu_g}(\nabla p_g - \rho_g g \nabla z), \tag{5.7}$$

where $\mathbf{v}_w$, $\mathbf{v}_g$ and $\mathbf{v}_s$ denote water, gas and sediment velocities, respectively; $\mathbf{k}$ is the absolute sediment permeability tensor; $k_{rw}$ and $k_{rg}$ are the relative permeabilities of water and gas; $\mu_w$ and $\mu_g$ are viscosities of water and gas; and $p_w$ and $p_g$ are the pore water and gas pressures, respectively.

### Absolute sediment permeability

Absolute sediment permeability is defined by a power law function of porosity (*Smith*, 1971):

$$\mathbf{k}(\phi) = \mathbf{k}_o\left(\frac{\phi}{\phi_o}\right)^8, \tag{5.8}$$

where $\mathbf{k}_o$ and $\phi_o$ are the initial sediment permeability and porosity at the seafloor.

Reduction in absolute sediment permeability due to formation of gas hydrates as a pore-filling structure is modeled by (*Kleinberg et al*., 2003):

$$\mathbf{k}(\phi, S_h) = \mathbf{k}(\phi)\left(1 - S_h^2 + \frac{2(1-S_h)^2}{\ln(S_h)}\right), \tag{5.9}$$

where $S_h$ is the hydrate saturation within the pore space.

**Relative permeability of water and gas**

Relative permeability of water and gas in the presence of each other are modeled as (*Bear*, 1988):

$$k_{rw} = k_{rw}^o (S_w^*)^4, \quad \mathrm{w}here \quad S_w^* = \frac{S_w - S_{wr}}{1 - S_{wr}}, \tag{5.10}$$

where $S_w^*$ is normalized water saturation, $k_{rw}^o$ is the end-point relative permeability of water, and $S_{wr}$ is the residual water saturation.

$$k_{rg} = k_{rg}^o (S_g^*)^2, \quad \mathrm{w}here \quad S_g^* = \frac{S_g - S_{gr}}{1 - S_{wr} - S_{gr}}, \tag{5.11}$$

where $S_g^*$ is normalized gas saturation, $k_{rg}^o$ is the end-point relative permeability of gas, and $S_{gr}$ is the residual gas saturation. The water, hydrate and gas saturations must equal unity:

$$S_w + S_h + S_g = 1. \tag{5.12}$$

**Capillary pressure**

Capillary pressure $P_c$ is defined as the difference between gas and pore water pressure:

$$P_c = p_g - p_w. \tag{5.13}$$

The Leverett J-function $J(S_w)$, is used to normalize capillary pressure profiles for different lithologies with different porosities and permeabilities as:

$$J(S_w) = \frac{P_{c,o}(S_w)}{\sigma_{gw}\cos\theta}\sqrt{\frac{\mathbf{k}_o}{\phi_o}}, \tag{5.14}$$

where $P_{c,o}(S_w)$ is the capillary pressure at reference absolute permeability $\mathbf{k}_o$ and porosity $\phi_o$; $\sigma_{gw}$ is the interfacial tension at the gas-water contact, and $\theta$ is the angle of contact. Assuming $\sigma_{gw}$ and $\mu$ as constants, capillary pressure for any $\phi$ and $\mathbf{k}$ is:

$$P_c(S_w) = J(S_w)\sigma_{gw}\cos\theta\sqrt{\frac{\phi}{\mathbf{k}}} = P_{c,o}(S_w)\sqrt{\frac{\mathbf{k}_o\phi}{\phi_o\mathbf{k}}} \tag{5.15}$$

The reference capillary pressure curve is defined by the Brooks-Corey model (*Bear*, 1988):

$$P_{c,o}(S_w) = P_{ce,o}(S_w^*)^{-1/n}, \tag{5.16}$$

where $P_{ce,o}$ is the capillary entry pressure at $\phi_o$ and $\mathbf{k}_o$, and $n$ is the pore-size distribution index.

### Effective stress and porosity

Sediment porosity is assumed to be controlled by effective stress (*Rubey and Hubbert*, 1959):

$$\phi = \phi_\infty + (\phi_o - \phi_\infty) e^{-\left(\frac{\sigma_v - p_w}{\sigma_\phi}\right)}, \tag{5.17}$$

where $\phi_\infty$ is minimum porosity achieved at the greatest depth, $\sigma_v$ is total vertical stress, and $\sigma_\phi$ is a characteristic stress of compaction.

### Lithostatic stress gradient

Lithostatic stress gradient is defined as a function of porosity and densities as:

$$\frac{\partial \sigma_v}{\partial z} = [(1-\phi)\rho_{sed} + \phi\rho_w]g. \tag{5.18}$$

## 5.4 Normalized Variables and Key Dimensionless Groups

The above equations are normalized using a specific scaling scheme discussed below (*Bhatnagar et al*., 2007; *Bhatnagar*, 2008; *Chatterjee et al*., 2011b).

### Porosity parameters

Reduced porosities are defined as:

$$\tilde{\phi} = \frac{\phi - \phi_\infty}{1 - \phi_\infty}, \quad \gamma = \frac{1 - \phi_\infty}{\phi_\infty}, \quad \eta = \frac{\phi_o - \phi_\infty}{1 - \phi_\infty}. \tag{5.19}$$

**Sediment parameters**

Sedimentation and compaction in the model are assumed to be 1-D with no lateral strain. This enables sediment to move and deform vertically (in the z-direction), but not horizontally (in the x or y direction). Basically, sediment accumulates on the seafloor and moves down with a sediment velocity ($v_s$) with positive z being down). Any gas hydrate within the formation and any free gas below critical saturation move with sediment at the same velocity. However, above a critical saturation, free gas becomes mobile, and can migrate up as well as laterally. The sedimentation rate, $\dot{S}$ at the seafloor can be defined as:

$$\dot{S} = v_s|_{\tilde{z}=0}. \tag{5.20}$$

The sediment flux is given by:

$$U_s = \dot{S}(1 - \phi_o), \tag{5.21}$$

**Peclet numbers**

Peclet numbers are defined by the ratio of advective fluid flux to methane diffusion. Peclet number one, $Pe_1$ is characterized by fluid flux related to sedimentation and compaction.

$$Pe_1 = \frac{U_{f,sed} L_t}{D_m}. \tag{5.22}$$

Similarly, Peclet number two, $Pe_2$ is characterized by the external fluid flux from deeper sediment.

$$Pe_2 = \frac{U_{f,ext} L_t}{D_m}. \tag{5.23}$$

$U_{f,sed}$ is the fluid flux due to sedimentation and compaction at hydrostatic pore pressure, $U_{f,ext}$ is the fluid flux due to external sources from depth, and $L_t$ is depth to the base of the GHSZ. The vertical fluid flux due to sedimentation and compaction $U_{f,sed}$ is shown as (*Bhatnagar et al*., 2007).

$$U_{f,sed} = \frac{1-\phi_o}{1-\phi_\infty} \dot{S} \phi_\infty. \tag{5.24}$$

**Damkohler number**

The Damkohler number is a dimensionless ratio of the methanogenesis reaction to methane diffusion:

$$Da = \frac{\lambda L_t^2}{D_m}, \tag{5.25}$$

where $\lambda$ is the reaction rate constant for methanogenesis , and $D_m$ is the diffusivity of methane.

**Other dimensionless parameters**

Overpressure often characterizes marine gas hydrate systems; that is, pore water pressure exceeds hydrostatic expectations. However, due to the presence

of high permeability zones, which provide low resistance to flow, fluids focus within high permeability conduits. Another dimensionless group is defined as the ratio of absolute permeability to the sedimentation rate quantifying the effects of overpressure genesis from sedimentation:

$$N_{sc} = \frac{k_o \rho_w g}{\mu_w \dot{S}} \tag{5.26}$$

Large values of $N_{sc}$ imply large sediment permeability and/or low sedimentation rate, which result in pore water pressures close to hydrostatic pressures. Conversely, smaller $N_{sc}$ values imply low permeability and/or high sedimentation rate, thereby producing overpressure. Dimensionless groups similar to $N_{sc}$ have been defined in earlier 1-D compaction models (*Yang and Fowler*, 1998; *Gutierrez and Wangen*, 2005). *Bhatnagar et al*., (2008b) explains the overpressure in hydrate bearing sediments with the help of this dimensionless group, $N_{sc}$.

The ratio of characteristic compaction depth to the depth to the base of the GHSZ is defined as:

$$N'_{t\phi} = \frac{L_\phi}{L_t} = \frac{\sigma_\phi / \rho_w g}{L_t} \tag{5.27}$$

Note the new dimensionless group is slightly different from the old definition (*Bhatnagar et al*., 2007).

$$N_{t\phi} = \frac{L_t}{L_\phi} = \frac{L_t}{\sigma_\phi / [(1 - \phi_\infty)(\rho_{sed} - \rho_w) g]} \tag{5.28}$$

**Scaled variables**

The normalized $CH_4$ phase concentrations are:

$$\tilde{c}_m^l = \frac{c_m^l}{c_{m,eqb}}, \quad \tilde{c}_m^h = \frac{c_m^h}{c_{m,eqb}}, \quad \tilde{c}_m^g = \frac{c_m^g}{c_{m,eqb}}. \tag{5.29}$$

The pore water $Cl^-$ concentrations are scaled relative to its seawater concentration:

$$\tilde{c}_{Cl}^l = \frac{c_{Cl}^l}{c_{Cl,o}}. \tag{5.30}$$

Lithostatic stress $\sigma_v$, water, gas and capillary pressures are normalized by the hydrostatic pore water pressure at the base of the GHSZ:

$$\tilde{\sigma}_v = \frac{\sigma_v}{\rho_w g L_t}, \quad \tilde{p}_w = \frac{p_w}{\rho_w g L_t}, \quad \tilde{p}_g = \frac{p_g}{\rho_w g L_t}, \quad \tilde{P}_c = \frac{P_c}{\rho_w g L_t}. \tag{5.31}$$

The vertical depth and lateral distance are scaled to the depth to the base of the GHSZ:

$$\tilde{z} = \frac{z}{L_t}, \quad \tilde{x} = \frac{x}{L_t} \tag{5.32}$$

The dimensionless time is defined as a combination of methane diffusivity $D_m$ and depth of the base of the GHSZ

$$\tilde{t} = \frac{t}{L_t^2 / D_m} \tag{5.33}$$

All phase densities are scaled by the density of water as:

$$\tilde{\rho}_h = \frac{\rho_h}{\rho_w}, \quad \tilde{\rho}_g = \frac{\rho_g}{\rho_w}, \quad \tilde{\rho}_{sed} = \frac{\rho_{sed}}{\rho_w} \tag{5.34}$$

The sediment velocity is normalized by the sedimentation rate at the seafloor.

$$\tilde{v}_s = \frac{v_s}{\dot{S}} \tag{5.35}$$

Finally, organic carbon content and initial organic carbon content are scaled as:

$$\tilde{\alpha} = \frac{\alpha}{\alpha_o}, \quad \beta = \frac{\alpha_o}{c_{m,eqb}}, \tag{5.36}$$

where $\alpha_o$ is organic carbon content at the seafloor and $c_{m,eqb}$ is the solubility of methane in seawater at the base of the GHSZ.

## 5.5 Dimensionless Mass Balance Equations, Initial Conditions and Boundary Conditions

The five mass balance equations (Equations 5.1 - 5.5) and the constitutive relationships are normalized using the scaling scheme discussed above and recast in their dimensionless form with their corresponding initial condition (I.C.) and boundary conditions (B.C.). The accumulation term is also expanded so that porosity can be expressed as a function of changing pore water pressure and

lithostatic stress.

**Time derivative term expansion**

The accumulation terms in the mass balance equations are basically a product of primary variables like saturation $S_j$, porosity $\phi$, and mass fraction $c_i^j$ of component $i$ in phase $j$. The time derivative can be expanded as shown:

$$\Delta_t(\phi S_i c_i^j) = \phi^{n+1} S_i^{n+1} c_i^{j,n+1} - \phi^n S_i^n c_i^{j,n} \tag{5.37}$$

where $\Delta_t$ represents the change in time and superscripts $n$ and $n+1$ represent different time steps. On adding and subtracting a term $\phi^{n+1} S_i^n c_i^{j,n}$:

$$\Delta_t(\phi S_i c_i^j) = \phi^{n+1} S_i^{n+1} c_i^{j,n+1} + \phi^{n+1} S_i^n c_i^{j,n} - \phi^{n+1} S_i^n c_i^{j,n} - \phi^n S_i^n c_i^{j,n} \tag{5.38}$$

On rearranging:

$$\Delta_t(\phi S_i c_i^j) = \phi^{n+1}(S_i^{n+1} c_i^{j,n+1} - S_i^n c_i^{j,n}) + S_i^n c_i^{j,n}(\phi^{n+1} - \phi^n) \tag{5.39}$$

which is restated as:

$$\Delta_t(\phi S_i c_i^j) = \phi^{n+1} \Delta_t(S_i c_i^j) + S_i^n c_i^{j,n} \Delta_t(\phi) \tag{5.40}$$

Porosity is a function of effective stress as shown (Equation 5.17) and is normalized using the scaling scheme (Equations 5.19 - 5.36). Reduced porosity $\tilde{\phi}$ is related to the dimensionless lithostatic stress $\tilde{\sigma}_v$ and dimensionless pore water pressure $\tilde{p}_w$:

$$\tilde{\phi} = \eta \exp\left[-\left(\frac{\tilde{\sigma}_v - \tilde{p}_w}{N'_{t\phi}}\right)\right] \tag{5.41}$$

Time derivative of porosity as a function of pore pressure can be written as follows:

$$\Delta_t(\phi S_i c_i^j) = \phi^{n+1}\Delta_t(S_i c_i^j) + S_i^n c_i^{j,n}\frac{\partial \phi}{\partial p_w}\Delta_t(p_w) \tag{5.42}$$

From the effective stress-porosity relationship, porosity was differentiated with respect to pore water pressure.

$$\Delta_t(\phi S_i c_i^j) = \phi^{n+1}\Delta_t(S_i c_i^j) + S_i^n c_i^{j,n}\left[\frac{\phi - \phi_\infty}{\sigma_\phi}\right]\left[1 - \frac{\sigma_v^{n+1} - \sigma_v^n}{p_w^{n+1} - p_w^n}\right]\Delta_t(p_w) \tag{5.43}$$

The time derivative expansion for accumulation terms in the following mass balance equations can be expanded using the same technique. These time derivative terms are now put back in the mass balance equations (Equations 5.1 - 5.5) and then normalized with the help of the scaled variables discussed above (Equations 5.19 - 5.36).

**Initial porosity profile**

At hydrostatic pressure, the porosity profile can be calculated as an analytical expression to serve as an initial condition:

$$\tilde{\phi} = \frac{\eta}{\eta + (1-\eta)\exp\left[\frac{\gamma\tilde{z}(\tilde{\rho}_{sed}-1)}{N'_{t\phi}(1+\gamma)}\right]} \tag{5.44}$$

**Water balance**

$$\begin{aligned}
&\left(\frac{1+\gamma\tilde{\phi}}{\gamma}\right)\frac{\partial}{\partial\tilde{t}}\left[S_w c_w^l + S_h c_w^h \tilde{\rho}_h\right] + \frac{\tilde{\phi}}{N_{t\phi}}[S_w c_w^l + S_h c_w^h \tilde{\rho}_h]\frac{\partial}{\partial\tilde{t}}(\tilde{p}_w - \tilde{\sigma}_v) \\
&+Pe_1\left(\frac{1+\gamma}{1-\eta}\right)\frac{\partial}{\partial\tilde{z}}\left[\left(\frac{1+\gamma\tilde{\phi}}{\gamma}\right)[S_w c_w^l + S_h c_w^h \tilde{\rho}_h]\tilde{v}_s\right] \\
&-Pe_1\left(\frac{1+\gamma}{1-\eta}\right)\frac{\partial}{\partial\tilde{z}}\left[N_{sc}\frac{1+\gamma}{\gamma}\left(\frac{1+\gamma\tilde{\phi}}{1+\gamma\eta}\right)^8 k_{rw}\left(\frac{\partial\tilde{p}_w}{\partial\tilde{z}} - 1\right)c_w^l\right] \\
&-Pe_1\left(\frac{1+\gamma}{1-\eta}\right)\frac{\partial}{\partial\tilde{x}}\left[N_{sc}\frac{1+\gamma}{\gamma}\left(\frac{1+\gamma\tilde{\phi}}{1+\gamma\eta}\right)^8 k_{rw}\left(\frac{\partial\tilde{p}_w}{\partial\tilde{x}}\right)c_w^l\right] = 0
\end{aligned} \tag{5.45}$$

The initial condition (I.C.) is assumed to be hydrostatic. The boundary condition (B.C.) at the seafloor is assumed hydrostatic, and the left and right extremes of the domain are considered as no-flow boundaries. The initial condition and boundary conditions are expressed as follows:

**Initial condition**

$$\tilde{p}_w(\tilde{z},\tilde{x},0) = \frac{\rho_w g L_o + \rho_w g z}{\rho_w g L_t} = \frac{L_o + z}{L_t} = \frac{L_o}{L_t} + \tilde{z} \quad (\text{Hydrostatic condition}) \tag{5.46}$$

**Boundary conditions**

$$\tilde{p}_w(0,\tilde{x},\tilde{t}) = \frac{L_o}{L_t} \quad (\text{Seafloor condition}) \tag{5.47}$$

$$\frac{\partial \tilde{p}_w}{\partial \tilde{x}}(\tilde{z},0,\tilde{t}) = \frac{\partial \tilde{p}_w}{\partial \tilde{x}}(\tilde{z},L_x,\tilde{t}) = 0 \quad (\text{No} - \text{flow conditions}) \tag{5.48}$$

The pore pressures in our 2-D model are no longer hydrostatic, so the pressure gradient at the lowermost boundary cannot be modeled as a hydrostatic pressure gradient $\frac{\partial \tilde{p}_w}{\partial \tilde{z}}(L_z,\tilde{x},\tilde{t}) = 1$. The bottommost boundary has been modeled by specifying the fluid flux and thereby specifying a constant non-hydrostatic pressure gradient. The specified fluid flux is equal to $U_{f,sed} + U_{f,ext}$ (for biogenic sources only, $U_{f,ext} = 0$). Rewriting the Darcy water flux (Equation 5.6) for the lowermost boundary as follows:

$$\mathbf{v}_w S_w \phi = \mathbf{v}_s S_w \phi - \frac{\mathbf{k} k_{rw}}{\mu_w}(\nabla p_w - \rho_w g \nabla z) = U_{f,sed} + U_{f,ext}, \tag{5.49}$$

On normalizing:

$$\tilde{\mathbf{v}}_w S_w \frac{1+\gamma\tilde{\phi}}{\gamma} = \tilde{\mathbf{v}}_s S_w \frac{1+\gamma\tilde{\phi}}{\gamma} - k_{rw}\left(\frac{1+\gamma}{\gamma}\right)\frac{\mathbf{k_o}\rho_w g}{\dot{S}\mu_w}\frac{\mathbf{k}}{\mathbf{k_o}}(\nabla\tilde{p}_w - \nabla\tilde{z})$$

$$= \left(\frac{1+\gamma}{\gamma}\right)\frac{(U_{f,sed}+U_{f,ext})}{\dot{S}}, \tag{5.50}$$

Substituting Equations 5.24 and 5.26, normalizing the term on the right and rearranging:

$$-N_{sc}\left(\frac{1+\gamma}{\gamma}\right)\frac{\mathbf{k}}{\mathbf{k_o}}k_{rw}(\nabla\tilde{p}_w - \nabla\tilde{z}) = \frac{(Pe_1+Pe_2)}{Pe_1\gamma/(1-\eta)} - \left(\frac{1+\gamma\tilde{\phi}}{\gamma}\right)\tilde{\mathbf{v}}_\mathbf{s}S_w, \tag{5.51}$$

The non-hydrostatic pressure gradient at the bottom boundary is expressed using Equation 5.51:

$$\frac{\partial\tilde{p}_w}{\partial\tilde{z}}(L_z,\tilde{x},\tilde{t}) = 1 - \frac{\frac{(Pe_1+Pe_2)}{Pe_1\gamma/(1-\eta)} - \left(\frac{1+\gamma\tilde{\phi}}{\gamma}\right)\tilde{\mathbf{v}}_\mathbf{s}S_w}{N_{sc}\left(\frac{1+\gamma}{\gamma}\right)\left(\frac{1+\gamma\tilde{\phi}}{1+\gamma\eta}\right)^8 k_{rw}(L_z)} \quad (\text{Non}-\text{hydrostatic pressure gradient}) \tag{5.52}$$

where $L_o$ is seafloor depth and $L_x$ is the width of the domain, and $L_z$ is the thickness of the domain.

Notably, the relative permeability of water at this boundary is unity, $k_{rw}(L_z) = 1$. Thus, a non-hydrostatic boundary condition at the lowermost boundary (Equation 5.52) is derived by specifying a finite fluid flux at the boundary. Infinite $N_{sc}$ represents infinite permeability, which implies hydrostatic conditions. For $N_{sc} = \infty$, Equation 5.52 reduces the pressure gradient to unity which corresponds to a

hydrostatic pressure gradient at the lowermost boundary of our simulation domain.

**Sediment balance**

$$-\frac{\tilde{\phi}}{N_{t\phi}}\frac{\partial}{\partial\tilde{t}}(\tilde{p}_w-\tilde{\sigma}_v)+Pe_1\left(\frac{1+\gamma}{1-\eta}\right)\frac{\partial}{\partial\tilde{z}}\left[(1-\tilde{\phi})\tilde{v}_s\right]=0 \tag{5.53}$$

The initial sediment velocity profile is evaluated assuming hydrostatic pressure, whereas the boundary condition for velocity of sediment at the seafloor is the normalized sedimentation rate and equal to unity.

**Initial condition**

$$\tilde{v}_s(\tilde{z},\tilde{x},0)=\left(\frac{1-\eta}{1-\tilde{\phi}}\right)\quad(\text{Hydrostatic condition}) \tag{5.54}$$

**Boundary condition**

$$\tilde{v}_s(0,\tilde{x},\tilde{t})=1\quad(\text{Seafloor condition}) \tag{5.55}$$

**Organic balance**

$$-\frac{\tilde{\phi}\tilde{\alpha}}{N_{t\phi}}\frac{\partial}{\partial\tilde{t}}(\tilde{p}_w-\tilde{\sigma}_v)+(1-\tilde{\phi})\frac{\partial\tilde{\alpha}}{\partial\tilde{t}}+Pe_1\left(\frac{1+\gamma}{1-\eta}\right)\frac{\partial}{\partial\tilde{z}}\left[(1-\tilde{\phi})\tilde{v}_s\tilde{\alpha}\right]=-Da(1-\tilde{\phi})\tilde{\alpha} \tag{5.56}$$

Initially, there is no organic carbon present within the sediment, whereas the boundary condition of organic concentration at the seafloor is normalized to unity.

**Initial condition**

$$\tilde{\alpha}_s(\tilde{z},\tilde{x},0)=0 \tag{5.57}$$

**Boundary condition**

$$\tilde{\alpha}_s(0,\tilde{x},\tilde{t})=1 \quad \text{(Seafloor condition)}$$

**Methane balance**

$$\left(\frac{1+\gamma\tilde{\phi}}{\gamma}\right)\frac{\partial}{\partial\tilde{t}}\left[S_w\tilde{c}_m^l+S_h\tilde{c}_m^h\tilde{\rho}_h+S_g\tilde{c}_m^g\tilde{\rho}_g\right]$$

$$+\frac{\tilde{\phi}}{N_{t\phi}}[S_w\tilde{c}_m^l+S_h\tilde{c}_m^h\tilde{\rho}_h+S_g\tilde{c}_m^g\tilde{\rho}_g]\frac{\partial}{\partial\tilde{t}}(\tilde{p}_w-\tilde{\sigma}_v)$$

$$+Pe_1\left(\frac{1+\gamma}{1-\eta}\right)\frac{\partial}{\partial\tilde{z}}\left[\left(\frac{1+\gamma\tilde{\phi}}{\gamma}\right)[S_w\tilde{c}_m^l+S_h\tilde{c}_m^h\tilde{\rho}_h+S_g\tilde{c}_m^g\tilde{\rho}_g]\tilde{v}_s\right]$$

$$-Pe_1\left(\frac{1+\gamma}{1-\eta}\right)\frac{\partial}{\partial\tilde{z}}\left[N_{sc}\left(\frac{1+\gamma}{\gamma}\right)\left(\frac{1+\gamma\tilde{\phi}}{1+\gamma\eta}\right)^8 k_{rw}\left(\frac{\partial\tilde{p}_w}{\partial\tilde{z}}-1\right)\tilde{c}_m^l\right]$$

$$-Pe_1\left(\frac{1+\gamma}{1-\eta}\right)\frac{\partial}{\partial\tilde{z}}\left[N_{sc}\left(\frac{1+\gamma}{\gamma}\right)\left(\frac{1+\gamma\tilde{\phi}}{1+\gamma\eta}\right)^8 k_{rg}\left(\frac{\partial\tilde{p}_g}{\partial\tilde{z}}-\tilde{\rho}_g\right)\left(\frac{\mu_w}{\mu_g}\right)\tilde{\rho}_g\tilde{c}_m^g\right]$$

$$-Pe_1\left(\frac{1+\gamma}{1-\eta}\right)\frac{\partial}{\partial\tilde{x}}\left[N_{sc}\left(\frac{1+\gamma}{\gamma}\right)\left(\frac{1+\gamma\tilde{\phi}}{1+\gamma\eta}\right)^8\left[k_{rw}\frac{\partial\tilde{p}_w}{\partial\tilde{x}}\tilde{c}_m^l+k_{rg}\frac{\partial\tilde{p}_g}{\partial\tilde{x}}\left(\frac{\mu_w}{\mu_g}\right)\tilde{\rho}_g\tilde{c}_m^g\right]\right]$$

$$=\frac{\partial}{\partial\tilde{z}}\left[\frac{1+\gamma\tilde{\phi}}{\gamma}S_w\frac{\partial\tilde{c}_m^l}{\partial\tilde{z}}\right]+\frac{\partial}{\partial\tilde{x}}\left[\frac{1+\gamma\tilde{\phi}}{\gamma}S_w\frac{\partial\tilde{c}_m^l}{\partial\tilde{x}}\right]+\frac{M_{CH_4}\tilde{\rho}_{sed}Da(1-\tilde{\phi})\tilde{\alpha}\beta}{M_{org}} \quad (5.58)$$

Initially, there is no methane in the system. At the seafloor, methane concentration is equal to zero; methane flux is set to zero at the right and left boundaries of the domain; the bottom boundary has a choice of boundary condition, depending on the methane source. The methane concentration gradient is equal to zero for a system with biogenic sources only (Equation 5.62), whereas the methane concentration is set to be a constant value for deeper methane sources (Equation 5.63).

**Initial condition**

$$\tilde{c}_m^l(\tilde{z},\tilde{x},0)=0, \quad (5.59)$$

**Boundary conditions**

$$\tilde{c}_m^l(0,\tilde{x},\tilde{t})=0,(\text{Seafloor condition}) \quad (5.60)$$

$$\frac{\partial\tilde{c}_m^l}{\partial\tilde{x}}(\tilde{z},0,\tilde{t})=\frac{\partial\tilde{c}_m^l}{\partial\tilde{x}}(\tilde{z},L_x,\tilde{t})=0,(\text{No}-\text{flow conditions}) \quad (5.61)$$

$$\frac{\partial\tilde{c}_m^l}{\partial\tilde{z}}(L_z,\tilde{x},\tilde{t})=0,(\text{Biogenic sources only}) \quad (5.62)$$

$$\tilde{c}_m^l(L_z,\tilde{x},\tilde{t}) = \tilde{c}_{m,ext}^l, (\text{Thermogenic sources only}) \tag{5.63}$$

**Chloride balance**

$$\left(\frac{1+\gamma\tilde{\phi}}{\gamma}\right)\frac{\partial}{\partial\tilde{t}}\left[S_w\tilde{c}_{cl}^l\right] + \frac{\tilde{\phi}}{N_{t\phi}}S_w\tilde{c}_{cl}^l\frac{\partial}{\partial\tilde{t}}(\tilde{p}_w-\tilde{\sigma}_v) + Pe_1\left(\frac{1+\gamma}{1-\eta}\right)\frac{\partial}{\partial\tilde{z}}\left[\left(\frac{1+\gamma\tilde{\phi}}{\gamma}\right)S_w\tilde{c}_{cl}^l\tilde{v}_s\right]$$

$$-Pe_1\left(\frac{1+\gamma}{1-\eta}\right)\frac{\partial}{\partial\tilde{z}}\left[N_{sc}\left(\frac{1+\gamma}{\gamma}\right)\left(\frac{1+\gamma\tilde{\phi}}{1+\gamma\eta}\right)^8 k_{rw}\left(\frac{\partial\tilde{p}_w}{\partial\tilde{z}}-1\right)\tilde{c}_{cl}^l\right]$$

$$-Pe_1\left(\frac{1+\gamma}{1-\eta}\right)\frac{\partial}{\partial\tilde{x}}\left[N_{sc}\left(\frac{1+\gamma}{\gamma}\right)\left(\frac{1+\gamma\tilde{\phi}}{1+\gamma\eta}\right)^8 k_{rw}\left(\frac{\partial\tilde{p}_w}{\partial\tilde{x}}\right)\tilde{c}_{cl}^l\right]$$

$$= \tilde{D}_{cl}\frac{\partial}{\partial\tilde{z}}\left[\frac{1+\gamma\tilde{\phi}}{\gamma}S_w\frac{\partial\tilde{c}_{cl}^l}{\partial\tilde{z}}\right] + \frac{\partial}{\partial\tilde{x}}\left[\frac{1+\gamma\tilde{\phi}}{\gamma}S_w\frac{\partial\tilde{c}_{cl}^l}{\partial\tilde{x}}\right] \tag{5.64}$$

The initial and boundary conditions are used to solve the dimensionless chloride mass balance equation shown above. Initially, the pore water has seawater salinity. At the seafloor and at the bottom boundary, chloride concentration is set to its seawater value; chloride flux is set to zero at the right and left boundaries of the domain assuming them to be no-flow boundaries.

**Initial condition**

$$\tilde{c}_{cl}(\tilde{z},\tilde{x},0) = 1 \quad (\text{Hydrostatic condition}) \tag{5.65}$$

**Boundary conditions**

$$\tilde{c}_{cl}(0, \tilde{x}, \tilde{t}) = 1 \quad (\text{Seafloor condition}) \tag{5.66}$$

$$\tilde{c}_{cl}(\tilde{L}_z, \tilde{x}, \tilde{t}) = \tilde{c}_{cl,\ ext} \quad (\text{Bottom boundary condition}) \tag{5.67}$$

$$\frac{\partial \tilde{c}_{cl}}{\partial \tilde{x}}(\tilde{z}, 0, \tilde{t}) = \frac{\partial \tilde{c}_{cl}}{\partial \tilde{x}}(\tilde{z}, \tilde{L}_x, \tilde{t}) = 0 \quad (\text{No} - \text{flow conditions}) \tag{5.68}$$

## 5.6 Numerical Algorithm

The five coupled dimensionless mass balance equations (Equations 5.45, 5.53, 5.56, 5.58 and 5.64) are solved using a fully implicit numerical scheme using the initial condition and boundary conditions discussed above. A single-point, upstream weighting was used to formulate the relative permeability terms. The primary variables are $p_w$, $v_s$, $\alpha$, $(S_w c_{cl})$ and one of the three from the following ($c_m^l$, $S_h$, $S_g$) depending on the local thermodynamic conditions of the grid block at any given time. All the component mass balance equations are then recast in their residual form and the Newton-Raphson method is implemented to iterate on them to converge to the finite solution.

## 5.7 2-D model Development and Validation

The 2-D model is tested, validated and benchmarked against 1-D results (*Bhatnagar et al*., 2007). The seafloor parameters used are: seafloor depth =

2700 m below sea level, seafloor temperature = 3$^{o}$C, and geothermal gradient = 0.04$^{o}$C/m. The primary dimensionless transport parameters defined in the model used for simulations are: $Pe_1 = 0.1$, $Da = 10$, $\beta = 6$, $\eta = 6/9$, $\gamma = 9$, $N_{sc} = 10^4$ and $N'_{t\phi} = 1.485$, unless specified otherwise. Critical gas saturation, $S_{gr}$ is specified as 100% and free gas is assumed to be immobile for the base cases . The 2-D code was first tested with homogeneous sediment permeability (i.e., permeability varies vertically due to burial and compaction but does not vary laterally), essentially a 1-D implementation of the 2-D model. Steady-state hydrate and free gas saturations were simulated (Figure 5.1). The hydrate saturation with only in situ methane sources in a homogeneous sediment column increases to a peak saturation of $\sim$11% at the base of the GHSZ with an average hydrate saturation equal to 5.7%. The 2-D profiles match the 1-D results. Due to lithologic homogeneity, the hydrate and free gas saturations are uniform laterally and this case is analogous to a simple 1-D system.

There is no flow focusing or preferential accumulation of hydrate and free gas within the sediment due to absence of heterogeneity. To assess deeper sources, methane concentration is specified in the pore fluid migrating upwards for cases simulated with upward fluid flux ($Pe_2 < 0$). This enables methane charged fluids to migrate upwards from deeper sources which results in higher hydrate and free gas saturations. The average hydrate saturation is computed ($\langle S_h \rangle$) within the hydrate stability zone, multiplied by $Pe_1$ and this product is related with the net fluid flux

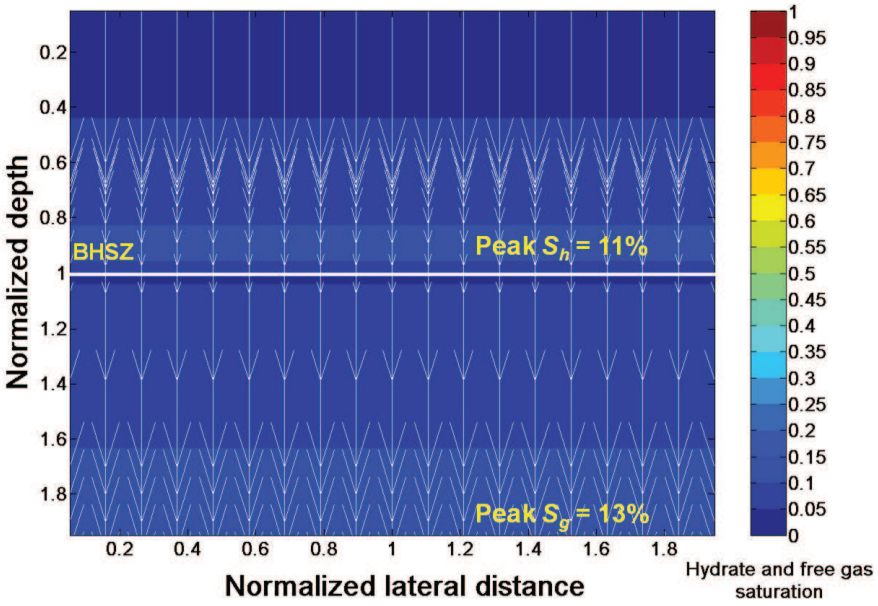


Figure 5.1 : Steady-state gas hydrate and free gas saturation contours for homogeneous sediment. The white line at unit normalized depth represents the base of the GHSZ. The color bars represent hydrate and free gas saturations. The fluid flux relative to the seafloor is scaled by the maximum flux and depicted by white arrows. The following parameters were used for this simulation: $Pe_1 = 0.1$, $Pe_2 = 0$, $Da = 10$, $\beta = 6$, $\tilde{c}_{m,ext} = 0$, $\gamma = 9$, $\eta = 6/9$, $k_v/k_h = 1$, $N'_{t\phi} = 1.485$ and $N_{sc} = 10^4$.

($Pe_1 + Pe_2$). The results identically correlate the net fluid flux to the average hydrate saturation from the 1-D model (Figure 5.2). Therefore, such correlations can now be used to quantify hydrate saturations using net fluid flux as the primary input.

With the validated 2-D model, heterogeneities are simulated to show how high permeability conduits localized fluid flux, and these localized fluxes resulted in concentrated hydrate deposits. To study heterogeneity using the 2-D model, two sources of methane are considered: in situ biogenic and external deeper sources. To simulate deeper sources, the model was extended to include higher pressure at the bottom boundary to simulate higher fluid flux and methane input at depth.

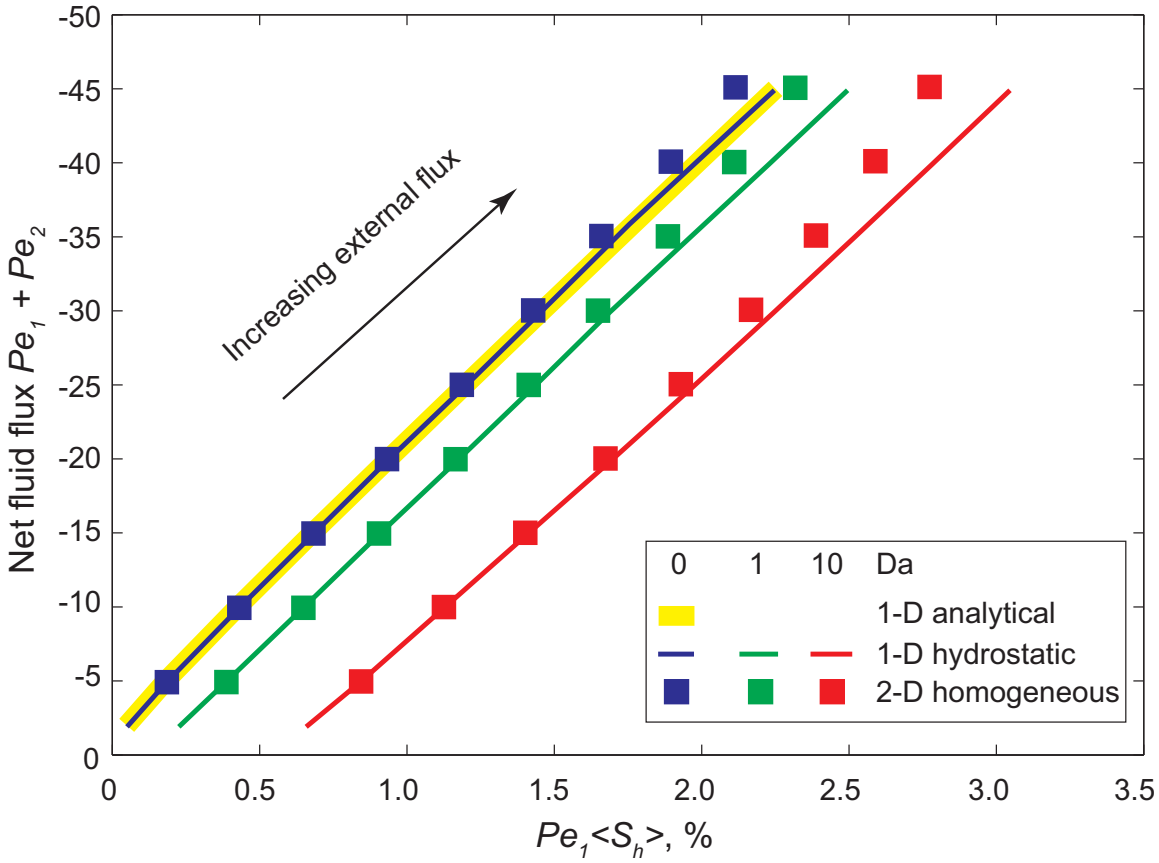


Figure 5.2 : Average hydrate flux, $Pe_1\langle S_h\rangle$ as a function of net fluid flux, $Pe_1 + Pe_2$ for 1-D (lines) and homogeneous 2-D sediment (squares) for a range of $Da$ values. The assumption of negligible volume change due to methane dissolved in water in the 1-D model approximates the mass fraction of water in liquid phase, $c_w^l$ equal to unity (*Bhatnagar et al*., 2007). In the 2-D model, volume change due to methane is not assumed to be zero and thus results in a small change in fluid volume when methane comes out of solution to form hydrates. Therefore, the volumetric net fluid flux, ($Pe_1 + Pe_2$) shows a slight deviation from the 1-D results with increasing external flux.

# Chapter 6

# Effects of Lithologic Heterogeneity and Salinity on Gas Hydrate Distribution

## 6.1 Effect of Vertical Fracture Systems

*† Fractures are common in geologic settings such as the Hydrate Ridge in the Cascadia Margin varying over different length scales (*Trehu et al*., 2004; *Weinberger and Brown*, 2006). Previous studies have hypothesized on the significance of fracture networks in gas hydrate systems, and their impact was quantified by implementing a vertical fracture system of higher permeability in the gas hydrate accumulation model (Figure 6.1). Vertical fracture systems are modeled since the time they are introduced ($\tilde{t} = 0$) in the system and gas hydrate and free gas accumulation are tracked over time. Simulations are completed with a vertical fracture system 100 times more permeable than the surrounding sediment (i.e., $N_{sc} = 10^2$ for sediment and $10^4$ for the vertical fracture system).

---

*Chatterjee S., G. Gu, G. Bhatnagar, W.G. Chapman, B. Dugan, G.R. Dickens, G.J. Hirasaki (2011), Effects of heterogeneous lithology and focused fluid flow on gas hydrate distribution in marine sediments, *Proceedings of the 7th International Conference on Gas Hydrates* (ICGH), Edinburgh, Scotland, United Kingdom, July 17-21, 2011

†Chatterjee S., G. Bhatnagar, B. Dugan, G.R. Dickens, W.G. Chapman, and G.J. Hirasaki (2012), Lithologic heterogeneity and focused fluid flow governing gas hydrate distribution in marine sediments, *to be submitted*

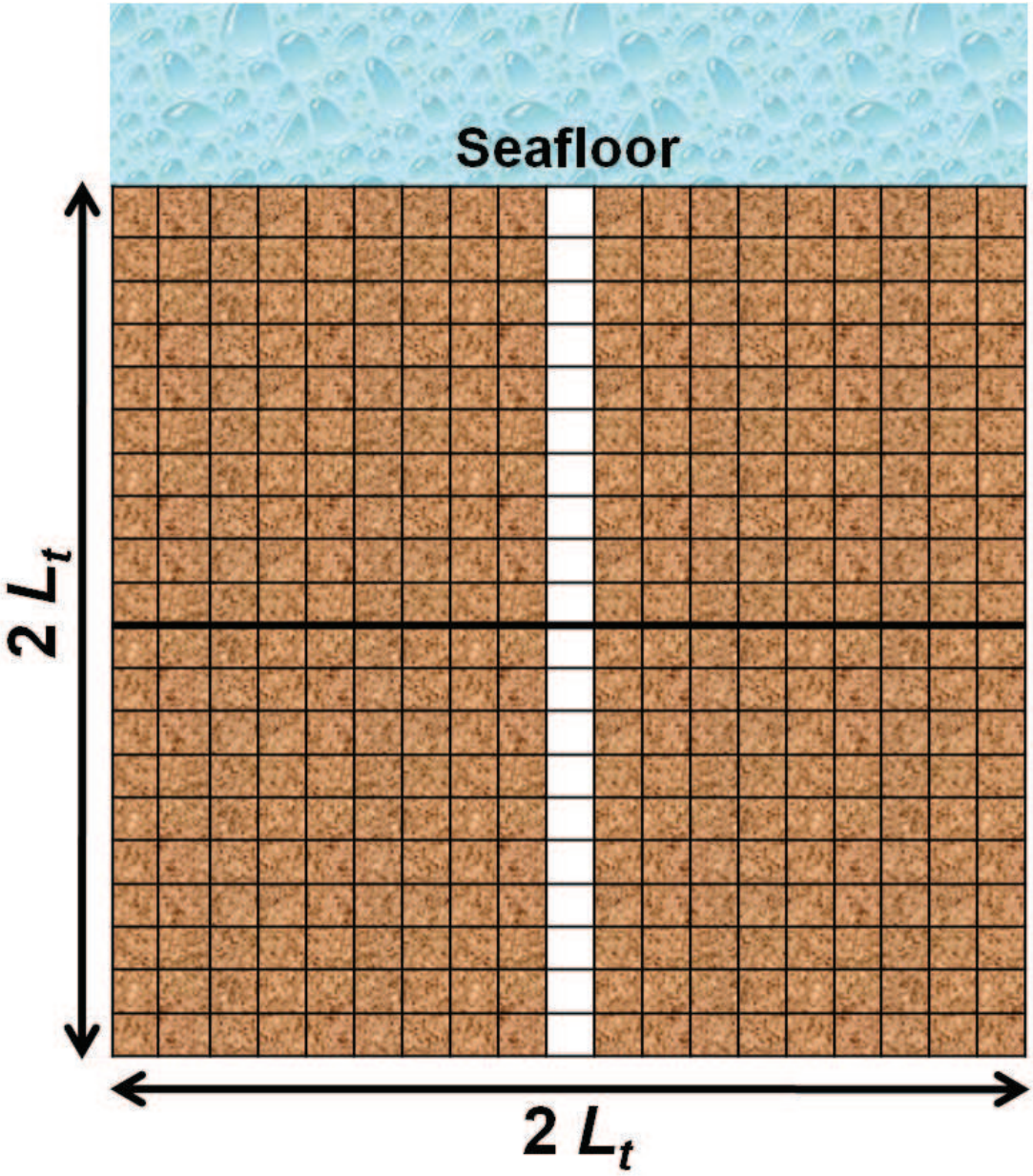


Figure 6.1 : Schematic showing permeability map representing a vertical fracture system (white). The fracture system is 100 times more permeable than the surrounding formation. The aspect ratio for the sediment formation is 1:1.

Simulations with a vertical fracture network, show focused fluid flow resulting in higher hydrate and free gas saturation within the high permeability fracture system compared to the surrounding lower permeability sediment. First, a case with isotropic permeability was considered. Steady state peak hydrate saturation within the fracture system is $\sim$26%, while that in the surrounding low permeability sediment matrix is $\sim$10% (Figure 6.2). Steady state free gas shows peak saturation of 29% within the fracture column at the base of the domain.

A second case is simulated with a specified fluid flux from external sources at depth representing a geologic model with thermogenic methane in deeper strata. Higher hydrate and free gas saturation is predicted due to increased fluid flux and greater methane input into the system from deeper sources. Simulations show higher hydrate and free gas saturation within the high permeability fracture system (Figure 6.3) as compared to the simulation case with biogenic in situ methane only (Figure 6.2). Peak hydrate and free gas saturations within the fracture system are 48% and 42%, respectively.

These higher saturations were achieved by specifying external flux ($Pe_2 = -2$), throughout the model domain. It is shown that increased fluid flux from external sources results in higher fluid focusing which produces higher hydrate and free gas accumulations within the fracture system. As the fluid flux is increased, more dissolved methane saturated water migrates into high permeability zones which result in concentrated deposits of hydrates and free gas. Using the correlation

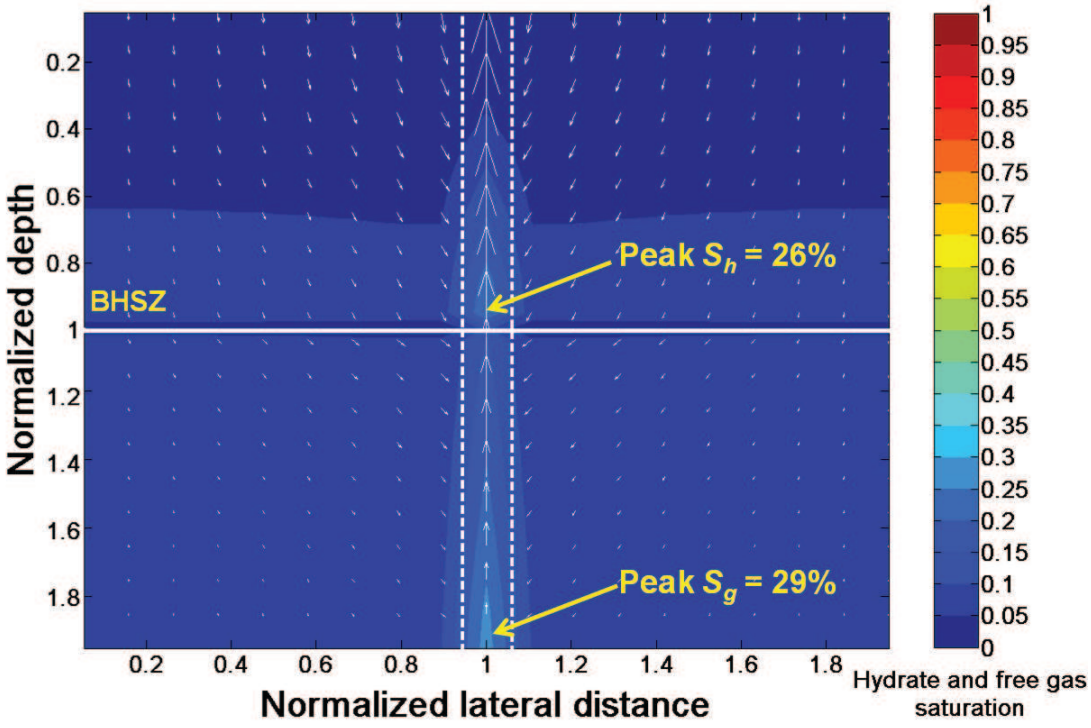


Figure 6.2 : Steady state gas hydrate and free gas saturation contours for isotropic system ($k_v/k_h = 1$) with biogenic in situ source ($Pe_2 = 0$) and a vertical fracture system. The location of the fracture is shown by a set of white, vertical dashed lines. A vector field plot shown by white arrows represents the focused fluid flow. The fluid flow within the sediment formation is in the downward direction because it is plotted relative to the seafloor. The effect of the fracture in focusing flow is clearly illustrated through enhanced hydrate and free gas saturations within the high permeability conduit. The following parameters were used for this simulation: $Pe_1 = 0.1$, $Pe_2 = 0$, $Da = 10$, $\beta = 6$, $\tilde{c}_{m,ext} = 0$, $\gamma = 9$, $\eta = 6/9$, $k_v/k_h = 1$, $N'_{t\phi} = 1.485$ and $N_{sc} = 10^2$.

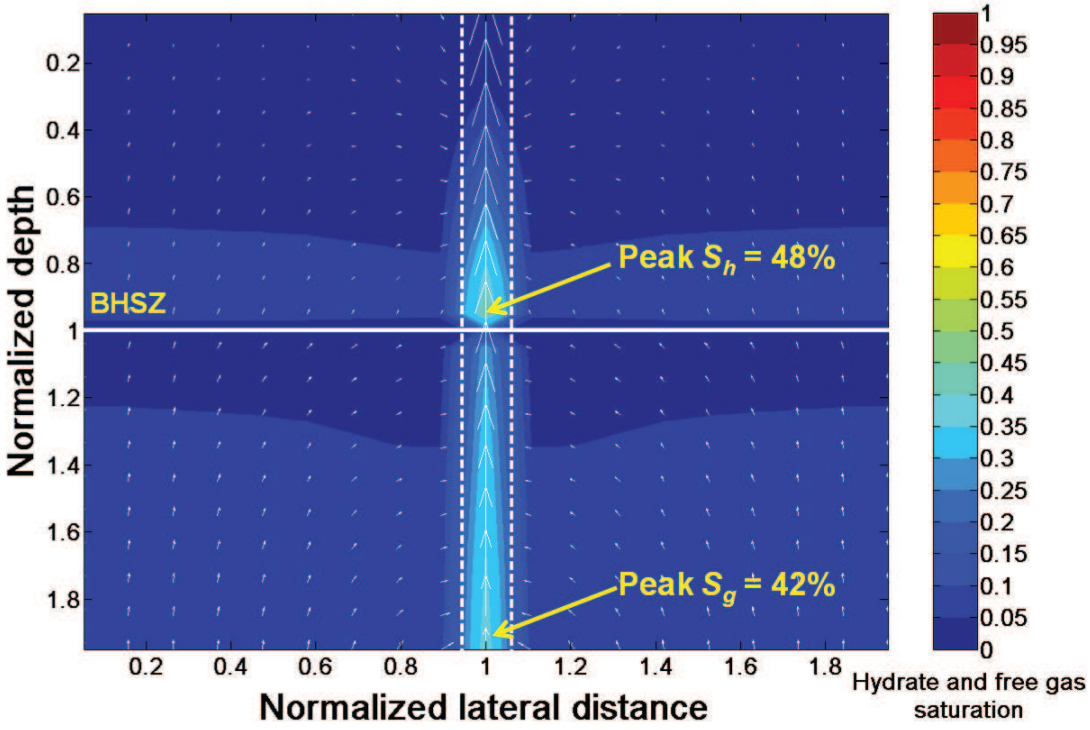


Figure 6.3 : Steady state gas hydrate and free gas saturation contours with a vertical fracture system, deep methane source, specified external fluid flux at the lower boundary ($Pe_2 = -2$), and all other parameters same as in Figure 6.2. The following parameters were used for this simulation: $Pe_1 = 0.1$, $Pe_2 = -2$, $Da = 10$, $\beta = 6$, $\tilde{c}_{m,ext} = 0.897$, $\gamma = 9$, $\eta = 6/9$, $k_v/k_h = 1$, $N'_{t\phi} = 1.485$ and $N_{sc} = 10^2$.

shown above (Figure 5.2), it is expected that more hydrate and free gas will accumulate if higher flux is specified.

## 6.2 Effect of Mesh Refining

The general model framework was set up with coarse grid spacing (nz = 20, nx = 19) to enable faster computations. However, to test and illustrate the effect of mesh refining, finer grid spacing was chosen for the lateral dimension for an example simulation. The horizontal grid was refined three times while maintaining a coarse grid spacing for the vertical domain. Although the grid spacing was refined, the spatial dimensions were kept unchanged. Therefore, the fracture network system was represented by three grid columns (as opposed to a single grid column in the above simulations).

Simulations were completed using this refined grid spacing and steady state solutions were obtained (Figure 6.4). The peak and average saturations for gas hydrate and free gas were identical in the three grid blocks comprising the high permeability fracture system. This result validates that our numerical model is independent on mesh size and the saturations within the high permeability conduit appear as broad peaks as compared to a sharp peak in our coarse grid simulations. However, due to limitation of computational time, the subsequent simulations will be restricted to coarser grid size to elucidate the primary controls on the amount and distribution of hydrate accumulation within these high permeability conduits.

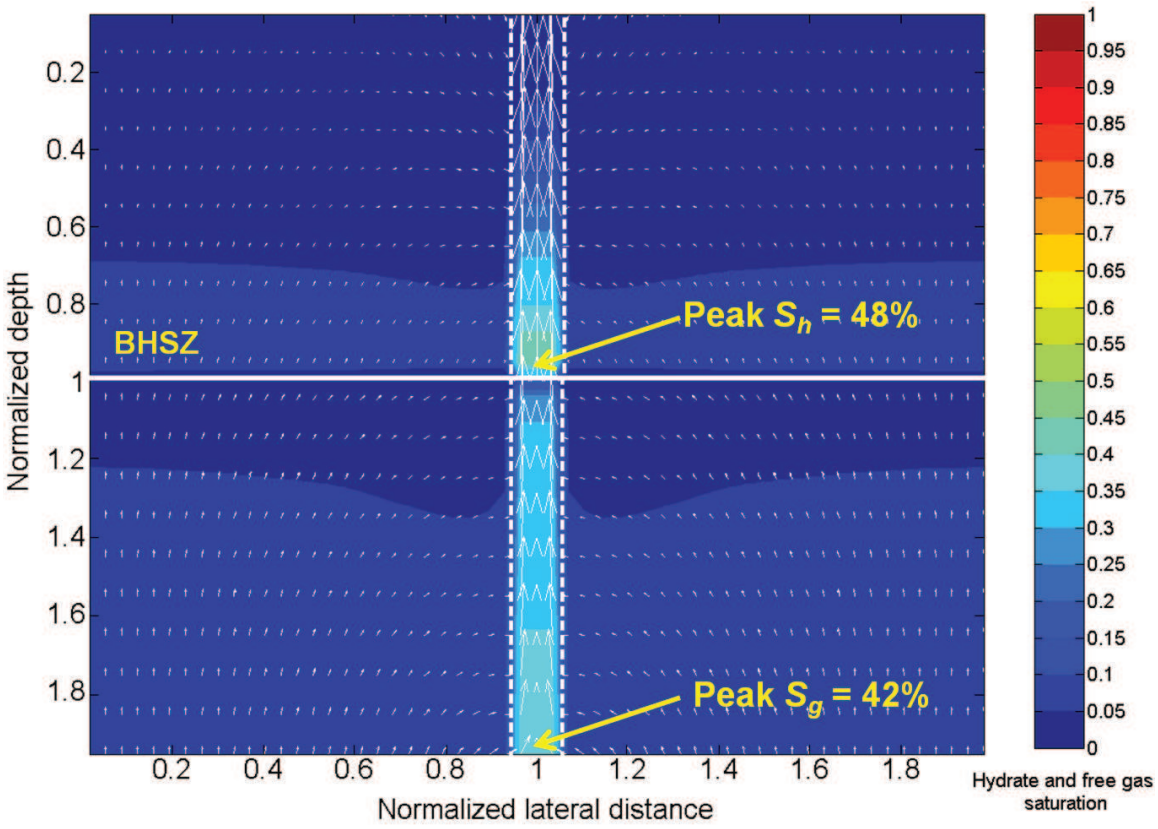


Figure 6.4 : Steady state gas hydrate and free gas saturation contours with a vertical fracture system (3 central grid columns), deep methane source, specified external fluid flux at the lower boundary, and all other parameters same as in Figure 6.3. The grid spacing used in the lateral dimension was refined 3 times keeping the spatial dimensions and vertical grid spacing the same as in Figure 6.3.

## 6.3 Effect of Permeability Anisotropy

Natural systems are anisotropic, with the ratio of vertical to horizontal permeability ($k_v/k_h$) less than unity. In such systems, greater horizontal permeability would focus more fluids from neighboring regions to the high permeability conduits by lateral migration. Anisotropic cases with a lower $k_v/k_h$ ratio (order of $10^{-2}$) are expected to show relatively higher hydrate saturations within the high permeability conduits as compared to isotropic cases (Figure 6.5). Higher horizontal permeability would charge more fluids into these high permeability conduits as a result of flow focusing. Simulations show peak hydrate and gas saturations are 53% and 40% respectively (Figure 6.5). Increased horizontal permeability results in more fluid flux towards the fracture system even from sediment formation farther away from the fracture column.

Key findings of this thesis characterize the impact that high permeability vertical fractures have on gas hydrate and free gas distribution by focusing fluid flow along these fracture systems in the presence biogenic and/or thermogenic methane sources. These models generally quantify the effects of flow focusing.

## 6.4 Local Flux within High Permeability Zones

The localized, focused fluid flux is computed and the local flux ($Pe_{local}$) is related to the average hydrate saturation within the high permeability conduits in the GHSZ (Figure 6.6). The results follow the same correlation established between net

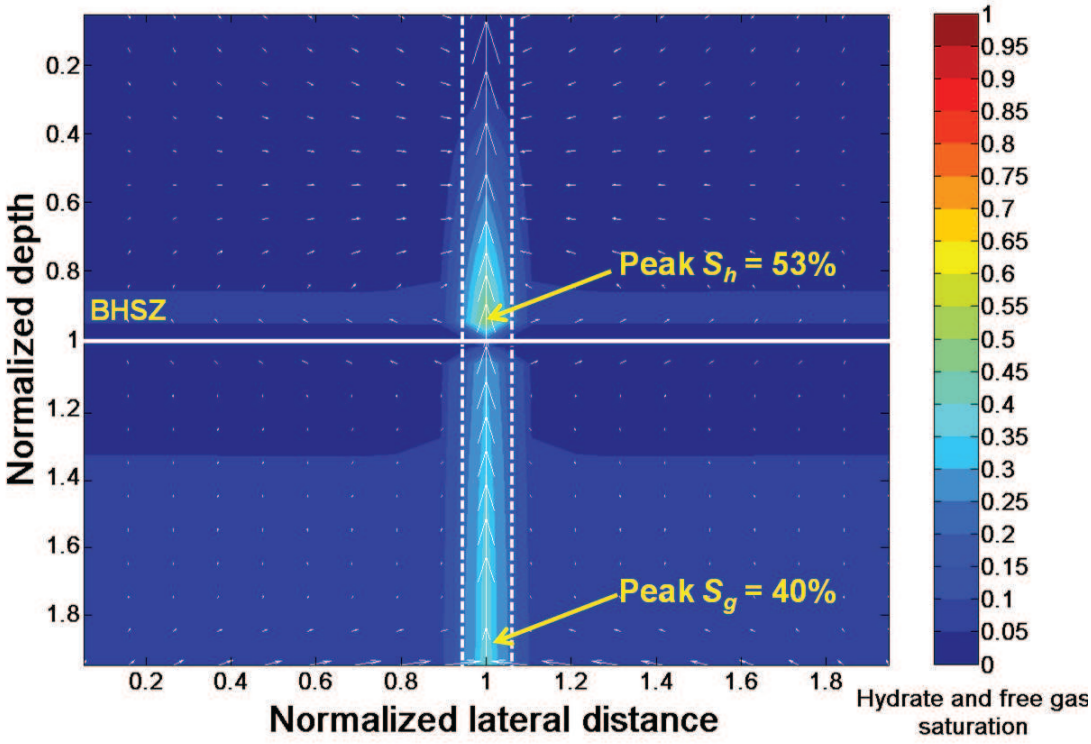


Figure 6.5 : Steady state gas hydrate and free gas saturation contours for an anisotropic system ($k_v/k_h = 10^{-2}$) with a vertical fracture system and all other parameters same as in Figure 6.3. The following parameters were used for this simulation: $Pe_1 = 0.1$, $Pe_2 = -2$, $Da = 10$, $\beta = 6$, $\tilde{c}_{m,ext} = 0.897$, $\gamma = 9$, $\eta = 6/9$, $k_v/k_h = 10^{-2}$, $N'_{t\phi} = 1.485$ and $N_{sc} = 10^2$.

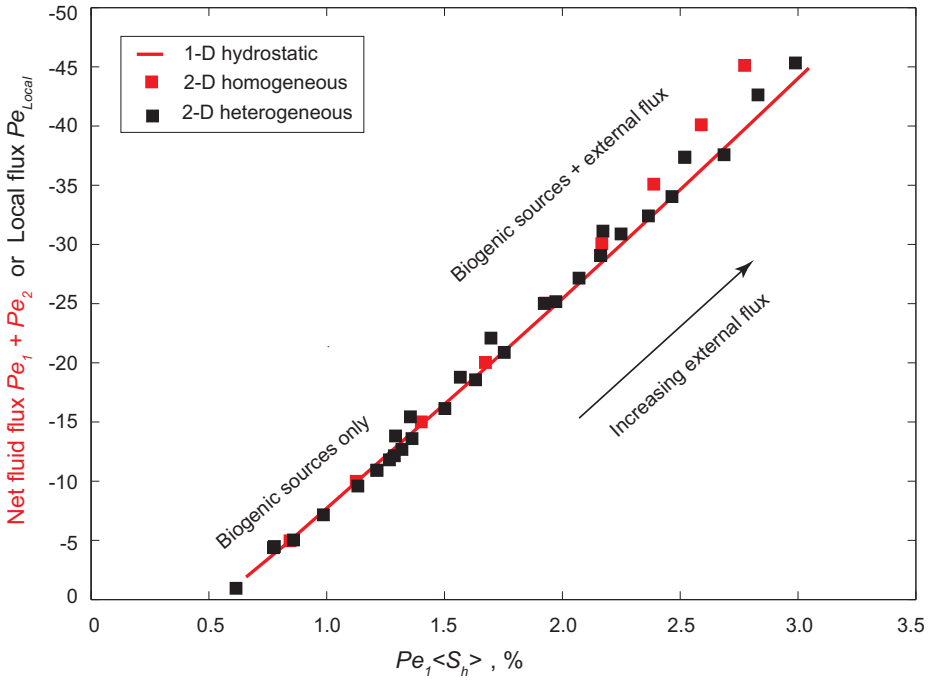


Figure 6.6 : Steady state average gas hydrate flux, $Pe_1\langle S_h\rangle$ and local fluid flux, $Pe_{local}$ (black squares).

fluid flux and average hydrate saturation in 1-D systems (Figure 5.2). For lower values of $Da(< 10)$, methane generated in the system is not enough for hydrate accumulation even with high local flux focused in the high permeability zones. The gas hydrate and free gas saturations in these lithologically heterogeneous systems can be characterized by the local Peclet number ($Pe_{local}$; localized, focused, vertical, advective fluid flux relative to diffusion). This characterization is consistent with the net Peclet number ($Pe_1$ + $Pe_2$) characterization in 1-D homogeneous systems. This suggests that local hydrate and free gas saturations in lithologically complex systems can be characterized by basic parameters (local flux and diffusivity).

## 6.5 Effect of Permeability Contrast

Heterogeneous models have shown that higher permeability conduits increase the ability to capture methane thereby enhancing saturations of gas hydrate and free gas (Figure 6.7). The above simulations show vertical permeable conduits which are 100 times more permeable than the surrounding matrix. Higher permeability contrast (of the order $10^3$ - $10^6$) are more representative of natural marine sediment with fractures and sand beds. Sensitivity tests are performed by varying the permeability contrasts ($k_{fracture}/k_{shale}$) from 2 to 1000 (Figure 6.7). Large permeability contrast ($k_{fracture}/k_{shale}$) enables greater fluid focusing and leads to greater gas hydrate and free gas accumulation within these conduits. This may explain elevated saturations in high flux conduits like pipes, vents, and dipping reservoirs in advective systems.

## 6.6 Effect of Horizontal High Permeability Layers

Heterogeneity is now modeled as a horizontal layer parallel to the seafloor. This horizontal layer is buried and its downward movement is tracked over long timescales. However, it is acknowledged that fluids need a conduit to flow from depth to the seafloor. Therefore, the formation is short-circuited with two vertical fracture systems at the two ends of the simulation domain. This allows fluids to flow from depth through the left vertical fracture system and then across the simulation domain through the horizontal layer ultimately towards the seafloor

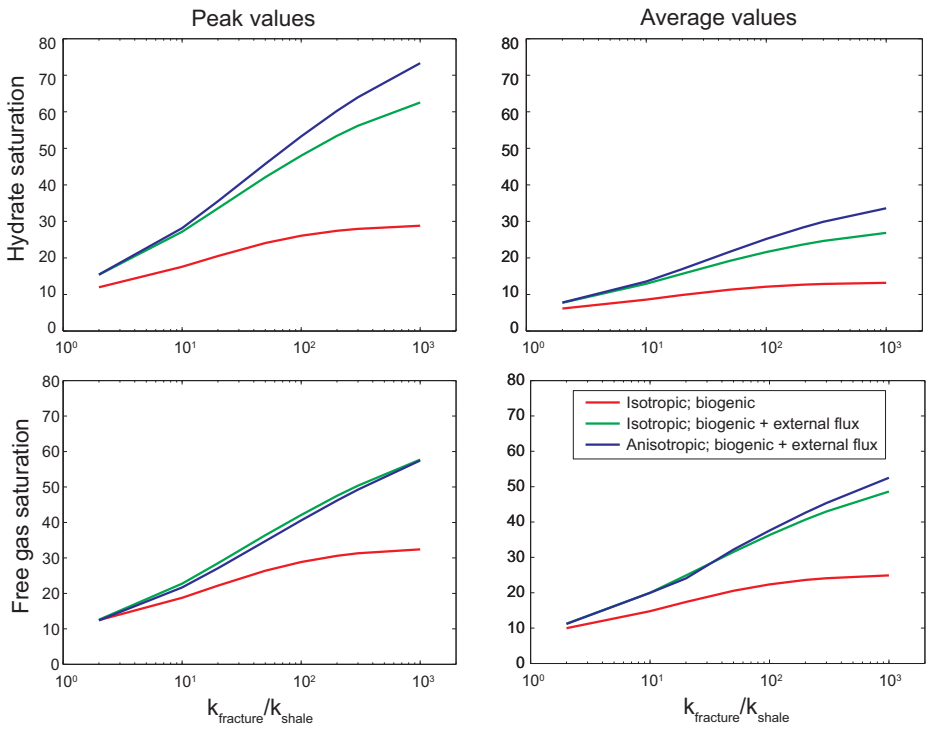


Figure 6.7 : Model results showing the importance of permeability contrasts and permeability anisotropy on the accumulation and saturation of gas hydrate and free gas. As permeability contrast between a fracture system (or sand) and the shale increases ($k_{fracture}$ or $k_{sand} >> k_{shale}$) the hydrate and free gas saturations in the permeable conduit increases. As anisotropy decreases ($k_v/k_h$) in the shale, the saturations also increase.

through the right vertical fracture system (Figure 6.8). These lithologic structures are geologically unrealistic, however, they provide a clear understanding of the system to assess the dependence of dip angle of these permeable layers.

Steady state simulations are run with the same parameter set used in Figure 6.3, while the horizontal layer and vertical fractures are buried down through geologic time. The steady state simulations show that high focused fluid flow through the permeable layers from depth to the horizontal layer, then across the simulation domain and then towards the seafloor (Figure 6.9). The fluid flow in these horizontal conduits is mostly horizontal. However, unlike the vertical fracture systems extending through the GHSZ, gas hydrate and free gas do not accumulate along the horizontal layer. Even though high fluid flux gets focused and flows through the permeable conduit, it does not result in elevated hydrate saturation. Therefore, the localized fluid flux within these systems cannot be used to evaluate local gas hydrate saturation and distribution. Thus, it is determined that these horizontal fluid flux components do not influence hydrate precipitation. Therefore, it is shown that the vertical flux in these heterogeneous relative to the methane diffusion is what drives these elevated hydrate saturations in these lithologically complex systems.

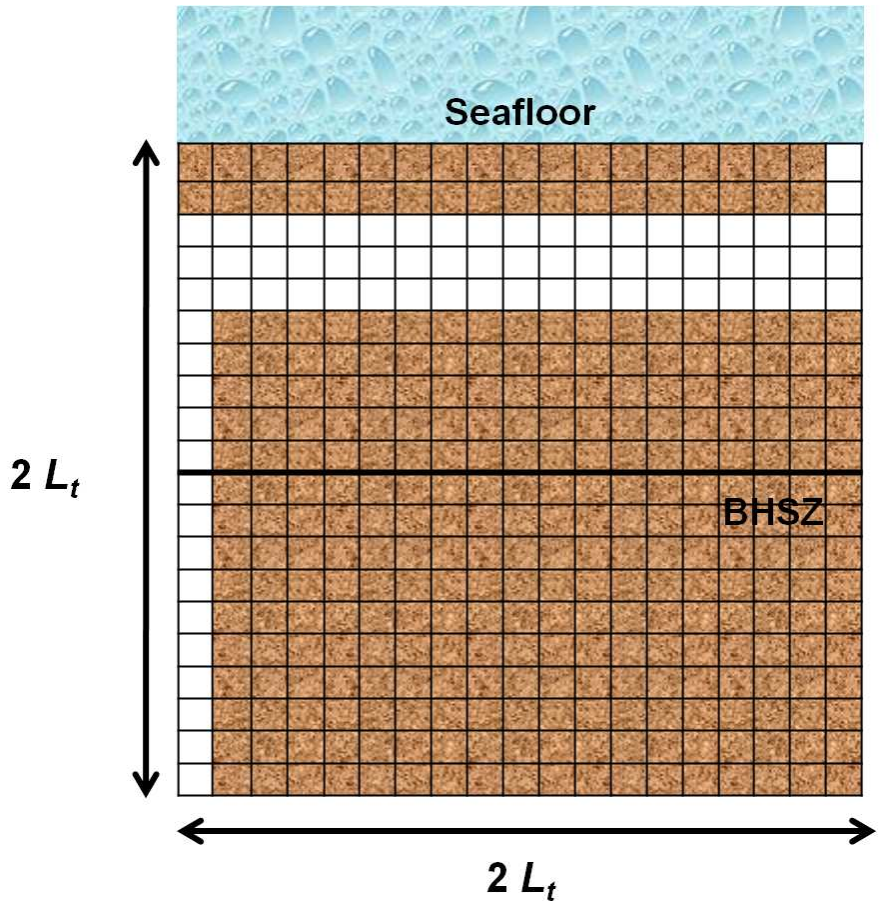


Figure 6.8 : Schematic showing initial permeability map representing high permeability horizontal sand layer deposited between two low permeability sediment layers. The horizontal layer has two high permeability vertical fluid conduits on either ends to channel the fluid flow from depth to the seafloor. The high permeability layer (white) is 100 times more permeable than the surrounding formation.

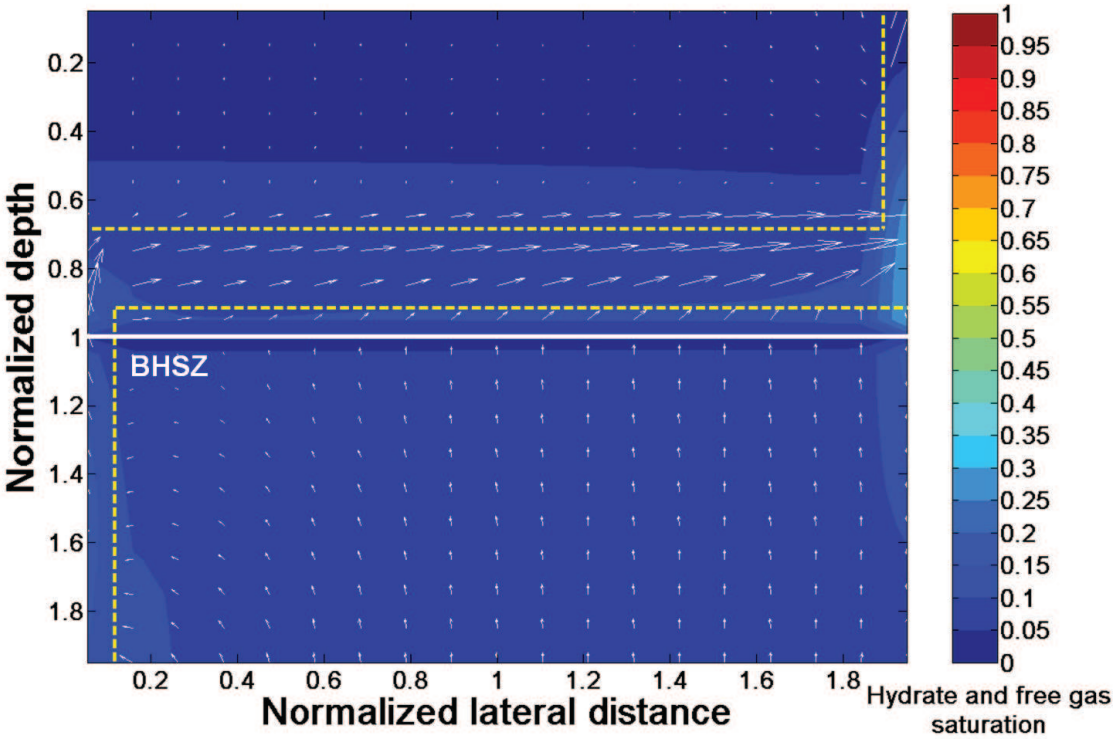


Figure 6.9 : Steady state gas hydrate and free gas saturation contours for a system with high permeability horizontal sand bed flanked between two vertical fracture systems on either ends. The position of the high permeability layer (100 times more permeable than surrounding formation) is delineated by a set of yellow dashed lines. Parameters used for this simulation are same as used in Figure 6.3.

## 6.7 Effect of Dip Angle of High Permeability Layers

A steady state, 1-D analytical theory is derived to illustrate the effect of dip angle of the high permeability layer. The mathematical model shows that the inclination of the permeable conduit (to the vertical axis) dictates hydrate saturation and distribution (Appendix D). The net fluid flux ($Pe_1 + Pe_2$) is related to the average hydrate flux ($Pe_1\langle S_h \rangle$) within a fluid conduit inclined in any orientation to the vertical (not shown here). This generates a series of plots for a range of dip angle values relating the net fluid flux and the average hydrate flux. However, this does not generalize results as these plots are dependent on the dip angle. In order to eliminate the dependence of dip angle, the model is further extended to collapse all the above information over a wide range of configurations into one single contour plot (Figure 6.10). Interestingly, there is no longer any dependence on the dip angle, thereby reducing the parameter space. All the points collapse on a single line for a range of configurations ($\theta$). These plots can be used to compute the average hydrate saturation given the fluid flux and the methane solubility gradient is known for marine hydrate systems in any configuration. It is shown that the vertical fluid flux is what dictates hydrate saturation and accumulation as opposed to the net fluid flux for a case where the conduit is inclined at an angle, to the vertical. These results can be extended to any geologic setting, by adapting the site-specific parameters (Figure 6.10).

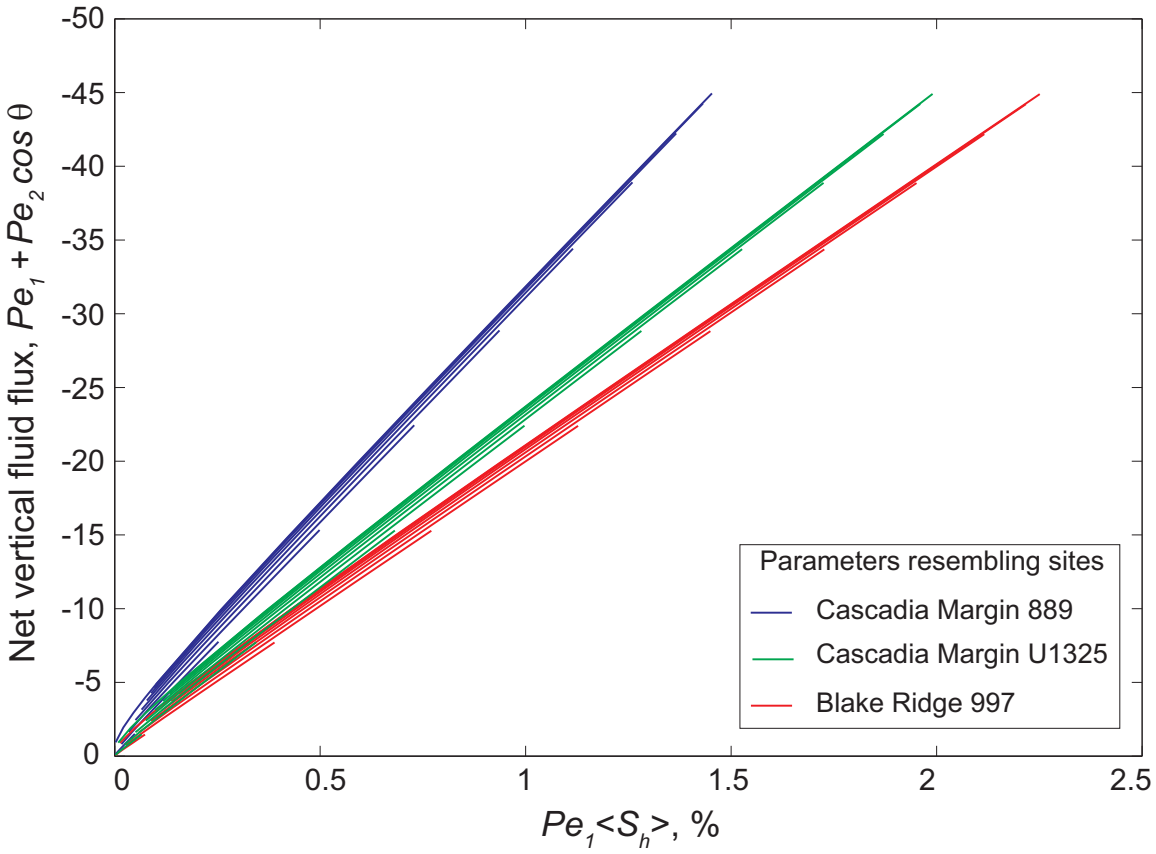


Figure 6.10 : Average hydrate flux, $Pe_1\langle S_h\rangle$ is related to the net vertical fluid flux for marine hydrate systems inclined in any angle to the vertical axis. Systems with vertical fractures correspond to 0°, whereas horizontal conduits correspond to 90°. As orientation changes from vertical to horizontal, the saturation decreases, even though high flux flows through these systems. This would imply that the vertical fluid flux relative to methane diffusion is what drives hydrate saturation and accumulation in these marine hydrate systems. Similarly, this can be extended to 2-D systems where localized vertical fluid flux relative to methane diffusion can be correlated to localized average hydrate saturation in systems with complex lithology. These results are adapted for site-specific transport and geologic parameters that resemble three classic hydrate settings.

## 6.8 Effect of Free Gas Migration into the GHSZ

Focusing of methane-charged liquid (water) enhances hydrate and free gas saturations within the high permeability zones. However, free gas can also migrate vertically and laterally if the critical gas saturation is exceeded. To simulate such migration, critical gas saturation ($S_{gr}$) is set to 5% and free gas exceeding this critical value is free to migrate. Free gas migrates upwards due to buoyancy and gets sealed by the low permeability hydrate layer at the base of the GHSZ. Hydrate formation at the base of the GHSZ causes an increase in the capillary entry pressure and creates a hindrance for free gas to enter the GHSZ from below. This results in accumulation of free gas beneath the GHSZ into a connected gas column.

### 6.8.1 Vertical Fracture Systems

Simulations show free gas accumulation below the base of the GHSZ (Figure 6.11). A long gas column is formed before the gas pressure exceeds the capillary entry pressure and gas migrates into the GHSZ. Free gas converts to hydrate immediately at the base of the GHSZ giving rise to a spike in hydrate saturation. Constant salinity is assumed hence phase equilibrium is unaffected even when free gas migrates into the GHSZ. The high hydrate saturation in the fracture zone causes a permeability reduction resulting in lateral fluid migration beneath the GHSZ. High hydrate saturation also restricts further free gas invasion into the

GHSZ. Free gas then migrates laterally from the high permeability fracture system to the neighboring sediment below the base of the GHSZ. Peak hydrate and free gas saturation reach 75% and 62% right above and below the base of the GHSZ within the fracture system. At this enhanced saturation, free gas is mobile and migrates laterally, causing sediment near the fracture to also have relatively higher saturations.

The length of a connected gas column has been shown to be dependent on the dimensionless group $N_{sc}$ (*Bhatnagar et al*., 2008b). Lower values of $N_{sc}$ (lower permeability and/or higher sedimentation rate) result in development of higher overpressure in the system, which further results in thicker gas columns and increased gas pressure at the base of the GHSZ close to the lithostatic stress (e.g., *Flemings et al*., 2003; *Hornbach et al*., 2004). Fractures tend to open up at this point (*Daigle and Dugan*, 2010a). This fracturing process is not modeled in any of these simulations, and the simulations are terminated as soon as gas pressure equals total vertical stress.

### 6.8.2 Dipping Sand Layers

Lithologic heterogeneity is modeled in another configuration (non-vertical), in which dipping sand beds bounded by low permeability shale is illustrated. To model a sand layer, a high permeability sand layer is included at a given dip angle ($\sim 3^{o}$) within the sediment (Figure 6.12) and buried through geologic time. The downward

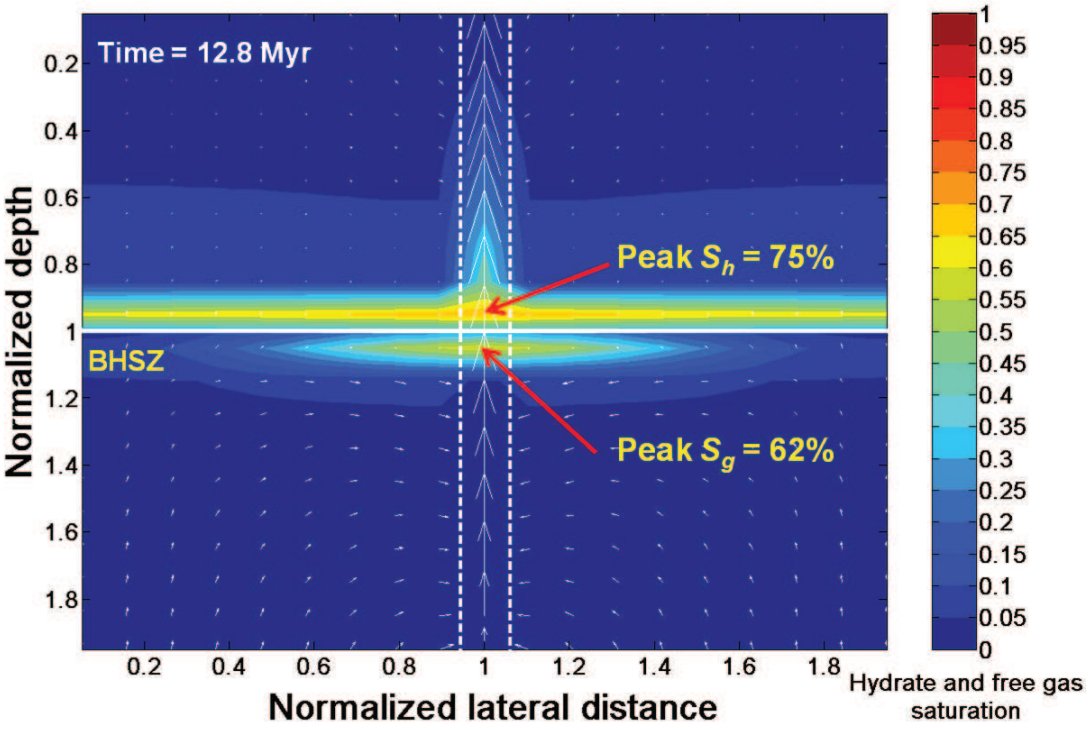


Figure 6.11 : Steady state gas hydrate and free gas saturation contours for an isotropic system with a vertical fracture system, mobile gas ($S_{gr}$ = 5%) and all other parameters same as in Figure 6.3. The following parameters were used for this simulation: $Pe_1 = 0.1$, $Pe_2 = -2$, $Da = 10$, $\beta = 6$, $\tilde{c}_{m,ext} = 0.897$, $\gamma = 9$, $\eta = 6/9$, $k_v/k_h = 1$, $N'_{t\phi} = 1.485$ and $N_{sc} = 10^2$.

movement of this sand layer and the corresponding transient hydrate and free gas evolution are simulated. The sand layer is assigned an absolute permeability 100 times greater than the surrounding shale. Sediment compacts with burial ($N_{sc} = 10^2$ for shale and $10^4$ for sand layers). The seafloor and transport parameters are same as in the simulations with vertical fracture network except $Da = 1$. During burial, absolute permeability of any grid block can be computed by interpolation and therefore, interface between zones of different permeabilities are recorded over time. The interface position is used to compute the horizontal and vertical permeabilities and track the location of the sediment over time.

Systems with dipping sand layers show localized, enhanced concentrations of hydrate and free gas within the high permeability sand layers (Figure 6.13). Free gas is focused within the sand layer. Steady state peak hydrate saturation within the sand layer is about 59%, significantly higher than the 43% peak hydrate saturation in the low permeability sediment within the GHSZ. Peak free gas saturation is 38% within the sand layer just below the GHSZ, and similar to fracture network case (Figure 6.11), free gas migrates laterally into the low permeability sediment around the sand layer. Thus, presence of higher permeability sand layer leads to relatively higher fluid focusing and hydrate saturation within the GHSZ. These results elucidate that lithology plays a significant role in accumulating gas hydrate and free gas in heterogeneous sediment in most natural systems. These generalized models can be adapted to specific field examples such as the Walker

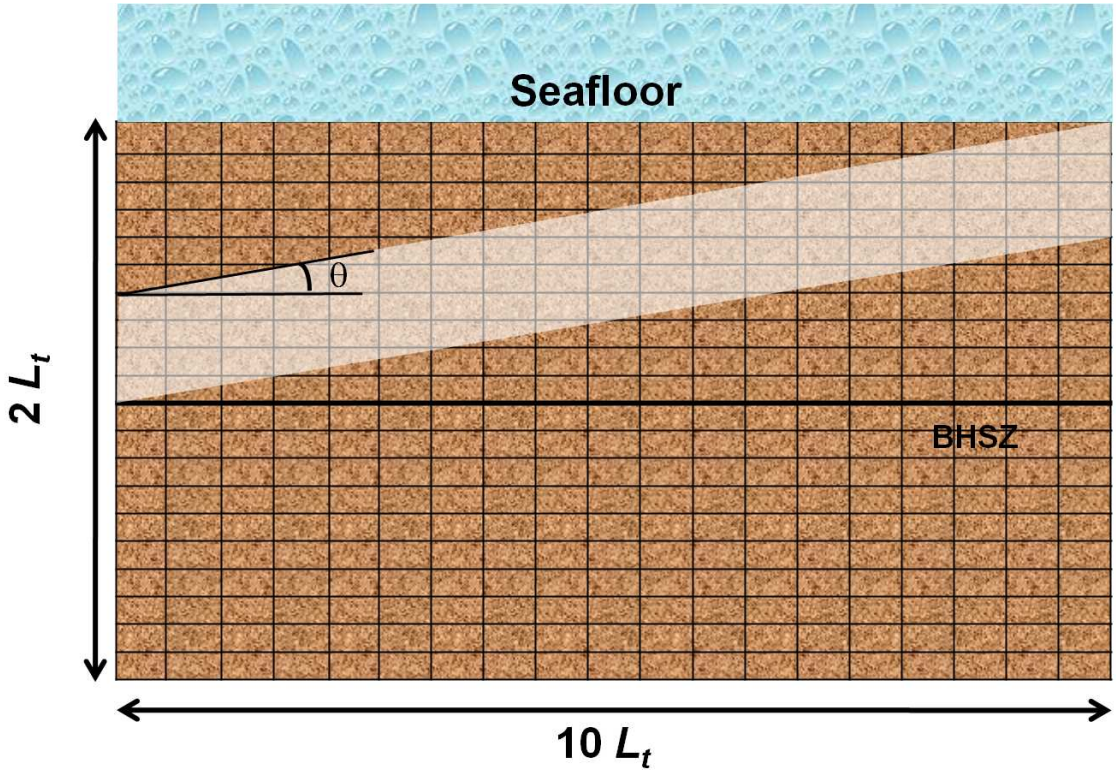


Figure 6.12 : Schematic showing initial permeability map representing high permeability sand layer (lighter shade) deposited between two low permeability sediment layers. The sand layer is 100 times more permeable than the surrounding formation. A 5:2 vertical exaggeration (VE) is used to plot the sediment space.

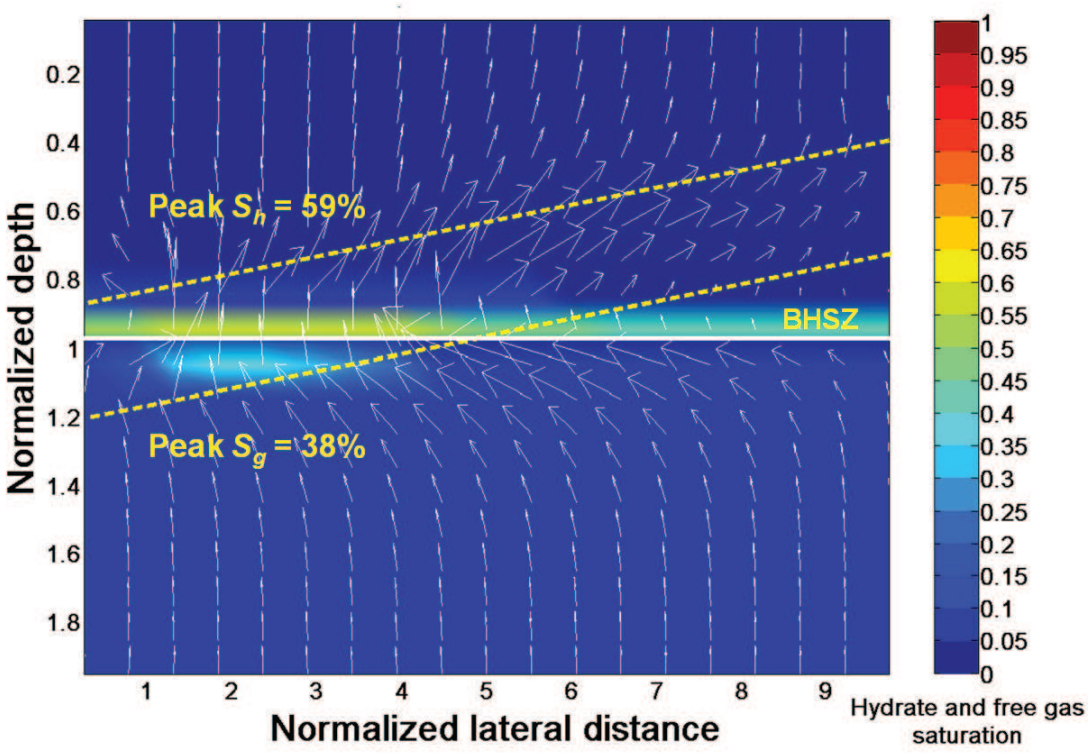


Figure 6.13 : Steady state gas hydrate and free gas saturation contours for a system with high permeability dipping sand bed between two anisotropic ($k_v/k_h = 10^{-2}$) shale beds. The position of the sand layer is depicted by the set of yellow dashed lines. Vertical exaggeration of 5:1 is used and the physical domain for normalized depth and lateral distance are [0, 2] and [0, 10], respectively. The following parameters were used for this simulation: $Pe_1 = 0.1$, $Pe_2 = -2$, $Da = 1$, $\beta = 6$, $\tilde{c}_{m,ext} = 0.897$, $\gamma = 9$, $\eta = 6/9$, $k_v/k_h = 10^{-2}$ (in shales), $N'_{t\phi} = 1.485$ and $N_{sc} = 10^2$.

Ridge in the Gulf of Mexico to explain the enhanced saturations (60% - 80%) in the dipping sand layers.

## 6.9 Effect of Hydrate Formation and Dissociation on Pore Water Salinity

Gas hydrate formation and its dissociation to free gas alters the pore water salinity, which in turn affects the phase equilibrium of the system (e.g., *Zatsepina and Buffett*, 1998; *Egeberg and Dickens*, 1999; *Milkov et al*., 2004; *Liu and Flemings*, 2006). Moreover, high gas flux typical of specific sites have dominant salinity anomalies caused due to enormous hydrate formation (*Milkov et al*., 2004; *Liu and Flemings*, 2006, 2007). The salinity effects had been assumed to be negligible in the previous 1-D modeling (e.g., *Davie and Buffett*, 2001, 2003a; *Bhatnagar et al*., 2007) since salt ($NaCl$, or equivalently, $Cl^-$) mass balance was not coupled with the phase equilibrium thermodynamics. In the 2-D model developed above, salinity changes have been neglected as well. However, if simulations with mobile free gas discussed above in Figures 6.11 and 6.13 are investigated, it is realized that free gas can only invade the GHSZ until the first grid block. As soon as free gas invades the GHSZ, the $CH_4$ phase changes from free gas to hydrate due to thermodynamic equilibrium. This is not true in many geologic settings where free gas is observed to independently exist near the seafloor (*Trehu et al*., 2003; *Milkov et al*., 2004). Recently, several papers have shown coexistence of hydrate and free

gas phases of $CH_4$ within the GHSZ due to salinity effects in 1-D (e.g., *Liu and Flemings*, 2007; *Daigle and Dugan*,2010b).

A 2-D chloride mass balance is expressed in Equation 5.5 and rewritten in its dimensionless form in Equation 5.64, normalized using the scaling scheme discussed in *Bhatnagar et al*. (2007). The chloride balance is incorporated and coupled with the benchmarked 2-D model developed in this study. During hydrate formation, the chlorides are released by the pore fluids when fresh water forms the cage structure during hydrate formation. This leads to local elevation of salinity where hydrates are formed. By contrast, the pore fluids become less saline due to local freshening during hydrate dissociation. The chloride concentrations are tracked in the model over space and time (same as the other dissolved constituents) as they move by advection and diffusion and the salinity is computed from these chloride profiles. The model is tested against the field data from Blake Ridge Site 997 where pore water chlorinity (and other geochemical datasets) exist. The hydrate and free gas peaks at 7% and 12% respectively (Figure 6.14). The modeled pore water chloride profile show a peak at depths corresponding to elevations hydrate saturation. The chloride profile is also computed assuming hydrate dissociation during core recovery and these resemble that measured at the site (Figure 6.14). Interestingly, the observed profiles match favorably for $Pe_2 = -1$, which is equivalent to upward fluid velocity values of 0.085 mm/yr at the seafloor. These upward fluid velocities resemble previously reported values of 0.08 mm/yr

(*Egeberg and Dickens*, 1999) and 0.097 mm/yr (*Frederick and Buffett*, 2011) near the seafloor.

## 6.10 Effect of Salinity on Phase Equilibrium and Methane Solubility

The pore water chlorinity is often related to the pore water activity and salinity. The effect of salinity variation on $CH_4$ hydrate stability conditions is related to the pore water activity (*Dickens and Quinby-Hunt*, 1994, 1997). In this study, the spatial $Cl^-$ profiles are used to track space- and time-dependent salinity during hydrate formation and dissociation processes. In the above 2-D model, $CH_4$ solubility curve is computed as a function of pressure and temperature, neglecting salinity effects. In this section, $CH_4$ solubility is coupled with salinity changes in the hydrate accumulation model. This leads to recomputing the phase equilibrium and $CH_4$ solubility with variations in salinity (Figure 6.15). This leads to a zone of three-phase coexistence, as opposed to a single point representing the triple-point of $CH_4$ in the salinity-independent model discussed above. In essence, this would enable coexistence of free gas and hydrate phase within the GHSZ over a depth horizon. This would allow free gas existence in the hydrate stability zone and lead to focused free gas and enhanced hydrate saturations. A three-phase flash calculation is required to be set up to calculate the fractions of different phases (aqueous, hydrate, and gas) present within a specific gridblock at each timestep

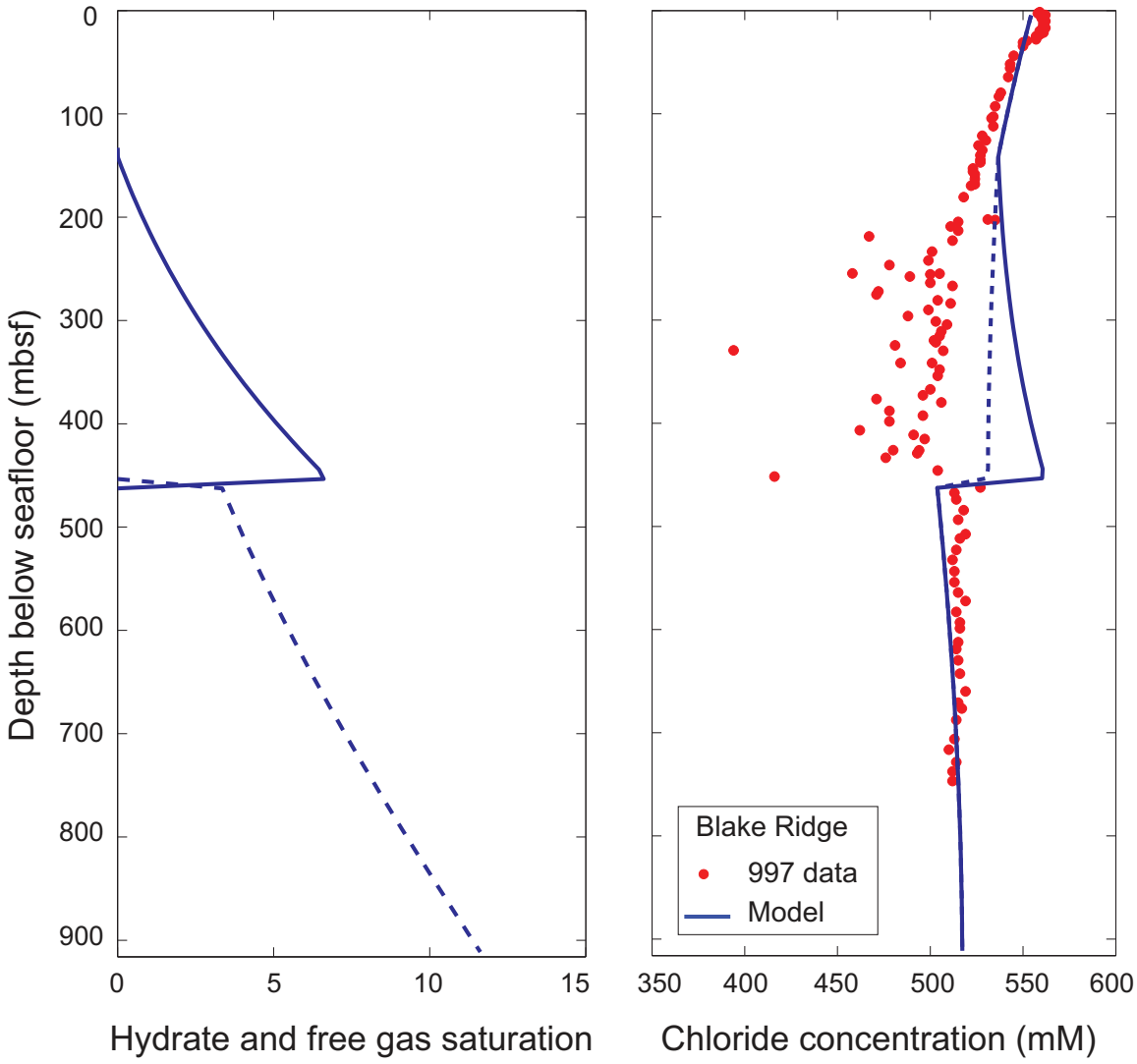


Figure 6.14 : Steady state gas hydrate and free gas saturation coupled with a chloride concentration profile at Blake Ridge Site 997. The bold line represents in situ chloride concentration profile before recovery and dashed lines represents concentration profiles due to hydrate dissociation during core recovery. The chloride anamoly at this site in the hydrate zone is due to hydrate dissociation as the cores were sampled. The chloride profile best matches the data with the following geologic and transport parameters: $Pe_1 = 0.1065$, $Pe_2 = -1$, $Da = 2.1$, $\beta = 4.16$, $\tilde{c}_{m,ext} = 0.9$, $c_{cl,ext} = 503$ mM, $c_{cl,o} = 559$ mM, $\gamma = 9$, $\eta = 6/9$, $N'_{t\phi} = 1.485$ and $N_{sc} = 10^4$.

depending on the thermodynamic conditions. The current 2-D multiphase transport model with the three-phase flash calculation should be capable of simulating conditions with three-phase co-existence within the GHSZ. This is not been modeled here and has evolved as one of the future work arising from this study.

## 6.11 Conclusions

A generalized 2-D model was developed to simulate gas hydrate and free gas accumulation in heterogeneous marine sediment. The model allows incorporation of lithologic heterogeneity and lateral fluid flow in the system. Focused fluid flow through a vertical fracture network or high permeability sand layers increases local hydrate accumulation and saturation.

Previous one-dimensional work, showed that the accumulated hydrate saturation was dependent on Peclet number, $Pe$, the ratio of advective flux to the diffusive flux of methane. In this 2-D work, it is shown that the localized, focused, vertical advective fluid flux relative to diffusion ($Pe_{local}$) determines the magnitude of hydrate and free gas saturation. Average local Peclet numbers is related to the average hydrate flux ($Pe_1\langle S_h\rangle$) within high permeability conduits, which compare favorably with the previous 1-D correlation.

Simulations with specified fluid flux and methane input from deeper sources, allows comparison of local methanogenesis and deeper methane sources on flow pathways and hydrate/free gas accumulation. Increased fluid flux from deeper

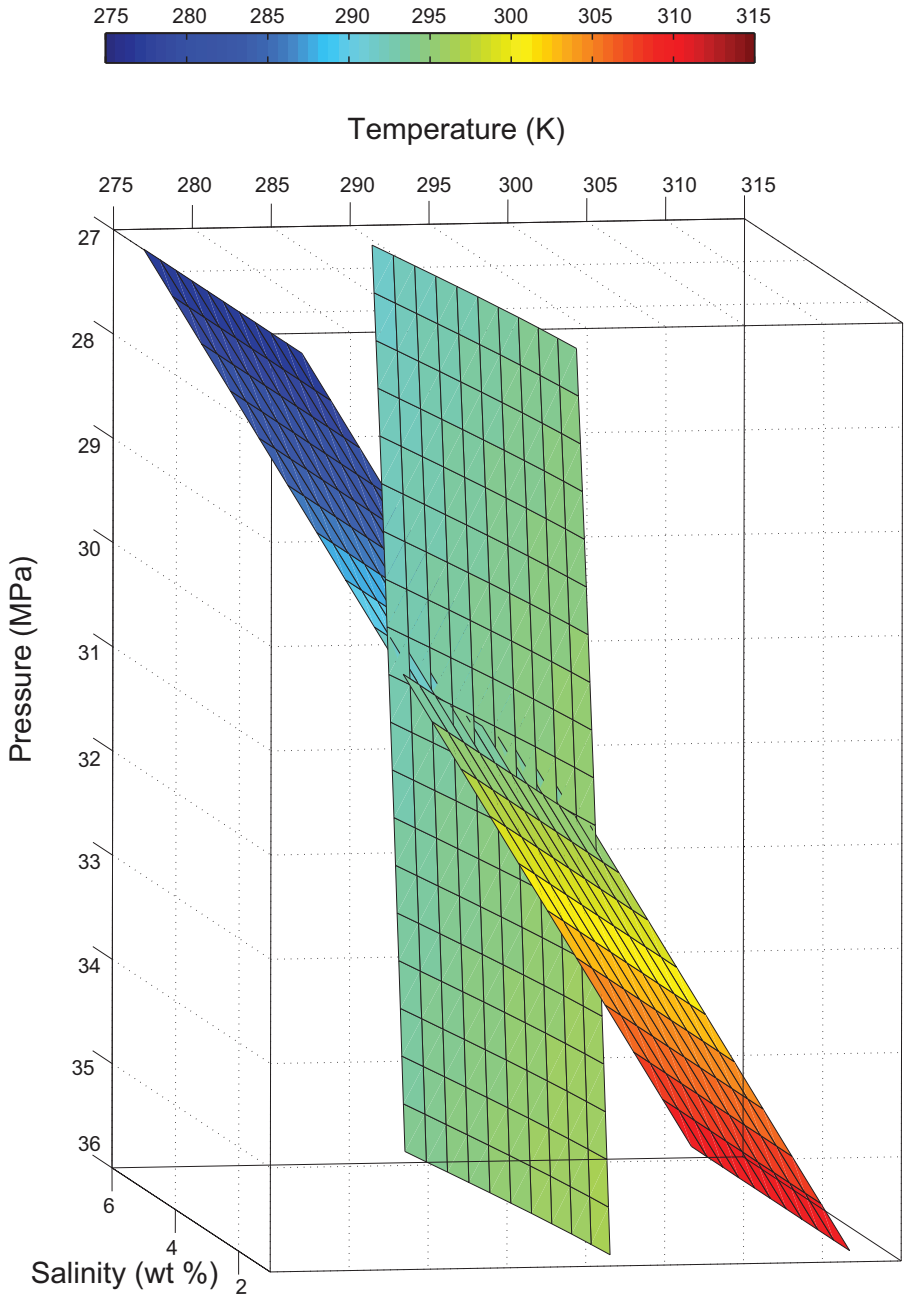


Figure 6.15 : Three-phase $CH_4$ hydrate-water-gas stability boundary contours for a wide range of temperature, pressure and salinity. The temperature profile along a geotherm intersects this 3-phase equilibrium curve over a zone, rather than a single point as in the constant salinity case described in (e.g., *Davie and Buffett*, 2001, 2003a; *Bhatnagar et al*., 2007). Salinity variations can be used to model the co-existence of hydrate and free gas phases within the GHSZ leading to enhanced saturations of hydrates and gas in systems dominated by flux from depth.

external sources results in increased concentrations of hydrate and free gas.

Permeability anisotropy, with a lower ratio of vertical to horizontal permeability show enhanced hydrate concentrations within the high permeability conduits because anisotropy focuses more methane-charged fluid into these conduits. The 2-D model results quantify how focused fluid flow through high permeability zones affects regional and local hydrate accumulation and saturation.

Currently, relatively simple systems with fracture systems and/or dipping sand layers are simulated, whereas realistic geologic settings are characterized by much more heterogeneous stratigraphy in terms of vertical fracture networks, multiple sand layers embedded within shale layers and fracture connectivity of sand layers with vertical fracture systems. These preliminary results, however, serve as a starting point and demonstrate that heterogeneity in natural gas hydrate systems is important for controlling hydrate and free gas saturations, and that these systems can be modeled. This generalized model is intended to adapt to specific field examples such as Walker Ridge in the Gulf of Mexico where enhanced hydrate saturation is noted in dipping sand layers.

# Chapter 7

# Effect of Gas Hydrate Distribution on Slope Failure in Subsea Sediments

## 7.1 Introduction

Gas hydrates have been implicated as a geohazard that may have caused slope failure and slumping in marine settings (e.g., *Borowski and Paull*, 1997; *Briaud and Chaouch*, 1997; *Sultan et al.,* 2004; *Nixon and Grozic*, 2007; *Kwon et al*., 2010; *Scholz et al*., 2011). Compaction of clay results in lowering the porosity of the sediment. This porosity reduction is related to the decrease in absolute sediment permeability. Furthermore, hydrate accumulation in the pore space lowers the permeability and hinders fluid flow. In addition to lowering the sediment permeability, free gas accumulation below the base of the gas hydrate stability zone (GHSZ) can lead to generation of overpressure in the sediments. The overpressure development in these gas hydrate systems may drive conditions for sediment failure by faulting and fluid leakage or by shear failure. Some of the key factors responsible for overpressure development to the point of sediment failure were summarized with the help of dimensionless groups such as $N_{sc}$, relating sediment permeability and the sedimentation rate at the seafloor (*Bhatnagar et*

*al.*, 2008b). In this study we briefly discuss the theory of sediment instability and examine some of the stability effects of this dimensionless parameter, $N_{sc}$ as previously reported by e.g., *Bhatnagar et al.* (2008b).

Subsea sediment stability in hydrate systems are assessed through two different approaches. First, a rigorous stability analysis that assesses the failure condition by evaluating fracture genesis and how that relates to in situ observations of fracture-hosted hydrate in fine-grained settings (e.g., Gulf of Mexico, Cascadia Margin, Krishna-Godavari Basin, India). This builds upon previous models that address the feedbacks between fluid flow, hydrate accumulation, and fracture genesis (e.g., *Nimblett and Ruppel*, 2003; *Flemings et al.*, 2003; *Daigle and Dugan*, 2010a). However, there are a series of papers addressing this rigorous analysis (*Daigle and Dugan*, 2010a, 2010b) and is not included here.

Second, an infinite slope stability analysis discussed here and linked to the existing geologic hydrate accumulation models (*Bhatnagar*, 2008; *Chatterjee et al*., 2011b). Notably, this is the first step in trying to address the evolution of geohazards related to natural gas hydrate systems. This technique is computationally inexpensive, applicable in geologic and reservoir models, and provides a quick look at stability to identify locations for detailed stability analysis.

## 7.2 Slope Stability Modeling

Sediment failure occurs when the downslope shearing stress exceeds the resisting stresses of the sediment. In this study, slope stability calculations have been coupled with the basin-scale hydrate accumulation model and the subsea sediment instability are discussed. For a quick assessment of slope stability evolution, the factor of safety (FS) is calculated using an infinite slope approximation (e.g., *Lambe and Whitman*, 1969; *Dugan and Flemings*, 2002).

### 7.2.1 Infinite Slope Approximation

The infinite slope approximation relates the maximum resisting force, $F_{r,max}$ and the shearing force, $F_s$.

$$FS = \frac{F_{r,max}}{F_s} \tag{7.1}$$

where $FS > 1$ represents a stable slope and $FS \leq 1$ represents an unstable slope. The analysis assumes that the failure surface is parallel to the seafloor, fluid pressure is constant along the failure plane, end effects and stresses are neglected, and sediments on the slide surface are homogeneous (*Lambe and Whitman*, 1969; *Loseth*, 1998; *Dugan and Flemings*, 2002). A schematic is illustrated to represent the infinite slope approximation (Figure 7.1).

The shearing force, $F_s$ is the downslope component of the normal force, controlled by the mass of the overlying sediment, acceleration due to gravity, and the angle of the failure plane. Assuming unit length of the potential sliding sediment

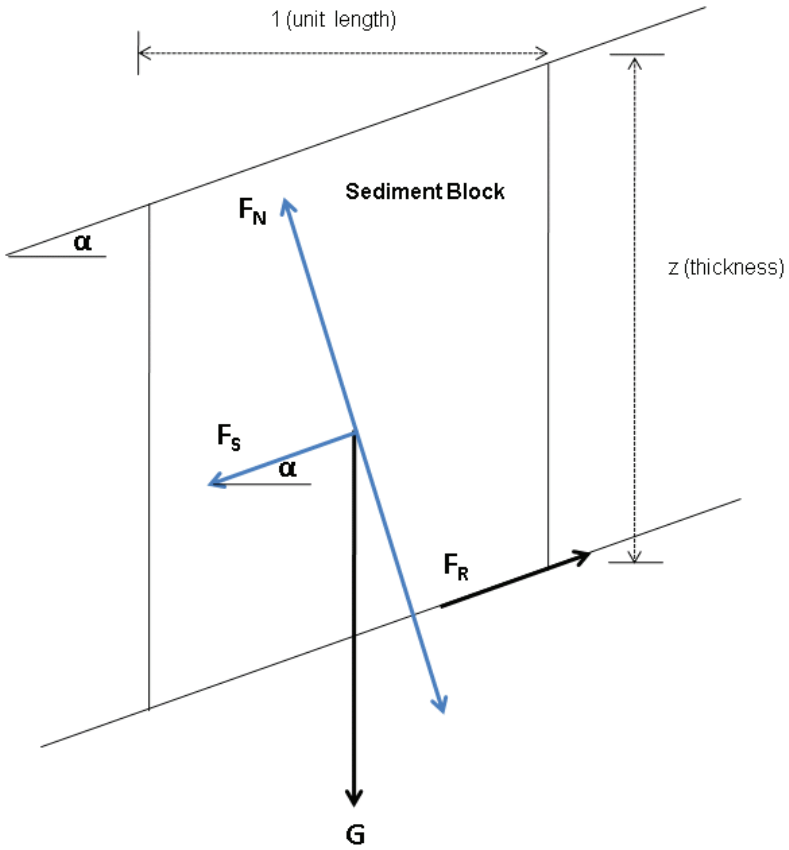


Figure 7.1 : Infinite slope model for slope-stability analysis where $\alpha$ is the slope angle for the assumed failure plain (parallel to the sediment surface), $z$ is the thickness of the sediment block, $G$ = buoyant weight of the sediment, $F_N$ is the normal force, $F_s =$ shearing force, and $F_r$ is the resisting force (Taken from *Loseth*, 1998).

block, the effective shearing force can be expressed as:

$$F_s = (\sigma_v - \rho_w g z) sin\alpha \tag{7.2}$$

where $\sigma_v$ is the total vertical stress, $\rho_w$ is the water density, $g$ is the acceleration due to gravity, $z$ denotes the thickness of the potential sliding block, and $\alpha$ is the slope angle. The slope angle, $\alpha$ is based on an average seafloor gradient and is set a constant value of $2^{\circ}$ for our study.

The frictional resistance to sliding (or shear strength) for porous sediments depends on the angle of internal friction, the cohesion of the sediment, and the effective normal force. The most common representation of shear strength $S$ is given by the classic equation in terms of effective stress (*Coulomb*, 1776):

$$S = c + [(\sigma_v - \rho_w g z) cos^2\alpha - p_w^*] tan\phi_f \tag{7.3}$$

where $c$ is the sediment cohesion, $\phi_f$ is the angle of internal friction and $p_w^*$ is the overpressure equal to the porewater pressure in excess of the hydrostatic pressure. Assuming unit sediment block width, the basal area of the sediment block shown in Figure 7.1 is equal to $\frac{1}{\cos\alpha}$. Since stress is defined as force per unit area, the maximum resisting force is:

$$F_{r,max} = \frac{c + [(\sigma_v - \rho_w g z) cos^2\alpha - p_w^*] \tan\phi_f}{\cos\alpha} \tag{7.4}$$

Substituting $F_{r,max}$ (equation 7.4) and $F_s$ (equation 7.2) in equation 7.1:

$$FS = \frac{c + [(\sigma_v - \rho_w g z)\cos^2\alpha - p_w^*]\tan\phi_f}{(\sigma_v - \rho_w g z)\sin\alpha\cos\alpha} \tag{7.5}$$

In the above formulation, sediment cohesion $(c)$ is set to be zero, for simplicity. A typical value of $c$ is normally 25 KPa for consolidated clays (*Lambe and Whitman*, 1969). Notably, gas hydrate accumulation may alter this assumption and increase the stability. Therefore, the cohesion parameter needs to be varied to model slope instability during hydrate accumulation as it may increase due to hydrate formation. The angle of internal friction, $\phi_f$ is assumed constant (26$^o$) based on average values in marine sediments. Internal friction angles range from 20-35$^o$ for clays and between 27 and 30$^o$ for silty sand (*Dugan and Flemings*, 2000, *Dugan*, 2003). These assumptions ensure minimum stability is estimated since non-zero cohesion and a higher angle of friction will increase the shear strength (Equation 7.3) and thus will increase the factor of safety (Equation 7.5). These parameters can be updated for specific hydrate settings now that the model has been tested.

## 7.3 Results and Discussion

In the presence of lithologic heterogeneities, fluid focusing in high permeability conduits results in higher hydrate and free gas saturation and accumulation (*Chatterjee et al*., 2011b). Infinite slope approximation can be used to

assess slope stability for different heterogeneous simulation cases using our hydrate accumulation model. We present one case where hydrate accumulates preferentially in high permeable vertical fracture systems due to focused flow (Figure 6.2). Although we acknowledge that these vertical fracture systems with a horizontal seafloor violates many of the infinite slope approximation assumptions, we present these simulations as base cases to validate and benchmark our model calculations. These systems are evaluated by varying the dimensionless parameter, $N_{sc}$ relating to permeability and sedimentation rate. Pore water overpressure is shown to develop with decreasing values of $N_{sc}$ (Figure 7.2). Last, the FS plots are constructed (Figure 7.3) as a function of normalized depth and normalized lateral distance.

These models show two key results that are consistent with previous studies: (1) high factors of safety throughout the model domain; and (2) that permeability heterogeneity influences stability. The high FS values are controlled by the low overpressures in this base case and are used to validate the numerical computations as they are consistent with other stability analyses of hydrostatic systems. The influence of permeable conduits is also consistent with previous studies (e.g., *Dugan and Flemings*, 2002); coupled with the influence of permeable conduits on hydrate saturation, this could be crucial to understand slope stability in hydrate settings.

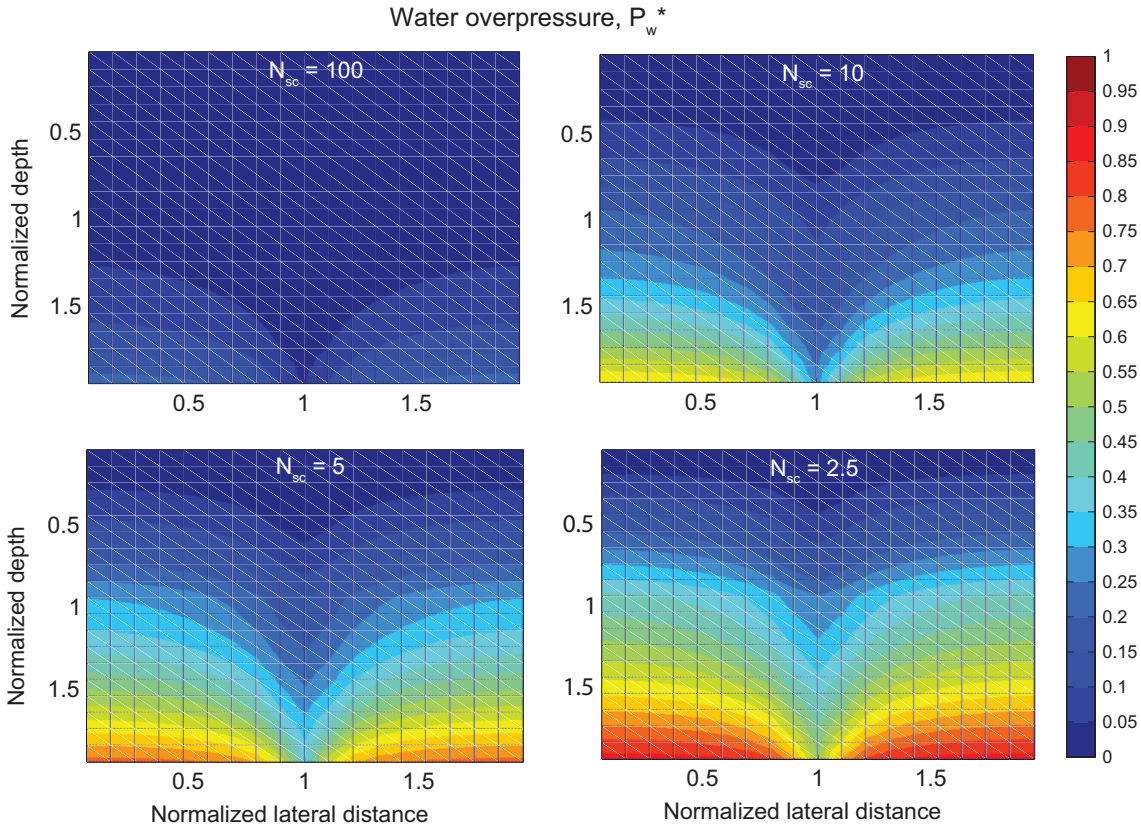


Figure 7.2 : Pore water overpressure contour plot for a 2-D marine hydrate accumulation model with an isotropic vertical fracture system extending through the gas hydrate stability zone. Unit normalized lateral distance delineate the boundary of the fracture system.

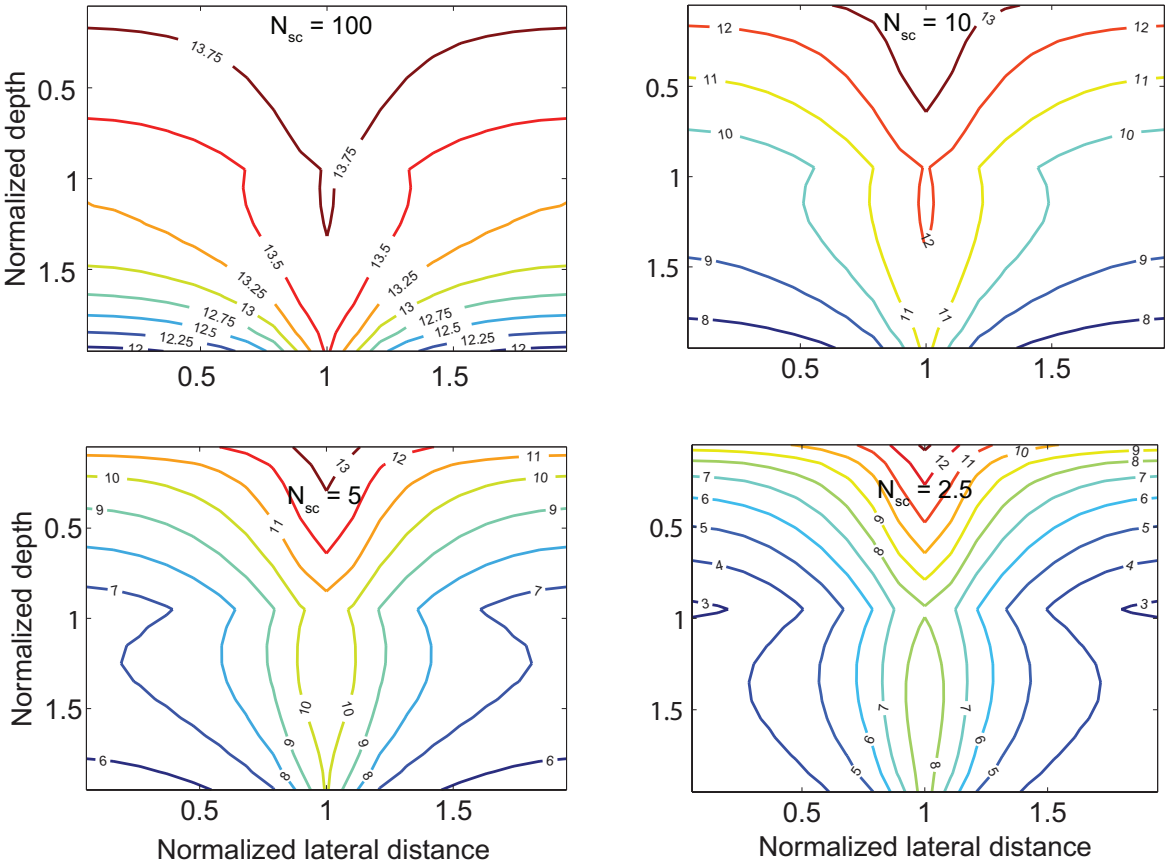


Figure 7.3 : Factor of safety (FS) contour plot for a 2-D hydrate system with a vertical fracture system extending through the gas hydrate stability zone at unit normalized lateral distance. High FS values indicate stable conditions controlled by low overpressure. Future evaluations will look at how changes in pressure and hydrate saturation in fracture affect stability.

## 7.4 Conclusions

A short additional routine in the 2-D hydrate accumulation simulator is developed to perform the factor of safety calculations. This approximation provides a reliable stability calculation for regional slope failures in hydrate-bearing heterogeneous sediments. This simple assessment can identify potentially unstable regions that may require more advanced failure analysis, such as for deep-seated rotational failures (e.g., *Bishop*, 1955). Therefore, this analysis provides an initial stability calculation and identifies regions that warrant detailed stability calculations.

# Chapter 8

# Conclusions and Future Work

## 8.1 Conclusions

Generalized numerical models developed in this thesis determine factors governing hydrate and free gas distribution in marine sediment. This chapter summarizes the conclusions of this dissertation and highlights some future research directions that stem from this study. The overall conclusions of this thesis can be divided into three broad categories:

1. Pore water chemistry above gas hydrate systems
2. Lithology and fluid flow governing hydrate distribution
3. Slope failure in subsea sediments

**Pore Water Chemistry across Sulfate-Methane Transition and Gas Hydrate Systems**

Previous 1-D models showed depth of the sulfate-methane transition (SMT) as a direct proxy to evaluate average gas hydrate saturation in marine sediments. This research revisits and revises an existing 1-D model and includes two competing

reduction pathways for porewater sulfate causing the SMT in shallow sediment. The revised 1-D model includes constituents such as dissolved $CH_4$, $SO_4^{2-}$, DIC, $Ca^{2+}$, $\delta^{13}\mathrm{C}$ of DIC, gas hydrate and free gas which enhances our understanding of carbon cycling processes in shallow sediment below the seafloor, specifically the chemical changes across the SMT. The model is tested with site-specific parameters at three distinct hydrate settings with differing carbon chemistry. The simulated pore water profiles resemble those measured at the sites, and the model explains the similarities and differences in pore water chemistry. At all sites, an upward flux of $CH_4$ consumes most net $SO_4^{2-}$ at a shallow SMT, and calcium carbonate removes a portion of DIC at this horizon. However, a large flux of $^{13}\mathrm{C}$-enriched $HCO_3^-$ enters the SMT from depth at Site 1230 and 1244, but not at Site KC151-3. This leads to elevated concentrations of pore water DIC with a $\delta^{13}\mathrm{C}$ much greater than that of $CH_4$ ($>$ -60 $‰$), even though AOM causes the SMT. The proportion of DIC flux from depth determines the concentration and $\delta^{13}\mathrm{C}$ of DIC at the SMT. The addition of $HCO_3^-$ from depth impacts the slope of certain concentration crossplots. Crucially, neither the DIC concentration nor its carbon isotope composition at the SMT can be used to discriminate between sulfate reduction pathways. A 1:1 flux balance between alkalinity (essentially DIC) and sulfate across the SMT confirms that AOM is the dominant cause for SMT in these systems. Thus, the upward methane flux consuming the pore water sulfate to form the SMT relates the SMT depth, fluid flux and the average hydrate saturation

in marine gas hydrate systems.

**Effects of Heterogeneous Lithology and Focused Fluid Flow on Gas Hydrate Distribution**

A generalized 2-D numerical model has been developed to simulate spatial and temporal distribution of gas hydrate and free gas in marine sediments over geologic timescales. Fracture network systems and dipping sand layers are common examples of lithologic heterogeneities in natural gas hydrate systems and are simulated using the 2-D model.

Simulations with a vertical fracture network, which extends through the gas hydrate stability zone and which has a permeability much greater than surrounding shale, show that focused fluid flow causes higher saturations of gas hydrate (25-70%) and free gas (30-60%) within the fracture network compared to the surrounding shale. Simulations with dipping sand layers of high permeability also result in elevated saturations of gas hydrate (60%) and free gas (40%) within the sand because of focused fluid flow.

Permeability anisotropy, with a vertical to horizontal permeability ratio on the order of $10^{-2}$, enhances gas hydrate concentrations within high permeability conduits because anisotropy enhances transport of methane-charged fluid to high permeability conduits. The 2-D, heterogeneous models quantify how focused fluid flow through high permeability zones affects local hydrate accumulation and

saturation. Increased fluid flux and deep source methane input result in enhanced concentrations of hydrate and free gas, and also increase the flow focusing effects.

From these 2-D results, hydrate and free gas saturations can be characterized by the local Peclet number (localized, focused, vertical, advective fluid flux relative to diffusion); which is consistent with Peclet number characterization in 1-D homogeneous systems. This characterization suggests that even in lithologically complex systems, local hydrate and free gas saturations can be characterized by basic parameters (local flux and diffusivity). To illustrate the importance of local flux on simple and complex natural hydrate systems this generalized model can be used to simulate hydrate distribution for specific field examples such as the Walker Ridge in the Gulf of Mexico where enhanced hydrate saturation is noted in dipping sand layers.

**Effect of Gas Hydrate Distribution on Slope Failure in Subsea Sediments**

The infinite slope approximation evaluates the slope's factor of safety to elucidate the potential for slope failure in subsea sediments associated with the hydrate accumulation model. This approximation provides a reliable stability criterion for regional slope failures in hydrate-bearing heterogeneous sediments. This simple assessment identifies potentially unstable regions that may require more advanced failure analysis and provides an initial stability calculation to identify regions that warrant detailed stability calculations.

## 8.2 Future Research Directions

This thesis highlights some primary factors which govern gas hydrate and free gas distribution in marine sediments. However, some other factors emerge out as future research directions that will contribute to a more complete understanding of gas hydrate distribution and accumulation in marine sediments.

1. Enhanced saturations in complex lithology
2. Amplitude attenuation and chaotic zones
3. Coexistence of hydrate and gas phases in GHSZ
4. Sensitivity analysis to model slope failure condition
5. Application of models and case studies

**Enhanced Saturations of Gas Hydrate and Free Gas**

The 2-D model developed in this study can be used to simulate lateral migration and elevated concentration of gas hydrate and free gas in heterogeneous marine sediments to illustrate field examples where focused fluid flow enhances hydrate and free gas saturation. The model can be adapted to illustrate the accumulation of hydrate occurrence sufficiently concentrated for economic gas production enhanced by focused fluid flow within high permeability conduits formed because of lithology and geometry. In addition to stratigraphic features, the potential of structural traps in focusing hydrate and free gas could also be examined. The future research would also identify parameters and factors controlling the

phenomenon of localized upward migration of free gas along fracture systems and lateral transfer to dipping sediment beds that could lead to chaotic zones and possible accumulation of concentrated hydrates. It is of paramount importance to understand whether localized upwelling of free gas represents its escape from deeper sources of methane or if it offers potential for concentrated accumulation of hydrate.

**Amplitude Attenuation and Chaotic Zones due to Hydrate Distribution**

Preferential hydrate formation in coarse-grained, heterogeneous sediments can be simulated by coupling the fluid flux and the permeability distribution. The acoustic impedance can be computed from the lithology and hydrate distribution, and synthetic seismograms can be constructed to quantify the level of attenuation as a function of the system parameters. Furthermore, these simulations can be used to validate the hypothesis that preferential accumulation of hydrates in heterogeneous lithology result in amplitude attenuation. Focused flux of free gas into the stratified hydrate stability zone should be modeled to investigate governing conditions that lead to formation of chaotic zones. Modeling chaotic zones and seismic wipeouts would elucidate the migration of free gas into the hydrate stability zone which results in regions of strongly contrasting acoustic impedance.

**Co-existence of Hydrate and Free Gas Phases**

The two-dimensional model described in this thesis simulates spatial and temporal saturations of gas hydrate and free gas in pore space coupled with salinity (or chlorinity). Salinity profiles generated using this model is dependent on hydrate formation and dissociation and varies with depth and lateral dimension. This invariant salinity due to hydrate formation and dissociation shifts the phase equilibrium and alters the solubility of methane. A flash calculation routine can be developed coupled with the current simulator to calculate different components (methane, water and chloride) existing in different phases (aqueous, hydrate and free gas). At every time-step, new values of salinity will be computed, which would alter the phase equilibrium and methane solubility in all gridblocks. The flash calculation routine would calculate the new amounts of different components in thermodynamic equilibrium. This would result in free gas phase invasion into the GHSZ. These models will be used to exemplify co-existence of hydrate and free gas phases within the gas hydrate stability zone (GHSZ). High gas flux from depth scenarios will be simulated to illustrate cases where hydrate, free gas and water phases would co-exist within the GHSZ. Field examples like Hydrate Ridge would represent such simulations which will show peak hydrate and free gas saturations close to the seafloor. Gas venting from the seafloor or chimney structures as observed in seismic studies could also be explained using these simulations. Models simulating high water flux from depth would sweep the chlorides and

reduce local salinity, thereby forming peak hydrate at the base of the hydrate stability zone with very little or no free gas within the GHSZ as observed in hydrate settings such as the Blake Ridge.

**Modeling Slope Failure Conditions in Subsea Sediments**

A new aspect of modeling slope failure will be to evaluate how the stability parameters (e.g., friction angle, cohesion) vary with lithology and hydrate saturation. Some of these data exist (*Waite et al*., 2009) however they are limited. We will continue to search the literature for other stability data and will run sensitivity studies and parameter to isolate the key driving forces for unstable conditions. There will be dynamic interactions between hydrate saturation, which will increase cohesion and friction angle and thus increase stability, but can also influence overpressure and decrease stability. With hydrate formation, cohesive forces which are currently assumed to be constant will change and significantly affect the slope stability. The feedbacks between permeability, hydrate accumulation, and slope stability should be explored as an extension of this study.

**Application of Models to Interpretation of Case Studies**

The fully developed 2-D numerical model can be applied to case studies involving the interpretation of geochemical and geophysical data. Interesting data already available from the Gulf of Mexico, East sea in Korea, Nankai trough in Japan,

Integrated Ocean Drilling Program (IODP) legs, National Gas Hydrate Program (NGHP) expeditions in the Krishna-Godavari basin and Mahanadi basin in India where this generalized model can be adapted to understand the localized hydrate and associated free gas distribution and accumulation. Previously, the depth of SMT has been used to interpret average hydrate saturation. In this study, it is shown that AOM is the dominant sulfate reduction pathway causing the SMT at steady-state conditions. Indeed, if AOM causes the SMT, and the SMT depth can be used to evaluate the upward methane flux and the average hydrate saturation, these one-dimensional models can be used for quick assessment of hydrate saturation and distribution using SMT depth as the primary input. This idea can be extended to develop proxies to find favorable conditions for economic gas production and recovery using the correlations developed in the study relating the local SMT depth, local fluid flux, local hydrate saturation and other local parameters even in lithologically complex gas hydrate systems.

# Bibliography

Allison, P.A., S.P. Hesslebo, and C.E. Brett (2008), Methane seeps on an Early Jurassic dysoxic seafloor , *Palaeogeogr. Palaeoclimatol. Palaeoecol.*, 270, 230-238, doi:10.1016/j.palaeo.2008.01.033.

Archer D. (2007), Methane hydrate stability and anthropogenic climate change, *Biogeosciences*, 4, 521-544.

Archer, D., B.A. Buffett, and V. Brovkin (2009), Ocean methane hydrates as a slow tipping point in the global carbon cycle, *Proc. Natl. Acad. Sci. U.S.A*., 106(49), 20596-20601, doi:10.1073/pnas.0800885105.

Archie, G.E. (1942), The electrical resistivity log as an aid in determining some reservoir characteristics, *Trans. Am. Inst. Min. Metall. Pet. Eng*., 146, 54-62.

Bear J. (1988), *Dynamic of fluids in porous media*, New York, Dover Publications Inc.

Berner, R.A. (1980), *Early Diagenesis: A Theoretical Approach*, Princeton Univ. Press, Princeton, N.J.

Bhatnagar G. (2008), Accumulation of gas hydrates in marine sediments, Ph.D. dissertation, Rice University.

Bhatnagar, G., W.G. Chapman, G.R. Dickens, B. Dugan, and G.J. Hirasaki (2007), Generalization of gas hydrate distribution and saturation in marine sediments by scaling of thermodynamic and transport processes, *Am. J. Sci*., 307, 861-900, doi:10.2475/06.2007.01.

Bhatnagar, G., W.G. Chapman, G.R. Dickens, B. Dugan, and G.J. Hirasaki (2008a), Sulfate-methane transition as a proxy for average methane hydrate saturation in marine sediments, *Geophys. Res. Lett*., 35, L03611, doi:10.1029/2007GL032500.

Bhatnagar, G., W.G. Chapman, G.R. Dickens, B. Dugan, and G.J. Hirasaki (2008b), Effect of Overpressure on Gas Hydrate Distribution, *Proc. 6th International Conference on Gas Hydrates* (ICGH), Vancouver, British Columbia, Canada, July 6-10, 2008.

Bhatnagar, G., S. Chatterjee, W.G. Chapman, B. Dugan, G.R. Dickens, and G.J. Hirasaki (2011), Analytical theory relating the depth of the sulfate-methane transition to gas hydrate distribution and saturation, *Geochem. Geophys. Geosyst*., 12, Q03003, doi:10.1029/2010GC003397.

Biddle, J.F., J.S. Lipp, M. Lever, K. Lloyd, K. Sorensen, R. Anderson, H.F. Fredricks, M. Elvert, T.J. Kelly, D.P. Schrag, M.L. Sogin, J.E. Brenchley, A. Teske, C.H. House, and K. Hinrichs (2006), Heterotrophic Archaea dominate sedimentary subsurface ecosystems off Peru, *Proc. Natl. Acad. Sci. U.S.A*., 103, 10, 3846-3851.

Bishop, A.W. (1955), The use of the slip circle in the stability analysis of earth slopes, *Geotechnique*, 5, 7-17.

Bohrmann, G., J. Greinert, E. Suess, and M.E. Torres (1998), Authigenic carbonates from the Cascadia subduction zone and their relation to gas hydrate stability, *Geology*, 26, 647-650, doi:10.1130/0091-7613, 026-0647:ACFTCS-2.3.CO;2.

Borowski, W.S., and C.K. Paull (1997), The gas hydrate detection problem: Recognition of shallow-subbottom gas hazards in deep-water areas, OTC-8297, *Proc. Offshore Tech. Conf*., 1, 211-216, Houston, Tex.

Borowski, W.S., C.K. Paull, and W. Ussler III (1996), Marine pore water sulfate profiles indicate in situ methane flux from underlying gas hydrate, *Geology*, 24(7), 655-658.

Borowski, W.S., C.K. Paull, and W. Ussler III (1999), Global and local variations of interstitial sulfate gradients in deep-water, continental margin sediments: Sensitivity to underlying methane and gas hydrates, *Mar. Geol*., 159, 131-154, doi:10.1016/S0025-3227(99)00004-3.

Borowski, W.S., N. Cagatay, Y. Ternois, and C.K. Paull (2000), Data report: Carbon isotopic composition of dissolved $CO_2$, $CO_2$ gas, and methane, Blake-Bahama Ridge and northeast Bermuda Rise, ODP Leg 172, *Proc. Ocean Drill. Program, Sci. Res.*, 172, 1-16, doi:10.2973/odp.proc.sr.172.201.2000.

Botz, R., E. Faber, M.J. Whiticar, and J.M. Brooks (1988), Authigenic carbonates in sediments from the Gulf of Mexico, *Earth Planet. Sci. Lett*., 88, 263-272, doi:10.1016/0012-821X(88)90083-0.

Boudreau, B.P., and J.T. Westrich (1984), The dependence of bacterial sulfate reduction on sulfate concentration in marine sediments, *Geochim. Cosmochim. Acta*, 48, 2503-2516, doi:10.1016/0016-7037(84)90301-6.

Briaud, J.L., and A. Chaouch (1997), Hydrate melting in soil around hot conductor, *J. Geotech. Geoenviron. Eng*., 123, 645-653, doi:10.1061/(ASCE)1090-0241(1997)123:7(645).

Buffett, B.A., and D. Archer (2004), Global inventory of methane clathrate: Sensitivity to changes in the deep ocean, *Earth Planet. Sci. Lett*., 227, 185-199, doi:10.1016/j.epsl.2004.09.005.

Burdige, D. (2011), Temperature dependence of organic matter remineralization in deeply-buried marine sediments, *Earth Planet. Sci. Lett*., 311, 396-410, doi: 10.1016/j.epsl.2011.09.043.

Campbell, K.A. (2006), Hydrocarbon seep and hydrothermal vent paleoenvironments and paleontology: Past developments and future research directions, *Palaeogeogr. Palaeoclimatol. Palaeoecol*., 232, 362-407, doi:10.1016/j.palaeo.2005.06.018.

Castellini, D.G., G.R. Dickens, G.T. Snyder, and C.D. Ruppel (2006), Barium recycling in shallow sediment above active mud volcanoes in the Gulf of Mexico, *Chem. Geol*., 226, 1-30, doi:10.1016/j.chemgeo.2005.08.008.

Chatterjee, S., G.R. Dickens, G. Bhatnagar, W.G. Chapman, B. Dugan, G.T. Snyder, and G.J. Hirasaki (2011a), Pore water sulfate, alkalinity, and carbon isotope profiles in shallow sediment above marine gas hydrate systems: A numerical modeling perspective, *J. Geophys. Res*., 116, B09103, doi:10.1029/2011JB008290.

Chatterjee S., G. Gu, G. Bhatnagar, W.G. Chapman, G.R. Dickens, B. Dugan and G.J. Hirasaki (2011b), Effects of heterogeneous lithology and focused fluid flow on gas hydrate distribution in marine sediments, *Proc. 7th International Conference on Gas Hydrates* (ICGH), Edinburgh, Scotland, United Kingdom, July 17-21, 2011.

Claypool, G.E., A.V. Milkov, Y.J. Lee, M.E. Torres, W.S. Borowski, and H. Tomaru (2006), Microbial methane generation and gas transport in shallow sediments of an accretionary complex, southern Hydrate Ridge (ODP Leg 204), offshore Oregon, USA, *Proc. Ocean Drill. Program, Sci. Res.*, 204, 1-52, doi:10.2973/odp.proc.sr.204.113.2006.

Collett, T.S. (2002), Energy resource potential of natural gas hydrates, *AAPG Bull*., 86, 1971-1992.

Conrad, R. (2005), Quantification of methanogenic pathways using stable carbon isotopic signatures: A review and a proposal, *Org. Geochem*., 36, 739-752, doi:10.1016/j.orggeochem.2004.09.006.

Cook, A.E., D. Goldberg, and R.L. Kleinberg (2008), Fracture-controlled gas hydrate systems in the northern Gulf of Mexico, *Mar. Pet. Geol*., 25, 932-941, doi:10.1016/j.marpetgeo.2008.01.013.

Coulomb, C.A. (1776), Essai sur une application des regles des maximis et minimis a quelquels problemesde statique relatifs, a la architecture, *Mem. Acad. Roy. Div. Sav*., 7, 343-387.

D'Hondt., S.L., S. Rutherford and A.J. Spivack (2002), Metabolic activity of subsurface life in deep-sea sediments, *Science*, 295(5562), 2067-2070, doi:10.1126/science.1064878.

D'Hondt, S.L., B.B. Jorgensen, D.J. Miller et al. (2003), *Proc. ODP, Init. Repts*., 201: College Station, TX (Ocean Drilling Program), doi:10.2973/odp.proc.ir.201.2003.

Daigle, H., and B. Dugan (2010a), Origin and evolution of fracture-hosted methane hydrate deposits, *J. Geophys. Res*., 115, B11103, doi:10.1029/2010JB007492.

Daigle, H., and B. Dugan (2010b), Effects of multiphase methane supply on hydrate accumulation and fracture generation, *Geophys. Res. Lett*., 37, L20301, doi:10.1029/2010GL044970.

Davie, M.K., and B.A. Buffett (2001), A numerical model for the formation of gas hydrate below the seafloor, *J. Geophys. Res*., 106, 497-514, doi:10.1029/2000JB900363.

Davie, M.K., and B.A. Buffett (2003a), Sources of methane for marine gas hydrate: Inferences from a comparison of observations and numerical models, *Earth Planet. Sci. Lett*., 206, 51-63, doi:10.1016/S0012-821X(02)01064-6.

Davie, M.K., and B.A. Buffett (2003b), A steady state model for marine hydrate formation: Constraints on methane supply from pore water sulfate profiles,

*J. Geophys. Res*., 108(B10), 2495, doi:10.1029/2002JB002300.

Dickens, G.R. (2001a), The potential volume of oceanic methane hydrates with variable external conditions, *Org. Geochem*., 32, 1179-1193, doi:10.1016/S0146-6380(01)00086-9.

Dickens, G.R. (2001b), Sulfate profiles and barium fronts in sediment on the Blake Ridge: Present and past methane fluxes through a large gas hydrate reservoir, *Geochim. Cosmochim. Acta*, 65, 529-543, doi:10.1016/S0016-7037(00)00556-1.

Dickens, G.R. (2003), Rethinking the global carbon cycle with a large, dynamic and microbially mediated gas hydrate capacitor, *Earth Planet. Sci. Lett*., 213, 169-183, doi:10.1016/S0012-821X(03)00325-X.

Dickens, G.R. (2011), Down the Rabbit Hole: toward appropriate discussion of methane release from gas hydrate systems during the Paleocene-Eocene thermal maximum and other past hyperthermal events, *Clim. Past*, 7, 831-846, doi:10.5194/cp-7-831-2011.

Dickens, G.R. and M.S. Quinby-Hunt (1994), Methane hydrate stability in seawater, *Geophys. Res. Lett*., 21, 21152118.

Dickens, G.R. and M.S. Quinby-Hunt (1997), Methane hydrate stability in seawater: A simple theoretical approach for geophysical applications, *J. Geophys. Res*., 102(B1), 773-783, doi:10.1029/96JB02941.

Dickens, G.R., and G.T. Snyder (2009), Interpreting upward methane flux, *Fire in the Ice*, Winter, 7-10.

Dickens, G.R., C.K. Paull, and P. Wallace, and the ODP Leg 164 Shipboard Scientific Party (1997), Direct measurement of in situ methane quantities in a large gas hydrate reservoir, *Nature*, 385, 426-428, doi:10.1038/385426a0.

Dickens, G.R., D. Schroeder, K-U. Hinrichs, and the Leg 201 Scientific Party (2003), The pressure core sampler (PCS) on ODP Leg 201: general operations and gas release, In D'Hondt, S.L., B.B. Jorgensen, D.J. Miller et al., *Proc. ODP, Init. Repts*., 201: College Station, TX (Ocean Drilling Program), 1-22.

Donohue, C.M., G.T. Snyder, and G.R. Dickens (2005), Data report: Major cation concentrations of interstitial waters collected from deep sediments of eastern equatorial Pacific and Peru margin (ODP Leg 201), In D'Hondt, S.L., B.B. Jorgensen, D.J. Miller, (Eds.), *Proc. ODP, Sci. Res.*, 201, 1-19.

Dugan B., Ph.D. Thesis (2003), Hydrodynamics of the US Mid-Atlantic Continental Slope, Offshore New Jersey, Pennsylvania State University.

Dugan, B. (2008), Fluid flow in the Keathley Canyon 151 mini-basin, northern Gulf of Mexico, *Mar. Pet. Geol*., 25, 919-923, doi:10.1016/j.marpetgeo.2007.12.005.

Dugan, B., and P.B. Flemings (2000), Overpressure and fluid flow in the New Jersey continental slope: implications for slope failure and cold seeps, *Science*, 289, 288-291.

Dugan, B., and P.B. Flemings (2002), Fluid flow and stability of the US continental slope offshore New Jersey from the Pleistocene to the present, *Geofluids*, 2, 137-146.

Egeberg, P.K., and G.R. Dickens (1999), Thermodynamic and pore water halogen constraints on gas hydrate distribution at ODP Site 997 (Blake Ridge), *Chem. Geol*., 153, 53-79, doi:10.1016/S0009-2541(98)00152-1.

Flemings, P.B., X. Liu, and W. Winters (2003), Critical pressure and multiphase flow in Blake Ridge hydrates, *Geology*, 31, 1057-1060.

Formolo, M.J., T.W. Lyons, C. Zhang, C. Kelley, R. Sassen, J. Horita, and D.R. Cole (2004), Quantifying carbon sources in the formation of authigenic carbonates at gas hydrate sites in the Gulf of Mexico, *Chem. Geol*., 205, 253-264, doi:10.1016/j.chemgeo.2003.12.021.

Frederick, J.M., and B.A. Buffett (2011), Topography- and fracture-driven fluid focusing in layered ocean sediments, *Geophys. Res. Lett*., 38, L08614, doi:10.1029/2010GL046027.

Garg, S.K., J.W. Pritchett, A. Katoh, K. Baba, and T. Fujii (2008), A mathematical model for the formation and dissociation of methane hydrates in the marine environment, *J. Geophys. Res*., 113, B01201, doi:10.1029/2006JB004768.

Gieskes, J.M., T. Gamo, and H. Brumsack (1991), Chemical methods for interstitial water analysis aboard JOIDES Resolution, *ODP Tech*, Note, 15.

Gering, K.L. (2003), Simulations of methane hydrate phenomena over geologic timescales. Part I : Effect of sediment compaction rates on methane hydrate and free gas accumulations, *Earth Planet. Sci. Lett*., 206, 6581.

Goni, M.A., K.C. Ruttenberg, and T.I. Eglington (1998), A reassessment of the sources and importance of land-derived organic matter in surface sediments from the Gulf of Mexico, *Geochim. Cosmochim. Acta*, 62, 3055-3075, doi:10.1016/S0016-7037(98)00217-8.

Greinert, J., G. Bohrmann, and E. Suess (2001), Methane-venting and gas hydrate-related carbonates at the hydrate ridge: Their classification, distribution and origin, in Natural Gas Hydrates: Occurrence, Distribution, and Detection, *Geophys. Monogr. Ser*., 124, edited by C. K. Paull and W. P. Dillon, 99-113, AGU, Washington, D.C.

Gu, G., P. Jaiswal, W.G. Chapman, C.A. Zelt, G.J. Hirasaki (2008), Compositional Effect on Hydrate/Free Gas Transition and BSR, *Eos Trans. AGU*, 89(53), Fall Meet. Suppl., Abstract, OS41D-1256.

Gu, G., G.R. Dickens, G. Bhatnagar, F.S. Colwell, G.J. Hirasaki, and W.G. Chapman (2011), Abundant Early Palaeogene marine gas hydrates despite warm deep ocean temperatures, *Nat. Geosci.*, 4, 848-851, doi:10.1038/ngeo1301.

Gutierrez, M., and M. Wangen (2005), Modeling of compaction and overpressuring in sedimentary basins, *Mar. Pet. Geol*., 22(3), 351-363.

Haeckel, M., E. Suess, K. Wallman, and D. Rickert (2004), Rising methane gas bubbles form massive hydrate layers at the seafloor, *Geochim. Cosmochim. Acta*, 68, 4335-4345.

Hesse, R., and W.E. Harrison (1981), Gas hydrates (clathrates) causing pore water freshening and oxygen isotope fractionation in deep-water sedimentary sections of terrigenous continental margins, *Earth Planet. Sci. Lett*., 55, 453-462.

Hiruta, A., G.T. Snyder, H. Tomaru, and R. Matsumoto (2009), Geochemical constraints for the formation and dissociation of gas hydrate in an area of high methane flux, eastern margin of the Japan Sea, *Earth Planet. Sci.*

*Lett*., 279, 326-339, doi:10.1016/j.epsl.2009.01.015.

Hornbach, M.J., D.M. Saffer, and W.S. Holbrook (2004), Critically pressured free-gas reservoirs below gas hydrate provinces, *Nature*, 427, 142-144.

Iversen, N., and B.B. Jorgensen (1993), Diffusion coefficients of sulfate and methane in marine sediments: Influence of porosity, *Geochim. Cosmochim. Acta*, 57, 571-578, doi:10.1016/0016-7037(93)90368-7.

Jones, E., T. Latham, D. McConnell, M. Frye, J. Hunt Jr., W. Shedd, D. Shelander, R. Boswell, K. Rose, C. Ruppel, D. Hutchinson, T.S. Collett, B. Dugan, W. Wood (2008), Scientific Objectives of the Gulf of Mexico Gas Hydrate JIP Leg II Drilling, Paper OTC 19501, *Proc. Offshore Tech. Conf*., Houston TX, 5-8 May 2008.

Kastner, M., K.A. Kvenvolden, and T.D. Lorenson (1998), Chemistry, isotopic composition, and origin of a methane-hydrogen sulfide hydrate at the Cascadia subduction zone, *Earth Planet. Sci. Lett*., 28, 337344.

Kastner, M., M.E. Torres, E. Solomon, and A.J. Spivack (2008a), Marine pore fluid profiles of dissolved sulfate: Do they reflect in situ methane fluxes?, *Fire in the Ice*, Summer, p.6-8.

Kastner, M., G.E. Claypool, and G. Robertson (2008b), Geochemical constraints on the origin of the pore fluids and gas hydrate distribution at Atwater Valley and Keathley Canyon, northern Gulf of Mexico, *Mar. Pet. Geol*., 25, 860-872, doi:10.1016/j.marpetgeo.2008.01.022.

Kharaka, Y.K., A.S. Maest, W.W. Carothers, L.M. Law, and P.J. Lamothe (1987), Geochemistry of metal-rich brines from central Mississippi Salt Dome basin, USA, *Appl. Geochem*., 2, 543-561, doi:10.1016/0883-2927(87)90008-4.

Kim, J.H., M.H. Park, U. Tsunogai, T.J. Cheong, B.J. Ryu, Y.J. Lee, H.C. Han, J.H. Oh, and H.W. Chang (2007), Geochemical characterization of the organic matter, pore water constituents and shallow methane gas in the eastern part of the Ulleung Basin, East Sea (Japan Sea), *Isl. Arc*, 16, 93-104, doi:10.1111/j.1440-1738.2007.00560.x.

Kim, J. H., M.H. Park, J.H. Chun, and Y.J. Lee (2011), Molecular and isotopic signatures in sediments and gas hydrate of the central/southwestern Ulleung Basin: High alkalinity escape fuelled by biogenically sourced

methane, *Geo Mar. Lett*., 31, 37-49, doi:10.1007/s00367-010-0214-y.

Klauda, J.B., and S.I. Sandler (2005), Global distribution of methane hydrate in ocean sediment, *Energy Fuels*, 19, 459-470, doi:10.1021/ef049798o.

Kleinberg R.L, C. Flaum, D.D. Griffin, P.G. Brewer, G.E. Malby, E.T. Peltzer, and J.P. Yesinowski (2003), Deep sea NMR: Methane hydrate growth habitat in porous media and its relationship to hydraulic permeability, deposit accumulation, and submarine slope stability, *J. Geophys. Res*., 108, B102508, doi:10.1029/2003JB002389.

Kraemer, M., R.M. Owen, and G.R. Dickens (2000), Lithology of the upper gas hydrate zone, Blake Outer Ridge: A link between diatoms, porosity, and gas hydrate, In Paull, C.K., R. Matsumoto, P.J. Wallace, and W.P. Dillon, editors, *Proc. ODP, Sci. Res.*, 164, 229-236, College Station, TX. Ocean Drilling Program.

Kvenvolden, K.A. (1988), Methane hydrate - A major reservoir of carbon in the shallow geosphere, *Chem. Geol*., 71:41-51.

Kvenvolden, K.A. (1993), Gas hydrates: Geological perspective and global change, *Rev. Geophys*., 31, 173-187, doi:10.1029/93RG00268.

Kvenvolden, K.A. (1995), A review of the geochemistry of methane in natural gas hydrate, *Org. Geochem*., 23, 997-1008, doi:10.1016/0146-6380(96)00002-2.

Kvenvolden, K.A. and M. Kastner (1990), Gas hydrates of the Peruvian outer continental margin, In Suess, E. and von Huene, et al., R., editors, *Proc. ODP, Sci. Res.*, 112, 517-526, College Station, TX, Ocean Drilling Program.

Kwon, T.H., K.I. Song, and G.C. Cho (2010), Destabilization of marine gas hydrate-bearing sediments induced by a hot wellbore: A numerical approach, *Energy Fuels*, 24, 5493-5507, doi:10.1021/ef100596x.

Lambe, T.W. and R.V. Whitman (1969), *Soil Mechanics*, John Wiley & Sons, New York.

Lee, M.W., and T.S. Collett (2006), Gas hydrate and free gas saturations estimated from velocity logs on Hydrate Ridge, offshore Oregon, U.S.A., *Proc. ODP, Sci. Res.*, 204, 1-25, doi:10.2973/odp. proc.sr.204.103.2006.

Lee, M.W., and T.S. Collett (2008), Integrated analysis of well logs and seismic data to estimate gas hydrate concentrations at Keathley Canyon, northern Gulf of Mexico, *Mar. Pet. Geol.*, 25, 924-931, doi:10.1016/j.marpetgeo.2007.09.002.

Li, Y., and S. Gregory (1974), Diffusion of ions in sea water and in deep-sea sediments, *Geochim. Cosmochim. Acta*, 38, 703-714, doi:10.1016/0016-7037(74)90145-8.

Lisiecki, L.E., and T.D. Herbert (2007), Automated composite depth scale construction and estimates of sediment core extension, *Paleoceanography*, 22, PA4213, doi:10.1029/2006PA001401.

Liu, X., and P.B. Flemings (2006), Passing gas through the hydrate stability zone at southern Hydrate Ridge, offshore Oregon, *Earth Planet. Sci. Lett*., 67:3403-3421.

Liu, X.L., and P.B. Flemings (2007), Dynamic multiphase flow model of hydrate formation in marine sediments, *J. Geophys. Res*., 112, B03101, doi:10.1029/2005JB004227.

Lorenson, T.D., G.E. Claypool, and J.A. Dougherty (2008), Natural gas geochemistry of sediments drilled on the Gulf of Mexico JIP cruise, *Mar. Pet. Geol*., 25, 873-883, doi:10.1016/j.marpetgeo.2008.01.017.

Loseth, T.M. (1998), *Submarine massflow sedimentation: Computer modeling and basin fill stratigraphy* Springer Press.

Lowenstein, T.K., M.N. Timofeeff, S.T. Brennan, L.A. Hardie, and R.M. Demicco (2001), Oscillations in Phanerozoic seawater chemistry: Evidence from fluid inclusions, *Science*, 294, 1086-1088, doi:10.1126/science.1064280.

Luff, R., and K. Wallman (2003), Fluid flow, methane fluxes, carbonate precipitation and biogeochemical turnover in gas hydrate-bearing sediments at Hydrate Ridge, Cascadia Margin: Numerical modeling and mass balances, *Geochim. Cosmochim. Acta*, 67, 3403-3421, doi:10.1016/S0016-7037(03)00127-3.

MacKay, M.E., R.D. Jarrard, G.K. Westbrook, R.D Hyndman (1994), and the Shipboard Scientific Party of Ocean Drilling Program Leg 146, Origin of bottom-simulating reflectors: Geophysical evidence from the Cascadia accretionary prism, *Geolog*, 22, 459-462.

Macpherson, G.L. (1989), Lithium, boron and barium in formation waters and sediments, northwestern Gulf of Mexico sedimentary basin, Ph.D. dissertation, Univ. of Tex., Austin.

Malinverno, A. (2010), Marine gas hydrates in thin sand layers that soak up microbial methane, *Earth Planet. Sci. Lett*., 292, 399-408, doi:10.1016/j.epsl.2010.02.008.

Malinverno, A., and J.W. Pohlman (2011), Modeling sulfate reduction in methane hydrate-bearing continental margin sediments: Does a sulfate-methane transition require anaerobic oxidation of methane?, *Geochem. Geophys. Geosyst*., 12, Q07006, doi:10.1029/2011GC003501.

Malinverno, A., M. Kastner, M.E. Torres, and U.G. Wortmann (2008), Gas hydrate occurrence from pore water chlorinity and downhole logs in a transect across the northern Cascadia margin (Integrated Ocean Drilling Program Expedition 311), *J. Geophys. Res*., 113, B08103, doi:10.1029/2008JB005702.

Marquardt M., C. Hensen, E. Pinero, K. Wallmann and M. Haeckel (2010), A transfer function for the prediction of gas hydrate inventories in marine sediments, *Biogeosciences*, 7, 2925-2941.

Meister, P., M. Prokopenko, C.G. Skilbeck, M. Watson, and J.A. McKenzie (2005), Data report: compilation of total organic and inorganic carbon data from Peru margin and eastern equatorial Pacific drill sites (ODP Legs 112, 138, and 201). In Jorgensen, B.B., S.L. D'Hondt, and D.J. Miller, (eds.), *Proc. ODP, Sci. Res.*, 201: College Station, TX (Ocean Drilling Program), 1-20, doi:10.2973/odp.proc.sr.201.105.2005.

Meister, P., J.A. Mckenzie, C. Vasconcelos, S. Bernasconi, M. Frank, M. Gutjahr, and D.P. Schrag (2007), Dolomite formation in the dynamic deep biosphere: results from the Peru Margin, *Sedimentology*, 54, 1007-1031, doi:10.1111/j.1365-3091.2007.00870.x.

Middleburg, J. (1989), A simple rate model for organic-matter decomposition in marine-sediments, *Geochim. Cosmochim. Acta*, 53, 7, 1577-1581.

Milkov, A.V. (2004), Global estimates of hydrate-bound gas in marine sediments: How much is really out there?, *Earth Sci. Rev*., 66, 183-197, doi:10.1016/j.earscirev.2003.11.002.

Milkov, A.V. (2005), Molecular and stable isotope compositions of natural gas hydrates: A revised global dataset and basic interpretations in the context of geological settings, *Org. Geochem*., 36, 681-702, doi:10.1016/j.orggeochem.2005.01.010.

Milkov, A.V., and R. Sassen (2000), Thickness of the gas hydrate stability zone, Gulf of Mexico continental slope, *Mar. Pet. Geol*., 17:981991.

Milkov, A.V., G.E. Claypool, Y.J. Lee, W. Xu, G.R. Dickens, and W.S. Borowski, and the ODP Leg 204 Scientific Party (2003), In situ methane concentrations at Hydrate Ridge, offshore Oregon: New constraints on the global gas hydrate inventory from an active margin, *Geology*, 31, 833-836, doi:10.1130/G19689.1.

Milkov, A.V., G.R. Dickens, G.E. Claypool, Y.J. Lee, W.S. Borowski, M. E. Torres, W. Xu, H. Tomaru, A.M. Trehu, and P. Schultheiss (2004), Co-existence of gas hydrate, free gas, and brine within the regional gas hydrate stability zone at Hydrate Ridge (Oregon margin): Evidence from prolonged degassing of a pressurized core, *Earth Planet. Sci. Lett*., 222, 829-843, doi:10.1016/j.epsl.2004.03.028.

Milkov, A.V., G.E. Claypool, Y.J. Lee, and R. Sassen (2005), Gas hydrate systems at Hydrate Ridge offshore Oregon inferred from molecular and isotopic properties of gas hydrate-bound and void gases, *Geochim. Cosmochim. Acta*, 69, 1007-1026, doi:10.1016/j.gca.2004.08.021.

Mucci, A. (1983), The solubility of calcite and aragonite in seawater at various salinities, temperature, and one atmosphere total pressure, *Am. J. Sci*., 283, 780-799.

Nimblett, J., and C. Ruppel (2003), Permeability evolution during the formation of gas hydrates in marine sediments, *J. Geophys. Res*., 108(B9), 2420, doi:10.1029/2001JB001650.

Nixon, M.F. and J.L.H. Grozic (2007), Submarine slope failure due to gas hydrate dissociation: a preliminary quantification, *Can. Geotech. J*., 44, 314-325.

Paull, C.K., and R. Matsumoto (2000), Leg 164 overview, *Proc. ODP, Sci. Res.*, 164, 3-10, doi:10.2973/odp.proc.sr.163.204.2000.

Paull, C.K., R. Matsumoto, P.J. Wallace, and W.P. Dillon (1996), *Proc. ODP, Init. Repts.*, 164, Ocean Drilling Program, College Station, Tex, doi: 10.2973/odp.proc.ir.164.1996.

Paull, C.K., T.D. Lorenson, G.R. Dickens, W.S. Borowski, W. Ussler III, and K. Kvenvolden (2000a), Comparisons of in situ and core gas measurements in ODP Leg 164 bore holes, *Ann. N. Y. Acad. Sci*., 912, 23-31, doi:10.1111/j.1749-6632.2000.tb06756.x.

Paull, C.K., T.D. Lorenson, W.S. Borowski, W. Ussler III, K. Olsen, and N.M. Rodriguez (2000b), Isotopic composition of $CH_4$, $CO_2$ species, and sedimentary organic matter within samples from the Blake Ridge: Gas source implications, *Proc. OP, Sci. Res*., 164, 67-78, doi:10.2973/odp.proc.sr.164.207.2000.

Paull, C.K., R. Matsumoto, P.J. Wallace, and W.P. Dillon (eds) (2000c), *Proc. ODP Sci. Res.*, 164, College Station, TX, Ocean Drilling Program.

Paull, C.K., W. Ussler III, T. Lorenson, W. Winters, and J. Dougherty (2005), Geochemical constraints on the distribution of gas hydrates in the Gulf of Mexico, *Geo Mar. Lett*., 25, 273-280, doi:10.1007/s00367-005-0001-3.

Pecher, I.A., N. Kukowski, C. Huebscher, J. Greinert, J. Bialas (2001), The link between bottom-simulating reflections and methane flux into the gas hydrate stability zone: new evidence from Lima Basin, Peru Margin, *Earth Planet. Sci. Lett*., 185(3/4): 343-354.

Peckmann, J., and V. Thiel (2004), Carbon cycling at ancient methane-seeps, *Chem. Geol*., 205, 443-467, doi:10.1016/j.chemgeo.2003.12.025.

Pohlman, J., C. Ruppel, D.R. Hutchinson, R. Downer, and R.B. Coffin (2008), Assessing sulfate reduction and methane cycling in a high salinity pore water system in the northern Gulf of Mexico, *Mar. Pet. Geol*., 25, 942-951, doi:10.1016/j.marpetgeo.2008.01.016.

Pohlman, J., M. Kaneko, V.B. Heuer, R.B. Coffin, and M. Whiticar (2009), Methane sources and production in the northern Cascadia margin gas hydrate system, *Earth Planet. Sci. Lett*., 287, 504-512, doi:10.1016/j.epsl.2009.08.037.

Price, P.B., and T. Sowers (2004), Temperature dependence of metabolic rates for microbial growth, maintenance, and survival, *Proc. Natl. Acad. Sci*.,

USA, 101, 4631-4636.

Reeburgh, W.S. (1976), Methane consumption in Cariaco trench waters and sediments, *Earth Planet. Sci. Lett*., 28, 337-344, doi:10.1016/0012-821X(76)90195-3.

Rempel, A.W., and B.A. Buffett (1997), Formation and accumulation of gas hydrate in porous media, *J. Geophys. Res*., 102, 10151-10164, doi:10.1029/97JB00392.

Riedel, M., T.S. Collett, M.J. Malone, and the Expedition 311 Scientists, eds (2006), *Proc. IODP, 311*, Washington, D.C., Integrated Ocean Drilling Program Management International Inc.

Rodriguez, N.M., C.K. Paull, and W.S. Borowski (2000), Zonation of authigenic carbonates within gas hydrate-bearing sedimentary sections on the Blake Ridge: Offshore southeastern North America, *Proc. ODP, Sci. Res*., 164, 301-312, doi:10.2973/odp.proc.sr.164.227.2000.

Roy, R.N., L.N. Roy, K.M. Vogel, C. Porter-Moore, T. Pearson, C.E. Good, F.J. Millero, D.M. Campbell (1993), The dissociation constants of carbonic acid in seawater at salinities 5 to 45 and temperatures 0 to 45($^{o}$C), *Mar. Chem.*, 44, 2-4, 249-267, doi:10.1016/0304-4203(93)90207-5.

Rubey W.W., and M.K. Hubbert (1959), Role of fluid pressure in mechanics of overthrust faulting; ii. Overthrust belt in geosynclinal area of western Wyoming in light of fluid pressure hypothesis, *Geol. Soc. Am. Bull*., 70, 167-206.

Ruppel, C., R. Boswell, and E. Jones (2008), Scientific results from Gulf of Mexico Gas Hydrates Joint Industry Project Leg 1 Drilling: Introduction and overview, *Mar. Pet. Geol*., 25, 819-829, doi:10.1016/j.marpetgeo.2008.02.007.

Scholz, N.A., M. Riedel, G.D. Spence, R.D. Hyndman, T. James, N. Naegeli, B. Dugan, J. Pohlman, T. Hamilton (2011), Do dissociating gas hydrates play a role in triggering submarine slope failures? A case study from the northern Cascadia margin, *Proc. 7th International Conference on Gas Hydrates*, 17-21 July 2011, Edinburgh, Scotland.

Schnurle, P., C.S. Liu (2011), Numerical modeling of gas hydrate emplacements in oceanic sediments, *Mar. Pet. Geol*., 28, 1856-1869,

doi:10.1016/j.marpetgeo.2011.03.011.

Shipboard Scientific Party (1988), Site 685, In Suess, E., R. von Huene, et al., *Proc. ODP, Init. Repts*., 112, College Station, TX, Ocean Drilling Program, 597-704, doi:10.2973/odp.proc.ir.112.116.1988.

Shipboard Scientific Party (1996), Sites 997, In Paull, C. K., R. Matsumoto, P.J. Wallace, and W.P. Dillon et al., *Proc. ODP, Init. Repts*., 164, College Station, TX, Ocean Drilling Program, 277-334, doi:10.2973/odp.proc.ir.164.110.1996.

Shipboard Scientific Party (2003a), Site 1230, In D'Hondt, S.L., B.B. Jorgensen, D.J. Miller, et al., *Proc. ODP, Init. Repts*., 201: College Station, TX (Ocean Drilling Program), 1-107, doi:10.2973/odp.proc.ir.201.111.2003.

Shipboard Scientific Party (2003b), Site 1244, In Trehu, A.M, Bohrmann, G., Rack, F.R., Torres, M.E., et al., Proc. ODP, Init. Rep., 204, College Station, TX, Ocean Drilling Program, 1-132, doi:10.2973/odp.proc.ir.204.103.2003.

Sloan, E.D. (2003), Fundamental principles and applications of natural gas hydrates, *Nature*, 426(6964), 353-359.

Sloan, E.D.J., and C. Koh (2007), *Clathrate Hydrates of Natural Gases*, 3rd ed., CRC Press, Boca Raton, Fla.

Smith J.E. (1971), The dynamics of shale compaction and evolution of pore-fluid pressures, *Math. Geol*. 3, 239-263.

Smith, D.C. (2005), Data report: dissolved organic carbon in interstitial waters, equatorial Pacific and Peru margin, ODP Leg 201. In Jorgensen, B.B., S. L. D'Hondt, and D. J. Miller, (Eds.), *Proc. ODP Sci. Res.*, 201, College Station, TX, Ocean Drilling Program, 1-10, doi:10.2973/odp.proc.sr.201.111.2005.

Snyder, G.T., A. Hiruta, R. Matsumoto, G.R. Dickens, H. Tomaru, R. Takeuchi, J. Komatsubara, Y. Ishida, and H. Yu (2007), Pore water profiles and authigenic mineralization in shallow marine sediments above the methane-charged system on Umitaka Spur, Japan Sea, *Deep-Sea Res*., Part II, 54, 1216-1239, doi:10.1016/j.dsr2.2007.04.001.

Spivack, A.J., C. McNeil, N.G. Holm, and K.U. Hinrichs (2006), Determination of in situ methane based on analysis of void gas. In Jorgensen, B.B., S.L.

D'Hondt, D.J. Miller et al., *Proc. ODP, Sci., Res.*, 201, College Station, TX, Ocean Drilling Program, 1-11.

Subramanian, S., A.L. Ballard, R.A. Kini, S.F. Dec, and E.D. Sloan (2000), Structural transitions in methane plus ethane gas hydrates - part i: upper transition point and applications, *Chem. Eng. Sci*., 55(23):5763-5771.

Suess, E., R. von Huene, et al. (1988), *Proc. ODP, Init. Repts*., 112, College Station, TX, Ocean Drilling Program, doi:10.2973/odp.proc.ir.112.1988.

Sultan, N., P. Cochonat, J.P. Foucher, and J. Mienert (2004), Effect of gas hydrates melting on seafloor slope instability, *Mar. Geol*., 213, 379-401.

Torres, M.E., and W.D. Rugh (2006), Data report: Isotopic characterization of dissolved inorganic carbon in pore waters, Leg 204, *Proc. ODP, Sci. Res.*, 204, doi:10.2973/odp.proc.sr.204.117.2006.

Torres, M.E., and M. Kastner (2009), Data report: Clues about carbon cycling in methane-bearing sediments using stable isotopes of the dissolved inorganic carbon, IODP Expedition 311, *Proc. Integrated Ocean Drill. Program, 311*, doi:10.2204/iodp.proc.311.206.2009.

Torres, M.E., K. Wallman, A.M. Trehu, G. Bohrmann, W.S. Borowski, and H. Tomaru (2004), Gas hydrate growth, methane transport, and chloride enrichment at the southern summit of Hydrate Ridge, Cascadia margin off Oregon, *Earth Planet. Sci. Lett*., 226, 225241.

Trehu, A.M, G. Bohrmann, F.R. Rack, M.E. Torres, et al., (2003), *Proc. ODP, Init. Repts*., 204, College Station, TX, Ocean Drilling Program, doi:10.2973/odp.proc.ir.204.2003.

Trehu, A.M., P.E. Long, M.E. Torres, G. Bohrmann, F.R. Rack, T.S. Collett, et al. (2004), Three-dimensional distribution of gas hydrate beneath southern Hydrate Ridge: Constraints from ODP Leg 204, *Earth Planet. Sci. Lett*., 222, 845-862, doi:10.1016/j.epsl.2004.03.035.

Valentine, D.L., and W.S. Reeburgh (2000), New perspectives on anaerobic methane oxidation, *Environ. Microbiol*., 2, 477-484, doi:10.1046/j.1462-2920.2000.00135.x.

von Huene, R., and Pecher, I.A. (1999), Vertical tectonics and the origins of BSRs along the Peru margin, *Earth Planet. Sci. Lett*., 166(1-2), 47-55.

Waite, W.F, C. Santamarina, D. Cortes, B. Dugan, N. Espinoza, J. Germaine, J. Jang, J. Jung, T. Kneafsey, H. Shin, K. Soga, W. Winters, T-S. Yun (2009), Physical properties of hydrate-bearing sediments, *Rev. Geophys*., 47, RG4003, doi:10.1029/2008RG000279.

Wallman, K., G. Aloisi, M. Haeckel, A. Obzhirov, G. Pavlova, and P. Tishchenko (2006), Kinetics of organic matter degradation, microbial methane generation, and gas hydrate formation in anoxic marine sediments, *Geochim. Cosmochim. Acta*, 70, 3905-3927.

Walsh, M.R., S.H. Hancock, S.J. Wilson, S.L. Patil, G.J. Moridis, R. Boswell, T.S. Collett, C.A. Koh, and E.D. Sloan (2009), Preliminary report on the commercial viability of gas production from natural gas hydrates, *Energy Econ*., 31, 815-823, doi:10.1016/j.eneco.2009.03.006.

Weinberger, J.L. and K.M. Brown (2006), Fracture networks and hydrate distribution at Hydrate Ridge, Oregon, *Earth Planet. Sci. Lett*., 245(1), 123136.

Weinberger, J.L., K.M. Brown, and P.E. Long (2005), Painting a picture of gas hydrate distribution with thermal images, *Geophys. Res. Lett*., 32, L04609, doi:10.1029/2004GL021437.

Wellsbury P., K. Goodman, T. Barth, B.A. Cragg, S.P. Barnes, and R.J. Parkes (1997), Deep marine biosphere fuelled by increasing organic matter availability during burial and heating, *Nature*, 388, 573-576.

Westbrook, G.K., B. Carson, and R.J. Musgrave et al., editors (1994), *Proc. ODP, Init. Repts.*, 146 (Pt. 1), College Station, TX, Ocean Drilling Program.

Winters, W.J., B. Dugan, and T.S. Collett (2008), Physical properties of sediments from Keathley Canyon and Atwater Valley, JIP Gulf of Mexico gas hydrate drilling program, *Mar. Pet. Geol*., 25, 896-905, doi:10.1016/j.marpetgeo.2008.01.018.

Xu, W., and C. Ruppel (1999), Predicting the occurrence, distribution, and evolution of methane gas hydrate in porous marine sediments, *J. Geophys. Res*., 104, 5081-5095, doi:10.1029/1998JB900092.

Yang, X.S. and A.C. Fowler (1998), Fast and slow compaction in sedimentary basins, *SIAM J. Appl. Math*., 59(1), 365-385.

Yu, X., J. Li, J. Gong, J. Chen, X. Jin, L. Young-Lee, H. Li, and J. Xu (2006), Stable carbon and nitrogen isotopic composition of gas hydrate-bearing sediment from Hydrate Ridge, Cascadia Margin, *Sci. China Ser. D: Earth Sci*., 49, 872-880.

Zatsepina, O.Y., and B.A. Buffett (1998), Thermodynamic conditions for the stability of gas hydrate in the seafloor, *J. Geophys. Res*., 103(B10), 2412724139, doi:10.1029/98JB02137.

Zeikus, J.G., and M.R. Winfrey (1976), Temperature limitations of methanogenesis in aquatic sediments, *Appl. Environ. Microbiol*., 31, 99-107.

# Appendix A

# Chemical Reactions - Methanogenesis

Methanogenesis is complex but can be represented with a simplified set of reactions (e.g., *Conrad*, 2005)

Fermentation:

$$6\mathrm{CH_2O} + 2\mathrm{H_2O} \longrightarrow 2\mathrm{CH_3COOH} + 2\mathrm{CO_2} + 4\mathrm{H_2} \quad \text{(A.1)}$$

Acetate methanogenesis and $CO_2$ reduction:

$$2\mathrm{CH_3COOH} \longrightarrow 2\mathrm{CH_4} + 2\mathrm{CO_2} \quad \text{(A.2)}$$

$$\mathrm{CO_2} + 4\mathrm{H_2} \longrightarrow \mathrm{CH_4} + 2\mathrm{H_2O} \quad \text{(A.3)}$$

Overall reaction:

$$2\mathrm{CH_2O} \longrightarrow \mathrm{CH_4} + \mathrm{CO_2} \quad \text{(A.4)}$$

The carbon dioxide generated will form DIC:

$$\mathrm{CO_2 + H_2O \quad \longrightarrow \quad HCO_3^- + H^+} \tag{A.5}$$

Carbon isotope fractionation during methanogenesis is also complex and depends on the composition of precursors, various fractionation factors, and the relative contribution of methanogenic pathways (e.g., *Conrad*, 2005). By combining fermentation and both pathways for methanogenesis (equations A.1-A.4), we have implicitly integrated carbon isotope fractionation within intermediate reactions.

# Appendix B

## Carbon Isotope Composition of Organic Matter at Site 1230E

These measurements were made by Bill Peterson in sediment cores recovered at Site 1230E drilled during Leg 201 operations (*Dickens G.R., pers. comm*., 2008). Pore water data was not collected at this hole. This hole was drilled primarily to analyze the bulk sediment for C and N masses and their respective carbon isotope compositions. A total of 34 samples of bulk sediment were analyzed from the upper 24 m for their carbon isotope composition. The average value as tabulated below is -22 $^{0}/_{00}$.

Table B.1 : Carbon Isotope Composition of Organic Matter at Site 1230E

| Core | Section | Section top (m) | Interval (cm) | Depth (mcd) [a] | TOC (%) [b] | $\delta^{13}C$ (‰) |
|---|---|---|---|---|---|---|
| 1H | 1 | 0 | 20-22 | 0.21 | 2.3 | -21.1 |
| 1H | 1 | 0 | 35-37 | 0.36 | 2.7 | -21.7 |
| 1H | 1 | 0 | 140-142 | 1.41 | 1.8 | -22.2 |
| 1H | 2 | 1.5 | 40-42 | 1.91 | 3.6 | -21.9 |
| 2H | 1 | 4 | 25-27 | 4.26 | 2.4 | -22.3 |
| 2H | 1 | 4 | 63-67 | 4.65 | 2.8 | -22.2 |
| 2H | 2 | 5.5 | 85-87 | 6.36 | 2.4 | -22.7 |
| 2H | 3 | 7 | 31-33 | 7.32 | 3.0 | -22.1 |
| 2H | 3 | 7 | 65-67 | 7.66 | 2.6 | -22.4 |
| 2H | 3 | 7 | 71-73 | 7.72 | 2.3 | -22.2 |
| 2H | 3 | 7 | 112-114 | 8.13 | 2.3 | -22.1 |
| 2H | 3 | 7 | 125-127 | 8.26 | 2.6 | -22.3 |
| 2H | 4 | 8.5 | 5-7 | 8.56 | 2.6 | -22.6 |
| 2H | 4 | 8.5 | 23-27 | 8.75 | 2.4 | -22.6 |
| 2H | 4 | 8.5 | 123-127 | 9.75 | 2.7 | -22.9 |
| 2H | 4 | 8.5 | 143-144 | 9.935 | 2.0 | -22.4 |
| 2H | 5 | 10 | 75-78 | 10.765 | 2.6 | -22.2 |
| 2H | 5 | 10 | 95-97 | 10.96 | 2.2 | -22.6 |
| 2H | 5 | 10 | 126-127 | 11.265 | 2.3 | -22.8 |
| 2H | 6 | 11.5 | 45-47 | 11.96 | 2.7 | -22.2 |
| 2H | 6 | 11.5 | 105-107 | 12.56 | 2.3 | -22.7 |
| 2H | 7 | 13 | 25-27 | 13.26 | 2.1 | -22.8 |
| 2H | 7 | 13 | 65-67 | 13.66 | 2.3 | -22.6 |
| 3H | 1 | 13.5 | 70-72 | 14.21 | 2.7 | -22.6 |
| 3H | 1 | 13.5 | 120-122 | 14.71 | 2.7 | -22.7 |
| 3H | 2 | 15 | 20-22 | 15.21 | 2.1 | -23.0 |
| 3H | 2 | 15 | 70-72 | 15.71 | 2.6 | -23.5 |
| 3H | 3 | 16.5 | 20-22 | 16.71 | 2.3 | -22.8 |
| 3H | 3 | 16.5 | 120-122 | 17.71 | 2.2 | -22.9 |
| 3H | 4 | 18 | 20-22 | 18.21 | 2.3 | -22.6 |
| 3H | 4 | 18 | 70-72 | 18.71 | 2.5 | -23.2 |
| 3H | 5 | 19.5 | 20-22 | 19.71 | 2.6 | -22.5 |
| 3H | 5 | 19.5 | 70-72 | 20.21 | 2.2 | -22.9 |
| 4H | 1 | 23 | 120-122 | 24.21 | 2.2 | -22.4 |

[a]Depth scales are reported (mcd) although core gaps and overlaps adjustments were not made to the sample data.

[b]TOC refers to the amount of C (by mass) in the original sample prior to acidification.

# Appendix C

# 1-D Mathematical Model for Pore Water Constituents in Shallow Sediments

Compiling all the component mass balance equations described in previous publications (*Bhatnagar et al*., 2007, 2008a; *Chatterjee et al*., 2011a), and normalizing them with the help of the scaling scheme developed in *Bhatnagar et al*. (2007), we discuss the dimensionless mass balance equations for all the components that constitute our model.

**Organic carbon**

Particulate organic carbon lands on the seafloor and gets buried as a result of sedimentation. A small portion of this amount is utilizable (labile) under microbial action. Microbes act on this labile fraction to consume pore water $SO_4^{2-}$ by organoclastic sulfate reduction (Equation 3.2) and to generate methane by the methanogenesis reaction (Equation 3.3). The dimensionless mass balance equation for labile organic carbon is:

$$\frac{\partial}{\partial \tilde{t}}\left[(1-\tilde{\phi})\tilde{\alpha}\right] + Pe_1 \frac{\partial}{\partial \tilde{z}}\left[\left(\frac{1+\gamma}{\gamma}\right)\tilde{U}_{sed}\tilde{\alpha}\right] = -Da(1-\tilde{\phi})\tilde{\alpha}$$

$$-\left[\frac{(1-\tilde{\phi})(1+\gamma\tilde{\phi})}{1+\gamma}S_w\right]\frac{D_s M_{POC} c_{s,o}}{D_m M_{SO_4} c_{m,eqb}} Da_{POC}\tilde{\alpha}\tilde{c}_s^l. \tag{C.1}$$

**Initial and boundary conditions**

Initially, there is no organic carbon in the sediment. At $t = 0$, organic carbon lands on the seafloor and organic carbon content in the sediment is normalized to this seafloor value.

$$\tilde{\alpha}(\tilde{z}, 0) = 0, \quad \tilde{\alpha}(0, \tilde{t}) = 1. \tag{C.2}$$

where $\tilde{\alpha}$ is the dimensionless organic carbon content in sediment, normalized by the amount of initial organic carbon ($\alpha_o$) that lands on the seafloor at the time of deposition. $c_i^j$ represents mass fraction of component $i$ in phase $j$, $S_j$ represents saturation of phase $j$ in pore space, $D_i$ and $M_i$ represent the diffusivity and molecular weight of component $i$. Subscripts $w$, $POC$, $m$, $s$, $b$, $Ca$, $CaCO_3$ denote water, particulate organic carbon, $CH_4$, $SO_4^{2-}$, DIC (or $HCO_3^-$), $Ca^{2+}$, calcite, respectively. Superscripts $sed$, $l$, $h$, and $g$ represent the sediment, liquid, hydrate and free gas phases respectively. We scale vertical depth as $\tilde{z} = z/L_t$, where $L_t$ is the depth to the base of the GHSZ. Time is normalized by combining $L_t$ and diffusivity of methane $D_m$ ($\tilde{t} = t/(L_t^2/D_m)$).

The two Peclet numbers $Pe_1$, $Pe_2$ and the three Damkohler numbers $Da$, $Da_{AOM}$ and $Da_{POC}$ are defined as:

$$Pe_1 = \frac{U_{f,sed} L_t}{D_m}, \quad Pe_2 = \frac{U_{f,ext} L_t}{D_m},$$

$$Da = \frac{\lambda L_t^2}{D_m}(\text{Methanogenesis}), \quad Da_{AOM} = \frac{\rho_w c_{m,eqb}}{M_{CH_4}} \frac{\lambda_{AOM} L_t^2}{D_m}(\text{AOM}),$$

$$Da_{POC} = \frac{\rho_w c_{m,eqb}}{M_{POC}} \frac{\lambda_{POC} L_t^2}{D_s}(\text{OSR}). \tag{C.3}$$

where $U_{f,sed}$ is the fluid flux due to sedimentation and compaction, $U_{f,ext}$ is the upward fluid flux due to external sources and $\lambda$, $\lambda_{AOM}$ and $\lambda_{POC}$ represent the rate of three kinetic reactions. The fluid flux due to sedimentation-compaction, $U_{f,sed}$ is related to the sedimentation rate at the seafloor ($\dot{S}$) and the reduced porosities (*Bhatnagar et al*., 2007)

The reduced porosity parameters ($\tilde{\phi}$ and $\gamma$) and the normalized sediment flux, $\tilde{U}_{sed}$ are defined as in (*Bhatnagar et al*., 2007; *Chatterjee et al*., 2011a). Porosity loss due to compaction is modeled as a function of effective stress, which leads to a porosity profile with respect to depth (*Berner*, 1980; *Bhatnagar et al*., 2007).

**Methane**

Methane forms from the organic carbon in the sediment pore space due to methanogenesis (Equation 3.3) that can accumulate as dissolved gas, hydrate, and free gas. The dissolved $CH_4$ can also react with the pore water sulfate by AOM reaction (Equation 3.1). Following *Bhatnagar et al*. (2007, 2008a), the three-phase (liquid, hydrate and free gas) dimensionless methane mass balance equation is rewritten to include the AOM and methanogenesis reaction in dimensionless form

as:

$$\frac{\partial}{\partial\tilde{t}}\left[\left(\frac{1+\gamma\tilde{\phi}}{\gamma}\right)\left((1-S_h-S_g)\tilde{c}_m^l+S_h\tilde{\rho}_h\tilde{c}_m^h+S_g\tilde{\rho}_g\tilde{c}_m^g\right)\right]+\left(\frac{1+\gamma}{\gamma}\right)(Pe_1+Pe_2)\frac{\partial\tilde{c}_m^l}{\partial\tilde{z}}$$

$$+\left(\frac{1+\gamma}{\gamma}\right)\frac{\partial}{\partial\tilde{z}}\left[-\frac{Pe_1\tilde{U}_s(1+\gamma\tilde{\phi})}{\gamma(1-\tilde{\phi})}S_hc_w^h\tilde{\rho}_h\tilde{c}_m^l+\frac{Pe_1\tilde{U}_s(1+\gamma\tilde{\phi})}{\gamma(1-\tilde{\phi})}(S_h\tilde{\rho}_h\tilde{c}_m^h+S_g\tilde{\rho}_g\tilde{c}_m^g)\right]$$

$$=\frac{\partial}{\partial\tilde{z}}\left[\left(\frac{1+\gamma\tilde{\phi}}{\gamma}\right)S_w\frac{\partial\tilde{c}_m^l}{\partial\tilde{z}}\right]+\frac{M_{CH_4}\tilde{\rho}_{sed}Da(1-\tilde{\phi})\tilde{\alpha}\beta}{2M_{POC}}$$

$$-\left(\frac{1+\gamma\tilde{\phi}}{\gamma}\right)\frac{S_wM_{CH_4}c_{s,o}Da_{AOM}\tilde{c}_m^l\tilde{c}_s^l}{M_{SO_4}c_{m,eqb}}. \tag{C.4}$$

where $\tilde{\rho}_i$ is the density of phase $j$ normalized by water density $\rho_w$, the methane mass fraction in phase $j$ ($c_m^j$) is scaled by the methane solubility in the liquid phase at the base of the GHSZ ($c_{m,eqb}$), while $SO_4^{2-}$, DIC, and $Ca^{2+}$ mass fractions in pore water ($c_s^l$, $c_b^l$, and $c_{Ca}^l$) are normalized to their respective seawater values, ($c_{s,o}$, $c_{b,o}$, and $c_{Ca,o}$):

$$\tilde{c}_m^i=\frac{c_m^i}{c_{m,eqb}}\text{for } i\in\{l,h,g\},\quad \tilde{c}_s^l=\frac{c_s^l}{c_{s,o}},\quad \tilde{c}_b^l=\frac{c_b^l}{c_{b,o}},\quad \tilde{c}_{Ca}^l=\frac{c_{Ca}^l}{c_{Ca,o}}. \tag{C.5}$$

**Initial and boundary conditions**

Initially, there is no methane in the pore fluids, consequently, no hydrates or free gas. Seafloor methane is set to zero and a finite value is specified at the bottom

boundary.

$$\tilde{c}_m^l(\tilde{z},0)=0, \quad \tilde{c}_m^l(0,\tilde{t})=0, \quad \tilde{c}_m^l(\tilde{L}_z,\tilde{t})=\tilde{c}_{m,ext}=c_{m,eqb}(\tilde{L}_z). \tag{C.6}$$

**Sulfate**

As discussed above, the pore water sulfate can be consumed by two sources: (a) dissolved $CH_4$ in pore fluid, and (b) the organic carbon in the sediment. The overall dimensionless sulfate mass balance equation incorporating both these reduction pathways is (*Bhatnagar et al*., 2007, 2008a; *Chatterjee et al*., 2011a):

$$\frac{\partial}{\partial\tilde{t}}\left[\left(\frac{1+\gamma\tilde{\phi}}{\gamma}\right)S_w\tilde{c}_s^l\right]+\left(\frac{1+\gamma}{\gamma}\right)\frac{\partial}{\partial\tilde{z}}\left[\left(Pe_1+Pe_2-\frac{Pe_1\tilde{U}_s(1+\gamma\tilde{\phi})}{\gamma(1-\tilde{\phi})}S_h c_w^h\tilde{\rho}_h\right)\tilde{c}_s^l\right]$$

$$=\frac{\partial}{\partial\tilde{z}}\left[\left(\frac{1+\gamma\tilde{\phi}}{\gamma}\right)\frac{D_s}{D_m}S_w\frac{\partial\tilde{c}_s^l}{\partial\tilde{z}}\right]-\left[\frac{(1+\gamma\tilde{\phi})}{\gamma}S_w\right]Da_{AOM}\tilde{c}_m^l\tilde{c}_s^l$$

$$-\left[\frac{(1+\gamma\tilde{\phi})(1-\tilde{\phi})}{1+\gamma}S_w\right]\frac{D_s}{2D_m}\tilde{\rho}_{sed}Da_{POC}\tilde{\alpha}\beta\tilde{c}_s^l. \tag{C.7}$$

**Initial and boundary conditions**

At initial time, pore space contains seawater, so pore water $SO_4^{2-}$ is at its seawater concentration. At the seafloor, sulfate concentration is set to its seawater value and there is no sulfate specified at the bottom boundary.

$$\tilde{c}_s^l(\tilde{z},0)=1, \quad \tilde{c}_s^l(0,\tilde{t})=1, \quad \tilde{c}_s^l(\tilde{L}_z,\tilde{t})=\tilde{c}_{s,ext}=0, \tag{C.8}$$

**Dissolved inorganic carbon (DIC)**

As a result of the two sulfate consumption reactions; AOM (Equation 3.1) and OSR (Equation 3.2), DIC is formed in stoichiometric amounts. However, DIC is also formed in deep sediment as a result of methanogenesis (Equation 3.3) and this DIC can upflux from depth and mix with the DIC generated by the AOM at the SMT. The overall DIC mass balance equation includes accumulation, advection, and diffusion terms, source terms discussed in the three reactions above and the sink term where calcium reacts with the DIC to precipitate as calcite (or dolomite). The dimensionless mass balance equation is shown as (*Chatterjee et al*., 2011a):

$$\frac{\partial}{\partial\tilde{t}}\left[\left(\frac{1+\gamma\tilde{\phi}}{\gamma}\right)S_w\tilde{c}_b^l\right]+\left(\frac{1+\gamma}{\gamma}\right)\frac{\partial}{\partial\tilde{z}}\left[\left(Pe_1+Pe_2-\frac{Pe_1\tilde{U}_s(1+\gamma\tilde{\phi})}{\gamma(1-\tilde{\phi})}S_h c_w^h\tilde{\rho}_h\right)\tilde{c}_b^l\right]$$

$$=\frac{\partial}{\partial\tilde{z}}\left[\left(\frac{1+\gamma\tilde{\phi}}{\gamma}\right)\frac{D_b}{D_m}S_w\frac{\partial\tilde{c}_b^l}{\partial\tilde{z}}\right]+\frac{M_{HCO_3}c_{m,eqb}}{2M_{POC}c_{b,o}}\tilde{\rho}_{sed}Da(1-\tilde{\phi})\tilde{\alpha}\beta$$

$$+\left[\frac{1+\gamma\tilde{\phi}}{\gamma}S_w\right]\frac{M_{HCO_3}c_{s,o}}{M_{SO_4}c_{b,o}}Da_{AOM}\tilde{c}_m^l\tilde{c}_s^l$$

$$+\left[\frac{(1+\gamma\tilde{\phi})(1-\tilde{\phi})}{1+\gamma}S_w\right]\frac{M_{HCO_3}c_{s,o}}{M_{SO_4}c_{b,o}}\frac{D_s}{D_m}\tilde{\rho}_{sed}Da_{POC}\tilde{\alpha}\beta\tilde{c}_s^l-\left[\frac{1+\gamma\tilde{\phi}}{\gamma}S_w\right]\frac{C_{Ca,o}}{C_{b,o}}\frac{\Delta\tilde{c}_{CaCO_3}}{\Delta\tilde{t}}. \quad \text{(C.9)}$$

**Initial and boundary conditions**

At initial time, pore space contains seawater, so DIC present in pore water is at its seawater concentration. At the seafloor, DIC is set to its seawater value and there

is finite DIC concentration specified at the bottom boundary.

$$\tilde{c}_b^l(\tilde{z},0)=1,\;\;\tilde{c}_b^l(0,\tilde{t})=1,\tilde{c}_b^l(\tilde{L}_z,\tilde{t})=\tilde{c}_{b,ext}, \tag{C.10}$$

**Calcium**

Pore water calcium can advect and diffuse in the pore space and react with DIC to precipitate as authigenic carbonates. The overall dimensionless mass balance equation is expressed as (*Chatterjee et al*., 2011a):

$$\frac{\partial}{\partial\tilde{t}}\left[\left(\frac{1+\gamma\tilde{\phi}}{\gamma}\right)S_w\tilde{c}_{Ca}^l\right]+\left(\frac{1+\gamma}{\gamma}\right)\frac{\partial}{\partial\tilde{z}}\left[\left(Pe_1+Pe_2-\frac{Pe_1\tilde{U}_s(1+\gamma\tilde{\phi})}{\gamma(1-\tilde{\phi})}S_hc_w^h\tilde{\rho}_h\right)\tilde{c}_{Ca}^l\right]$$

$$=\frac{\partial}{\partial\tilde{z}}\left[\left(\frac{1+\gamma\tilde{\phi}}{\gamma}S_w\right)\frac{D_{Ca}}{D_m}\frac{\partial\tilde{c}_{Ca}^l}{\partial\tilde{z}}\right]-\left[\frac{1+\gamma\tilde{\phi}}{\gamma}S_w\right]\frac{\Delta\tilde{c}_{CaCO_3}}{\Delta\tilde{t}}. \tag{C.11}$$

**Initial and boundary conditions**

At initial time, pore space contains seawater, so $Ca^{2+}$ present in pore water is at its seawater concentration. At the seafloor, calcium is set to its seawater value and there is finite $Ca^{2+}$ concentration specified at the bottom boundary (in equilibrium with DIC at depth).

$$\tilde{c}_{Ca}^l(\tilde{z},0)=1,\;\;\tilde{c}_{Ca}^l(0,\tilde{t})=1,\tilde{c}_{Ca}^l(\tilde{L}_z,\tilde{t})=\tilde{c}_{Ca,ext}, \tag{C.12}$$

**Carbon isotope composition of $CH_4$ and DIC**

In addition to the $CH_4$ and DIC concentration, we need to account for changes in the carbon isotope composition in pore fluids. Our model accounts for advection, diffusion and fractionation of carbon isotope due to various reactions associated with the carbon (especially for $CH_4$ and DIC). The overall dimensionless mass balance equations for carbon isotopes of $CH_4$ and DIC are shown as (*Chatterjee et al*., 2011a):

$^{12}\mathrm{C}$ and $^{13}\mathrm{C}$ of $CH_4$:

$$\begin{aligned}
&\frac{\partial}{\partial\tilde{t}}\left[\left(\frac{1+\gamma\tilde{\phi}}{\gamma}\right)\left((1-S_h-S_g)\tilde{c}_m^l+S_h\tilde{\rho}_h\tilde{c}_m^h+S_g\tilde{\rho}_g\tilde{c}_m^g\right)\delta^{13}\mathrm{C}_{CH_4}\right]\\
&\qquad+\left(\frac{1+\gamma}{\gamma}\right)(Pe_1+Pe_2)\,\frac{\partial\left(\tilde{c}_m^l\delta^{13}\mathrm{C}_{CH_4}\right)}{\partial\tilde{z}}\\
&\qquad-\left(\frac{1+\gamma}{\gamma}\right)\frac{\partial}{\partial\tilde{z}}\left[\frac{Pe_1\tilde{U}_s(1+\gamma\tilde{\phi})}{\gamma(1-\tilde{\phi})}S_h c_w^h\tilde{\rho}_h\tilde{c}_m^l\delta^{13}\mathrm{C}_{CH_4}\right]\\
&\qquad+\left(\frac{1+\gamma}{\gamma}\right)\frac{\partial}{\partial\tilde{z}}\left[\frac{Pe_1\tilde{U}_s(1+\gamma\tilde{\phi})}{\gamma(1-\tilde{\phi})}(S_h\tilde{\rho}_h\tilde{c}_m^h+S_g\tilde{\rho}_g\tilde{c}_m^g)\delta^{13}\mathrm{C}_{CH_4}\right]\\
&=\frac{\partial}{\partial\tilde{z}}\left[\left(\frac{1+\gamma\tilde{\phi}}{\gamma}\right)S_w\frac{\partial\left(\tilde{c}_m^l\delta^{13}\mathrm{C}_{CH_4}\right)}{\partial\tilde{z}}\right]+\frac{M_{CH_4}\tilde{\rho}_{sed}Da(1-\tilde{\phi})\tilde{\alpha}\beta\delta^{13}\mathrm{C}_{CH_4,meth}}{2M_{POC}}\\
&\qquad-\left(\frac{1+\gamma\tilde{\phi}}{\gamma}\right)\frac{S_w M_{CH_4}c_{s,o}Da_{AOM}\tilde{c}_m^l\tilde{c}_s^l\delta^{13}\mathrm{C}_{CH_4}}{M_{SO_4}c_{m,eqb}}. \qquad \text{(C.13)}
\end{aligned}$$

$^{12}\mathrm{C}$ and $^{13}\mathrm{C}$ of DIC:

$$\frac{\partial}{\partial\tilde{t}}\left[\left(\frac{1+\gamma\tilde{\phi}}{\gamma}\right)S_w\tilde{c}_b^l\delta^{13}\mathrm{C}_{HCO_3}\right]$$

$$+\left(\frac{1+\gamma}{\gamma}\right)\frac{\partial}{\partial\tilde{z}}\left[\left(Pe_1+Pe_2-\frac{Pe_1\tilde{U}_s(1+\gamma\tilde{\phi})}{\gamma(1-\tilde{\phi})}S_h c_w^h\tilde{\rho}_h\right)\tilde{c}_b^l\delta^{13}\mathrm{C}_{HCO_3}\right]$$

$$=\frac{\partial}{\partial\tilde{z}}\left[\left(\frac{1+\gamma\tilde{\phi}}{\gamma}\right)\frac{D_b}{D_m}S_w\frac{\partial\left(\tilde{c}_b^l\delta^{13}\mathrm{C}_{HCO_3}\right)}{\partial\tilde{z}}\right]+\frac{M_{HCO_3}c_{m,eqb}}{2M_{POC}c_{b,o}}\tilde{\rho}_{sed}Da(1-\tilde{\phi})\tilde{\alpha}\beta\delta^{13}\mathrm{C}_{HCO_3,\ meth}$$

$$+\left[\frac{1+\gamma\tilde{\phi}}{\gamma}S_w\right]\frac{M_{HCO_3}c_{s,o}}{M_{SO_4}c_{b,o}}Da_{AOM}\tilde{c}_m^l\tilde{c}_s^l\delta^{13}\mathrm{C}_{CH_4}$$

$$+\left[\frac{(1+\gamma\tilde{\phi})(1-\tilde{\phi})}{1+\gamma}S_w\right]\frac{M_{HCO_3}c_{s,o}}{M_{SO_4}c_{b,o}}\frac{D_s}{D_m}\tilde{\rho}_{sed}Da_{POC}\tilde{\alpha}\beta\tilde{c}_s^l\delta^{13}\mathrm{C}_{HCO_3,\ POC}$$

$$-\left[\frac{1+\gamma\tilde{\phi}}{\gamma}S_w\right]\frac{C_{Ca,o}}{C_{b,o}}\frac{\Delta\left(\tilde{c}_{CaCO_3}\delta^{13}\mathrm{C}_{HCO_3}\right)}{\Delta\tilde{t}}. \qquad \text{(C.14)}$$

where $\delta^{13}\mathrm{C}_{CH_4}$, $\delta^{13}\mathrm{C}_{POC}$ and $\delta^{13}\mathrm{C}_{HCO_3}$ are the $\delta^{13}\mathrm{C}$ of $CH_4$, POC and DIC, respectively, $\delta^{13}\mathrm{C}_{CH_4,\ meth}$ and $\delta^{13}\mathrm{C}_{HCO_3,\ meth}$ are the $\delta^{13}\mathrm{C}$ of $CH_4$ and DIC generated by methanogenesis, and $\delta^{13}\mathrm{C}_{HCO_3,\ POC}$ is the $\delta^{13}\mathrm{C}$ of DIC generated by OSR.

**Initial and boundary conditions**

At initial time, pore space contains seawater, so seawater conditions exist at all depth. The $\delta^{13}\mathrm{C}$ is calculated relative to a marine carbonate. Therefore, the $\delta^{13}\mathrm{C}$ is set to its seawater value at the seafloor.

$$\delta^{13}\mathrm{C}_{CH_4}(\tilde{z},0)=\delta^{13}\mathrm{C}_{HCO_3}(\tilde{z},0)=0,\quad \delta^{13}\mathrm{C}_{CH_4}(0,\tilde{t})=\delta^{13}\mathrm{C}_{HCO_3}(0,\tilde{t})=0. \qquad \text{(C.15)}$$

The basal boundary ($\tilde{L}_z$) values of $\delta^{13}\mathrm{C}$ of $CH_4$ ($\delta^{13}\mathrm{C}_{CH_4}$) and DIC ($\delta^{13}\mathrm{C}_{HCO_3}$) are specified as observed in field data at Site 1230 (*Biddle et al*., 2006).

$$\delta^{13}\mathrm{C}_{CH_4}(\tilde{L}_z,\tilde{t}) = \delta^{13}\mathrm{C}_{CH_4,ext} = -70\,{}^0\!/\!_{00},, \quad \delta^{13}\mathrm{C}_{HCO_3}(\tilde{L}_z,\tilde{t}) = \delta^{13}\mathrm{C}_{HCO_3,ext} = +17\,{}^0\!/\!_{00}. \tag{C.16}$$

During methanogenesis, a range of solid organic carbon with a range of carbon isotope compositions produces $CH_4$ relatively depleted in $^{13}\mathrm{C}$, and DIC relatively enriched in $^{13}\mathrm{C}$. The pathways involved are somewhat complex, especially regarding isotope fractionation (*Conrad*, 2005). To simplify the modeling, we assume a fixed (site-specific) $\delta^{13}\mathrm{C}$ for labile POC ($\delta^{13}\mathrm{C}_{POC}$), and a fixed (site-specific) $\delta^{13}\mathrm{C}$ for $CH_4$ generated during methanogenesis ($\delta^{13}\mathrm{C}_{CH_4,\ meth}$). The $\delta^{13}\mathrm{C}_{CH_4,\ meth}$ values are determined by computing the average values of $\delta^{13}\mathrm{C}$ of $CH_4$ measured at Site 1230. For Site 1230, the values are:

$$\delta^{13}\mathrm{C}_{POC} = -22\,{}^0\!/\!_{00}, \quad \delta^{13}\mathrm{C}_{CH_4,meth} = -65\,{}^0\!/\!_{00}. \tag{C.17}$$

This implies that the fractionation factor ($\epsilon_m$) and the $\delta^{13}\mathrm{C}$ of DIC generated during methanogenesis ($\delta^{13}\mathrm{C}_{HCO_3,\ meth}$) will also be fixed. Fractionation factor ($\epsilon_m$) is defined as the ratio of $\delta^{13}\mathrm{C}$ of labile POC and $CH_4$.

$$\epsilon_m = \frac{\delta^{13}\mathrm{C}_{POC} + 1000}{\delta^{13}\mathrm{C}_{CH_4,meth} + 1000}. \tag{C.18}$$

The $\delta^{13}\mathrm{C}_{HCO_3,\ meth}$ values and the fractionation factors at Site 1230 are calculated using the carbon isotope compositions $\delta^{13}\mathrm{C}_{POC}$ , and $\delta^{13}\mathrm{C}_{CH_4,\ meth}$ .

$$\delta^{13}\mathrm{C}_{HCO_3,meth} = +21\ {}^{0}\!/_{00}, \quad \epsilon_m = 1.046. \tag{C.19}$$

The carbon isotope composition of DIC ($\delta^{13}\mathrm{C}_{HCO_3}$) generated by OSR is equated to that of POC ($\delta^{13}\mathrm{C}_{POC}$). For Site 1230:

$$\delta^{13}\mathrm{C}_{HCO_3,POC} = \delta^{13}\mathrm{C}_{POC} = -22\ {}^{0}\!/_{00}. \tag{C.20}$$

# Appendix D

## Analytical Theory Relating Fluid Flux and the Average Hydrate Saturation

An analytical theory is developed to relate the average hydrate saturation to the fluid flux through porous media in any orientation to the vertical axis (Figure D.1). This model revisits the approach developed by *Bhatnagar et al.,* (2011) to correlate the depth of the SMT to the average hydrate saturation in marine sediments dominated by methane rising with pore fluids from depth. Likewise, in this model, it is assumed that there is no microbial generation of methane, and methane-charged pore fluids rising from depth is the only source of methane. Furthermore, pore water sulfate is assumed to be absent in pore fluids and methane can escape into the seafloor even though some of the detailed pore water chemistry models have been published in the last decade relating sulfate and methane fluxes at the SMT in shallow sediments (e.g. *Davie and Buffett.,* 2003b; *Bhatnagar et al.,* 2008b, 2011; *Chatterjee et al.,* 2011a; *Malinverno and Pohlman*, 2011).

**Water mass balance**

For simplicity, steady-state water mass balance is expressed as:

$$\frac{d}{dz}\left[U_f c_w^l \rho_w + \frac{U_s}{1-\phi}\phi S_h c_w^h \rho_h\right] = 0, \quad 0 < z < L_t \tag{D.1}$$

The invariant steady-state water flux can be restated as:

$$U_f c_w^l \rho_w + \frac{U_s}{1-\phi}\phi S_h c_w^h \rho_h = F_{H_2O} = (U_{f,sed} + U_{f,ext}\cos\theta)\rho_w, \quad 0 < z < L_t \tag{D.2}$$

where $\theta$ is the dip angle relative to the vertical axis. The net fluid (liquid) flux, $U_f$, sediment flux, $U_s$, and the fluid flux due to sedimentation and compaction, $U_{f,sed}$, are assumed to be vertical; whereas the external fluid flow, $U_{f,ext}$ is along the permeable conduit inclined at angle $\theta$ to the vertical. Therefore, the vertical component of the external fluid flux, $U_{f,ext}\cos\theta$ is added to the sedimentation-compaction driven fluid flux, $U_{f,sed}$ to obtain the net vertical fluid flux. Assuming low methane solubility in water, $c_w^l$ is approximated as unity and normalizing gas hydrate density by water density:

$$U_f = (U_{f,sed} + U_{f,ext}\cos\theta) - \frac{U_s}{1-\phi}\phi S_h c_w^h \tilde{\rho}_h, \quad 0 < \tilde{z} < 1 \tag{D.3}$$

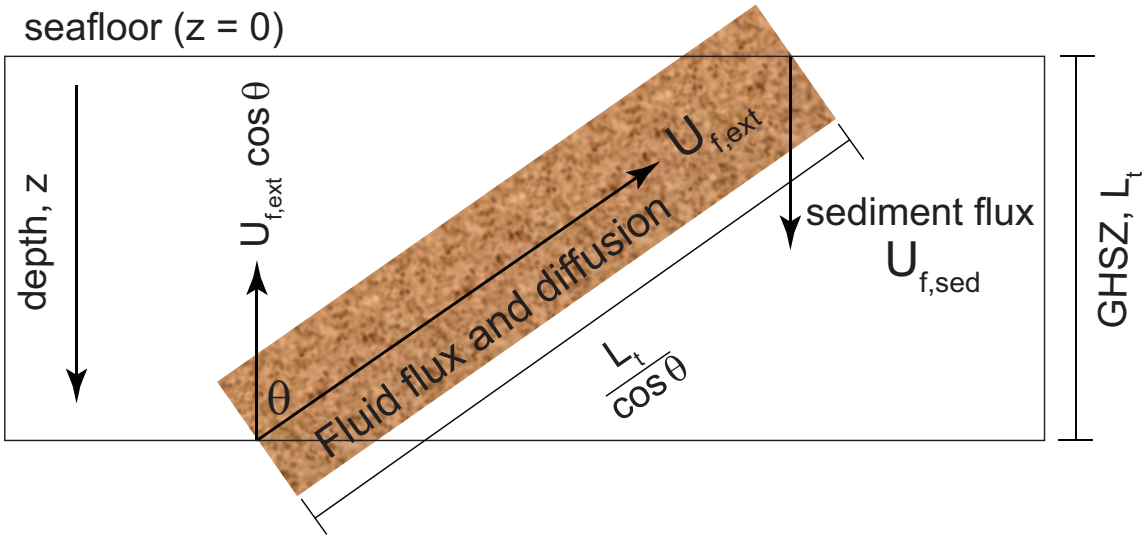


Figure D.1 : Schematic of porous media inclined at angle $\theta$ to the vertical. The diagram illustrates the lengths, depths and fluxes in geologic systems that are described in the model.

**Methane mass balance**

The steady-state two-phase (dissolved and hydrate), methane mass balance between the seafloor ($z = 0$) and the base of the GHSZ (z = $L_t$) is expressed assuming $S_g$ = 0 and no methane formation by methanogenesis reaction:

$$\frac{d}{dz}\left[U_f c_m^l \rho_w + \frac{U_s}{1-\phi}\phi S_h c_m^h \rho_h - \phi(1-S_h)\rho_w D_m \frac{dc_m^l}{dz}\cos\theta\right] = 0 \quad , \quad 0 < z < L_t \qquad \text{(D.4)}$$

where $U_f$ is the total water flux, $U_s$ is the sediment flux, $S_h$ is the gas hydrate saturation, and $c_m^h$ is the mass fraction of methane in the hydrate phase (a constant, $c_m^h = 0.134$) for structure I hydrate (*Sloan and Koh, 2007*). Therefore, steady-state

methane mass flux can be rewritten as:

$$U_f c_m^l \rho_w + \frac{U_s}{1-\phi}\phi S_h c_m^h \rho_h - \phi(1-S_h)\rho_w D_m \frac{dc_m^l}{dz}\cos\theta = F_{CH_4}$$
$$, \quad 0 < z < L_t \qquad \text{(D.5)}$$

where $F_{CH_4}$, is the methane mass flux. Using the same scaling scheme discussed in the main text and in (*Bhatnagar et al.,* 2007, 2011), sediment flux is scaled by $U_{f,sed}$, methane mass fractions by methane solubility at the base of the GHSZ ($c_{m,eqb}$) and substituting $U_f$ as in equation D.3. The scaled methane mass flux is:

$$Q\tilde{c}_m^l + \frac{Pe_1\tilde{U}_s}{1-\tilde{\phi}}\left(\frac{1+\gamma}{\gamma}\right)\left(\frac{1+\gamma\tilde{\phi}}{\gamma}\right)S_h\tilde{\rho}_h\left(\tilde{c}_m^h - c_w^h\tilde{c}_m^l\right) - \left(\frac{1+\gamma\tilde{\phi}}{\gamma}\right)(1-S_h)\frac{d\tilde{c}_m^l}{d\tilde{z}}\cos\theta$$
$$= \frac{F_{CH_4}L_t}{D_m c_{m,eqb}}\left(\frac{1+\gamma}{\gamma}\right) = f_{CH_4}, \quad 0 < \tilde{z} < 1 \qquad \text{(D.6)}$$

where $f_{CH_4}$ is normalized methane mass flux and $Q$ is defined as:

$$Q = \left(\frac{1+\gamma}{\gamma}\right)(Pe_1 + Pe_2\cos\theta) \qquad \text{(D.7)}$$

The depth domain can be divided into two distinct regions: between the seafloor and the shallowest occurrence of gas hydrate, $(1-\tilde{L}_h)$ and from this depth to the base of the GHSZ where $(\tilde{L}_h)$ is the thickness of the gas hydrate occurrence zone (GHOZ). Normalized methane mass flux (Equation D.6) is rewritten for these two zones with simplified expressions as discussed in *Bhatnagar et al.,* (2011). For the

lower region $1-\tilde{L}_h < \tilde{z} < 1$, $S_h$ is set to zero as $\tilde{z} \to 1-\tilde{L}_h^+$:

$$f_{CH_4} = \frac{Q\tilde{c}_{m,sol}(1-\tilde{L}_h)}{1-\exp\left[\frac{Q}{\cos\theta}\left[g(1-\tilde{L}_h)-g(0)\right]\right]} \quad , \quad 0 < \tilde{z} < 1-\tilde{L}_h$$

$$f_{CH_4} = Q\tilde{c}_{m,sol}(\tilde{z}) - \left(\frac{1+\gamma\tilde{\phi}}{\gamma}\right)\tilde{c}'_{m,sol}(\tilde{z})\cos\theta \quad , \quad 1-\tilde{L}_h < \tilde{z} < 1 \qquad \text{(D.8)}$$

where $\tilde{c}_{m,sol}(\tilde{z})$ is the methane solubility at any depth $\tilde{z}$ and is defined as a single-parameter model, $\tilde{c}_{m,sol}(\tilde{z}) = exp(-r_2(1-\tilde{z}))$ as shown in (*Bhatnagar et al.,* 2011) and $g(\tilde{z})$ represents the integral of the porosity term and is defined as:

$$g(\tilde{z}) = \int_0^{1-\tilde{L}_h}\left(\frac{\gamma}{1+\gamma\tilde{\phi}}\right)d\tilde{z} = \frac{N_{t\phi}\gamma\tilde{z}+\gamma^2\ln\left[\eta(1+\gamma)+(1-\eta)e^{\tilde{z}N_{t\phi}}\right]}{(1+\gamma)N_{t\phi}} \qquad \text{(D.9)}$$

The unknown parameter, $\tilde{L_h}$ is solved by equating the two methane mass fluxes in the two distinct zones (equation D.8) at $\tilde{z} = 1-\tilde{L}_h$ for different values of $Q$.

Rearranging equation D.6 and following the theory discussed in *Bhatnagar et al.,* (2011), the gas hydrate profile is rewritten as a function of the scaled depth $\tilde{z}$, as follows:

$$S_h(\tilde{z}) = \frac{\left(\frac{f_{CH_4}-Q\tilde{c}_{m,sol}(\tilde{z})}{\left(\frac{1+\gamma\tilde{\phi}}{\gamma}\right)}\right)+\tilde{c}'_{m,sol}(\tilde{z})\cos\theta}{\left[\frac{Pe_1\tilde{U}_s}{1-\tilde{\phi}}\left(\frac{1+\gamma}{\gamma}\right)\tilde{\rho}_h\left(\tilde{c}_m^h - c_w^h\tilde{c}_{m,sol}\left(\tilde{z}\right)\right)+\tilde{c}'_{m,sol}(\tilde{z})\cos\theta\right]}, \quad 1-\tilde{L}_h < \tilde{z} < 1 \qquad \text{(D.10)}$$

The mass fraction part of the first term in the denominator of equation (D.10) $\left(\tilde{c}_m^h - c_w^h\tilde{c}_{m,sol}(\tilde{z})\right)$ can be simplified further. In the main text, $\tilde{c}_m^h$ was defined as

$\tilde{c}_m^h = c_m^h / c_{m,eqb}^l$, which for most marine systems is of the order of $\tilde{c}_m^h = 0.134/10^{-3} \approx 10^2$. The remaining terms, $c_w^h \tilde{c}_{m,sol}(\tilde{z})$ and $\tilde{c}'_{m,sol}(\tilde{z})$ are usually less than unity implying that that $\tilde{c}_m^h$ is approximately two orders of magnitude greater than the remaining terms in the denominator. Thus, this approximates and simplifies equation (D.10) as:

$$S_h(\tilde{z}) \approx \frac{\left(\frac{f_{CH_4} - Q\tilde{c}_{m,sol}(\tilde{z})}{\left(\frac{1+\gamma\tilde{\phi}}{\gamma}\right)}\right) + \tilde{c}'_{m,sol}(\tilde{z})\cos\theta}{\frac{Pe_1\tilde{U}_s}{1-\tilde{\phi}}\left(\frac{1+\gamma}{\gamma}\right)\tilde{\rho}_h\tilde{c}_m^h}\ ,\ 1-\tilde{L}_h < \tilde{z} < 1 \qquad \text{(D.11)}$$

Integrating this saturation profile over the entire depth between the seafloor and the base of GHSZ and multiplying the integral by $Pe_1$, average hydrate flux, $Pe_1\langle S_h\rangle$ can be defined as a function of system parameters:

$$Pe_1\langle S_h\rangle \approx \int_{1-\tilde{L}_h}^{1} \frac{\left(\frac{f_{CH_4} - Q\tilde{c}_{m,sol}(\tilde{z})}{\left(\frac{1+\gamma\tilde{\phi}}{\gamma}\right)}\right) + \tilde{c}'_{m,sol}(\tilde{z})\cos\theta}{\frac{\tilde{U}_s}{1-\tilde{\phi}}\left(\frac{1+\gamma}{\gamma}\right)\tilde{\rho}_h\tilde{c}_m^h} d\tilde{z} \qquad \text{(D.12)}$$

Specifying the dip angle of the configuration ($\theta$), and other system parameters, and varying external fluid flux, $Pe_2$, top of gas hydrate zone, $1-\tilde{L}_h$ is first computed. Using this value and other system parameters, average hydrate flux $Pe_1\langle S_h\rangle$ is evaluated. The average hydrate saturation, $\langle S_h\rangle$ can be easily computed from this product since $Pe_1$ is a constant parameter at a given geologic setting as it depends on sedimentation rate at the seafloor. Therefore, the fluid flux within a flow conduit in any orientation (to the vertical axis) is related to the average hydrate saturation

in these gas hydrate systems using a simple analytical formulation.